RELIABILITY ANALYSIS AND PERFORMANCE-BASED CODE CALIBRATION FOR BLAST RESISTANT PANELS SUBJECTED TO AIR AND CONTACT BLAST

A Thesis Submitted

In Partial Fulfilment of the Requirements

for the Degree of

DOCTOR OF PHILOSOPHY

by

Kasturi Bhuyan

DEPARTMENT OF CIVIL ENGINEERING

INDIAN INSTITUTE OF TECHNOLOGY GUWAHATI

GUWAHATI – 781039

April, 2022

DECLARATION

I hereby declare that the work which is being presented in the thesis titled "**Reliability Analysis and Performance-Based Code Calibration for Blast Resistant Panels Subjected to Air and Contact Blast**" submitted in the fulfilment of the requirements for the award of the degree of DOCTOR OF PHILOSOPHY in CIVIL ENGINEERING, with specialization in STRUCTURAL ENGINEERING, is an authentic record of my own work carried out in the Department of Civil Engineering, Indian Institute of Technology Guwahati under the supervision of Dr. Hrishikesh Sharma, Associate Professor, Department of Civil Engineering, IIT Guwahati.

The matter embodied in this thesis work has not been submitted by me for the award of any other degree or diploma of this Institute or any other University/Institute.

Kasturi Bhuyan

Date: 26/04/2022

Kasturi Bhuyan

CERTIFICATE

It is certified that the work contained in the thesis entitled "**Reliability Analysis and Performance-Based Code Calibration for Blast Resistant Panels Subjected to Air and Contact Blast**", by **Kasturi Bhuyan** (156104001) has been carried out under my supervision and that this work has not been submitted elsewhere for the award of a degree or diploma.

Date: 26/04/2022

Dr. Hrishikesh Sharma
Associate Professor
Department of Civil Engineering
Indian Institute of Technology Guwahati

ACKNOWLEDGEMENTS

I want to grab this opportunity to acknowledge the kindness of all those who guided and helped me to complete this research.

First of all, I would like to express my sincere thanks to my guide Dr. Hrishikesh Sharma for his co-operation, suggestions and esteemed guidance thorough critical reviews of my work. I thank him for his valuable insights and support throughout my difficult times. Without him, this project would not be in its current shape. Secondly, I want to thank Dr. Bulu Pradhan for his valuable suggestions and all the other members of my Doctoral Committee for their faith and believe over my work.

I would also like to thank my parents, sisters and friends for their enormous support and wholehearted help in personal and professional life. I am deeply indebted to Mr. Manab Baruah, my husband for pushing me through the toughest phase of my life with continuous motivation.

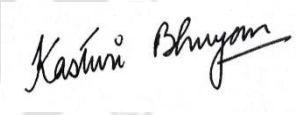

Kasturi Bhuyan

ABSTRACT

Blast threats call for an evolution of design approach for protective structure that can address both resiliency and sustainability aspects of construction. Blast resistant design is performed based on the empirical design charts, where the blast loading is simply characterized by charge weight and stand-off distance. These empirical formulations assume either a spherical free air blast or a hemispherical surface blast and do not account for variation in charge shape, orientation, point of detonation. The peak overpressure and its duration is applied on the structure uniformly which is non-uniform in case of contact blast. Therefore, while facing a contact blast problem, which is directly placed on a structure these empirical design charts are not much helpful. A multilevel Performance-based Design (PBD) framework is developed for slabs/walls of Protective structure subject to different blast loading to improve the present Blast resistant design approach in Code provisions which is currently based on ultimate strength of the structure only. The present research develops probabilistic deflection-based capacity and air blast demand models for three performance levels associated with four damage states of reinforced Normal Strength Concrete (NRC) and reinforced Ultra-High Strength Concrete (UHSC) slabs/walls of protective structures. It also investigates the NRC and UHSC Panel under contact blast and presents the probabilistic capacity and demand models for three performance levels of damage. For this, a set of data is generated through experimental design of numerical modeling and simulations that are carried with the help of commercial simulation software package LS-DYNA. The influence of blast on slabs/walls of protective structures is modeled using a validated Finite Element (FE) approach on a square panel arrangement. Validations are in close agreement with the previous experiments available. Fragility estimates are developed for effect of air and contact blast on NRC and UHSC panel to show the consistency of the developed FE model and probabilistic formulations. Hazard curves are also

established for mass of blast charge and stand-off distance to determine the distribution of the dataset. The reliability-based code calibration is performed for the development of PBD Load and Resistance Factors at the three performance levels based on the established probabilistic models and hazard curves; which circumvents the limitations of present Code provisions. The developed Load and Resistance Factors for Code provisions can be used for the design of NRC and UHSC panel when subject to air and contact blast without performing exhaustive analysis and/or experiments. A High Strength Concrete (HSC) matrix is also developed in reference with earlier studies in site with locally available materials under uncontrolled conditions for show the feasibility of adopting high strength concrete in practical field. The High Strength Concrete developed is then used in a blast resistant building frame and ground floor slab with analysis and simple design with SAP software.

TABLE OF CONTENTS

LIST OF FIGURES

LIST OF TABLES

Chapter 1. INTRODUCTION

1.1 GENERAL

Protective structures can be defined as establishments with the main objective of protecting personnel be it military or civilian, valued materials, or even structures from hazards of present times. These structures can be classified as shelters, barriers or containment structures based on their criteria of protection (US Department of Defense 2008). Shelters provide straight protection for injury of personnel, damage of valuables and detonation of sensitive explosive from blast pressures. The main purpose of a barrier structure is to act as a shield to discontinue fragments to impact potential detonating explosives. Structures providing confinement to the personnel or materials within its hardened element are the containment structures. The structures protecting life and materials for ages are commonly known as bunkers (defence, civilian and weapon storage). Bunker can be classified as Military bunker, Civilian bunker and Weapon storage or Ammunition storage bunker.

Military bunker can be defined as structures that protect military personnel and ammunition during combat from extreme loadings. Based on past extreme loading events, it is being realized that the threat of bombing a structure in areas of conflict in India is more and effort should be made to design such structure to resist the threat if it could not be prevented from happening. India shares its boundaries with many countries where, North-east India alone shares an international border of 5,182 kilometres which is about 99 percent of India's total geographical boundary with several neighbouring countries. Japan went on to take Burma (Myanmar) and attacked a part of North East India in 1944, but North East India was successfully recovered by Indian forces with a loss of more than 25,000 lives (Chhina 2014). The Sino-Indian border war in 1962 (Figure 1.1), made the relation between India and China

hostile and still have long been shadowed by mutual suspicion and distrust (Hu 1999). Since independence, India has had war thrust upon it once with China and four times with Pakistan (Chhina 2014). Aerial attacks, Artillery shelling and firing are very common between India and Pakistan. Recently in 2018, eight villages and a total population of around 8,000 to 9,000 has been affected in Uri due to shelling (Figure 1.2). Under such tension and pressure, and imminent threat of a war outbreak lurking around, Indian military requires better rapidly constructed protective bunker to serve as communication nodes, operational centres, pillbox and similar in difficult terrains. Army requires a modular, portable, bullet and blast-proof construction material for bunker as it fortifies the nation's borders against China and Pakistan (Gurung 2018).

Figure 1.1 Pictures from Sino-Indian War (India Times 2014; Joshi 2018)

Figure 1.2 Artillery shelling in Uri (left) (Hassan 2018) and damage due to shelling (right) (Kapoor 2019)

Ammunition and explosives are inherently lethal and are potential threats during packing, unloading, transportation and storage activities. To safeguard personnel and nearby ammunition, excessive caution is taken in conduct of these dangerous ammunitions. During the Operation Archery on 27 December 1941, British raided German positions on the island of Vågsøy, Norway and burned their ammunition dump (Figure 1.4(a)). In World War II, Germany designed a series of armour-piercing rocket propelled bombs while British designer Sir Barnes Wallis developed the five tonne Tallboy and the ten tonne Grand Slam, which in modern day is conceptualized as bunker busters. These weapons penetrate through the underground bunker and then explodes, and the shock wave transmitted through ground causes damage to the nearby bunkers as well. At present, the GBU-57A/B Massive Ordnance Penetrator (MOP) of United States (Mizokami 2018) is considered as the deepest penetrating bunker buster with a weight of 14,000 kg and capable of penetrating up to 61 m (Figure 1.3). Another threat of ammunition storage bunkers are accidents. The largest non-nuclear explosion in history is the Royal Air Force Fauld explosion, UK in 1944 which was an accident caused due to mishandling of detonator in the underground ammunitions storage facility shown in Figure 1.4(b). These type of accidents are rare but has devastating consequences. These type of storage facilities needs design for protection from internal multiple explosions.

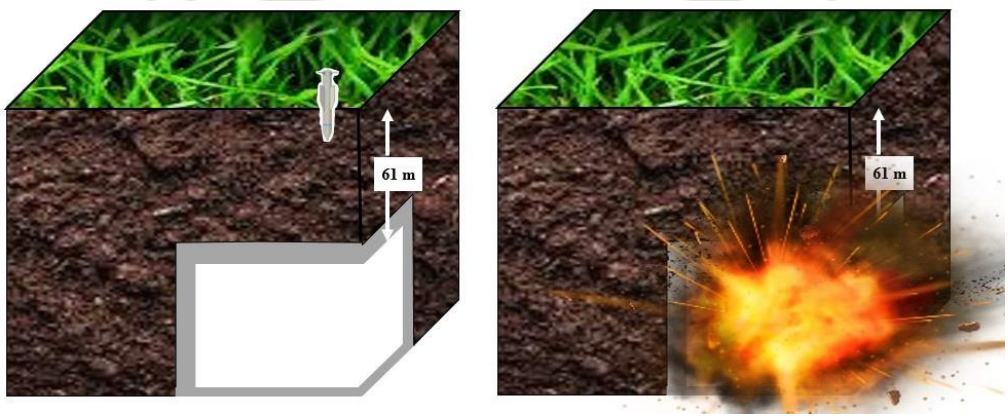

Figure 1.3 Schematic diagram showing working of a bunker buster

Figure 1.4 (a) British commandos watch as an ammunition dump burns (Malindine 1941) and (b) Bombs being stacked in one of the tunnels at RAF Fauld (Daventry 1944)

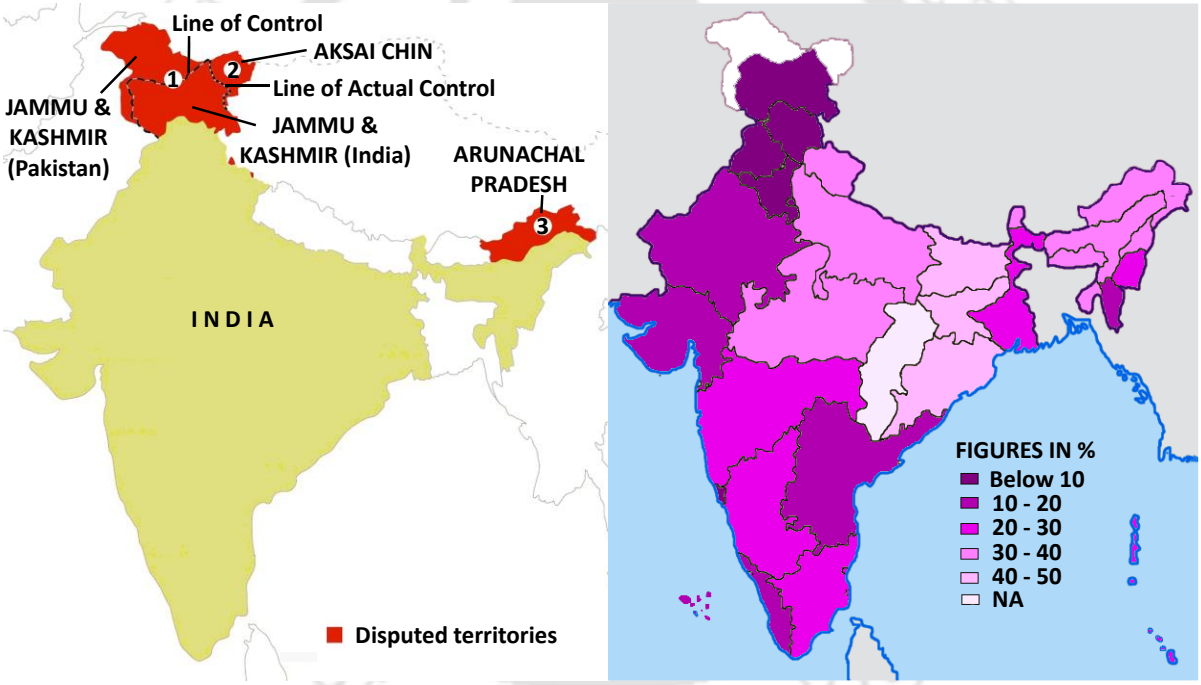

Figure 1.5 Map of disputed areas of India (Godement 2020) (left) and Poverty rates in India (Hunter 2014) (right)

Special types of bunker where civilians are kept safe during attacks are known as mass protection shelters or civilian bunkers. A dozen of civilian lives are claimed in shellings and gunfire in the disputed boundaries of India as shown in the left side of Figure 1.5. Moreover, India is a developing country, with the majority of its citizens living in poverty, as seen on the right side of Figure 1.5. Most of the North-Eastern (NE) states have a percentage of people living

below the poverty level of more than 30%, according to the 2011 census. Low - income families are unable to afford to construct safety shelters on their own. As a result, authorities must provide protection shelters for the people who live in such places. Besides these attacks, terrorism has immerged as one of the major global threats. According to FEMA 453, the maximum planned attacks in the past are caused by bombing which roots mass destruction of life land and property (Figure 1.6) (Smilowitz et al. 2006). In 2008, Assam was shocked by a scheduled terrorist attack of serial bomb blasts where more than 13 bombs exploded (Malik and Chaliha 2012). Figure 1.6 identifies NE India as a terrorist active area and both the military and civilian structures need protection against bombings. The Improvised Explosive Device (IED) is one of the most common methods used by terrorists in attacks around the world and Table 1.1 shows the types and range of IEDs. In today's world, with the ever increasing threats from explosions in the high risk areas, the need for a Mass Protective Shelter (MPS) for safety against explosive threats become paramount, especially for the needy and poor. These type of shelters assist in saving valuable life where the region is severely affected by such threats on a day to day basis.

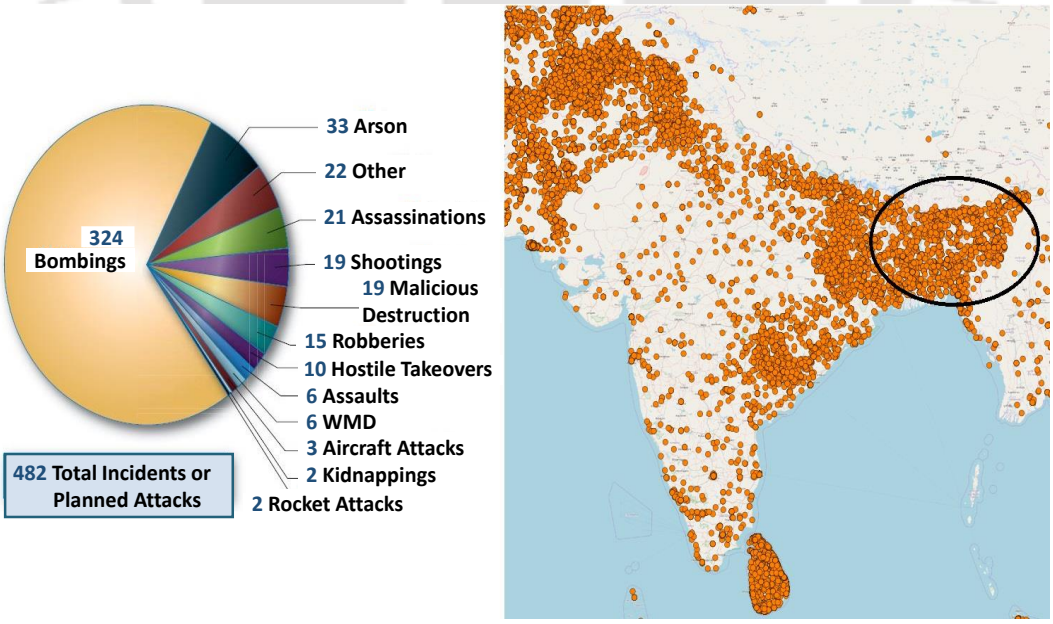

Figure 1.6 Terrorism by event 1980 through 2001 (Smilowitz et al. 2006) (left) and Terrorist Incidents Map of India (1970-2016) (Wikipedia 2017) (right)

Table 1.1 Types and range of Improvised Explosive Device (Chauhan et al. 2018)

Threat description Improvised Explosive Device (IED)		Explosives Capacity (TNT Equivalent)
	Pipe Bomb	5 LBS
	Suicide Bomber	20 LBS
	Briefcase/ Suitcase	50 LBS
	Car	500 LBS
	SUV/ Van	1,000 LBS
	Small Moving Van/ Delivery truck	4,000 LBS
	Moving Van/ Water Truck	10,000 LBS
	Semi-Trailer	60,000 LBS

1.2 EVOLUTION OF PROTECTIVE STRUCTURES

A system expected to protect personnel and valuables against effects of explosions is called protective structure, which include ammunition magazines, containment structures, and other types of military and civilian structures (Ginsburg and Kirsch 1983). Protective structures accounts for a wide classification of establishment. This research is focused on bunkers (military, ammunition and civilian). Thus, following section discusses the evolution of various bunkers (military, ammunition and civilian) over ages and their deficiencies.

1.2.1 Military Bunker

The defence buildings that are constructed for the safety of military and ammunition storage in war scenarios are called military bunker. The bunker originated from the trenches and defensive spaces of the First World War as an executive reaction to technological improvements in

warfare. Bunker can be classified based on accessibility and on construction materials. Jumeau et al. (2018) evaluated the accessibility of European bunkers as underground, partially buried and overground where, underground bunkers are almost entirely buried with only a visible roof. For construction of an underground shelter or bunker, the main aspects of consideration are usually strength and support, as it has to withstand the possible exerted pressure and support the soil overhead. Some are partially buried and the other bunkers have large entrance and easy access. Based on construction materials, bunker can be classified as mud, logs, stones and bricks, concrete and steel bunkers.

A German commander in the year 1914, started excavating mud trenches that could safeguard from French and British troops marching towards them. Military trenches were originally dug along fighting lines where troops were well-protected from the enemy arms fire. The mud trenches were improved to mud bunker as shown in Figure 1.7 and were intentional to offer a degree of security for short battles and were like foxholes or ditches but as the war went on, an obvious need of more intricate system was felt. Log bunker (Figure 1.8) was adopted in areas near woods or forests as logs were easily available in those areas.

Figure 1.7 Mud Trenches in World War (BBC Bitesize 2020; Tellgmann 1961)

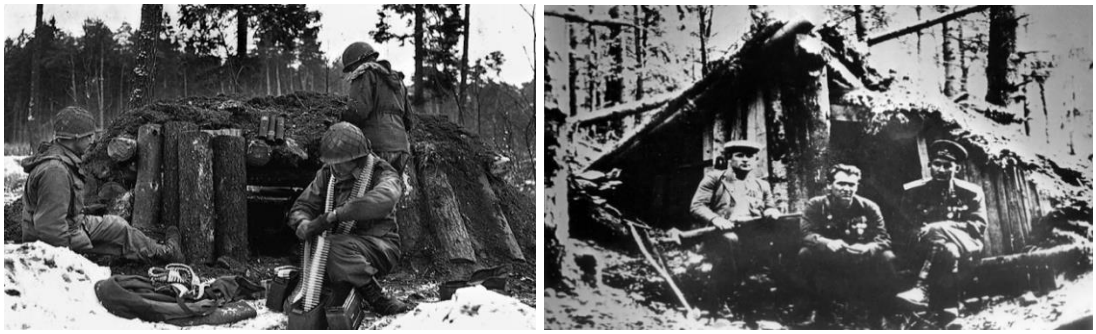

Figure 1.8 Log and Dirt bunker (Goldenberg 2020; Krošlák 2017)

Concealed stone and brick bunker was a part of German defensive system found blended into the rocky slopes, having core strata of rock which prevented excavation of positions without the use of demolitions (U.S. War Department 1944). These type of bunker were three-four feet high comprising of shallow and exposed emplacements enclosed by strong stone and earth walls and covered with packed earth. Both the bunker also used log and heavy timbers as reinforcements for overhead cover and had small firing openings close to the ground level as shown in Figure 1.9.

Figure 1.9 Stone (left) and Brick (right) Bunkers (Fabrizio 2004; Speier 2013)

After the bombings in those trenches in 1914-1918, the panic resulted in the protective material of choice for the next Great War as reinforced concrete rather than mud (Bennett 2011). The bunkers made of materials like mud, logs, stones, etc. can be only used for short span protection as they collapse under blast or explosion and are susceptible to natural calamities. Steel is a costly material and thus steel bunker (Figure 1.10) were very few in numbers. Also, even the large cast iron and steel casting techniques were developed long time ago, the transportation of

heavy steel and iron to the terrains that were difficult to access was a huge problem (Szydlowski and Bednarz 2018). With the development of modern cement in the late 18th century, concrete was adopted as building materials for the bunker as it could be moulded into any shape and also enhanced the resistance capacity of the structure against explosion (Figure 1.10).

Figure 1.10 Steel bunkers of World war II (Benjamin 2014) (left) and Concrete bunker (Altar 2010) (right)

1.2.2 Weapon or Ammunition Storage

Ammunition bunker or weapon storage buildings as the name suggests are used for storage of ammunition, weapons, explosives and other such dangerous materials required by any military personnel. Small scale use of underground munitions stores was done by many countries during the First World War. After the war ended, countries were left with enormous amount of ammunition and explosives with few storage areas. With so many abandoned airfields and foreseeable threat of air attacks, these were turned into ammunition storage facilities. But, with the development of more hazardous weapons like nuclear weapons and threats of aerial attacks, shelling and bombings, the storage of the explosions needed better protection strategy. Thus, many countries developed weapon storage areas where many danger building or weapon storage facilities were constructed as shown in Figure 1.11. These areas are isolated from civilian areas and well-guarded with limited access. Earth beams and buried pits are generally provided to divert the blast forces in case of detonation of ammunitions and safety distances

are maintained between storage bunkers with a specific maximum net explosive content. These bunkers (usually referred to as "igloos") are constructed with nominal reinforced concrete, i.e., conventional concrete that cannot resist high blast pressure (more than 0.7 MPa). The area required for an Igloo is approximately 648 m^2 which can store 136T of Net explosives with heavy concrete members, which are not designed for external loads.

Figure 1.11 Ammunition Storage bunker (Bendix 2019; Nichols 2016)

1.2.3 Mass Protection Shelter or Civilian Bunker

Civilian bunker are shelters provided to the general public of a country where they can keep themselves safe from natural as well as man-made calamities. The poor and deprived class of the society are the most effected people during an extreme event. Their safety is further compromised by relocating them in temporary camps throughout the risky situation. In the year 1943, confirmation of attack on the Third Reich industrial centres, lead to the systematic construction of a second type of bunkers called the civilian shelters (Klinke 2018). In the early 1940's, some partially buried civilian shelters were constructed to protect people during bombardment, like Anderson shelter, Brick-built shelter and Morrison shelter. Anderson shelter, named after John Anderson (Home Secretary who was responsible for Air Raid Precautions) was made by bolting straight and curved galvanised corrugated steel panels. Brick-built shelter sometimes had a concrete roof and were mostly built in gardens or back yards. Morrison shelter (termed after Herbert Morrison) were more of individual protection

basis where, a steel top was doubled as a table with wire mesh on four sides and an entry through one side.

Figure 1.12 Anderson shelter (Reddit 2015) (left) and Igloo-shaped Brick shelter (Harlow 2018) (right)

Figure 1.13 Swiss government bunker near Kandersteg in canton of Bern (Kecko 2015) (left) and Civilian bunker in Rajouri village, India (The Statesman 2020) (right)

Switzerland administration in the year 1963 took seriously the need of shelters for every civilian in case of atomic war and started building mass shelters that could cover the entire civilian population (Figure 1.13 (left)). This civilian bunker still exists with a capacity of accommodating 2,000 people instead 20,000 for which it was intended. The bunkers were constructed to safeguard the government and civilian population underground. Recently in India, a proposal of construction of 1,431 community bunker and 13,029 individual bunker is approved for the people living along international borders (The Economic Times 2018) for

protection against ceasefire and bombings. Among the sanctioned bunker, already 222 and 160 bunker are completed as shown in right of Figure 1.13 in Nowshera and Rajouri respectively and some others are under construction (The Statesman 2020).

The present materials used for building of protective bunker (military, civilian and ammunition storage) range from cement block or stone, wood, poured reinforced concrete, and steel.

1.2.4 Deficiencies

Since the twentieth century, safety structures are constructed by various countries to meet the safety requirements for the known threats. The deficiencies in current construction practices are as follows:

- These structures widely use Reinforced Concrete (RC) as building material against probable explosion events or terrorist attacks structure of approximately 25 MPa strength which is a conventional concrete and are designed to resist blast pressure only up to 7 bar (0.7 MPa).
- During war, a sudden need of military bunker construction as communication nodes and operational centres may arise in difficult terrains. Though steel and concrete are more suitable materials to be used in bunkers, but is difficult to transport at high-altitude areas.
- Military also need a rapid bunker construction material which can reduce the construction time as required in normal concrete construction.
- The construction of bunkers also requires more skilled manpower.
- Inflexibility for firing ammunitions openings is also considered as a limitation for the present construction materials.

- In the case of unknown targets of Artillery firing, direct attack of a shell, aerial attack, mortar etc. fragmentation of structure is caused and thus, military bunker located in areas of common outbreaks should be stronger enough to protect both personnel and ammunitions present.
- The present protective structure requires large area for construction along with heavy member sizes.
- External blast pressures are not taken into consideration for the current design of weapon storage areas.

The human life and valued materials is under severe risk in such an event and as such, there is an outmost need of safeguarding them by overcoming the drawbacks. Thus, military, ammunition and civilian bunkers needs a better design for mitigating blasts where the structural element size can be reduced without compromising the utility of the building. The construction time and labour requirement should be reduced for rapid deployment. The threat of external blast pressure should be considered.

A novel way to improve the resistance of bunkers to blast is to improvise the materials adopted for its construction. A bunker construction with reinforced concrete needs a lot of time. In areas of higher altitude and war zones, where protective structure needs to be constructed at the earliest, it is necessary for the concrete to have gained strength to resist the loadings. But, normal concrete achieves a certain strength only after 28 days of curing. For situations as such, panels can be adopted as building blocks in such structures, that are modular and have already gained its full strength. Figure 1.14 shows the construction stages with such panels. Panels are generally made of steel, plain concrete and reinforced concrete depending on their size, capacity and usage. Such panels are usually adopted as wall structure in buildings, decks in bridges, containment structures, etc. The current design philosophies do not account for the different performance-level associated with the structure and most of the times designed for a single limiting scenario of

blast, i.e., air blast. The details of the current practices of different blast loading scenarios and its analysis techniques are discussed in the next section.

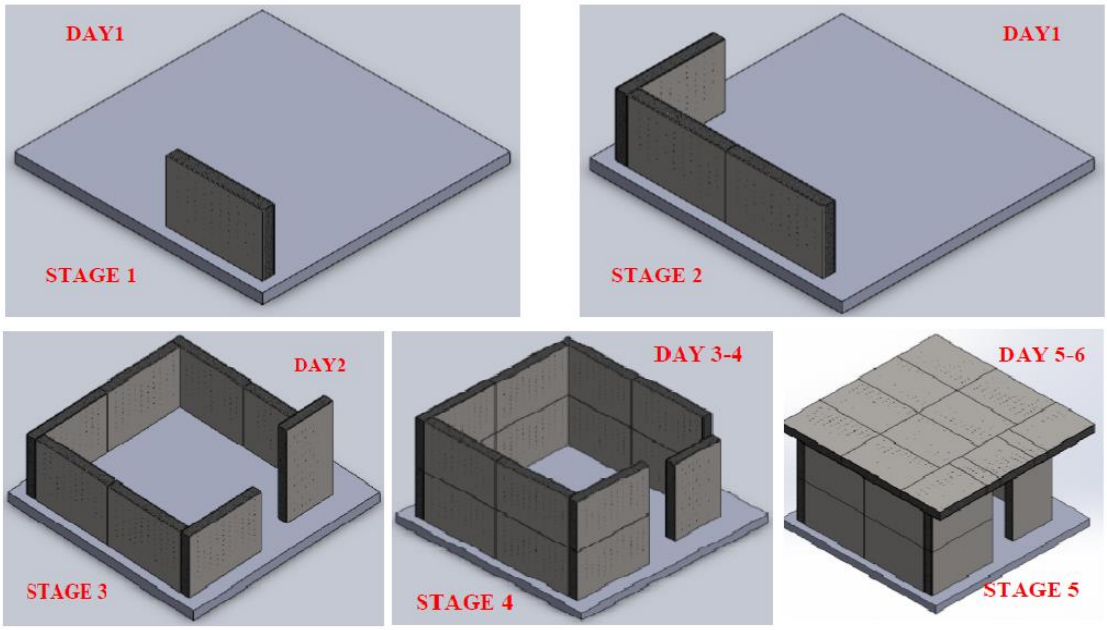

Figure 1.14 A schematic representing the rapid construction using panels.

1.3 LITERATURE REVIEW ON AIR BLAST LOADING

Protective structures are structures to protect personnel, equipment or explosives system from the hazardous output of the explosion (US Department of Defense 2008). The common threat identified in all these protective structures is blast or explosive loadings. So, bombing is one of the primary reason for construction of Protective structures and many researchers have conducted studies on the blast response of various materials. Bombings or Large explosions may cause large scale damage and even turn into a disaster because of the sudden release of energy within a limited volume, leading to an enormous increase in pressure, light and temperature. Thus, the study of mechanism of explosion is essential for designing blast resistant facilities.

Explosive materials can be classified as solids, liquids, or gases according to their physical state. Primarily solid explosives are considered as high explosives; however, other

materials such as flammable chemicals and propellants may also be classified as potentially explosive materials. Based on the explosive susceptibility of ignition, there are primary explosives and secondary explosives. Primary explosives are those which ignite from a simple spark, impact or a flame and when detonated, secondary explosives create blast wave or shock wave which creates widespread damage to surroundings.

1.3.1 Blast Wave Characteristics

Blast wave and its characteristics differ from explosive to explosive as each one differs in its properties. TNT is taken as the standard explosive and every other explosive is expressed in terms of equivalent mass of TNT based on the specific energy of explosives with that of TNT (Cooper 1994).

Blast waves are generated when the air surrounding the explosive is pushed backwards due to a compressive pulse travelling outward from the centre of the explosion (Kinney and Graham 1985). 'Detonation' is a process involving rapid decomposition of explosive and rapid transmission of mechanical forces with a speed called the 'detonation velocity'. As a consequence of detonation of an explosive charge, a layer of compressed air called 'shock wave' is formed in the front of gas volume carrying the most of the energy released by the explosion. The front of the wave, known as the shock front, has a pressure (overpressure) much greater than the region behind it and thus immediately begins to decay as the shock propagates outward (Beshara 1994). Figure 1.15(a) shows the propagation and decay of blast pressure in atmosphere.

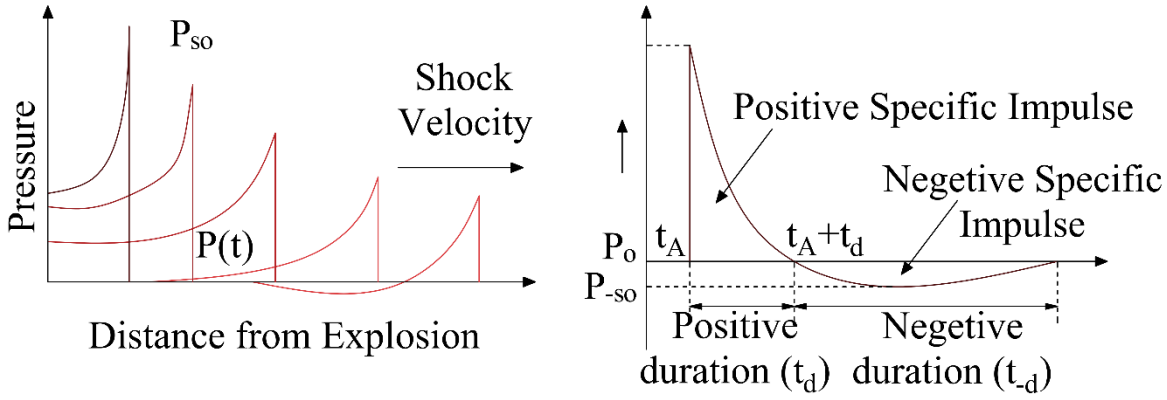

Figure 1.15 (a) Decay of Pressure with distance and time (b) Blast wave pressure-time history (Ngo et al. 2007a)

The typical pressure time history plot of blast explosion as shown in Figure 1.15(b) is represented with a Friedlander Profile. The blast pressure wave reaches the targeted structure at the arrival time t_A and the pressure in the structure rises to a peak over pressure of P_{so}. The peak side on pressure attenuates and reaches the ambient atmospheric pressure level as the wave propagates through the medium. This phase of the curve is called the positive phase and the time duration of the positive phase is denoted by t_d. Partial vacuum is created when the pressure value decreases further then ambient pressure value. This phase of the curve is called the negative phase and the time duration of the negative phase is denoted by t_{-d}. Eventually, the pressure returns to the ambient conditions.

The amplitude of pressure in the positive phase is considerably higher than in the negative phase, the pressure-time relationship can be simplified with a linear pressure decrease and the negative phase neglected due to its minor influence. Moreover, the duration in the positive phase is also shorter than in the negative phase.

Considering the many uncertainties involved in evaluating blast loads and their interaction with structures, it is recommended that approximated pressure-time profiles be adopted by equivalent triangular pulses.

1.3.2 Types of Blast Loading

Blast loading and its effects on a structure depends on the weight of charge, distance from the source called the stand-off distance and also configuration and orientation of the structure. A blast load on structures can be broadly categorized based on the confinement of the explosive charge as (US Department of Defense 2008):

A) Unconfined Explosion: Unconfined explosions can be further classified as –

- **Free Air Burst Explosion:** An explosion, which occurs in free air, produces an initial output where shock wave propagates away from the centre of the detonation striking the structure.
- **Air Burst Explosion:** An explosion which is located at a distance from and above the protective structure so that the ground reflections of the initial wave occur prior to the arrival of the blast wave at the structure.
- **Surface Burst Explosion:** A surface burst explosion occurs when the detonation is located close to or on the ground so that the initial shock is amplified at the point of detonation due to the ground reflections.

B) Confined Explosion: Confined explosions can be further divided as –

- **Fully Vented Explosion:** It is produced within cubicle type structure with one or more surfaces open to the atmosphere. The initial wave and the products of detonation are totally vented to the atmosphere (leakage) which propagates away from the structure.
- **Partially Confined Explosion:** A partially confined explosion is produced within the limited openings in the structure. The amplified initial waves are vented after a finite time. The temperature due to gaseous effects produces quasi-static pressure.

- **Fully Confined Explosions:** The explosion is totally (or near totally) confined inside the structure.

1.3.3 Blast Wave Scaling Law

Different explosives with varying stand-off distances can produce an explosion due to which scaling laws are introduced so as to identify the properties of blast. Scaling principle states that, when two explosive charges of same geometry and of the same explosives with different sizes are detonated in the same atmospherical condition and at identical scaled distances, then the same blast over pressure is produced. All blast wave parameters are primarily dependent on the energy released in detonation and the distance between target and the source. The most commonly used blast wave scaling is the 'cube root scaling law' also known as Hopkinson's Law (Baker et al. 1983). From this law, the scaled distance or Proximity factor (Z) is defined as:

$$Z = \frac{R}{Q^{1/3}} \tag{0.1}$$

where, R is the Stand-off distance (m) and Q is the explosive charge in equivalence of Tri-Nitro-toluene (kg-TNT). Air blast can be classified as far-field air blast and close-in air blast based on the scaled distance (Z). An explosion with scaled distance less than 1.2 m/kg$^{1/3}$ can be termed as close-in explosion (ASCE59-11 2011; Chen et al. 2019) and explosions with scaled distance more than 1.2 m/kg$^{1/3}$ are far-field explosion. Unlike far field blast, close-in blast pressure distribution in the structure is non-uniform. Localized punching and spalling occurs in structural components causing significant damage to the structure subjected to this type of blast loadings.

1.3.4 Prediction of Blast Pressure

Due to complexity of explosion process, it is difficult to find the blast wave parameters through theoretical analysis. Through a number of theoretical and experimental analysis, some empirical relations have been developed for finding the blast pressure parameters. Several authors have recommended their formulations for predicting the peak overpressure from conventional explosives. Brode (1955) analysed the differential equation of gas motion in Lagrangian form and presented the analytical solution for the peak positive over-pressure (P_m) in near-field and medium to far-field conditions as:

If $P_m > 10$ bar, $$P_m = \frac{6.7}{Z^3} + 1 \quad \text{(bar)} \;\; 00000000 \tag{1.1}$$

If $0.1 < P_m < 10$ bar, $$P_m = \frac{0.975}{Z} + \frac{1.455}{Z^2} + \frac{5.85}{Z^3} - 0.019 \quad \text{(bar)} \tag{1.2}$$

Newmark and Hansen (1961) introduced a relationship to calculate the maximum blast overpressure for a high explosive charge detonations at the ground surface –

$$P_m = 6784\frac{Q}{R^3} + 93\left(\frac{Q}{R^3}\right)^{0.5} \quad \text{(bar)} \tag{1.3}$$

where, Q is the Charge in tonne-TNT and R is the stand-off distance (m)

Kinney and Graham (1985), based on the experimental analysis of large explosion data, presented the following equation to compute the peak positive over pressure (bar) –

$$P_m = \frac{808\left[1+\left(\frac{Z}{4.5}\right)^2\right]}{\sqrt{\left[1+\left(\frac{Z}{0.048}\right)^2\right]\left[1+\left(\frac{Z}{0.32}\right)^2\right]\left[1+\left(\frac{Z}{1.35}\right)^2\right]}} \tag{1.4}$$

Based on the experimental analysis of explosion data, Held (1983) presented the following equation to compute the peak positive overpressure –

$$P_m = \frac{2}{Z^2} \qquad \text{(MPa)} \tag{1.5}$$

Similarly, Sadovskiy (2004) presented the following equation to compute peak positive over pressure based on explosion data analysis:

$$P_m = \frac{0.085}{Z} + \frac{0.3}{Z^2} + \frac{0.8}{Z^3} \qquad \text{(MPa)} \tag{1.6}$$

Izadifard and Foroutan (2010) based on numerical simulations gave the following equation to compute peak positive over pressure which is in agreement with TM 5-1300 (1990) which is derived from field experiment results and presents a good match with Brode's equation:

$$\log_{10}\left[\log_{10} P_m\right] = -0.1319X^2 - 0.3231X + 0.644 \tag{1.7}$$

Where $X = \log_{10} Z$ and P_m is the maximum overpressure in kPa.

1.3.5 Prediction of Blast Loading Duration

Duration of blast loading is defined as the time taken for the blast wave for decaying from its peak positive overpressure to the ambient pressure. This is the time duration of the positive overpressure phase. The peak overpressure value and the time duration of this phase determines the effect of blast loading damage to a structure. Henrych (1979) presented the positive over pressure duration in millisecond as –

$$t_d = \exp\left(-2.75 + 0.27\log Z + \log Q^{1/3}\right) \tag{1.8}$$

To compute the positive over pressure duration in millisecond, Kinney and Graham (1985) proposed the following equation –

$$t_d = Q^{1/3} \frac{980\left[1+\left(\frac{Z}{0.54}\right)^{10}\right]}{\left[1+\left(\frac{Z}{0.02}\right)^{3}\right]\left[1+\left(\frac{Z}{0.74}\right)^{6}\right]\sqrt{\left[1+\left(\frac{Z}{6.9}\right)^{2}\right]}} \tag{1.9}$$

Sadovskiy (2004) presented the positive overpressure duration as

$$t_d = 1.2\sqrt[6]{Q}\sqrt{R} \qquad \text{(m-sec)} \tag{1.10}$$

Similarly, Izadifard and Foroutan (2010) presented the formulation as

For $Z \le 0.37$, $t_d = Q^{1/3}\left(-64.86Z^4 + 52.32Z^3 - 15.68Z^2 + 1.794Z + 0.1034\right)$ (1.11)

For $0.37 < Z < 0.82$, $t_d = Q^{1/3}\left(4.64Z^2 - 3.86Z + 0.854\right)$ (1.12)

For $0.82 < Z < 2.5$, $t_d = Q^{1/3}\left(-2.7X^3 + 6.27X^2 + 0.358X + 0.763\right)$ (1.13)

For $Z > 2.5$, $t_d = Q^{1/3}\left(0.608X^3 - 2.38X^2 + 5.62X + 0.22\right)$ (1.14)

Where $X = \log_{10} Z$ and t_d is in millisecond.

1.3.6 Effect of Rate of Loading on Strength Enhancement

During an explosion or an impact event, within a very short period of time the structural materials experiences very high pressure. The dynamic mechanical properties of the materials are altered as a result of the structural materials being subjected to very high rates of loading. The stresses that are sustained for a certain period under dynamic loading attains values that are remarkably greater than under static conditions but the dynamic stiffness does not vary much with the static stiffness.

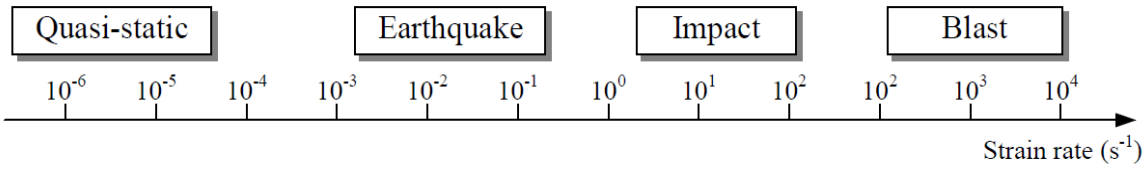

Figure 1.16 Strain rates exhibited by different types of loading (Ngo et al. 2007a)

The rate of loading has a significant influence on the response of visco-plastic structural materials including concrete. High strain rate loading affects the material properties including compressive and tensile strength, modulus of elasticity, ductility, and Poisson's ratio (Bischoff and Perry 1991). Based on the work performed by Curione (1958) referred in Bischoff and Perry (1991), the design compressive strength of concrete can increase about 25 to 30% percent during dynamic loading of concrete. In analysis and design of blast resistant structures, materials' enhanced strength due to high rate of loading is taken into account by using Dynamic Increase factor (DIF), which is the ratio of dynamic to static strength.

According to Malvar (1998), DIF for steel is given as –

$$DIF_{steel} = \left(\dot{\varepsilon}_s / 10^{-4}\right)^{\left(0.0074 - \frac{f_y}{414}\right)} \tag{1.15}$$

where, f_y is the yield stress of steel in MPa and $\dot{\varepsilon}_s$ is the strain rate of steel. DIF for concrete according to Mander et al. (1988), can be written as

$$DIF_{conc} = \left[1 + \left(\frac{\dot{\varepsilon}_c}{0.035 f_c'^2}\right)^{\frac{1}{6}}\right] \Bigg/ \left[1 + \left(\frac{0.00001}{0.035 f_c'^2}\right)^{\frac{1}{6}}\right] \tag{1.16}$$

where, f_c' is the quasi-static compressive strength of concrete in MPa and $\dot{\varepsilon}_s$ is the strain rate of concrete in s^{-1}. DIF values for steel and concrete are introduced in TM 5-1300 and UFC 3-340-02 which can be directly used in the design of blast resisting structures.

Introduction

The dynamic strength of Ultra high performance concrete is very limited in the available research. The load carrying capacity of steel fibre reinforced concrete increases due to strain-rate effects as found by Magnusson and Hallgren (2004) in the dynamic tests of concrete with compressive strength up to 200 MPa. With increase in concrete strength, Malvar et al. (2000) with the experimental data showed that there is a reduction in DIF. Ngo et al. (2007b) expressed the rate dependent peak stress $\left(f'_{cd}\right)$ (MPa) for a model applicable to concrete strengths varying from 32 to 160 MPa with strain rate up to 300 s^{-1} as:

For $\dot{\varepsilon} \le \dot{\varepsilon}_1$

$$DIF = \frac{f'_{cd}}{f'_{cs}} = \left(\frac{\dot{\varepsilon}}{\dot{\varepsilon}_s}\right)^{1.026\alpha} \tag{1.17}$$

For $\dot{\varepsilon} > \dot{\varepsilon}_1$

$$DIF = \frac{f'_{cd}}{f'_{cs}} = A_1 \ln(\dot{\varepsilon}) - A_2 \tag{1.18}$$

Where, f'_{cs} = static compressive strength (MPa); $\dot{\varepsilon}$ = strain rate; $\dot{\varepsilon} = 3\times10^{-5}$ in s^{-1} (quasi-static strain rate); $\alpha = 1/\left(20 + f'_{cs}/2\right)$; $\dot{\varepsilon} = 0.0022 f'^{2}_{cs} - 0.1989 f'_{cs} + 46.137$; $A_1 = -0.0044 f'_{cs} + 0.9866$; and $A_2 = -0.0128 f'_{cs} + 2.1396$.

Chen et al. (2011) observed the largest DIF as around 1.1 at a loading rate of 450 GPa/s when conducting dynamic tensile tests on steel fibre reinforced concrete with various fibre volume fraction. The value is significantly lower than that of normal strength concrete. In a series of drop hammer tests on both plain concrete and fibre reinforced high strength concrete conducted by Weidner (2013) it was seen that normal strength concrete specimens did perform as well as fibre reinforced concrete specimens when tested dynamically. A decrease in DIF was exhibited when fibre reinforced concrete specimens were tested in tension at elevated temperatures as compared to room temperature. The results of dynamic flexural tensile test on UHSC with different dosages of steel fibre performed by Millard et al. (2010) shows that the

strain rate enhancement of flexural strength for UHPFRC is reduced as the fibre percentage increases.

1.4 LITERATURE REVIEW ON CONTACT BLAST LOADING

Protective structure has the threat of contact explosion as a small amount of charge placed along the surface of the structure can cause huge damage to the structure. The charge weight adopted for contact explosion is dependent on the explosive carrying capacity of a person/vehicle or other medium to come in the close proximity of a protective structure. Contact blast is a special type of close-in blast where the explosive is placed in contact with the structural element. Thus, it is a surface explosion when the detonation is located on the structure so that the initial shock is amplified at the point of detonation due to the reflections. For this type of loading, pressure distribution is uneven and causes spalling of concrete in the rear face of the structural element under the charge.

In general, if the damage cannot be avoided in the structures the damage mode is preferred to be elastic than brittle. In case of blast loading, the excessive energy released need to be absorbed which can be done effectively with the increase in ductility of the material. But, concrete being brittle, brittle damage modes like shear damage and combine shear and flexural damage mode is observed (Li and Hao 2013). Short duration and large loading results in the shear damage whereas small loading and longer time duration loading results in the flexure failure. One such study to understand the failure modes was carried out (Luccioni et al. 2004) to understand the respective damage modes. In contact blast, in addition to flexure and shear damage, spalling also plays a predominant effect. In such scenarios, a large energy is released by the blast in form of stress waves propagation. The compressive (incident) and tensile (reflective) waves are generated due to the blast. If the strength after superposition exceeds the

dynamic tensile strength, then spalling damage occurs (McVay 1988). The fragments generated due to the spalling can impose threats to the human life and equipment in the structure.

1.4.1 Experimental Work

The effects and damages encountered in the blast loading can be used to improve the structures to mitigate the possible effects. For this, Li et al. (2015a, 2016) conducted experiments on normal strength concrete (NRC) and Ultra High Performance Concrete (UHPC) under contact explosion slab with different configuration of the slab dimensions and loading (Li et al. 2016). To get a better picture of the improvement, a comparative study was also carried on the behavior of NRC and UHPC (Li et al. 2015a). The damage observed was due to punching failure with a wedge shape formation of small diameter at the top and a larger diameter at the bottom in all of the cases. This is due to the wave propagation, that is when the reflected wave reaches the bottom of the element, some of the shock wave is reflected, and the remaining energy goes through the member thickness and reflects again. Tension cracking and concrete spalling occur on the back side of the structural part as a result of this reflection. The relative size of damage diameter decreased from NRC to UHPC due to the increase in compressive strength of concrete. In case of NRC, cracks and some amount of failure was also observed at the edges. This is clearly due to the propagation of wave and reflection through the edges causing change from compressive to tensile behavior (McVay 1988). Whereas in case of UHPC, the tensile strength was much higher to avoid the dynamic failure. Li et al. (2016) also studied the effect of change in depth of the panel on its performance under blast loading. As per the results, with the increase in depth, the size of the failure decreased in case of the slab with more thickness. In the results, there was not much change observed due to the decrease in reinforcement and that is due to lack of confinement effect of the steel bars. Along with this, the size of fragments on spalling was also studied. The study clearly stated that the size of the fragments decreased from NRC to UHPC and in both the cases. Similar kind of wedge

formation and punching failure was also observed by the experiments done by Zhao et al. (2019a) steel-concrete slabs. The experiments were done on Single-side- steel-concrete (SSSC) panel, centre steel-concrete (CSC) panel and reinforced concrete (RC) panel of same dimensions. The damaged areas were much higher in SSSC and CSC as compared to the RC but they did not face any penetration due to the presence of steel plate. Instead, RC panels faced the penetration and lost its bearing capacity. Yamaguchi et al. (2011) worked on utilisation of Poly Ethene Fibre Reinforced Concrete (PEFRC) for blast resistance and found its effectiveness in reducing the spall damage in case of contact loading. The experiments were performed on NRC and PEFRC to give a comparative outcome. The results clearly stated that PEFRC was much more effective in reducing the spall damage but the size of the fragments was same in both the cases.

1.4.2 Numerical Studies

Li et al. (2015a) did the numerical simulation for contact explosion test by adopting the coupled finite element and smooth particle hydrodynamics method. In case of UHPC, the shock response of UHPC was considered using the Mie-Gruneisen equation of state. The comparative results show that the numerical and experimental data exhibit high accuracy in case of NRC but the behaviour was underestimated in case of the UHPC. The possible reason might be due to the variation in the dynamic increase factor (DIF) that is prominent in case of dynamic loading.

Li and Hao (2014) performed numerical study using LS-DYNA 3D model of concrete columns and studied the spall damaged behaviour of the column. To validate the results, the outcome of the results was checked with the values from the UFC code and they were almost same. The diameters of the spall damages at top and bottom showed good accuracy when compared with the experimental data. Puryear et al. (2012) performed numerical simulation of

contact or near contact blasts on reinforced concrete columns using the Arbitrary Lagrangain-Eulerian (ALE) capability of LS-DYNA. The rate effect parameter in the study were not included which plays a major role in dynamic analysis. In this approach, the model appeared to be stable for large range of loading, standoff distance and various column geometries. Meso-scale modeling of concrete slab under contact blast was done by Zhou and Hao (2009). The two phase meso-scale model along with dynamic plastic damage model was incorporated in the hydrocode AUTODYN and image analysis method was used to analyze the outcomes. In this work, two aggregate distribution were taken and incorporated in the concrete slab model and compared the fragment size distribution from the above two model with the homogenous model and the results from the empirical equations. The results were comparable with the data from empirical formulas in this study.

1.4.3 Analytical Formulations

Several prediction methods for spall damages of concrete wall was given by Kot (1977), but the formulations are limited to light and moderate air blasts loading along with some assumptions that can affect the reliability of the study in practical use. The assumptions taken by Kot (1977) were; shape of bomb to be spherical, stresses are in elastic zone of concrete (below dynamic compressive strength), concrete is linearly elastic, propagation velocity is constant and the spalling instantaneously occurs when the peak stress exceeds the dynamic tensile strength of concrete. Li et al. (2016) also used the theoretical predicting methods to check the results and state the usefulness of the theoretical methods. One of such theoretical methods is proposed by McVay (1988) to predict the localized damages caused by blast loading. Using this method, a graph is plotted using the parameters, scaled slab thickness $\left(T/W^{1/3}\right)$ and scaled standoff distance where T is the slab thickness and W is the weight of charge in kg respectively. It was observed that the empirical results were in good agreement for the normal strength concrete but in case of the UHSC, it underestimates the value and gave

inaccurate predictions. Li et al. (2016) and Yamaguchi et al. (2011) mentioned about the equations given by Morishita et al. (2004) as

Shape of Crater:

$$\frac{C_d}{T} = 0.2\frac{L}{T} \qquad \left(\frac{C}{T} < 1.6\right) \tag{1.19}$$

$$\frac{C_d}{T} = 0.016\frac{C}{T} + 0.3 \qquad \left(\frac{C}{T} \geq 1.6\right) \tag{1.20}$$

where C_d is the Crater depth (mm), C is crater diameter (mm) and T is slab thickness (mm)

Shape of Spall:

$$\frac{S_d}{T} = \frac{0.155}{T} \qquad \left(\frac{S}{T} < 2.9\right) \tag{1.21}$$

$$\frac{S_d}{T} = 0.017\frac{S}{T} + 0.071 \qquad \left(\frac{C}{T} \geq 2.9\right) \tag{1.22}$$

where S_d is the Spall depth (mm), S is Spall diameter (mm) and T is slab thickness (mm)

Crater Depth and Total damage depth:

Crater depth, $$\frac{C_d}{T} = \left(-0.046\frac{T}{W_m^{1/3}} + 0.42\right) \qquad 3.6 < \frac{T}{W^{1/3}} \tag{1.23}$$

where, C_d is the Crater depth (cm) and $T/W_m^{1/3}$ is modified scaled concrete thickness and is calculated as,

$$\frac{T}{W_m^{1/3}} = \frac{T}{W^{1/3}}\left(\frac{K_{TNT}}{K}\right)^{1/3} \qquad \left(\text{cm/gm}^{1/3}\right) \tag{1.24}$$

where, T is the Panel thickness, K_{TNT} is Chapman-Jouguet (C-J) detonation energy of TNT [MJ/kg] and K is the C-J detonation energy of explosives used [MJ/kg].

Total damage depth, $\frac{C_d + S_d}{T} = \left(-0.49 \frac{T}{W_m^{1/3}} + 2 \right) \qquad 2 \le \frac{T}{W^{1/3}} \le 3.6$ (1.25)

Breaching condition, $\frac{C_d + S_d}{T} = 1 \qquad \frac{T}{W^{1/3}} < 2$ (1.26)

Breach diameter, $\frac{H}{T} = \left(-6.7 \log \frac{T}{W^{1/3}} + 2.7 \right)$ (1.27)

Based on the above equations, Yamaguchi et al. (2011) also gave an empirical equation for estimating the damage depths in case of PEFRC slabs as

$$\frac{C_d + S_d}{T} = 1.9 - 0.5 \frac{T}{W^{1/3}} - 0.048 \bar{\sigma}_b \tag{1.28}$$

Here, $\bar{\sigma}_b$ is the flexural toughness coefficient.

Remennikov et al. (2015) mentioned that, the weight of charge needed to breach concrete or masonry walls can be calculated using the empirical formula below

$$P = R^3 KC \tag{1.29}$$

where, P stands for the explosive charge (pounds TNT), R for the breaching radius (feet), K for the material factor, which represents the material's strength, hardness, and mass, and C for the tamping factor, which is determined by the charge position and tamping.

Yue et al. (2017) proposed numerical equations to calculate the threshold thickness of the slab in case of blast loading and spalling. The work was based on the assumptions that the chemical reaction is instantly completed, concrete will reach the plastic state instantaneously and energy will be dissipated through large deformations, elastic deformation is ignored in comparison of plastic deformations; and hemispherical distributed impulse is assumed over the slab area. In the work the non-dimensional equation is proposed by converting the threshold spalling thickness is

$$\frac{L}{Q^{1/3}} = \frac{g_1(\xi)}{(4\pi\rho_w/3)^{1/3}} \tag{1.30}$$

where, ξ non-dimensional factor defined in the function g_1, ρ_w is the density of the charge, L is the depth of the slab and Q is the charge. Yue et al. (2017) discussed the method for calculating the threshold thickness on perforation.

Along with this UFC 3-340-02 (US Department of Defense 2008) design guidelines were also used to study the concrete behaviour under blast load. The empirical work given by the code, gives concrete thickness h (ft) as:

$$\frac{h}{r} = \frac{1}{-0.02511 + 0.1004\Psi^{2.5} + 0.13613\Psi^{2.5}} \tag{1.31}$$

where r is the range from slab face to charge centre of gravity (ft), Ψ is Spall parameter for contact charges is given as

$$\Psi = 0.527 r^{0.972} f_c'^{0.308} W_{adj}^{-0.341} \tag{1.32}$$

where, f_c' is Concrete compressive strength (psi), $W_{adj} = B_f C_f W$ is the adjusted charge weight (lbs), B_f is burst configuration factor=1 (for surface bursts), C_f is Cylindrical charge factor.

An equation using the Buckingham's theorem was also developed by Lonnquist (1993) to calculate the breach diameter.

$$\frac{D}{h} = f\left(\frac{W_e \rho_e Q_e}{f_c' \rho_c h^3}\right) \tag{1.33}$$

where, ρ_e is explosive density (kg/m^3), ρ_c is concrete density (kg/m^3), W_e is the explosive weight (kg), Q_e is the explosive energy (J/kg), f_c' is the Concrete Strength (N/m^2), D is the diameter of the breach and h is the thickness of the slab.

1.5 LITERATURE REVIEW ON SLAB/WALLS

In this section, a brief state of art is presented on the NRC and UHSC concrete slab/walls, their current design along with their behaviour and limitations under air and contact blast loadings.

1.5.1 Normal strength Reinforced Concrete Panels

Protective structures and significant infrastructures widely uses Reinforced concrete (RC) as construction material against probable explosion events or terrorist attacks (Zhao et al. 2019b). Blast detonation induces high intensity of loading in a short duration. Such extreme loading conditions requires comprehensive dynamic analysis of concrete structures as it is a complex phenomenon which encompasses inertia effect as well. Structural performance under such loadings, results in varying strain rate of the material due to rapid change in loading rate and causes brittle spalling and damage of concrete due to its low tensile strength (Li and Hao 2014). Though column stiffness and boundary conditions does not affect spalling, increasing column depth and densifying helps in mitigating spall damage (Li and Hao 2014). Similarly, increase in longitudinal reinforcement ratio decreases displacement responses and damage degree of the RC beams significantly. Many researchers have conducted dynamic analysis of concrete element under blast scenarios, but studies are limited to external blast resistance of protective structures. As these structures are also used as storage for weapons and explosive materials, it needs accurate analysis and design for forces induced when the explosives are stored inside. The need to accurately estimate the dynamic capacity and demand on the panels associated with the protective structure construction is important.

Close-in or contact explosions predominantly causes concrete spall damage and brittle failure of concrete besides the flexural and shear damage and also imparts huge amount of energy on the structure in the form of stress waves. When the net stress, that is the incident and the reflected stresses exceed the dynamic tensile strength of concrete, the spall damage occurs.

Moreover, the flying high speed wreckages of the concrete can pose threats to the neighbouring structure and to personnel as well. Results from experimental and numerical analysis directed to study the impact of blast wave shows that localized damage occurs in concrete at the point of explosive contact (Leppänen 2005). However, with adoption of high compressive strength of concrete, the punching and the spall damage can be significantly reduced for contact blast (Li et al. 2015a).

Conventionally Reinforced Concrete (RC) walls typically consisting of orthogonal grids of rebar with adequate tie or stirrups, connecting the rebar grids together; designed in accordance with ACI 349 (ACI 2006). Important structures such as weapon storage, bunkers, and similar; uses normal reinforced concrete elements in the blast protective designs. But, high strength concrete has also proved its efficiency in blast resistance in many researches. Thus, this study is conducted in two parts, normal strength concrete panels and high strength concrete panels.

Concrete subjected to high strain rate loading behaves differently than under static loads. Researchers are devoting both experimental and numerical studies to understand the behaviour of concrete under explosive loading. Many researchers studied plain concrete panel or reinforced concrete panels under blast loading as their controlled specimens (Lan et al. 2005; Lin et al. 2014; Mao et al. 2014; Matsagar 2016; Tabatabaei et al. 2013a; Thiagarajan et al. 2015; Zhou et al. 2008). Reliability analysis of RC slabs and its failure modes under explosive loading determined that under high amplitude blast load with short duration, slab tends to fail in a direct shear mode and under relatively low amplitude blast load with longer duration, slab fails in flexure (Low and Hao 2001, 2002). Moreover, length of slab had no influence on the failure probability but increasing the thickness and percentage of steel rebar; and decreasing the slab rigidity by changing its support conditions had positive effect on the flexural response of RC slab.

Addition of fibres and mineral admixtures to concrete, to improve its brittle behaviour and strength respectively, are implemented for behavioural study of high strength under blast loading (Li et al. 2015b; Mao et al. 2015; Millard et al. 2010; Zhao et al. 2019a). Lan et al. (2005) did full-scale blast tests on steel fibre reinforced concrete slabs along with conventional reinforced concrete slabs. Finite element analysis was performed for RC panel subjected to air explosive loading to prediction of a reliable numerical model close to the experimental scenario (Castedo et al. 2015; Du and Li 2009; Jones et al. 2009; Zhou et al. 2008). Again, a series of tests were conducted by Tabatabaei et al. (2013b) proposed a method for improving the blast spalling resistance of concrete. The study compared conventional RC panel and long carbon fiber-reinforced concrete under blast load and concluded that addition of long carbon fibers causes less material loss and surface damage of the control panels. Lin et al. (2014) studied the effect of element size on the dynamic material model of concrete including the strain-rate effects on concrete separately for both tension and compression, through finite element modeling of RC panels subjected to blast loading using LS-DYNA. Because of the high energy absorption capacity, the plastic models are most effective in blast resistance followed by elasto-plastic and elastic models, respectively (Xu et al. 2014).

Adding steel-bar reinforcement reduced the deformation of the concrete slab due to blast loading (Kristoffersen et al. 2018; Yi et al. 2012). A change of 60° layout of reinforcements, results in reduced deflections with respect to the ordinary RC slab (Zhao et al. 2019a). Moreover, from close-in blast investigation on RC panels showed that increasing explosive charge slowly changes the damage degree from inelastic deformation to local spallation (Abbas et al. 2019; Wang et al. 2012; Yao et al. 2016). Deflection to thickness ratio of slab is also inversely proportional to the scale distance and the reinforcement ratio.

Investigations of retrofitted RC slabs were also conducted by some researchers as some of the retrofitting materials can increase the load bearing capacity of deficient structures and

prolongs the structural integrity of weakened structures. Blast investigation on RC panels retrofitted with glass fibre reinforced polymer (GFRP) composite was conducted by Razaqpur et al. (2007) and RC panels retrofitted with either carbon fiber reinforced polymer and Polyurea was done by Ha et al. (2011). Retrofitted panels showed better blast resistance than ordinary RC slabs. Naito et al. (2015) made numeriacal and experimental investigation on the performance of insulated wall panels subject to close-in blast and summarized that, the use of insulated concrete wall panels enhances the resistance to spall and breach of concrete due to the presence of an exterior layer.

1.5.2 Ultra-High Strength Concrete (UHSC) Panels

A great number of safety structures have been constructed successfully with traditionally placed high performance concrete in countries like India, France, UK, and Japan as it has superior workability, strength, and durability as compared to conventional concrete (Prabir et al. 2013). Hence, high strength concrete panels, and ultra-high performance fibre reinforced concrete under extreme loading are being investigated. The results of an experimental investigation conducted on concrete panels made of ultra-high-strength concrete (UHSC) in Woomera, South Australia in May 2004 was presented by Ngo et al. (2007a) and a finite-element computer code was developed for validation. Optimized ultra-high performance concrete panels can be an effective solution for mitigating the risks of blast threats (Rebentrost and Wight 2008). A series of tests were conducted by Wu et al. (2009) to investigate the blast resistances of slabs with normal and Ultra-High Performance Fibre Reinforced Concrete (UHPFRC) and plain ultra-high performance fibre concrete. In a blast test using ANFO was performed by Yi et al. (2012) on reinforced UHSC and RPC panels, it was concluded that addition of rebar and short steel fibers provides sufficient ductility, confers outstanding energy absorption and negates the brittle characteristics of the concrete.

A numerical investigation on the performance of ultra-high performance fibre reinforced concrete under blast loading with a concrete material model which takes into account the strain rate effect was presented by Mao et al. (2014) by validating with full scale blast tests. Inherent nature of concrete material is brittle and so addition of fibre reinforcement to the concrete or use of high strength concrete materials are adopted to further increase the concrete resistance to high strain rate loading. To generate model parameters, the automatic parameter generation method was used and the stress-strain relationship of the model was further configured to match the designed stress-strain relationship of UHPFRC. Overall, Ultra high performance slabs showed better resistance to blast as compared to conventional concrete slab. Mao et al. (2015) again tested UHPFRC slabs with varying amounts and types of steel fibres under close-in explosions.

Investigations on RC slabs under close-in blast predicts that factors like explosion weight, standoff distance and slab thickness have profound influence over the maximum central deflection and resistance of the slab. Comparing ordinary reinforced concrete slab to a novel RC slab in containment structure, Zhao et al. (2019b) concluded that, 60° layout of reinforcement improves close-in blast resistance and results in reduced deflections with respect to the ordinary RC slab subjected to the same loading. Furthermore, the maximum displacement and stress states are insensitive to yield strength of reinforcement in the slab.

1.6 LIMITATIONS OF EXISTING STUDIES

Protective structures are exclusive structures which require financial resources on a national scale (Ginsburg and Kirsch 1983) but the building codes of most of the countries in high risk areas have not included any special provisions for blast events in the design of such structures. In the present scenario, bunkers as protective structures are made with reinforced concrete with normal strength concrete but ultra-high strength concrete is identified as one of the potential

building material for the same. The shortcomings found in the current state of art can be summarized as follows:

- The existing studies are based on experimental results of NRC panels under air, close-in and contact blast in which due to restrictions, only one or two panels are tested under a calculated specific charge weight (Lan et al. 2005; Lin et al. 2014; Mao et al. 2014; Matsagar 2016; Tabatabaei et al. 2013b; Zhou et al. 2008).
- The blast effect is considered with the peak overpressure which is calculated based on the empirical equations developed for spherical and hemispherical blast in free air and ground surface blast respectively which does not account for contact blast loadings.
- For design of RC panels, proper empirical formulation for predicting the structural capacity and demand with different range and types of blasts are not available.
- Research carried out till now primarily focuses on RC panels subject to a blast loading, and the research on UHSC panels under such loading is minimal.
- Investigation on ultra-high performance concrete under different blast loading scenarios is limited.
- Proper empirical formulation for predicting the structural capacity and demand of UHSC panel under different blast loadings are also not presented.
- Performance-based design of panels which takes into account the deformation of the system by blast and energy absorbed and dissipated by the structural system is not well addressed in any literature on protective structures when subject to air as well as contact blast loading.

1.7 LIMITATIONS OF CODE PROVISIONS

Reliability-based code calibration was adopted to improve the structural design codes from allowable stress to limit state design, ensuring that the safety level of the new codes with collective knowledge and experience-based optimization over the years (Beck and De Souza

2010; Melchers and Beck 2018). Load and resistance factors determined with Reliability-based techniques accounts for appropriate safety gaps in guidelines and ensures decrease in the probability of failure due to insufficient capacities or excesses in demand when designing or evaluating structures (Beck and De Souza 2010). This method provides a design approach for structures under extreme and unpredicted loadings which is deficient in the limit state guidelines (Aktan et al. 2007; Easa and Yan 2019). Current Reliability based design provisions for the blast resistant design have the following limitations:

- The current provisions for design of protective structures against blast loading take into account the pressure generated by spherical air blasts only (US Department of Defense 2008) and does not account for contact blast pressure.
- As per the US Department of Defense Structures to Resist the Effects of Accidental Explosions (US Department of Defense 2008) and TM 5-1300 (1990), the capacity reduction and load factors for structural design can be taken as 1.0, which is the base for design of protective structures in many countries (Stewart 2019).
- Also, UFC 3–340-02 (US Department of Defense 2008) recommends a factor of 1.2 for mass of explosive in case of design accidental blast loading on structure.
- This assumption of resistance and load factors lack a probabilistic base and are based on the assumption that, increasing the design threat can lead to conservative design (Dusenberry 2010).
- BS EN 1991-1-7:(2006) however identifies hazard scenario for severity of potential failure caused by accidental loads and does not mentions any load and resistance factor.
- Allowable deformations are also sometimes considered as the measured safety factors which practically measures the strain energy absorption capacity and demand (Task Committee on Blast-Resistant Design of the Petrochemical Committee of the Energy Division of ASCE 2010).

- The factors adopted for blast design are inconsistent with the design practice for other loads (Razaqpur et al. 2012).
- Moreover, no such factors are found for contact blast resistant design.

So, the need of advance research on the development of a precise formulation for reliability-based design which accounts for both air and contact blast effects on NRC and UHSC panels subject to explosive loading becomes imperative.

1.8 SCOPE OF PRESENT STUDY

This research aims at developing a performance-based analysis and design methodology for panels that can be used as building blocks for protective structures subjected to not only air blast but also contact explosion. The study also considers different configurations of the panels with normal strength reinforced concrete (NRC) and ultra-high strength reinforced concrete (UHSC). The designed panels will target for rapid, resilient, sustainable and economic construction of bunkers without compromising on strength and its utility aspects. The scope also covers the development of high strength concrete matrix under uncontrolled conditions and its application in a realistic scenario. The study takes into account the inherent uncertainty associated with the blast phenomenon, material, boundary conditions and other epistemic and alleatory uncertainties.

1.9 OBJECTIVES

The current research has the following main objective:

- To develop a framework for reliability-based code calibration and design of Slabs/Walls of Protective structures modeled as normal strength concrete (NRC) and Ultra-high strength concrete (UHSC) panels subject to air blasts, which takes into

account the inherent uncertainty in the system properties, material and geometric configurations.

- To develop a framework for reliability based code calibration and design of Slabs/Walls of Protective structures modeled as NRC and UHSC panels subject to contact blasts which takes into account the inherent uncertainties associated with the system properties, material and geometric configurations.

This framework development will be accomplished in the following way:

First of all, based on the damage state of the panels, three performance levels tied to four damage states of the structure will be identified and quantified. These performance levels will be deformation based, viz., maximum deflection of panels, spalling and punching of concrete, and deformation of steel plate. Probabilistic models will be developed to accurately quantify these performance levels, so that the structure can be analysed and designed based on these different performance levels.

After that, a high strength concrete matrix will be developed by keeping the mix design of the high performance concrete as close to the mix proportions available in the present state of the art. The materials required for developing a high performance concrete mix are also being studied to know their effects on the concrete matrix. The developed concrete will be castoff on site to get a high strength concrete matrix with locally available materials and unskilled labour under uncontrolled conditions.

After obtaining the performance levels for NRC and UHSC panels, probabilistic capacity models will be developed corresponding to each performance level. The developed probabilistic capacity models will accurately estimate the capacity of these panels at the given performance level. The developed capacity models will be based on deformation-based formulations for air blasts and crater diameter based for contact blasts.

The probabilistic demand model will be developed with the same approach to estimate the demand imposed on NRC and UHSC panels subject to air and contact blast loading. The developed demand models will be based on deformation-based formulation as well.

The developed Performance-based capacity and demand model will have the following advantages, accounting for:

- The multi-modal response of the structure,
- The transition of failure modes and their interaction
- Inherent uncertainty associated with the modeling, configuration and material properties
- The model will be easy to use.
- The model will incorporate the uncertainty in modeling, material properties and configuration.
- The model will account for the increase in strength of material due to the strain rate.
- The model will account for the effect of inertia due to dynamic loading.
- The dynamic capacity of different modes of failure and the interaction will be estimated.

These developed capacity and demand models will be used to analyse the fragility (vulnerability) of any given protective structure subject to both air and contact blast. The code-calibration will also be developed for each panel under both loading scenarios.

The same formulation can also be used to design a bunker made of these panels subject to both the blasts. This procedure provides a performance-based framework for the analysis and design of NRC and UHSC panels of protective structures subject to air and contact blast.

The organization of the thesis is presented in the following section.

1.10 ORGANISATION OF THE THESIS

This thesis is organised into ten chapters. The first chapter presents a brief introduction to the need and motivation of research, the overview of existing state of the art with the shortcoming and objectives to be achieved in this research. In the second Chapter, step by step procedure that is to be followed to achieve the objective of this thesis is discussed is brief along with the quantified damage state and performance levels of the panels. The third Chapter discusses the finite element modeling of the panels, air and contact blast, interaction with the structure and the model validation. For conducting finite element analysis, Chapter four explains the experimental design procedure. Chapter five illustrates the development of the performance based capacity and demand model for all the panels for the air explosive loading, with model correction, assessment and parameter estimation. Sixth Chapter consists of the performance based capacity and demand model for the NRC and UHSC panel subject to contact blast. Seventh Chapter consists of fragility assessment of the vulnerability of all panels subject to the air and contact blast loading scenarios. Chapter eight presents hazard curves for the mass of charge and stand-off distance from it, code calibration for load and resistance factor with suitable target reliability and total probability of failure conditioned with mass of charge and stand-off distance for air and contact blast. A research on high strength concrete matrix, its state of art, materials proportioning and its development along with the compressive test results are compiled in Chapter nine. Construction of a blast resistant building frame with the in house material developed is detailed in Chapter ten. Lastly, the conclusions from this research with suggestions on future scope of research is enclosed.

The next chapter describes in brief the methodology to be adopted for this research.

Chapter 2. FRAMEWORK FOR DEVELOPMENT OF PERFORMANCE BASED DESIGN OF NRC & UHSC PANELS

In this Chapter the execution of the work plan is described for the development of a performance-based design framework for NRC and UHSC panels under air blast and contact blast loadings.

2.1 WORK PLAN TO ACHIEVE THE OBJECTIVES

This work aims to develop a performance-based analysis and reliability-base code calibration for the design of reinforced Normal strength Reinforced Concrete (NRC) panels and Ultra-High Strength Concrete (UHSC) panels exposed to realistic scenarios of air and contact explosion. The uncertainties of the system will also be taken into account. This progress will be achieved in the following way:

- Three performance level with four damage states will be identified and quantified based on the panel damage. Accurate probabilistic models will be proposed for analysis and design for the defined panel performance.
- Probabilistic capacity models will be then established for the NRC and UHSC panels for the defined deformation-based performance levels.
- Next, the probabilistic demand models will be estimated for air and contact blast loading on structures based on deformation formulation as well.
- Fragility assessment of each panel subjected to both loading condition will then be analysed to study the probability of failure.
- Reliability-based code calibration of the two panels subjected to both loading condition will be recognized.

- A high strength concrete matrix will also be developed with locally available materials with proper study and identification of materials, and numerous trial mixes adopted close to previous literature available.
- The mix proportion with better result will be then adopted for constructing a blast resistant framed-structure at site under unrestrained circumstances.

This formwork provides a performance-based formulation for analysis and design of NRC and UHSC panels that can be adopted as building blocks for Protective structures subject to air and contact blast.

2.2 PERFORMANCE-BASED DESIGN (PBD)

Performance-based Design (PBD) is a rational approach for designing a structure with expected levels of performance exposed to a defined demand or loading. This is done with the help of past literature predictions on the behaviour of the element subjected for the specified hazard (Becker 2008). Validation for this approach is done either with experiment or simulation or a combination of both. The basic procedure for PBD analysis is as follows:

- Identifying and defining performance criteria
- Selecting initial data range for the design
- Validating performance through analysis

The design principle adopted is that capacity should always be greater than the demand, certain requirements fixed by the consumer (Becker 2008). Traditional code objectives are quantitative based but objective of PBD approach is qualitative to meet the consumers demand.

Major area of practice of PBD method in structures is earthquake or seismic design of structures like building, bridges, containment structures, etc. (Choudhury and Singh 2013; Priestley 2000; Yamawaki et al. 2000). Use of this design approach is also seen in wind loading

(Ciampoli and Petrini 2010; Jeong and Tarrant 2018) and fire safety design (Johann et al. 2006) on buildings. Performance based design has been recently adopted in the extreme loading of structures like vehicle collisions (Sharma et al. 2012), missile impact (Gangolu et al. 2022) and blast loadings (Olmati et al. 2014; Whittaker et al. 2003). This method provides a design approach for structures subjected to extreme and unpredicted loading, which is deficient in the limit state guidelines (Aktan et al. 2007; Easa and Yan 2019). With the advantages of selection of desired performance objectives to satisfy the required criteria of consumers and flexibility of innovation and new design solutions, PBD is best suitable answer to serviceability and strength enhancement of the structure economically. The performance levels for each research is different based on deformation or operation criteria. The performance levels for the present research is defined in the next section.

2.3 PERFORMANCE LEVELS OF PANELS

2.3.1 Performance Levels for Air Blast

Blast force imparted on the slab/wall of protective structure is the demand imposed on the structure. Demand varies with charge weight and stand-off distance as well as properties and structural configuration of the panels. The resistance of the slab/wall modeled as panels is termed as capacity as it displays the strength of the panels which includes damping resistance, inertial resistance and local stiffness resistance. Deformation is taken as a measure of the capacity and demand on the slabs/walls of the panel of NRC and UHSC protective structure subject to air blast loading. As blast shock wave hits the target structure, a pressure is applied on the top fiber of the structure in the form of flexural compressive stress and when this compressive shock wave interacts with the free bottom surface fiber it reflects and is converted into a tensile wave. The concrete in the bottom fiber begins to crack as the increasing flexural stresses exceeds its flexural tensile strength and these formed cracks widens and propagates as

time of loading increases. The rapid increase in tensile strain causes increase in member curvature and deflection and finally results crushing of concrete or breaking of steel. At the point where the first crack in concrete is initiated, the member can be said to have reached its elastic limit and the point when crushing of concrete begin or breaking reinforcement in the member occurs, the member is said to have reached its plastic limit. The phase between these limits is considered as the elasto-plastic range.

Table 2.1 Performance Levels of panel subject to air blast loading

Damage Level	Damage Description	Performance Level	Performance Level Description
D1	Zero damage		
		→ P1	Operation with Minimum Damage
D2	A few visible cracks in concrete		
		→ P2	Medium damage
D3	Yielding of steel		
		→ P3	Collapse prevention
D4	Crushing of concrete or breaking of steel		

.

Based on the behaviour of the panels under air blast loading, the present research recommends four possible damage levels for deflection-based analysis of the panels subjected to blast as shown in Table 2.1. The damage levels rise from zero damage to crushing of concrete or breaking of steel in the panel. The corresponding three performance levels defined are Operation with Minimum damage (P1), Medium damage (P2), and Collapse prevention (P3). Performance level one with operation with minimum loss is the minimum damage, considering zero to a few visible cracks in the panel. Performance level P2 is considered from a few visible cracks to yielding of steel and performance level P3 collapse prevention is considered with yielding of steel thickness to crushing of concrete or breaking of steel in the panel. The

deflections are recorded at cracking strain of concrete (P1), yielding strain of steel (P2) and crushing strain of concrete (P3). Figure 2.1-2.3 shows the considered Performance levels of FE model of a panel.

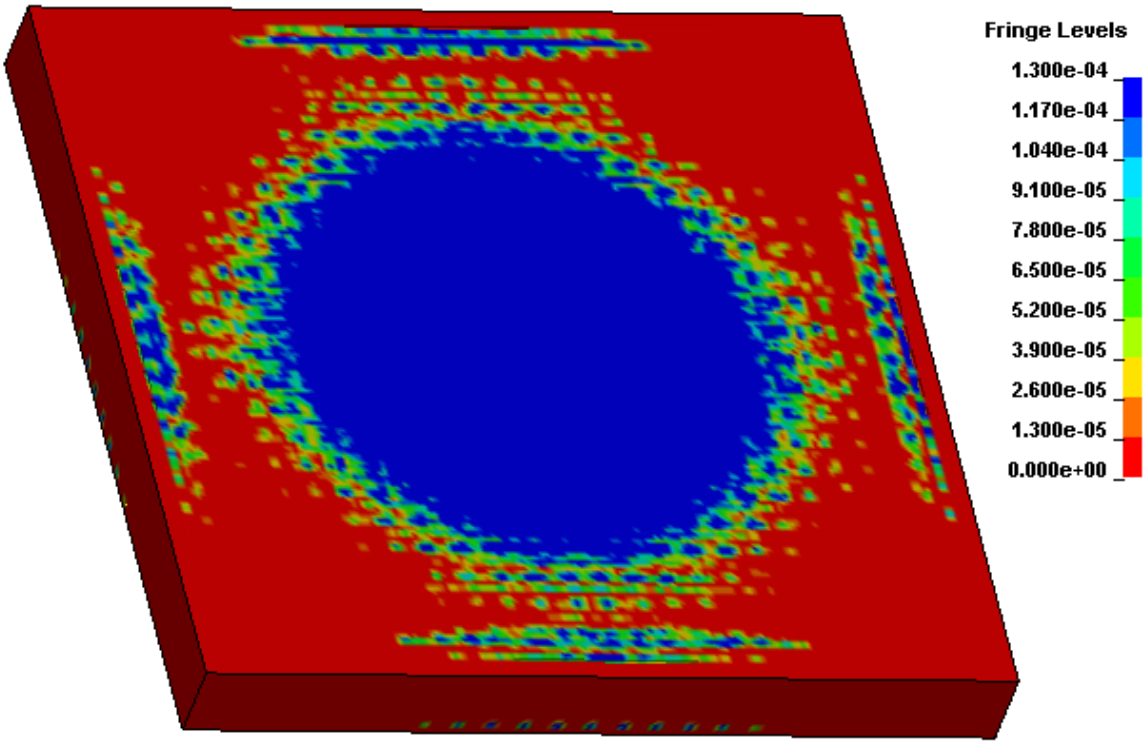

Figure 2.1 Panel when concrete reaches cracking strain (P1)

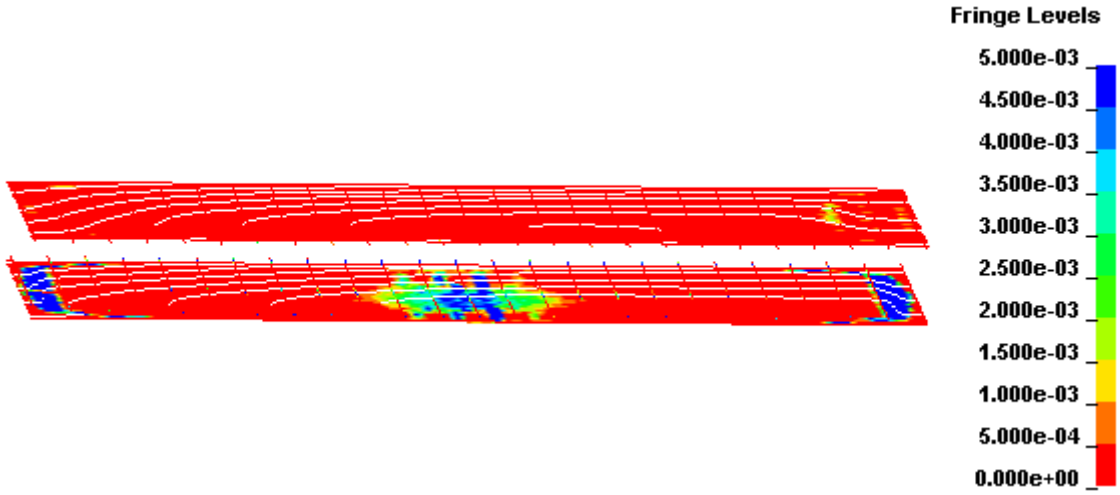

Figure 2.2 Panel when steel reaches yielding strain (P2)

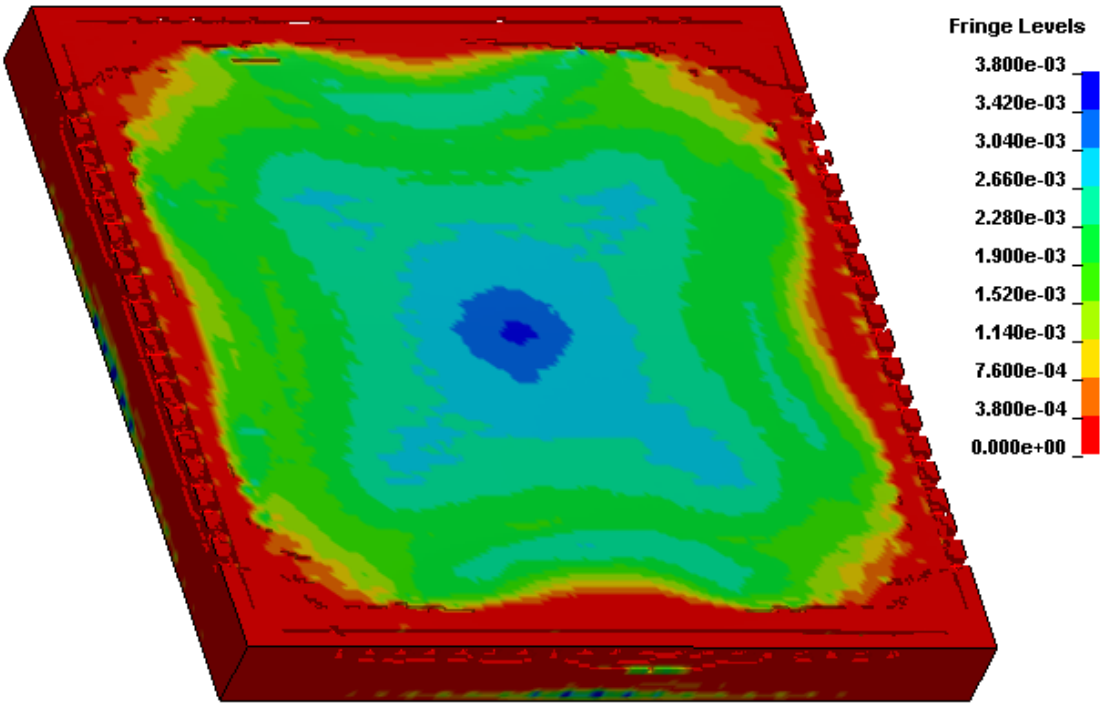

Figure 2.3 Panel when concrete reaches crushing strain (P3)

2.3.2 Performance Levels for Contact Blast

Contact explosion transmits a very high level of stress to the structural member which causes localized crushing of concrete and crater formation at the facing side immediately at detonation. Some part of the shock wave produced gets reflected and the remaining energy travels through the member thickness and reflects again when the reflected wave reaches the bottom of the element. Due to this reflection, tension cracking and concrete spalling at the back side of the structural member occurs. When the crater meets the spall damage diameter, and a hole is made in the member, it is called perforation. In case of a thin slab subject to high explosive detonation, punching failure is observed. This is also observed when the shock wave is severe enough to cause shear punching and the whole damage zone is total punched outwards. The damage states are therefore, Cratering, Spalling, Perforation and Punching as shown in Figure 2.4 (Zhang et al. 2006).

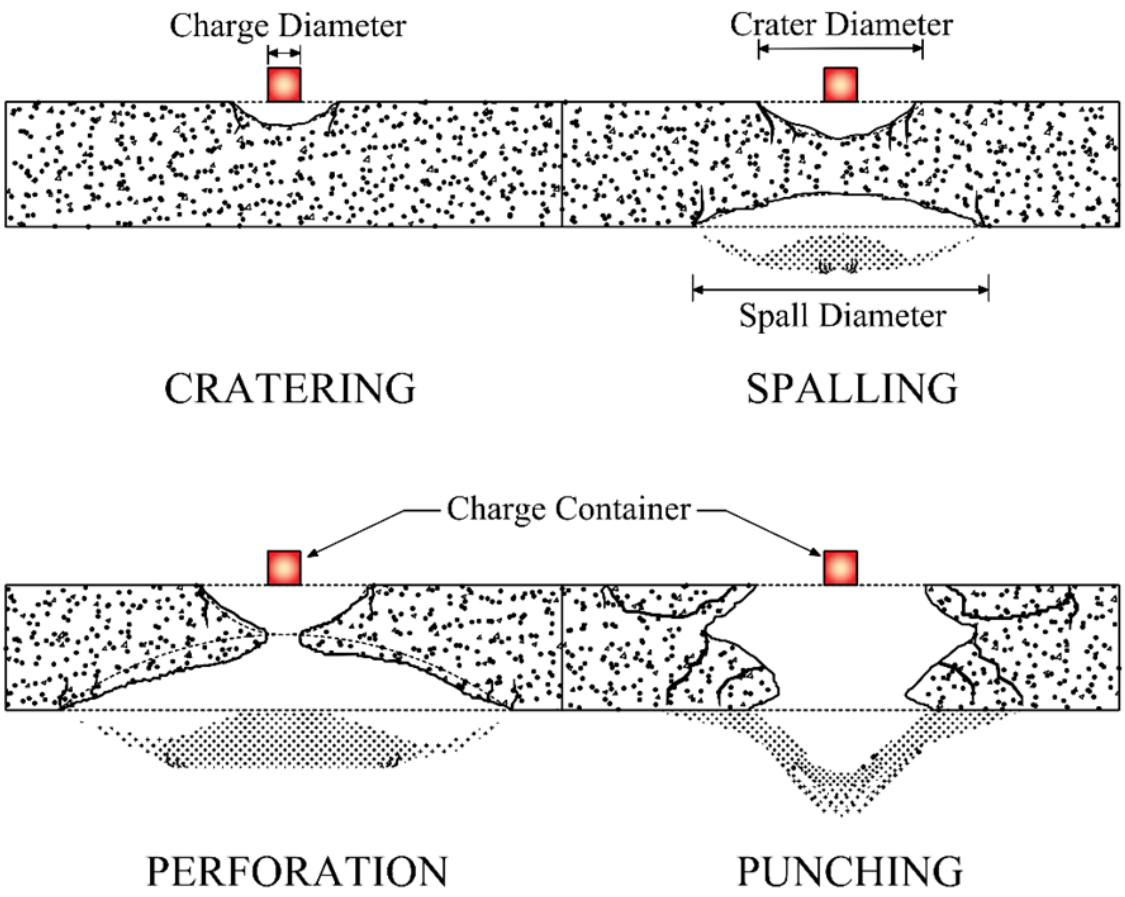

Figure 2.4 Damage modes of concrete panel caused by contact explosion

Based on the behaviour of the panels under contact blast, the present research recommends four possible damage levels for crater diameter formed based analysis of the panels subjected to contact blast as shown in Table 2.2. The damage levels accounts from crater formation to punching of concrete in the panel. Correspondingly three performance levels are considered as Operation with Minimum damage (P1), Medium damage (P2), and Collapse prevention (P3). Performance level one with operation with minimum damage considers the diameter of crater formed on the panel top at initiation of Spalling. Performance level two, P2 is considered from a crater diameter formed at initiation of Spalling to a stage when the panel is just perforated. Third performance level, collapse prevention is considered with crater diameter formed from initial perforation to punching failure of concrete, that is when a significant amount of breached diameter is reached and the whole damaged zone is total punched away. Figure 2.5-2.7 shows

the considered Performance levels of FE model of a panel and the point at which crater diameter is recorded.

Table 2.2 Performance Levels of panel subject to contact blast loading

Damage Level	Damage Description	Performance Level	Performance Level Description
D1	Cratering formation	→ P1	Operation with Minimum Damage
D2	Spalling of concrete	→ P2	Medium damage
D3	Perforation of panel	→ P3	Collapse prevention
D4	Punching failure or the whole damaged zone is total punched away		

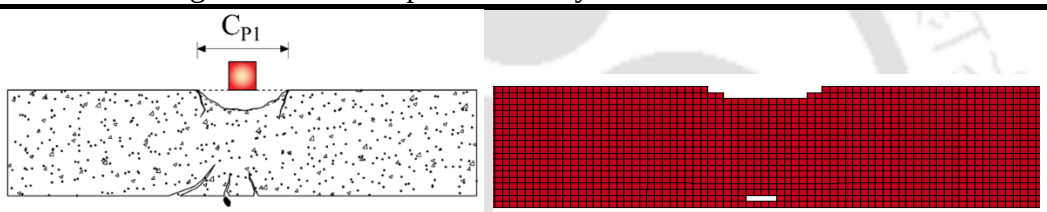

Figure 2.5 Panel at initiation of Spalling (P1)

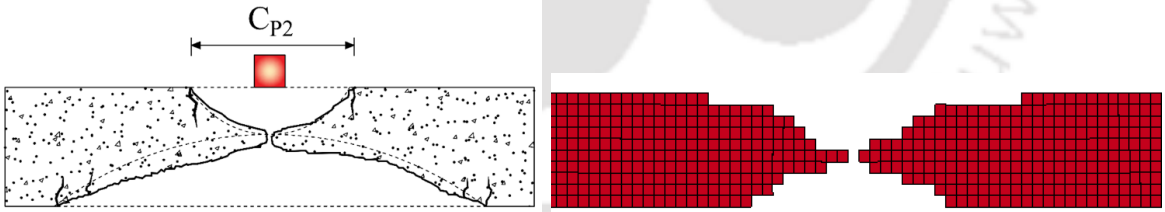

Figure 2.6 Panel at initiation of Perforation (P2)

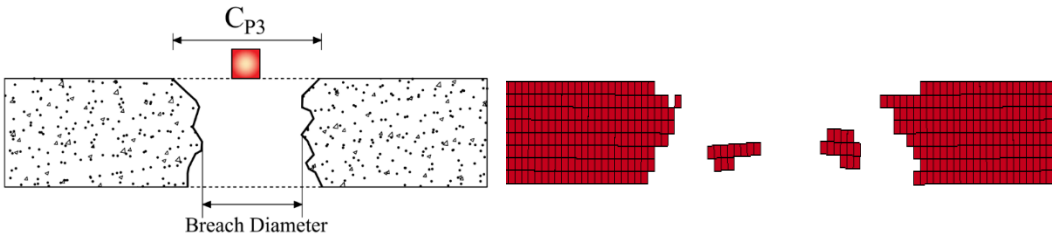

Figure 2.7 Panel at initiation of Punching (P3)

2.4 ILLUSTRATION OF PANEL ANALYSIS FOR PERFORMANCE LEVELS

Effect of uncertainties of blast load calculations, high strain rate loading, the non-linear inelastic material behaviour and the time-dependent deformations results in complications for analysing the dynamic response of a panel subject to blast-loading. To simplify the analysis, a number of assumptions related to the response of structures and the loads has been proposed and widely accepted. The assumptions and their potential implication on the results are discussed below –

— The proposed probabilistic model has two parts. It consists of an analytical part for which the panel is idealized as a single degree of freedom (SDOF) system. A model with a single degree of freedom (SDOF) is one in which each component may only move along one axis as presented in Figure 2.8 (a). As a result, the analytical part of the probabilistic model considers one degree of freedom. In order to account for the higher modes, the explanatory terms are constructed which accounts for the response from the higher modes. In this way the probabilistic model ensures that the predominant behaviour of the structure is captured via the analytical formulation and the effect due to the higher modes, and other associated uncertainties epistemic and aleatory uncertainties arising due to material, boundary conditions and the complex interaction is accounted by the explanatory functions used in the development of the probabilistic model.

— The blast load is idealised as a simple triangular loading considering only the positive phase duration. A typical blast loading profile is shown in Figure 1.15 (b) and the assumed loading is depicted in Figure 2.8 (b). Since the amplitude of pressure in the positive phase is much higher then its negative phase, the pressure-time relation may typically be simplified by using a linear pressure drop and the negative phase can be overlooked due to its minimal contribution and shorter duration. Thus the response does

not account for the negative pressure direction. However, because the triangle load area is the same as the actual positive phase pressure, the load imposed is unaffected. Furthermore, reinforcement mesh is included at both the top and bottom of the panel, which will act during the negative phase. As a result, the designed panels are conservative.

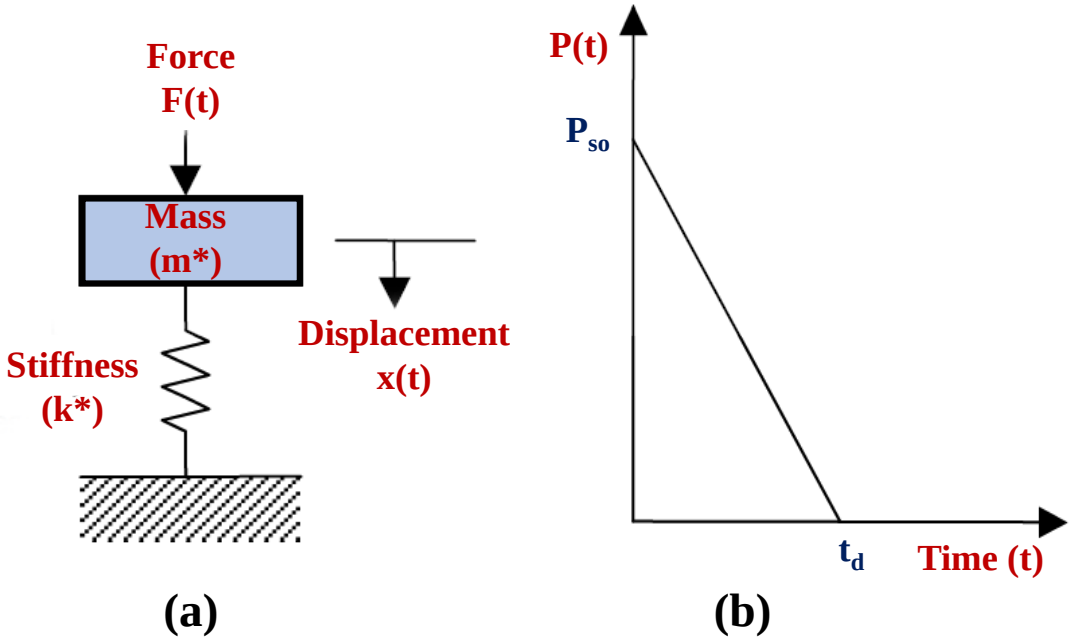

Figure 2.8 Schematic diagram of (a) SDOF system and (b) triangular blast loading

The mass, stiffness, and external force values used in the SDOF equation of motion are accurate only if all of the mass elements of the structure are subjected to the same force and hence move as a single unit, with the total mass considered to be concentrated at the its centre of gravity. In the case of blast loading, the motion of particles of mass varies along the length of the member for which the assumption of uniform motion of entire mass cannot be made. Therefore, transformation factors are required for the structure to be represented as an equivalent SDOF system. Transformation or equivalent factors can be calculated for the panels with a specific boundary and loading conditions. These factors are used to obtain the effective mass, force and resistance terms; and to make the SDOF system response equivalent to that of the real system.

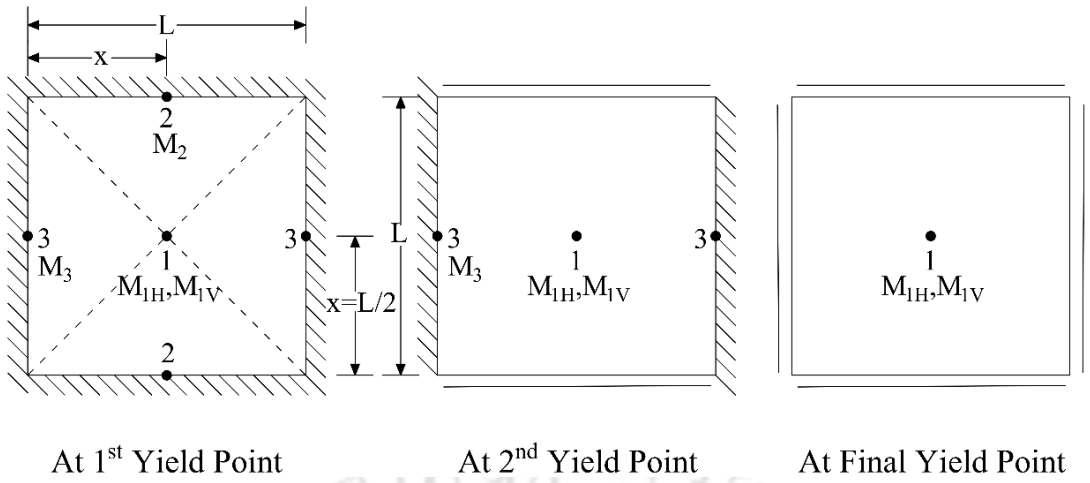

Figure 2.9 Simplified yield lines of a Square two-way Slab with all edges fixed

To analyse the panels and arrive at the effective mass, resistances and equivalent stiffness, the failure pattern of panels are assumed with the help of yield lines. Yield line theory is based on the assumption that after initial cracking of the concrete at points of maximum moment, yielding spreads until the full moment capacity is developed along the length of the cracks on which failure will take place (US Department of Defense 2008). Figure 2.9 shows the simplified yield lines of a square two-way element at each stage of plastic hinge formation as considered in this research. Analysis of a panel is explained with an example panel analysis as shown in Figure 2.10.

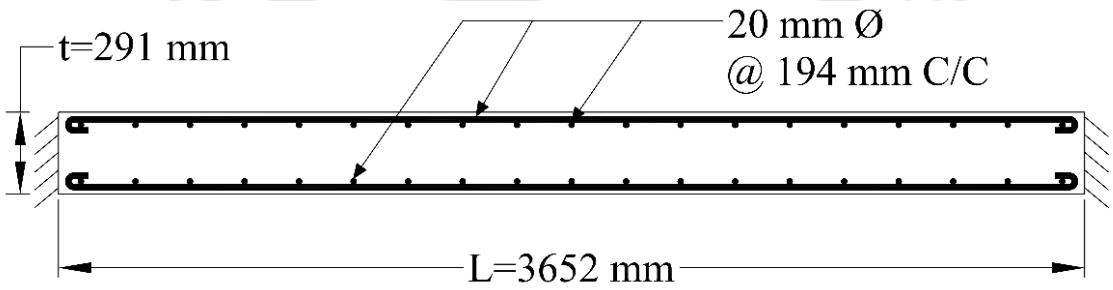

Figure 2.10 Detailing of an example Panel

Details of the Panel: Length of panel, L = 3652 mm

Thickness of panel, t = 291 mm

Unit length of panel, b = 1000 mm

Clear cover = 25 mm

Compressive strength of Concrete, f_c' = 45.96 N/mm^2

Yield strength of Steel, f_y = 550 N/mm^2

Young's Modulus of steel, E_s = 200000 MPa

Young's Modulus of concrete, E_c = 33897 MPa

Effective depth of panel, $d_{eff,H} = 291 - 25 - \frac{20}{2} = 256$ mm

$$d_{eff,V} = 256 - 20 = 236 \text{ mm}$$

Average effective depth, $d_{avg} = \left(d_{eff,H} + d_{eff,V}\right)/2 = 246$ mm

Provided reinforcement, $A_{st} = \frac{(\pi/4)20^2 \text{b}}{194} = 1619.4$ mm^2

Average reinforcement ratio, $\rho_{avg} = \frac{A_{st}}{bd_{avg}} = 0.0066$

Depth of equivalent rectangular stress block, $a_{sHV} = \frac{A_{st} f_y}{0.8\text{x}bf_c'} = 24.2$ mm

Moment Capacity is given by:

$$M = \frac{A_{st} f_y}{b}\left(d_{eff} - \frac{a_{sHV}}{2}\right) \tag{2.1}$$

Therefore, $M_H = 217234$ Nmm and $M_V = 199421$ Nmm

Gross Moment of Inertia, $I_g = \frac{t^3}{12} = \frac{291^3}{12} = 2.05\text{x}10^6$ mm^4

From Figure 2.11, for $n = \frac{E_s}{E_c} = \frac{2\text{x}10^5}{33897} \approx 6$ and ρ_{avg} = 0.0066, F = 0.028

Moment of Inertia of cracked section, $I_{c-net} = Fd_{avg}^3 = 0.028\text{x}246^3 = 0.42\text{x}10^6$ mm^4

Average moment of inertia, $I_a = \frac{I_g + I_{c-net}}{2} = 1.23\text{x}10^6 \text{ mm}^4$

Flexural rigidity, $D = \frac{E_c I_a}{1-\upsilon^2} = \frac{33897\text{x}1.23\text{x}10^6}{1-0.17^2} = 4.3\text{x}10^{10} \text{ Nmm}^2$

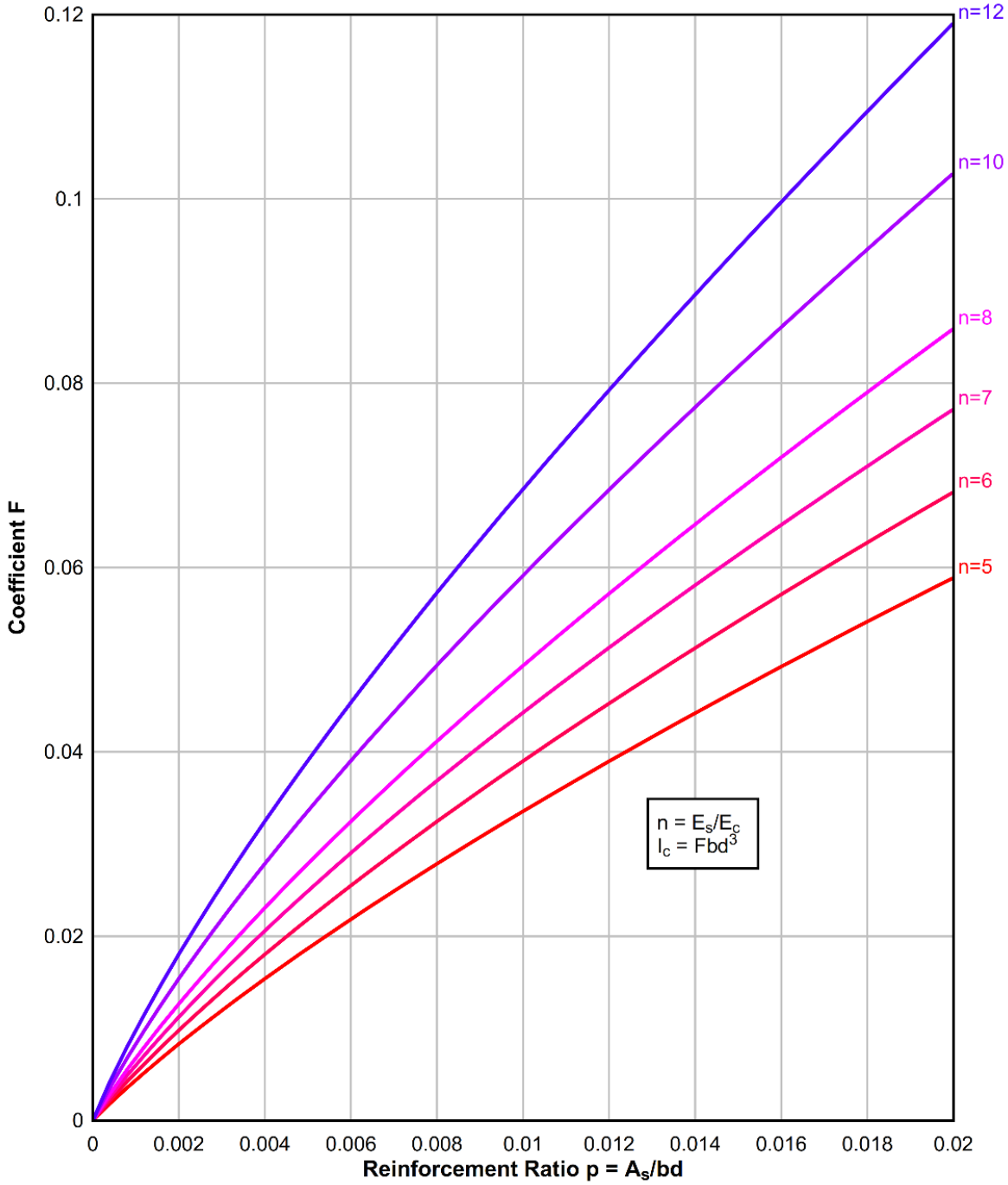

Figure 2.11 Coefficient for Moment of Inertia of Cracked Sections with Equal Reinforcement on Opposite Faces (US Department of Defense 2008)

At First Yield Point:

As the panel are square, $\beta_{1H} = \beta_{1V} = 0.024$; $\beta_2 = \beta_3 = 0.051$ and $\gamma = 0.0014$

Unit resistance is given by

$$r = \frac{M}{\beta L^2} \tag{2.2}$$

Therefore, $r_{1H} = 0.068$ MPa; $r_{1V} = 0.62$ MPa; $r_2 = 0.32$ MPa; $r_3 = 0.29$ MPa

Elastic unit resistance, $r_e = \min\left(r_{1H}, r_{1V}, r_2, r_3\right) = 0.29$ MPa

Deflection can be calculated by-

$$X = \frac{\gamma r L^4}{D} \tag{2.3}$$

So, Elastic deflection, $X_e = \frac{0.0014\text{x}0.29\text{x}3652^4}{4.3\text{x}10^{10}} = 1.7$ mm

Corresponding moment capacity, $M = \beta r_e L^2$

$M_{1H,1} = M_{1V,1} = 0.024\text{x}0.29\text{x}3652^2 = 9.3\text{x}10^4$ Nmm

$M_{2,1} = 0.051\text{x}0.29\text{x}3652^2 = 2\text{x}10^5$ Nmm

At Second Yield Point:

As the panel are square, $\beta_{1H} = 0.025$; $\beta_{1V} = 0.034$; $\beta_2 = 0.07$ and $\gamma = 0.0019$

Resistances, $r_{1H} = \frac{M_H - M_{1H,1}}{\beta_{1H} L^2} = 0.37$ MPa ; $r_{1V} = 0.23$ MPa; and $r_2 = 0.019$ MPa

Elastic unit resistance, $r_{ep} = r_e + \min\left(r_{1H}, r_{1V}, r_2\right) = 0.31$ MPa

Elasto-plastic deflection, $X_{ep} = X_e + \Delta X = X_e + \frac{\gamma\left(\min\left(r_{1H}, r_{1V}, r_2\right)\right)L^4}{D} = 1.85$ mm

At Final Yield Point:

As the panel are square, γ = 0.004

For a square panel as considered in this research, both parts are equal as the yield lines form an angle of 45° with both the edges of the panel, and therefore, ultimate unit resistance r_u of a two-way panel can be expressed as

$$r_u = \frac{5(M_V + M_H)}{x^2} = \frac{20(M_V + M_H)}{L^2} \tag{2.4}$$

where, M_{pV} = ultimate unit positive moment capacity in the vertical direction, M_{pH} = ultimate unit positive moment capacity in the horizontal direction and x is the location of yield line in both direction, i.e, $x = L/2$. Thus, x/L =0.5.

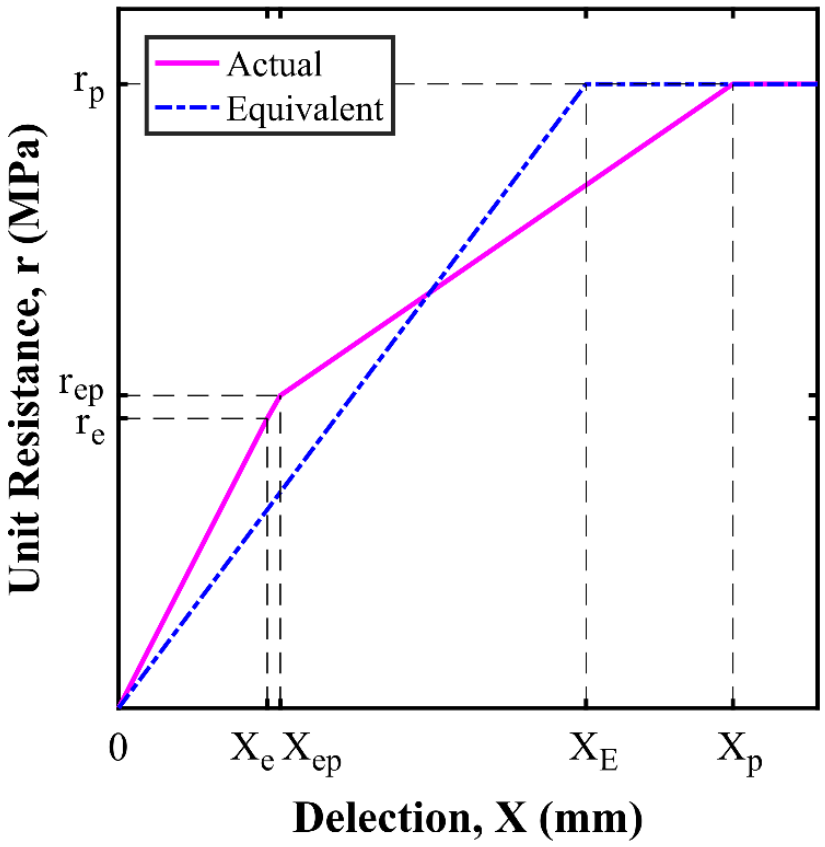

Figure 2.12 Resistance Deflection curve of an example of NRC Panel

Therefore, Ultimate unit resistance, $r_u = \dfrac{20\left(M_V + M_H\right)}{L^2} = 0.63$ MPa

Plastic deflection, $X_p = X_{ep} + \Delta X = X_{ep} + \dfrac{\gamma\left(r_u - r_{ep}\right)L^4}{D} = 7.03$ mm

Equivalent elasto-plastic deflection, $X_E = X_e\left(\dfrac{r_{ep}}{r_u}\right) + X_{ep}\left(1 + \dfrac{r_e}{r_u}\right) + X_p\left(1 + \dfrac{r_{ep}}{r_u}\right) = 5.35$ mm

The obtained parameters of resistance and deflection can be depicted as in Figure 2.12. The slope of the equivalent elasto-plastic deflection with respect to ultimate unit resistance is the equivalent stiffness of the panel and can be given as:

$$K_E = \frac{r_u}{X_E} \tag{2.5}$$

Therefore, equivalent stiffness, $K_E = \dfrac{0.63}{5.35} = 0.12$ N/mm/mm^2

Unit mass of panel, $M = \rho \text{ x } t = 2500 \text{ x } 0.291 = 727.41$ kg/m^2

Average load mass factor, $K_{LM} = 0.6$ [averaged for a fixed square panel]

Equivalent unit mass of panel, $M_E = M \text{ x } K_{LM} = 727.41\text{x}0.6 = 436.44$ kg/m^2

Natural time period of panel, $T_N = 2\pi\sqrt{\dfrac{M_E}{K_E}} = 2\pi\sqrt{\dfrac{436.44}{0.12\text{x}10^9}} = 0.012$ sec

Ultimate shear stress for a square panel is calculated be calculated as

$$\tau_u = \max\left(V_{uH}, V_{uV}\right) \tag{2.6}$$

$$V_u = \frac{3r_u\left(1 - 2d_{eff}/L\right)^2}{2d_{eff}/L\left(5 - 8d_{eff}/L\right)} \tag{2.7}$$

2.5 PANELS CONFIGURATION AND MATERIALS

The protective structure as a whole is typically a huge establishment, be it a bunker or nuclear safety structure. Civilian, military or ammunition storage bunkers are of many types like RC Box Type, RC Circular Arch type, Igloo type, Oval type, etc. with its width varying from 10 m to 40 m and height from 3.3 m to 12 m and conventionally designed for a pressure of 0.7 MPa (TranSystems Corporation 2017). Figure 2.13 shows a Box-Type Standard Ammunition storage building. The casting of such massive structures is not performed in a continuous manner which leads to formations of construction gaps. In this study, the slabs/walls of the structure will be modeled as panel with sizes are in the range of 1.5 m to 7 m based on the occurrence of these construction gaps.

Conventional reinforced concrete is the most adopted material for construction of protective structures like bunker with wall thickness of 0.3 m and more. Similarly, containment structures are typically made with a single-walled structure with a metallic liner, double-wall structure with or without metallic liner, steel containment structure and similar. In case of double-wall structure, the outer layer is made up of reinforced concrete and the inner layer is made up of post-tensioned concrete with a rear side steel liner.

From studies discussed in Section 1.5, it can be concluded that the response of ultra-high strength concrete (UHSC) under blast loading is better than conventional normal strength concrete. Also with the adoption of UHSC, the element or panel thickness can be reduced (Rebentrost and Wight 2008). Considering the advantages seen in literature, ultra-high strength reinforced concrete panels along within normal strength reinforce concrete panels are adopted for this research. The compressive strength of reinforced normal concrete ranges from 25-60 MPa and ultra-high strength concrete ranges from 60-200 MPa.

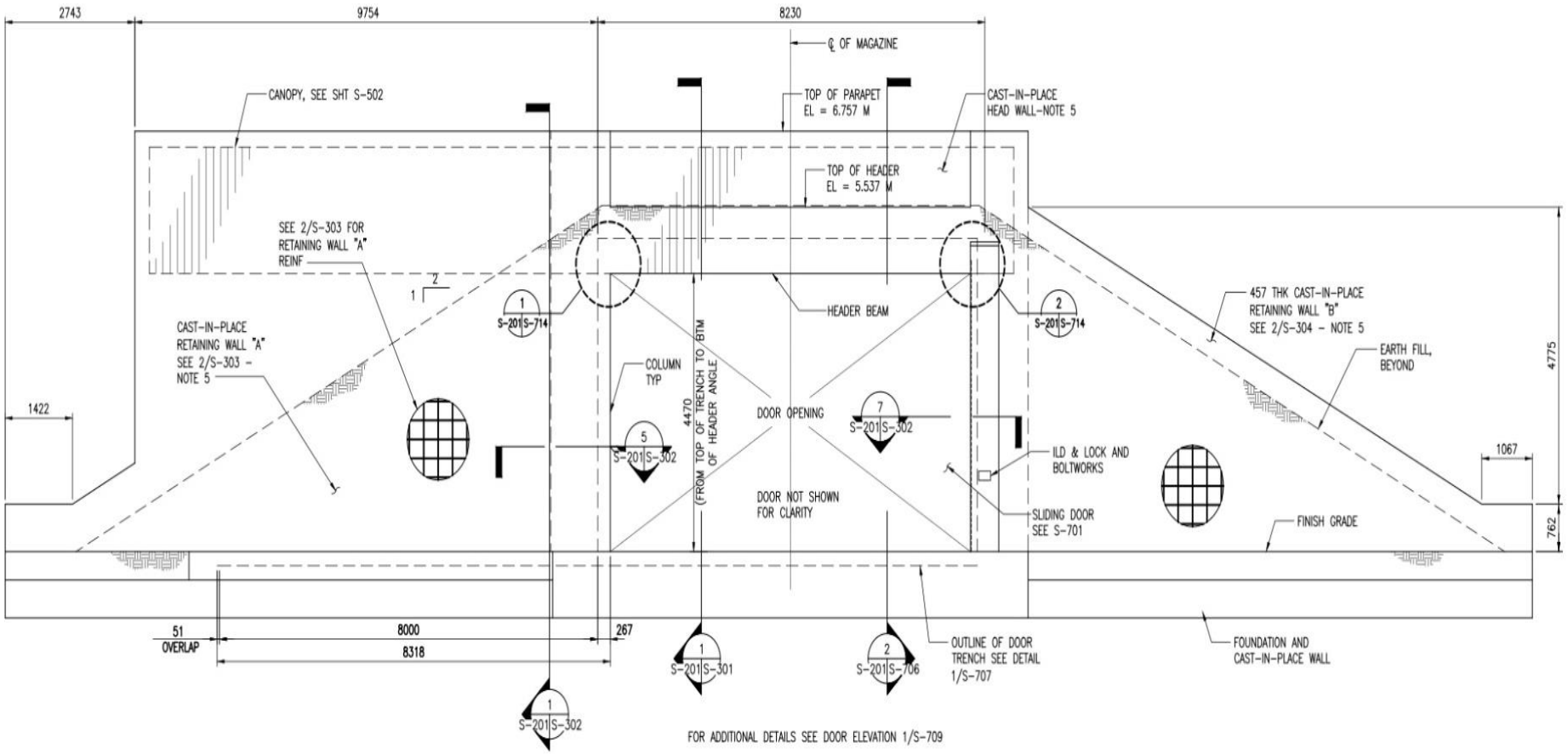

Figure 2.13 Ammunition storage building (Box-Type) (TranSystems Corporation 2017)

2.6 BLAST LOADING SCENARIOS AND ITS INTERACTION WITH THE STRUCTURE

Blast waves are generated when the air surrounding the explosive is pushed backwards due to a compressive pulse travelling outward from the centre of the explosion (Kinney and Graham 1985). 'Detonation' is a process involving rapid decomposition of explosive and rapid transmission of mechanical forces with a speed called the 'detonation velocity'. As a consequence of detonation of an explosive charge, a layer of compressed air called 'shock wave' is formed in the front of gas volume carrying the most of the energy released by the explosion. The front of the wave, known as the shock front, has a pressure (overpressure) much greater than the region behind it and thus immediately begins to decay as the shock propagates outward (Beshara 1994). Large explosions or blast may cause large scale damage and even turn into a disaster because of the sudden release of energy within a limited volume, leading to an enormous increase in pressure, light and temperature. Thus, the study of mechanism of explosion is essential for designing blast resistant facilities. The extreme loading conditions for which the analytical models will be established for air blast loading and contact blast loading.

LS-DYNA (LSTC 2007) is a commercially available software to simulate blast loading on structures. In LS-DYNA, mainly pure Lagrangian and Arbitrary Lagrangian Eulerian (ALE) are the available numerical techniques for analysing the structural response subjected to blast loadings. To obtain the blast pressure histories, a pure Lagrangian formulation with a simplified blast load description based on ConWep or an ALE formulation with a fluid-structure interaction can be used. Though, both method provides accurate results, but ALE formulation requires more computational effort compared to Lagrangian. In Lagrangian formulation, the material in an element remains in the element and does not flow in or out of it that is, the numerical mesh deforms according to the material flow. This analysis technique can lead to an erroneous results or termination when the simulation involves large angular distortion, which is the main disadvantage of this method. Another shortcoming of this

method is its applicability to blast problems involving large mass flow and limited fluid structure interaction.

An Eulerian analysis involves material flow through stationary mesh unlike Lagrangian formulation. It has a disadvantage over Lagrangian as the material moves from one element to the other and the use of advection algorithms are necessary for material flow, thus making it more complex and costlier. In this solver, coupling with other solver is required to identify fluid-structure interaction problems. It is facilitated by cell centering all variables in a mesh. Lagrangian and Eulerian method are suitable for solid and fluid respectively. Numerical simulation of detonation comprises both fluid and structural dynamics specifying shock wave propagation through air and collaboration with the structure and its response.

ALE formulation is developed by combining the Lagrangian and Eulerian formulation, for addressing both the structural and fluid dynamics of a detonation. This method rezones the nodes to an optimal position unlike Eulerian solver. ALE simulation is costlier compared to Lagrangian as most of the time is spent in calculating the material to be transported between the elements. ALE handles large distortion and preserves the ability to identify interfaces covering the shortcomings of Lagrangian and Eulerian method.

2.6.1 Air Blast

An explosion, which occurs in free air, produces an initial output where shock wave propagates away from the centre of the detonation striking the structure. This type of explosions occurs above the ground surface and at a distance away from the protective structure so that the initial shock wave, propagating away from the explosion, impacts the ground surface prior to the structure (US Department of Defense 2008). Experimental and numerical study of structural elements exposed to air blast showed that far field air blast cause flexural failure in panels or slabs and spallation of concrete occurs at bottom face together with deflection when

charge is located at the central axis along the depth. Increasing the charge weight and decreasing the scaled distance results in changing of failure mode from flexural damage to perforation damage (Rao et al. 2018).

The far-field air blast and contact blast is only adopted in this research as from the previous studies it is seen that the damage in near-field air blast is similar to that of a contact blast, i.e, localized spallation of concrete. The term used as air blast used for the future work is only to refer far-field air blast. This research aims to contribute a low to medium level blast protection and therefore a blast threat level from a bomb or any explosive which can be carried by luggage, automobile and medium van is considered as described in FEMA-428 /BIPS-07 (2012) for air blast. Conwep formulation in LS-DYNA is adopted to model the slabs under air blast loading.

2.6.2 Contact Blast

Panels subjected to contact blast shows a blast crushing crater with some circumference around the contact area along with radial cracks in the concrete on the face of contact and back side of the panel. Significant reduction in concrete punching and spall damage in UHSC as compared with the NRC slab was observed from the experimental results (Li et al. 2015a). Spalling of concrete occurs due to escalation in net primary stresses over the concrete resistance forces and dynamic tensile strength. Presence of steel plate effectively reduced the mid-span deflections of steel-concrete composite panels and delivered adequate loading bearing capacity than the RC slab (Zhao et al. 2019a). Significant spalling and crater leads to perforation and then the whole damaged area to punch out (Zhang et al. 2006).

This study considers, a blast threat level from an explosive which can be carried in a pipe bomb to a Suitcase Bomb is considered for contact blast as described in (FEMA-428

/BIPS-07 2012). A multi-material ALE finite element formulation is adopted to model the interaction between the panels and the contact charge.

2.7 DEVELOPMENT OF PROBABILISTIC MODELS

The limitations and complications of conducting full-scale contact blast experiments involve high costs and obtaining permission to carry out the experiments. A finite element approach is thus adopted in order to get the required data. In order to get the data required, a finite element approach is adopted. In this research the panels i.e. normal reinforced concrete (NRC) panel and ultra-high strength concrete (UHSC) panel is considered. A total of 50 of each type of panels with different parameters in true ranges are selected and are exposed to air blast and contact blast of varying weight and stand-off distances, through finite element (FE) numerical analysis using LS-DYNA. Based on the obtained FE results, the probabilistic capacity models for each performance level of each panel and demand for each blast loading cases are estimated in Chapter 5 and Chapter 6 respectively. The probabilistic models in this research is developed based on Bayesian perception of probability.

2.7.1 Bayesian approach

The Bayesian approach combines sample information with other information that may be available prior to collecting the sample (Montgomery and Runger 2007). Details of Bayesian approach is given in Frangopol (2008) which is based on Bayes rule and is a proper tools for combining and updating the available data. In engineering, for formulation of a sound design approach we require significant amount of data to overcome the uncertainties in a system. Probabilistic analysis often considers two uncertainties. First, aleatory uncertainty associated with the inherent variability of the information which is irreducible and second, epistemic uncertainty associated with the lack of knowledge, ability to make predictions, measurement errors, statistical uncertainty, model inexactness, etc. (Gardoni et al. 2002). Bayesian approach

can evaluate these uncertainties by systematically updating the available information as new data is attained and combining both uncertainties in the estimation of parameters for the purpose of design formulations (Frangopol 2008). Unknown parameters are considered as random variables for parameter estimation with this approach so as to combine all uncertainty sources. Thus, purpose of Bayesian analysis is to determine posterior probabilities based on prior probabilities and new information and hence is suggested for decision-making process whenever additional information is gathered.

In this research a Bayesian based probabilistic models for capacity of the panels and demand on these structural components is presented that account for all the uncertainties, including model errors. Based on the formulations obtained through Bayesian approach the fragility analysis is accomplished.

2.8 FRAGILITY ANALYSIS

The probability of attaining or exceeding prescribed limit states of a structure for a given set of demand variables is termed as fragility (Gardoni et al. 2002). Demand variables are based upon the type of loading acting on the structure like ground motion for earthquake loading, impact loading for missile hitting, blast pressure for blast loading, etc. Probabilistic demand models are used to establish the fragility of the structural component by providing treatment to aleatory and epistemic uncertainties. Aleatory uncertainties are random in nature and also known as inherent variable and randomness. This uncertainty cannot be observed by the spectator or pattern of observation and is available in the set of quantifiable variables like material property constants, structural member dimensions, and imposed boundary conditions and partly in error terms (Gardoni et al. 2002). The Epistemic uncertainties arose due to our lack of knowledge, from measurement errors, from limited observation samples. This kind of uncertainty are available in capacity, demand models and partially in error terms. Fragility plots are generated

for each performance objectives defined in this research. Each performance level could generate particular fragility curve to show the vulnerability of the specimen.

2.9 RELIABILITY-BASED DESIGN PROCESS

Loads and resistances are subject to uncertainties and therefore, the load and resistance factor design (LRFD) codes are computed using Reliability-based techniques, which accounts for appropriate safety gaps in guidelines and ensures decrease in the probability of failure due to insufficient capacities or excesses in demand or loads when designing new structures or evaluating existing structure safety (Beck and De Souza 2010). Reliability theory can be defined as a branch of probability theory of a structure (Faber and Sørensen 2002; Jr 2009; Moan 2006) with adequate performance for an intended period of time under the encountered working conditions (Uche and Afolayan 2008) and that can rationally evaluate all possible sources of uncertainties (Ditlevsen and Madsen 1996).

Reliability-based code calibration was adopted to improve the structural design codes from allowable stress to limit state (partial factor) design, ensuring that the safety level of the new codes reflected the general safety level of old codes with collective knowledge and experience-based optimization over the years (Beck and De Souza 2010; Melchers and Beck 2018). Thoft-Christensen and Baker (1982) suggested using physical reasoning on the basis of each individual random variable and directed the choice of a lognormal distribution of probability for reliability calculated as the product of independent random variables and of a normal distribution for reliability calculated as the sum of the independent random variables. A Weibull distribution is recommended for large variation in the resistance data. With the help of the above mentioned reasoning, the dead or permanent load is generally modeled as normal distribution and live and transient loads are usually considered as normal, lognormal or extreme value distributions. First-order reliability moment method (FORM) is the most common

technique among the multiple available methods despite of availability of advanced methods such as second-order moment method (SORM) as it is applicable to all probabilistic problems. In particular, most code writing agencies, researchers and specialists used FORM and Monte Carlo simulation (MCS) algorithms due to advance processing speeds and efficiency, to build methods for the development of load and resistance factor design (LRFD) (Nowak and Collins 2012).

Based on simulation data, a reliability-based analysis will be done with the defined performance levels and hazard curve with different mass of the charge and stand-off distance from the charge with suitable probability distributions like normal, log normal, extreme type1, etc. will be generated. Next the code calibration to estimate factors with the performance levels for the NRC, and UHSC panels is done and total probability of the failure with a combined reliability index of the performance levels of all the panels are estimated.

In this chapter, the basic idea and methodology of research is summarized along with the specimen panel configuration and loading conditions. The next chapter gives the detailed structure of the finite element model to be adopted in this thesis for the performance-based capacity and design model development.

Chapter 3. FINITE ELEMENT MODEL

In the present chapter, a detailed analysis of Panels as well as detonation formulation to be applied on the panels is presented along with its material model, structural configuration and the element type. To establish the accuracy of the finite element method for simulation, one validation is carried out for detonation modeling in air and two validations are done for air and contact blast loading on structures.

3.1 NUMERICAL MODEL OF PANELS

Though experimental results are more accurate and realistic, performing a real experiment is time consuming, expensive and requires preparedness to handle dangerous materials like explosives. So, numerical analysis is often preferable for inexpensive and lesser time consuming approach to determine the dynamic response of a structure under extreme loads. The most acceptable modeling methods of RC structures are the smeared model, embedded model, and discrete model. For performing the dynamic response of individual structural components, the discrete model is the best method (Hentz et al. 2004).

In the present investigation, a 3D finite element model is adopted to predict and model the damage mechanism and the failure modes of the panels against blast. A geometric model of the panel is made and analysed in the commercial FE program LS-DYNA (Livermore Software Technology Corporation) as shown in Figure 3.1. The software is a general purpose finite element software capable of simulating the complex realistic problems. The codes origin lies in highly non-linear, transient dynamic finite element analysis using the explicit time integration method.

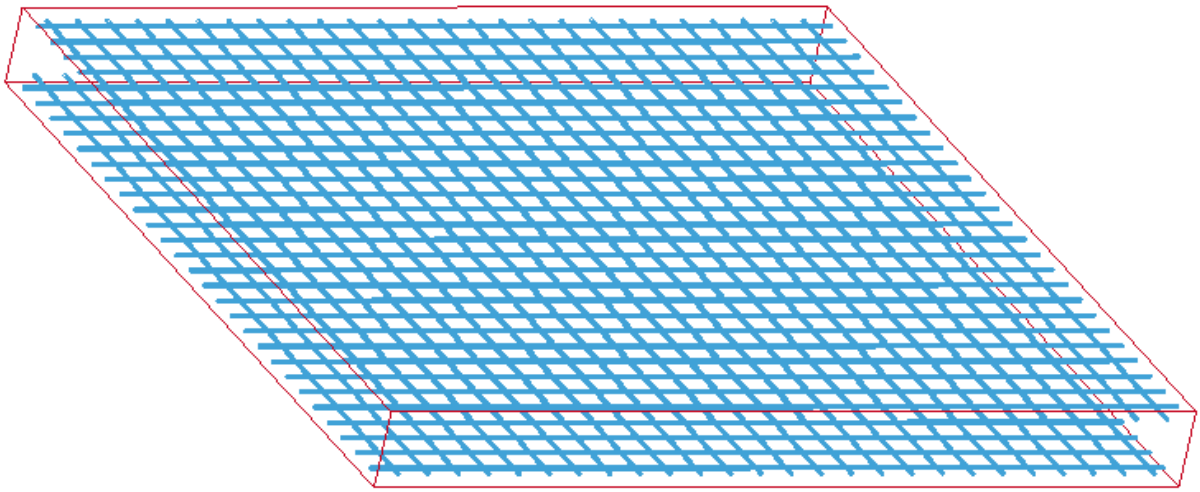

Figure 3.1 FE model showing reinforcement placements

3.1.1 Configurations of the Panels

The effect of mesh size on blast wave loading parameters and structural response is studied in depth, and minimum mesh design guidelines are proposed by Trajkovski et al. (2014). As the mesh is refined, it is ideal for a computational solution to converge. A mesh convergence research based on internal energy was conducted by many researchers (Alañón et al. 2018; Castedo et al. 2021; Feng et al. 2021). Convergence is aided by regulatory approaches that reduce or eliminate element-to-element variance in fracture energy (Alañón et al. 2018). The fracture energy of a material is a property of that material, and it must be treated as such. Regulating mesh size dependency can be accomplished in a variety of ways. To keep the fracture energy constant, one method is to manually change the damage parameters as a function of element size. However, since the user would have to input different sets of damage parameters for each size element, this solution is impractical. Incorporating an element length scale into the model provides a more automatic technique. This is accomplished by giving the element size to the material model, which calculates the damage parameters as a function of element size internally. Finally, to control mesh size dependency, viscous approaches for simulating rate effects have been presented (Alañón et al. 2018; Castedo et al. 2021). When

rate-independent computations are undertaken, however, viscous methods are rendered ineffective. The concrete model maintains constant fracture energy regardless of element size to regulate mesh size sensitivity. Regardless of the point that spherical mesh better represents the blast wave in free air (Kakogiannis et al. 2010), rectangular mesh was used for all the models because it is better in solving the leakage problem when Fluid–structure interaction (FSI) is involved (Olovsson and Souli 2000; Tan et al. 2012). The mesh size can affect Lagrangian models, therefore a convergence study is recommended (Castedo et al. 2021). Based on the prior mesh convergence experiments published in similar works using real-size slabs (Alañón et al. 2018; Castedo et al. 2021; Feng et al. 2021; Gong et al. 2009; Reifarth et al. 2021), a 20 mm rectangular mesh size is adopted for the present study for both air and contact blast modeling.

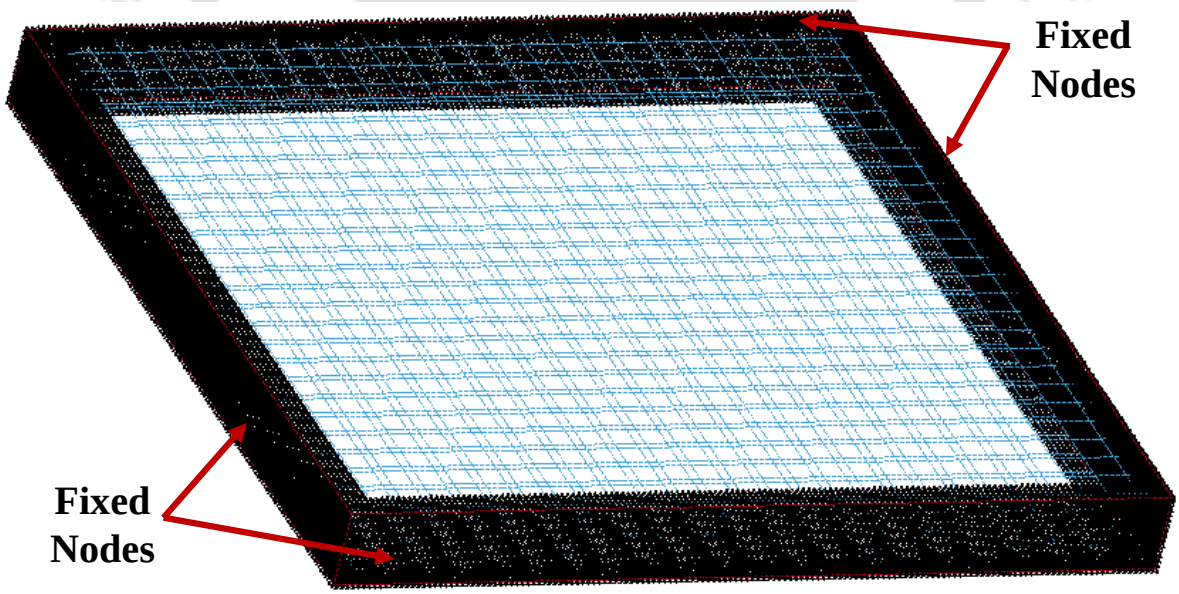

Figure 3.2 FE Model of panel showing boundary conditions

Based on the literature available, the specimens are limited to square shaped panels as for contact blast, effects are localized in the particular area of interaction between the charge and the specimen. The boundary condition is kept fixed-fixed for all the panels and a default 3D solid element formulation with mesh size 20 mm is used for panel modeling as shown in

Figure 3.2. Steel reinforcement in the panel are varied with different reinforcement ratios with one-dimensional Hughes-Liu beam elements model. The contact between the reinforcement and concrete is establish by Lagrangian coupling method where, concrete is the master and the reinforcements are defined as slaves for the reinforced concrete panels. Bearing of 50 mm is adopted for all the panels.

3.1.2 Material Models and Equation of State

Normal Concrete Modeling

Amongst the various concrete models available in LS-DYNA, Winfrith Concrete model is adopted for the study of NRC panels as the model includes the strain softening in tension with an attempt at regularization via crack opening width or fracture energy. This model basically is a plasticity model that includes third stress invariant for consistently considering the triaxial compression and tension. The model also allows the optional strain rate effects i.e., MAT084 includes the rate effects and MAT085 does not includes the strain rate effects. Smeared reinforcement can directly be included in this model, which is not offered by other concrete models. The pressure at uniaxial compression failure, p_1 is automatically generated by the equation given, when the volume compaction curve is omitted.

$$p_1 = \frac{f_c'}{3} \tag{3.1}$$

And the bulk unloading modulus, K is calculated by –

$$K = \frac{E_s}{3(1-2\upsilon)} \tag{3.2}$$

where, E_s is the tangent modulus of concrete, υ is Poisson's ratio and f' is the unconfined compression strength. Since the Winfrith concrete model may produces unrealistic simulation

results with the strain rate effects, the strain rate effects are not considered in this analysis. An erosion criterion of 0.01 maximum principal strain is incorporated in the analysis.

High Strength Concrete Modeling

Various material models such as Pseudo Tensor (MAT_16), Brittle Damage (MAT_96), Johnson Holmquist Concrete (MAT_111) and Concrete Damage Rel3 (MAT_72_REL3) can be used in LS-DYNA to model concrete for dynamic loading. These material models are appropriate for modeling the brittle behaviour of plain concrete but lacks in modeling the damage softening behaviour in post-yield stage of high strength concrete (HSC). In the present study, the material properties of UHSC are limited to the uniaxial compression. So, Johnson Holmquist Concrete (MAT_111) is adopted for modeling the dynamic behaviour of UHSC. Johnson Holmquist Concrete is an elastic-viscoplastic model coupled with isotropic damage, which can well define the mechanical behaviour of concrete subjected to large strains, high strain rates, and high pressures (Holmquist et al. 1993). The model separates hydrostatic and deviatoric response and presents the deviatoric response by equivalent strength model, where the normalized equivalent stress, $\sigma^* = \sigma / f_c'$ (actual equivalent stress by quasi-static uniaxial compressive strength) is defined as (LSTC 2007)

$$\sigma^* = \left[A(1-D) + BP^{*N} \right] \left[1 + C \ln\left(\dot{\varepsilon}^*\right) \right] \le S_{\max}, \tag{3.3}$$

where A and B are material constants that are related to elastoplastic deformation; $P^* = P / f_c'$ is the normalized pressure; C is the material coefficient relevant to strain rate; $\dot{\varepsilon}^* = \dot{\varepsilon} / \dot{\varepsilon}_0$ is the strain rate; $\dot{\varepsilon}$ is the actual strain rate and $\dot{\varepsilon}_0 = 1.0\text{s}^{-1}$ is the reference strain rate. N and $S_{\max}$ are the pressure hardening exponent and the normalized maximum strength, respectively; D is the damage parameter $(0 \le D \le 1)$ and is modeled as (Tai 2009)

$$D = \sum \frac{\Delta\varepsilon_p + \Delta\mu_p}{\varepsilon_p^f + \mu_p^f} = \sum \frac{\Delta\varepsilon_p + \Delta\mu_p}{D_1\left(P^* + T^*\right)^{D_2}} \tag{3.4}$$

here $\Delta\varepsilon_p$ and $\Delta\mu_p$ presents the equivalent plastic strain increment and the plastic volumetric strain increment, respectively, during a cycle of integration; and $\varepsilon_p^f + \mu_p^f = D_1\left(P^* + T^*\right)^{D_2}$ is the plastic stain under pressure. D_1 and D_2 are damage constants; $T^* = T/f_c'$ is the normalized largest tensile strength, T is the maximum tensile strength. The pressure response is governed by the EOS and given as below for fully dense material with K_1, K_2 and K_3 as material constants

$$P = K_1\bar{\mu} + K_2\bar{\mu}^2 + K_3\bar{\mu}^3 \tag{3.5}$$

where, $\bar{\mu} = \left(\mu - \mu_{lock}\right)/\left(1 + \mu_{lock}\right)$ is the modified volumetric strain and μ_{lock} is the locking volumetric strain. All the material parameters required, are calculated from the concrete model given in Comité Euro-International du Béton (1993) and Ren et al. (2017) with the available compressive strength value. An erosion criterion of 0.005 maximum principal strain is incorporated in the analysis.

Steel Modeling

Steel reinforcements are modeled as material plastic kinematic (MAT_003) model from LS-DYNA in the present work which can be defined as an isotropic and kinematic hardening plasticity model including the rate effects option. Moreover, it is a cost effective model and is available for beam, shell, and solid elements.

3.2 NUMERICAL MODEL OF BLAST LOADING

LS-DYNA was developed as an explicit numerical analysis code for highly nonlinear, transient dynamic finite element analysis. It is widely used in solving high strain-rate problems or dynamic and impulsive problems with its Eulerian, Lagrangian and Arbitrary Lagrangian-Eulerian (ALE) solvers. The finite element configuration of explosive adopted is explained in this section along with material model, equation of state and different modeling techniques. An investigative study is also presented to identify the propagation of blast wave in a close-in blast with a developed near-field cylindrical blast formulation.

3.2.1 Configuration for Blast Loads

Modeling the explosion involves the shock wave propagation through charge and the surrounding media. Finite element code, LS-DYNA (LSTC 2007) is used in this study for explicit modeling of detonation. In the explicit modeling, the explosive and the surrounding air is created by a finite element model. Meshing is the first step involved in the procedure followed by applying pertinent boundary conditions. The second step includes assigning material properties and initial condition by specifying the explosive mass, its energy and pressure of the surrounding air.

ConWep Modeling

Modeling of detonation can be carried out in a number of ways in LS-DYNA. ConWep (Hyde 1988) is a semi-empirical modeling technique which produces pressure histories that can be enforced on a structure thorough Load Blast enhanced (LBE). It is based on the empirical data and for a given explosive mass and stand-off distance. It predicts incident and reflected pressure histories. This method can be used to model free air blast of spherical charge and surface blast of hemispherical charge. In this formulation, exponential decay of the incident and the reflected pressure with time is considered which is more realistic method. The disadvantage of ConWep

formulation is that the shorter the stand-off distance becomes, the less accurate is the result. The blast load is applied to the slab surface through the *Load_Blast_Enhanced formulation. The major disadvantage of this formulation is that the reflections cannot be accounted. But, this technique of modeling can reduce the computational cost of analysis in the mid-air and far field substantially by avoiding the explicit modeling of detonation process.

Multi-Material ALE Modeling

The multi-material ALE formulation is suitable for air blast simulation, as an element can contain two or more different materials and it allows the mesh to move independently of the material flow. The modeling technique involves separate meshing of both the air and the explosive. This is particularly appropriate for problems involving fluid-structure interaction. Another way of modeling a detonation in air is by meshing only the air domain. The explosive is defined within the mesh of air by specifying the initial detonation fraction in air thought the *INITIAL_VOLUME_FRACTION_GEOMETRY option. It calls a volume filling command which defines the region in some specified ALE mesh set, to be occupied by various ALE multi-material groups (AAMG). The explosive geometry or the container can be defined as a shell element, segment set, a plane, conical surface, a sphere, a cuboid or a rectangle.

SPH Modeling

Smoothed particle hydrodynamics (SPH) method was initially established by Lucy (1977) and Gingold and Monaghan (1977), where discrete particles interacting with each other through an interpolation function like a set of fluid, are adopted instead of finite elements. This method can be used to formulate blast as it is appropriate for large deformation events including failure and fragmentations. But SPH modeling gives best results for finer mesh. The finer the mesh the closure the results gets to reality. This make the simulations costlier and time consuming.

Based on the numerical studies conducted earlier and FEMA-428 /BIPS-07 (2012), the charge weight range for air blast is adopted as 20-1000 kg TNT and stand-off distance of 3-30 m; and for contact blast it is taken in the range of 1-10 kg TNT based on its carrying capacity.

3.2.2 Interaction with the Structure

Air Blast

For all the panels described in Section 3.1, the far-field air blast is applied with the ConWep formulation (discussed in the previous section). Thus, a spherical air blast is simulated using *Load_Blast_Enhanced keyword with different charge weight and stand-off distance. For this, the first layers of the panels are converted into the contact surface to which the blast loads are applied. The method used in this study is purely Lagrangian approach in which the blast load is applied on the structure as triangular impulse. The deformation in the top of a panel is shown in Figure 3.3 and Figure 3.4 displays the deformation at the bottom of the panel.

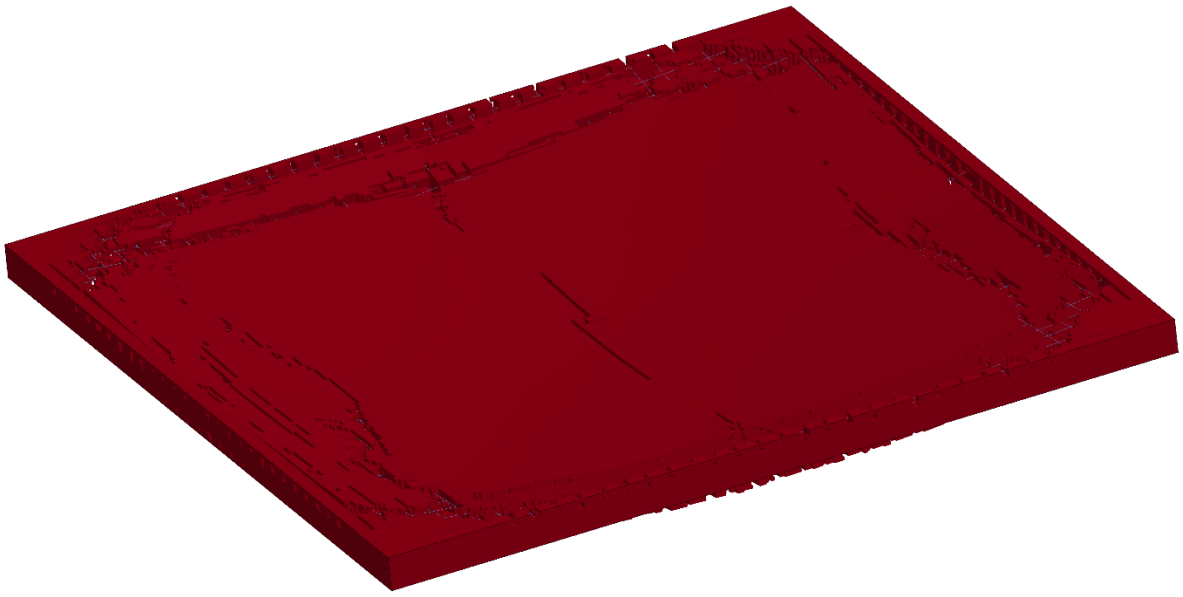

Figure 3.3 Deformation in the top of the panel in simulation

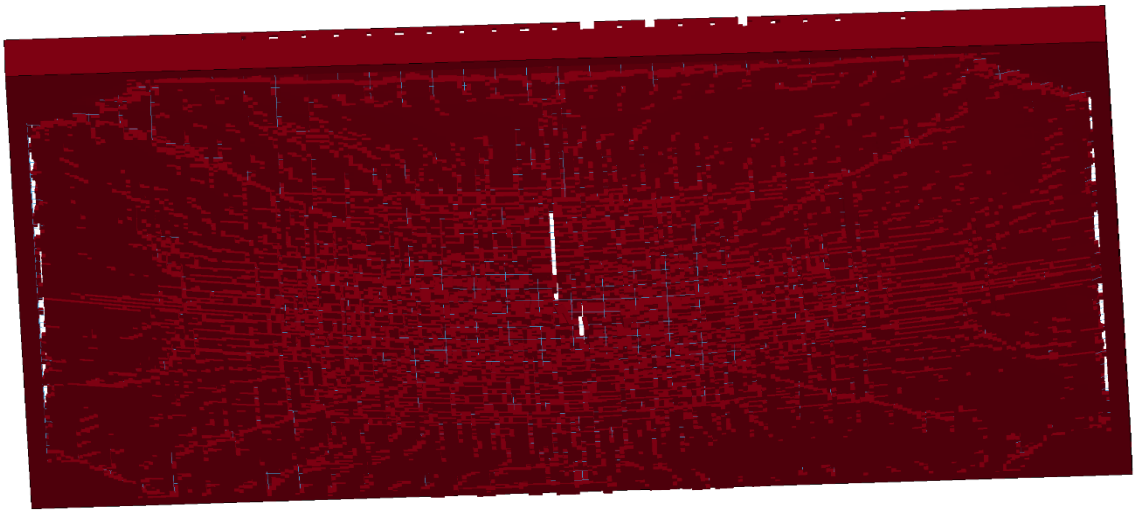

Figure 3.4 Deformation in bottom face of the panel

Contact Blast

To model the dynamic response of the panels under contact blast, a three-dimensional solid model is used. The multi-material ALE formulation is adopted for modeling to create a more realistic scenario. The air domain is meshed as a 3D solid model with 40 mm mesh size and explosive is defined as a part of the ALE air mesh set with the help of initial volume fraction geometry option available in LS-DYNA. In this particular study, the explosive geometry is considered as a cylindrical container. Air domain is modeled surrounding the panels which are modeled as described in Section 3.1. The boundary of the air domain is defined as non-reflective surface.

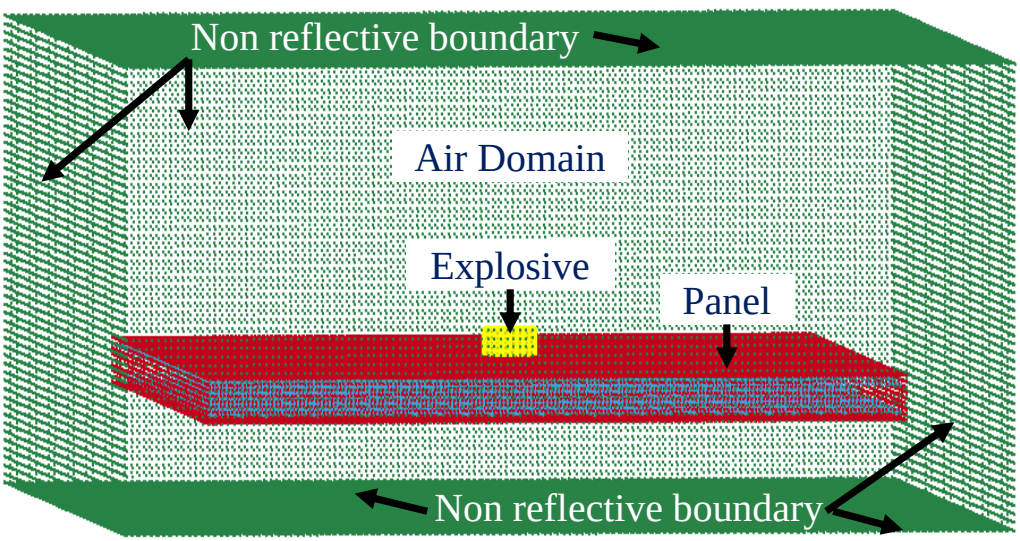

Figure 3.5 FE Model of Panel for Contact blast using MM-ALE

3.2.3 Material Model and Equation of State

Material models and equation of states (EOS) are necessary to formulate blast in MM-ALE and SPH Modeling techniques and are described as follows:

Explosive or Charge

For modeling the detonation of a high explosive, the *High_Explosive_Burn card is used along with an equation of state. This material model needs the mass density, detonation velocity and Chapman-Jouguet pressure as input parameters. The Beta burn flag command controls the release of chemical energy for detonation simulation. In a high explosive, pressure at any point of time is defined as

$$p = Fp_{eos}(V, E) \tag{3.6}$$

where, p_{eos} is the pressure calculated with the equation of state, V is the relative volume and E is the internal energy density per unit initial volume. The burn fraction, F is taken as

$$F = \max\left(F_1, F_2\right) \tag{3.7}$$

where, F_1 and F_2 are calculated as

$$F_1 = \begin{cases} \dfrac{2\left(t - t_l\right) DA_{e_{\max}}}{3v_e} & \text{if } t > t_l \\ 0 & \text{if } t \le t_l \end{cases} \tag{3.8}$$

$$F_2 = \beta = \frac{1 - V}{1 - V_{CJ}} \tag{3.9}$$

where, t is the current time and V_{CJ} is the Chapman-Jouguet relative volume, v_e is the element volume and $A_{e_{\max}}$ is the area of the largest side of an element. A lighting time, t_l is calculated for each element in the initialization phase by dividing the distance between the detonation

point and center of the element by detonation velocity, D. In the present study the beta is set as default 'beta +' programmed burn option.

Amongst a number of empirical EOS developed for high explosives, Jones-Wilkins-Lee (JWL) equation is the most popular as it is easily calibrated. The use of each of the developed EOS is limited to a range of experimental data from where it is derived but most explosives can be modeled using JWL Equation. This EOS defines pressure as

$$p = A\left(1-\frac{\omega}{R_1 V}\right)e^{-R_1 V} + B\left(1-\frac{\omega}{R_2 V}\right)e^{-R_2 V} + \frac{\omega E}{V} \tag{3.10}$$

and is usually used for modeling detonation products of high explosives. Here, A and B are linear coefficients and E_0 is detonation energy per unit volume of explosive having units of pressure. R_1, R_2 and ω are nonlinear coefficients and V_0 is ratio of the volume of detonation products and volume of undetonated high explosive. For high explosives, it is recommended to use the equation in the unit system of gram, centimetre, microsecond and where the pressure is in Mbar. Using this modeling technique one can model any charge shape, size and at any point of detonation allowing an accurate assessment of blast overpressure.

Air

Air is modeled as an ideal gas using *Null material model (LSTC 2007) along with the Linear Polynomial equation of state. The mass density and pressure cut-off are the parameters required for its application. The pressure cut-off is negative in tension and the null material has no shear stiffness. With this material card the material behaves as a fluid and has no yield strength. Hourglass coefficient should be carefully selected as default value may lead to significant energy loss.

Chemical explosion heats the nearby air which is considered in the numerical analysis by treating the surrounding air as ideal gas with a constant specific heat ratio, γ. A linear variation in the internal energy, E is generalized as an EOS, where pressure is given by:

$$p = C_0 + C_1\mu + C_2\mu^2 + C_3\mu^3 + \left(C_4 + C_5\mu + C_6\mu^2\right)E \tag{3.11}$$

where $C_0, C_1, C_2, C_3, C_4, C_5, C_6$ are 0^{th} to 6^{th} polynomial coefficient and $\mu = \rho/\rho_0 - 1$, where ρ and ρ_0 are the current and initial densities of air. E_0 represents initial internal energy per unit reference volume. The EOS can be utilized as an ideal gas equation by considering, $C_0 = C_1 = C_2 = C_3 = C_6 = 0$ and $C_4 = C_5 = \gamma - 1$, where γ is the ratio of specific heats. Thus equation (3.11) becomes,

$$p = (\gamma - 1)\frac{\rho}{\rho_0}E \tag{3.12}$$

when $C_0 = C_1 = C_2 = C_3 = C_6 = 0$, it does not necessarily indicates that the initial pressure is zero as the initial pressure is based on all the coefficients. The details of the material and EOS used in this work is shown in Table 3.1.

Table 3.1 Material and EOS parameters used for TNT and Air

TNT				**Air**			
High explosive burn material model		JWL EOS		Null material model		Linear polynomial EOS	
Parameter	Value	Parameter	Value	Parameter	Value	Parameter	Value
ρ (kg/m^3)	1630	A (GPa)	371.20			C_0	0
		B (GPa)	3.23	ρ (kg/m^3)	1.23	C_1	0
PCJ (GPa)	21	R_1	4.15			C_2	0
		R_2	0.95			C_3=C_6	0
D (m/s)	6930	ω	0.3	PC (GPa)	0	C_4=C_5	0.4
		E_0 (GPa)	7.0			E_0 (GPa)	0.00025

3.2.4 Near-Field Charge Shape Effect on Overpressure in Free Air

Blast resistant deign is conventionally performed based on the empirical design charts provided in the UFC-3-340 code, where the blast loading is simply characterized by charge weight and stand-off distance. From these charts, the obtained peak overpressure and its duration is applied on the structure uniformly with the empirical formulations for either a spherical free air or hemispherical surface blast and does not account for variation in charge shape, orientation and point of detonation. Therefore, while facing a near-field or contact blast problem with cylindrical shaped charge, which is directly placed on a structure these empirical design charts are not much helpful. The present work focuses on the change in peak overpressure due to change in charge shape. Three different shape of charges namely, spherical, cuboid and cylindrical each of 1, 2 and 3 gm equivalent weight of TNT are used for simulating the free air blast for the present study. The charge weight adopted is small to allow higher precision in fine mesh. Tracer particles are placed a spacing such that Z is equal to 0.1-0.5 $m/kg^{1/3}$ in the MM-ALE formulation. The study is performed on a 2D mesh air domain and TNT of the specific size and shape is defined as a part of air. The advection method used in the present validation model is 2^{nd} order Van-Leer algorithm and default number of time step between advection cycle (NADV). The validation for this finite element model is presented in Section 3.3.2.

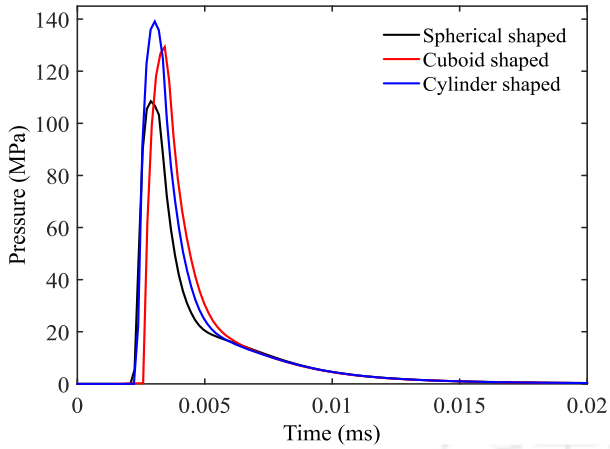

(a) Z = 0.1 m/kg$^{1/3}$

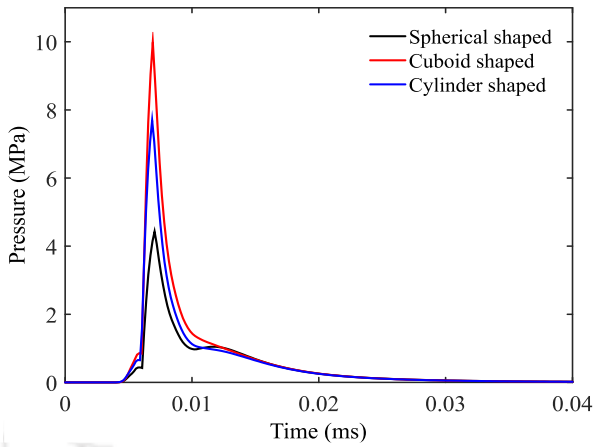

(b) Z = 0.2 m/kg$^{1/3}$

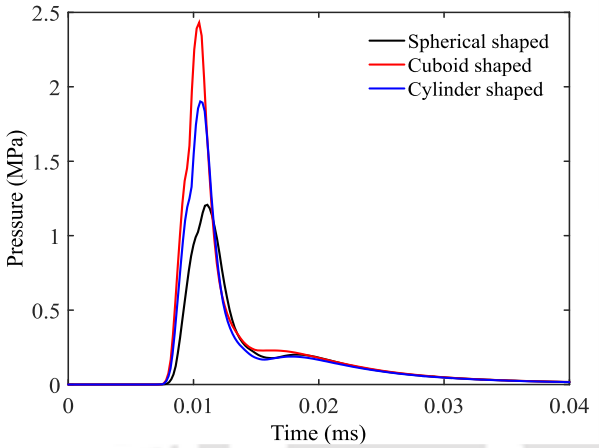

(c) Z = 0.3 m/kg$^{1/3}$

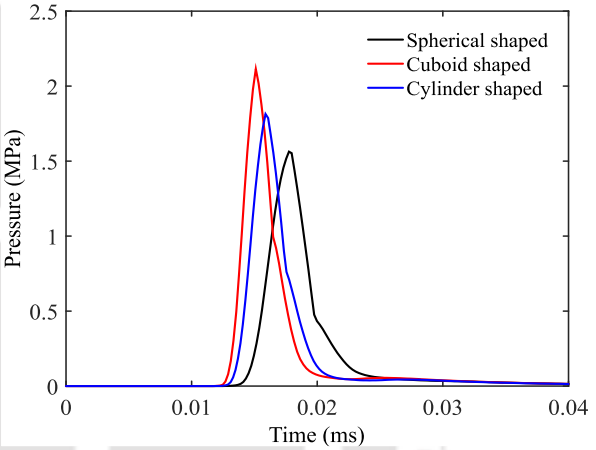

(d) Z = 0.4 m/kg$^{1/3}$

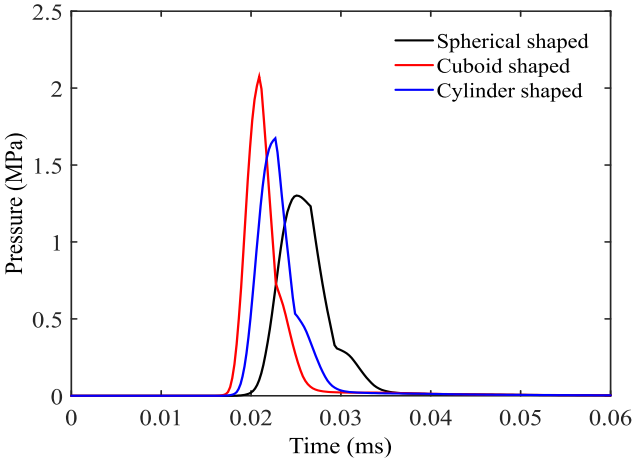

(e) Z = 0.5 m/kg$^{1/3}$

Figure 3.6 Pressure histories obtained from 1 gm of TNT with different charge shape

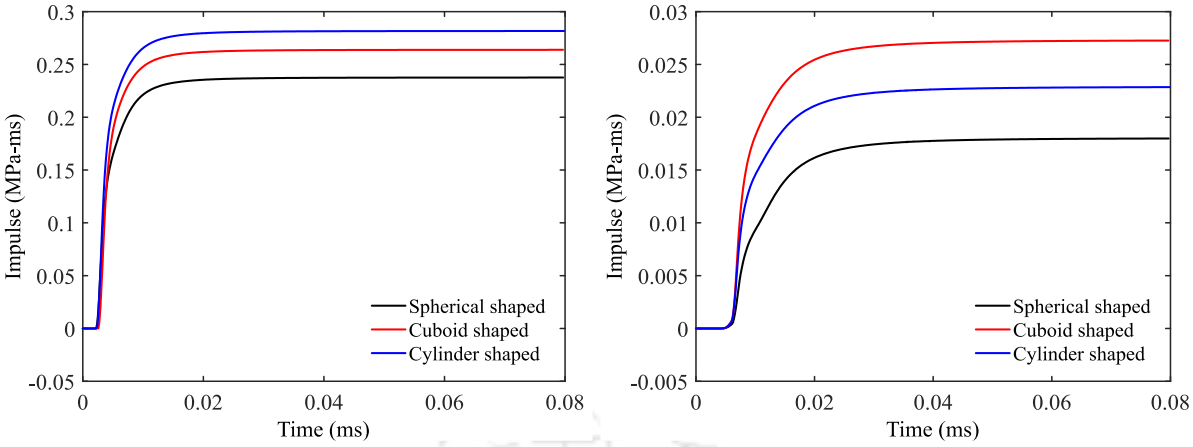

(a) Z = 0.1 m/kg$^{1/3}$ (b) Z = 0.2 m/kg$^{1/3}$

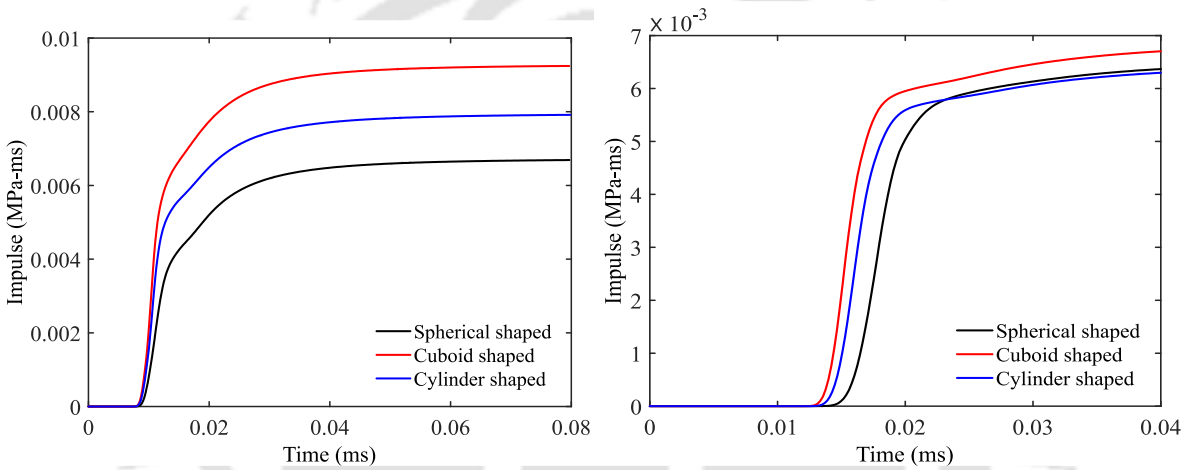

(c) Z = 0.3 m/kg$^{1/3}$ (d) Z = 0.4 m/kg$^{1/3}$

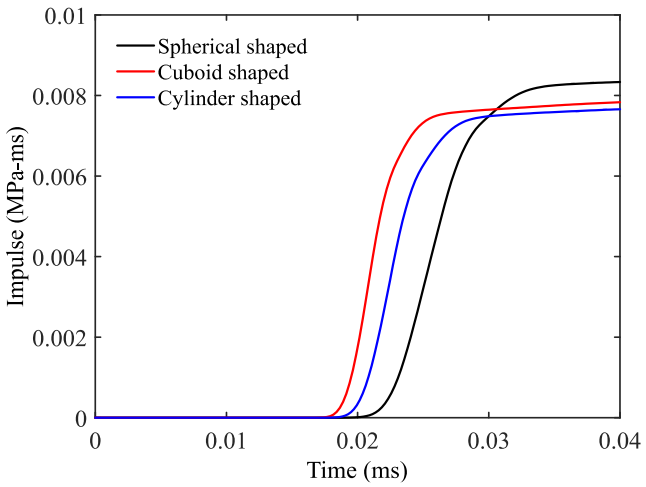

(e) Z = 0.5 m/kg$^{1/3}$

Figure 3.7 Impulse histories obtained from 1 gm of TNT with different charge shape

The variations of peak overpressure obtained is presented in Table 3.2. With the increase in charge weight, an increase in peak overpressure for any shape is obtained only when Z is greater than equal to 0.3 m/kg$^{1/3}$. No specific pattern can be seen at Z = 0.1 and 0.2 m/kg$^{1/3}$. Figure 3.6 and 3.7 shows the pressure and impulse histories respectively for spherical, cuboid and cylindrical charge of weight equal to 1 gm only.

Table 3.2 Peak overpressures (MPa) for different charge shape

Shape of Charge	**Z (m/kg$^{1/3}$)**	0.1	0.2	0.3	0.4	0.5
	W (kg)	**Peak over pressure (MPa)**				
Spherical	0.001	108.50	4.43	1.20	1.56	1.30
	0.002	37.20	2.65	1.89	2.09	1.54
	0.003	69.50	3.28	2.48	2.44	1.82
Cuboid	0.001	129.35	9.99	2.43	2.11	2.07
	0.002	67.47	7.26	2.76	3.00	2.71
	0.003	108.79	9.49	3.40	3.77	3.37
Cylindrical	0.001	139.09	7.69	1.90	1.81	1.67
	0.002	66.04	8.42	2.97	3.17	3.00
	0.003	115.16	12.67	4.02	4.32	4.22

From this study it is inferred that there is a significant effect of charge shape on peak overpressure. For Z equal to 0.2 to 0.5 m/kg$^{1/3}$ the cylindrical charge produces a greater peak incident overpressure than cubic or spherical charge. The time of arrival of blast wave does not change with change in charge shape. For all the charge shape, as Z increases i.e., when distance between charge centre to the point of pressure measurement increases, the peak overpressure decreases. From this study it is evident that the empirical equations given in previous literatures for spherical explosive in free air or hemi-spherical explosive in ground surface blast cannot be used for analytical calculations involving cylindrical explosives as they do not contemplate for effect.

3.2.5 Near-Field Cylindrical Blast Formulation

Regression analysis is adopted to arrive at the expression of pressure measured for Z value of 0.2 to 1 m/kg$^{1/3}$ for cylindrical explosive. Numerical models are developed for modeling the effect of cylindrical blast on overpressure. For the simulations, an air domain is considered where the explosive is in the form of a cylinder which is placed at the centre. The air domain is large enough to avoid reflection and also termination time is maintained for the same. The data set is developed for charge weighing from 0.1-5 kg of equivalent TNT. The peak blast pressure obtain for each blast for the selected range of charge weight is shown in Table 3.3.

Table 3.3 Peak blast pressure obtained from simulation of Cylindrical Explosive

Weight of TNT (kg)	Z (m/kg$^{1/3}$)								
	0.2	0.3	0.4	0.5	0.6	0.7	0.8	0.9	1
	Peak Blast Pressure (MPa)								
0.1	0.453	0.571	0.563	0.521	0.490	0.521	0.530	0.457	0.408
0.2	0.579	0.716	0.669	0.596	0.581	0.650	0.580	0.502	0.447
0.3	0.587	0.743	0.692	0.624	0.699	0.705	0.581	0.505	0.455
0.4	0.674	0.744	0.687	0.610	0.682	0.716	0.579	0.503	0.454
0.5	0.690	0.740	0.680	0.670	0.745	0.681	0.562	0.495	0.444
0.6	0.763	0.576	0.450	0.394	0.428	0.372	0.325	0.291	0.266
0.7	0.834	0.897	0.780	0.707	0.817	0.752	0.612	0.539	0.480
0.8	0.906	0.865	0.749	0.657	0.763	0.743	0.602	0.526	0.470
0.9	0.911	0.870	0.773	0.683	0.802	0.747	0.614	0.534	0.476
1.0	1.166	1.018	0.828	0.716	0.787	0.786	0.635	0.551	0.489
1.1	1.010	0.918	0.777	0.682	0.799	0.740	0.611	0.537	0.476
1.2	1.079	0.997	0.814	0.738	0.868	0.758	0.627	0.549	0.488
1.3	0.944	0.925	0.773	0.745	0.870	0.715	0.607	0.530	0.471
1.4	1.047	0.986	0.812	0.801	0.941	0.727	0.618	0.542	0.482
1.5	0.894	0.913	0.765	0.797	0.906	0.694	0.596	0.521	0.463
2.0	1.273	1.013	0.810	0.704	0.818	0.729	0.614	0.536	0.477
2.5	1.365	1.069	0.858	0.805	0.952	0.734	0.630	0.548	0.488
3.0	1.459	1.092	0.859	0.738	0.874	0.735	0.628	0.546	0.487
3.5	1.477	1.101	0.872	0.805	0.955	0.736	0.631	0.553	0.484
4.0	1.450	1.089	0.865	0.784	0.942	0.727	0.624	0.547	0.414
4.5	1.445	1.084	0.870	0.832	0.937	0.726	0.625	0.548	0.367
5.0	1.518	1.095	0.868	0.817	0.936	0.724	0.623	0.532	0.324

The estimate of the peak blast pressure proposed in this work is

$$P_{cyl} = \hat{P}_{so} \exp\left[0.0306+0.1247\frac{h}{r}+0.2973\frac{W}{\rho_a V_{a0}}-\frac{1.208}{Z}+\frac{0.1177}{Z^2}\right] \quad (3.13)$$

where, P_{cyl} is peak blast pressure by a cylindrical explosive in MPa, $\hat{P}_{so}$ is the mechanical overpressure calculated using Kinney's equation (1.4) (Kinney and Graham 1985) in MPa, h and r is the height and the radius of TNT container respectively, W is weight of equivalent TNT in kg, ρ_a is density of air (1.225 kg/m^3), V_{a0} is the volume of a cylindrical air of unit height and radius $\left(\pi\times1\times1^2=\pi \text{ m}^3\right)$ and Z is calculated as $Z = R/W^{1/3}$ (m/kg$^{1/3}$), where, R is the distance between centre of charge and pressure tracer in meters. The first term in the equation accounts for the potential constant bias present in the mechanical model. The second term accounts for slenderness ratio of cylindrical TNT container and the third for mass of the system. The fourth and fifth term accounts for the contribution of effect of scaled distance at which the pressure is measured or determined. The standard deviation of the model is 0.1256.

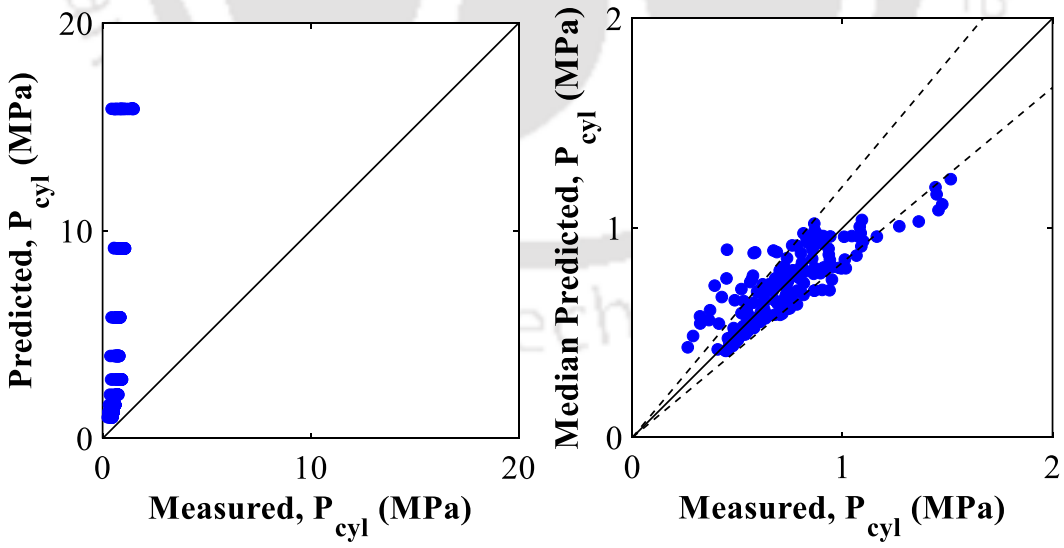

Figure 3.8 Comparison between Simulated, Predicted and Mean predicted overpressure

Figure 3.8 shows the simulated and predicted data lined with the dotted lines indicating the bounds obtained a the ± SD (Standard Deviation). For the predicted model to be perfect, data should line up along 1:1 line.

As panels are simulated by using an Conwep formulation and ALE formulation for the blasts with interaction between panel, air and explosion is coupled by Lagrange approach in this research, the validation of the adopted models are necessary. The next section presents the validations for this study.

3.3 MODEL VALIDATION

3.3.1 Comparative study of ConWep, MM-ALE and SHP Modeling with Validation

Studies shows that ConWep modeling is more cost effective and gives good results for air blast. But, for contact blasts, comparative study is necessary to figure out the best suited method for FE simulations. Numerical model for the contact blast to be applied on the panels, is to be developed for proper design of the structure. For this, contact explosion needs to be validated with previous experiment so that the model can capture the signature of load as well as the physical material properties, boundary condition and contact between the materials appropriately. Therefore, a comparison of theses modeling techniques are studied to validate as well as to arrive at the best formulation to be adopted for the FE simulations of contact blast. For this, a reinforced concrete slab of dimension 2 m x 1m x 0.1 m is validated using ConWep, MM-ALE and SHP technique. 1 kg of TNT in the form of a cylinder is placed as shown Figure 3.9. The boundary conditions of the FE model is kept close to the experimental details of the study (Li et al. 2015a). The slab has a 1.2% rebar ratio for 12 mm diameter reinforcement mesh and concrete Young's modulus of 28.3 GPa. The concrete compressive and tensile strength is considered as 39.5 MPa and 8.2 MPa respectively.

In this study, the NSC slab is modeled as a 3D solid element with the same dimensions as mentioned above with 20 mm mesh size and with 1D beam elements as reinforcements for ConWep formulations, i.e., load blast enhance is used to generate blast pressure. The same panel is within an air domain for MM-ALE formulation with initial volume fraction defining a part of air as a cylindrical TNT as shown in Figure 3.10. For SPH formulation, the high explosive material, i.e., TNT is simulated through SPH particles in the form of cylinder is placed in position on slab without any air domain. The material models for this study is tabulated in Table 3.4.

The material model of concrete for all the methods is adopted as Continuous surface cap model (CSCM), which is a plasticity based model available in LS-DYNA which requires only a single user input parameter. From the input value of unconfined compressive strength, the other remaining parameters are auto generated by a built-in algorithm in LS-DYNA. This material card also accounts for material erosion when the calculated the internal damage threshold reaches 99%. Hughes-Liu beam element (Hallquist 2006; Hughes and Liu 1981a; b) with cross section integration is used for modeling the reinforcement. The contact between the concrete and reinforcement is modeled using the Lagrangian coupling method.

Table 3.4 Keywords used for comparison study of ConWep, MM-ALE and SHP formulation

Material	**Keyword**
Concrete	Continuous surface cap model (CSCM) (MAT_159)
Reinforcement	Plastic Kinematic (MAT_003)
Explosive	High explosive (MAT_008) with EOS_JWL
Air	Null (MAT_009) with EOS_ LINEAR_POLYNOMIAL

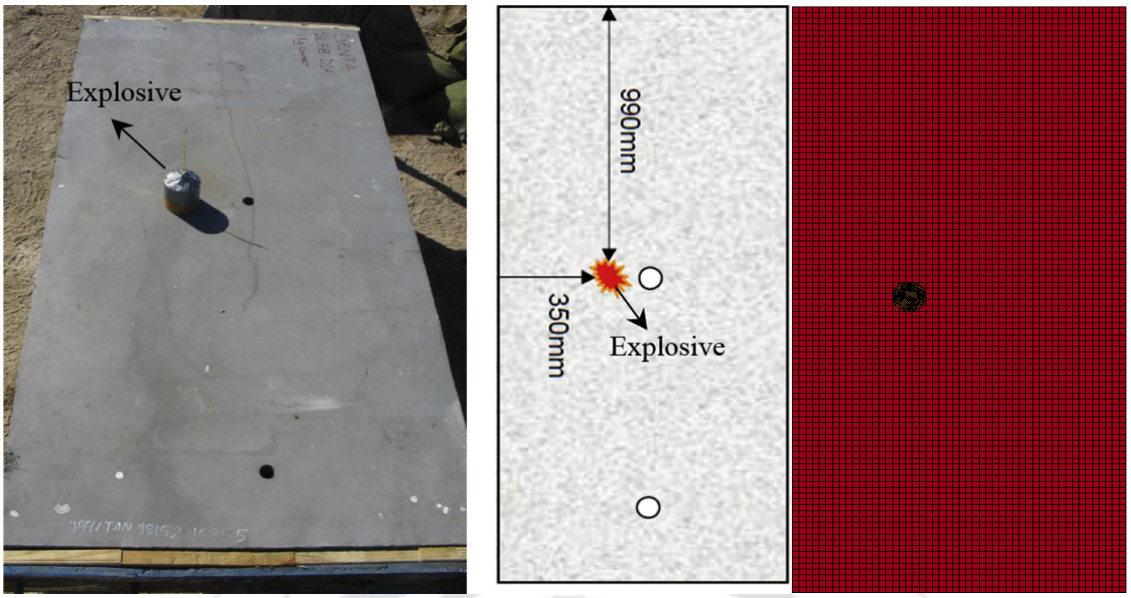

Figure 3.9 Experimental setup (Li et al. 2015a) on left and FE Model for Validation on right

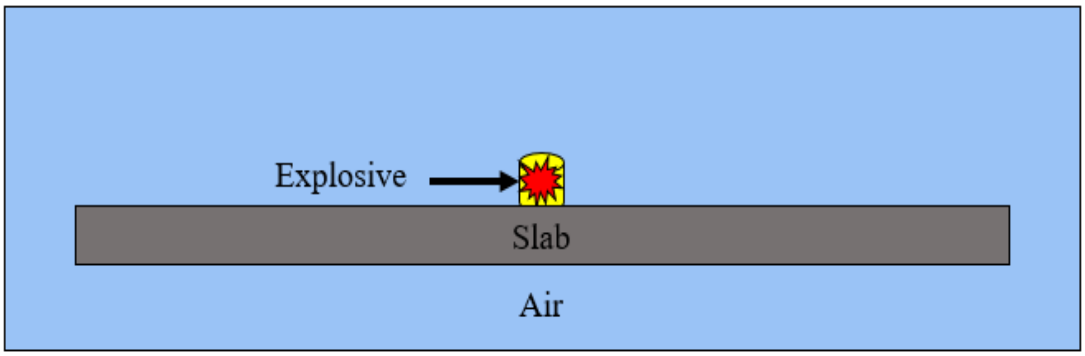

Figure 3.10 Schematic view of contact blast loading of the slab for MM-ALE method

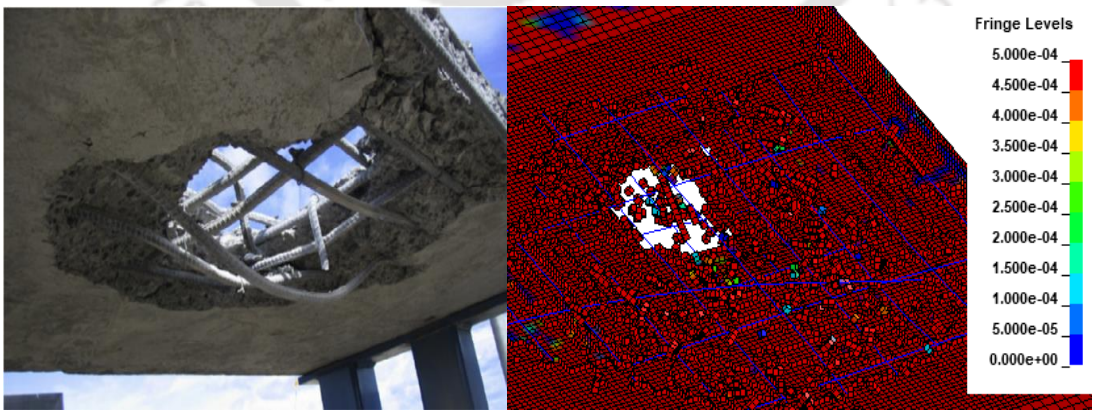

Figure 3.11 NSC bottom slab response comparison from the experiment (Li et al. 2015a)

(left) and ConWep Simulation (right)

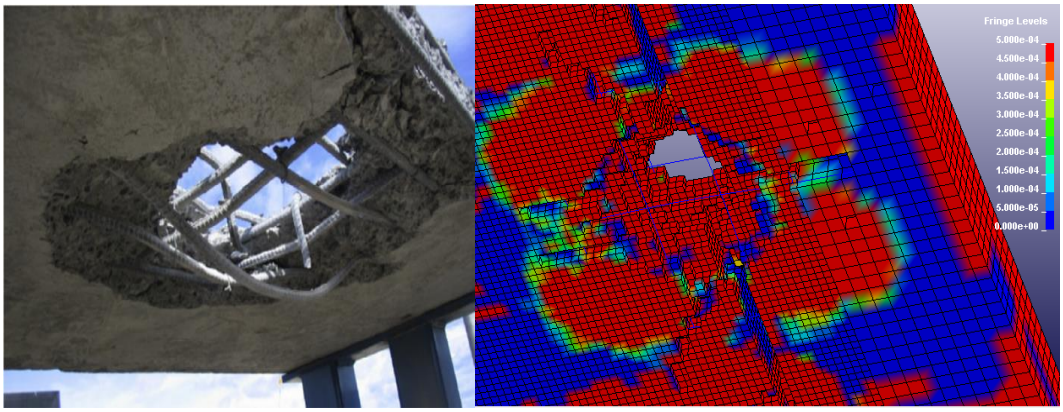

Figure 3.12 Comparison of Slab NSC bottom response of experiment (Li et al. 2015a) (left) and MM-ALE Simulation (right)

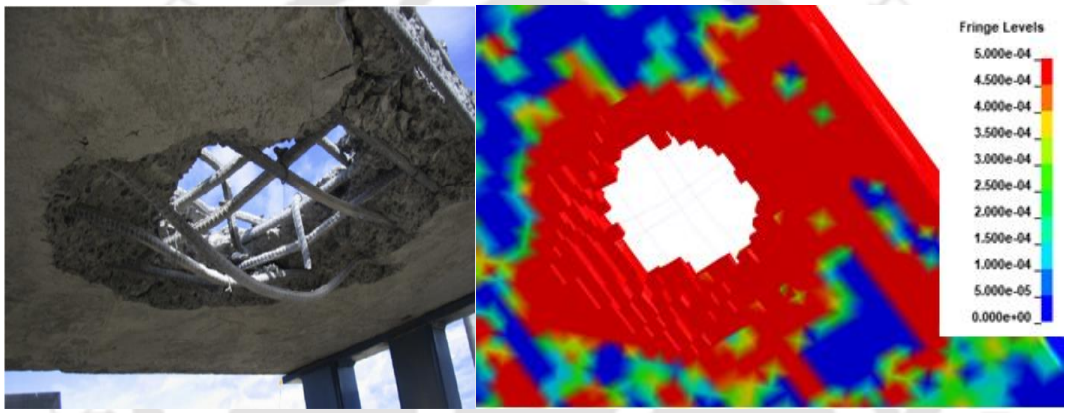

Figure 3.13 Comparison of Slab NSC bottom response of experiment (Li et al. 2015a) (left) and SPH Simulation (right)

This study focuses on the spall damage from the bottom surface of the numerical simulation with the experimental observation. The results obtained from the experiment and the results from this Conwep simulation is shown Figure 3.11. The bottom of the modeled slab is eroding more as compared to the experiment as can be seen in the image. Also the equations used in Conwep cannot give suitable results of a contact blast simulation. From the completed analysis with MM-ALE, the results are in good agreement with the experiment. The damage is also quite close to the damage seen in the experiment (Figure 3.12). The SPH formulation result underestimates the damage diameter as shown in Figure 3.13. The top damage diameter and

the bottom damage diameter as obtained from the simulation and the experiment is given in Table 3.5.

Table 3.5 Damage Dimension Comparison

	Damage diameters (mm)	
	Top	Bottom
Experimental observation	390	710
ConWep simulation	380	810
MM-ALE simulation	323	702
SPH simulation	302	625

Table 3.5 compares the experimental results with the results obtained in this section. More damage is visible in ConWep formulation than with MM-ALE and SPH. For contact blast it is not possible to measure the pressure or displacement at the point of contact of explosive and structural specimen, so the spall damage is taken as a parameter for validation. The numerical simulation with MM-ALE is in close agreement with the experiment but, the time taken for the MM-ALE numerical simulation is more compared to ConWep.

3.3.2 Validation for Detonation

The finite element model needs to replicate the actual load scenario, with the definite material model and boundary conditions ratifying to the realistic physical conditions. Moreover, the contact between materials used should be appropriately established to achieve the actual experimental set up. For this, validation is done using both 2D and 3D finite element model. The validation is compared using the results from a closed cylindrical chamber experiment conducted in Lawren Livermore National Laboratory (LLNL) and simulated by Schwer (2016). The details of the experiment as well as the simulation is reported in Schwer (2016). Similar techniques are adopted for modeling in this work with a 2D model. All four exterior edges are constrained from normal displacement and 875 gm of TNT charge placed as shown in Figure 3.14.

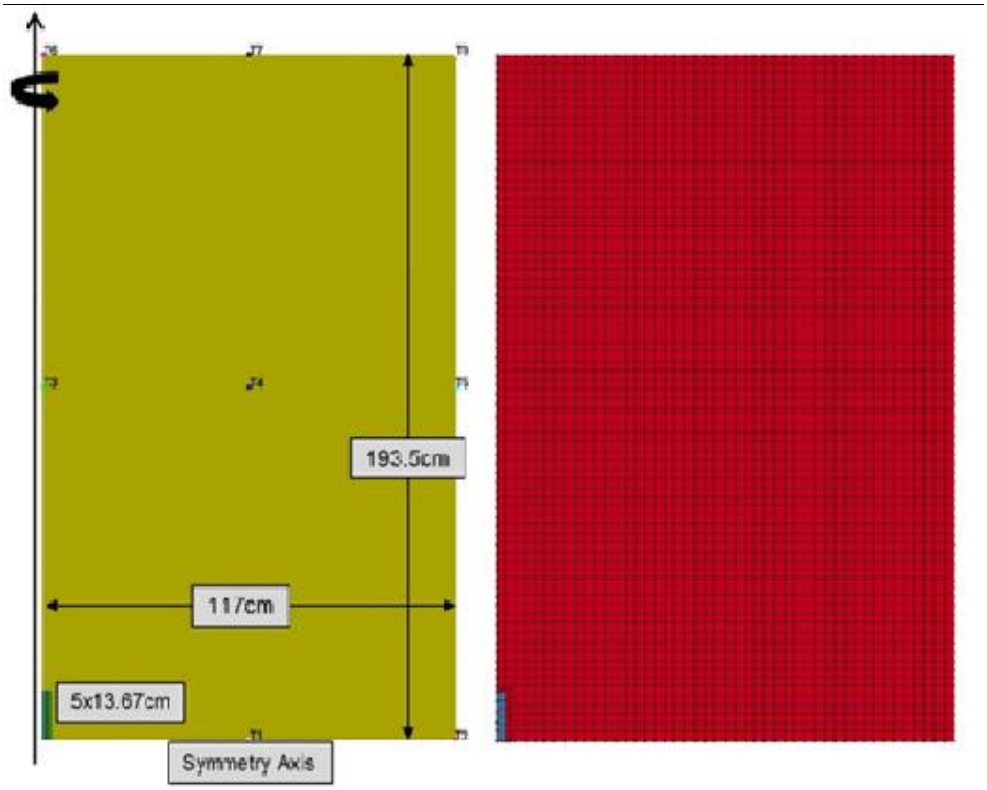

Figure 3.14 Axisymmetric half-length model of LLNL cylinder test with location of tracer particles (Schwer 2016) (left) and the present validation 2D model (right)

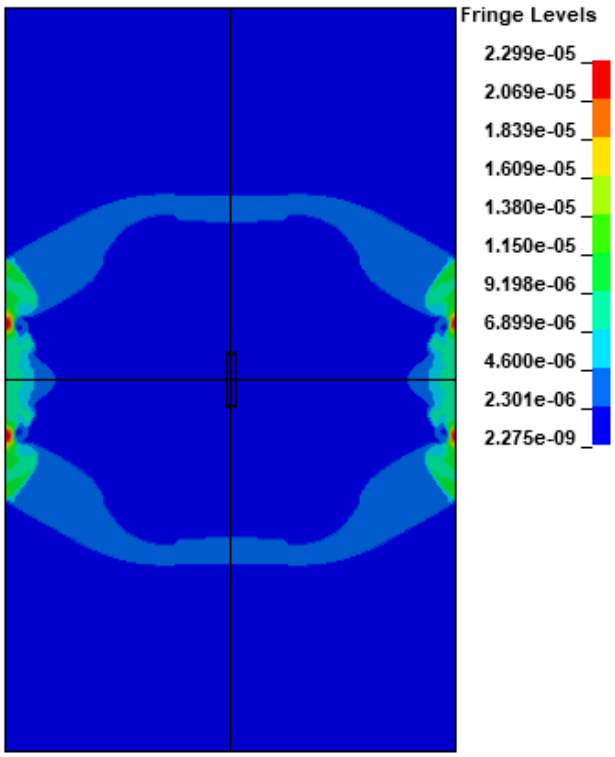

Figure 3.15 Visuals from 2D analysis at 1.05 ms

The validation of the present model is reported with two parameters, pressure and impulse. In 2D, it is clearly seen that the first shock waves hits the walls of the domain at 1.05 ms as shown in Figure 3.15. Figure 3.16 shows the comparison of pressure and impulse histories of the 2D simulation and given by Schwer (2016). The simulation result from 2D analysis is in good agreement with the previous study as for pressure peaks and the signature of the impulse history are matching.

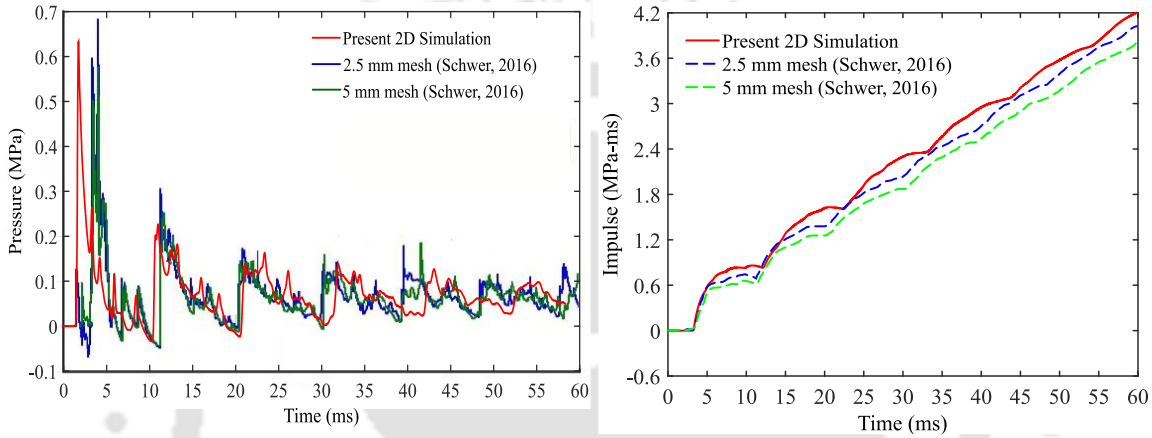

Figure 3.16 Pressure history (left) and Impulse history (right) comparison of simulated 2D analysis with (Schwer 2016)

3.3.3 Validation for Free Air blast

The FE models used in this research is validated with the experiment on reinforced concrete slab (NRC-1) subjected to air blast conducted by Wu et al. (2009). For the UHSC panel, an experimental and numerical investigation on ultra-high performance slabs (UHPC-D1 and UHPC-D3B) subjected to air blast conducted by Li et al. (2015b) is adopted for validation. The model of the slab is kept close to the experimental test setup with the material models as specified earlier as shown in Figure 3.17. The slab dimension is 2m x 1m x 0.1m with reinforcement ratio of 1.34% for NRC-1 and 0.8% for the UHPC slabs. The concrete compressive strength is adopted as 39.5 MPa and 128.9 MPa for normal strength and ultra-high strength respectively. Figure 3.18 displays a comparison of analytical, experimental and

numerical pressure histories for NRC-1 (left) and UHPC-D3B (right). The reflected pressure obtained was less than that obtained from experiment and the free air pressure obtained was more than that in experiment, but is seen to be in close agreement.

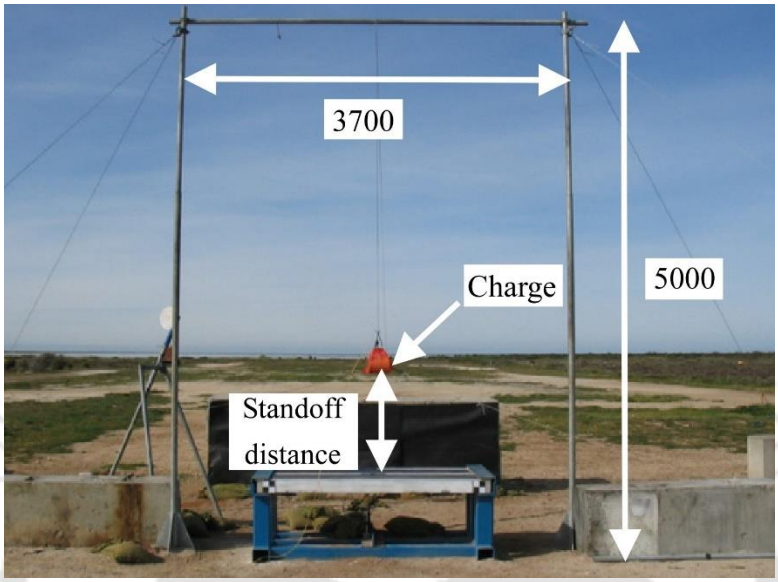

Figure 3.17 Experimental setup for air blast test (Wu et al. 2009)

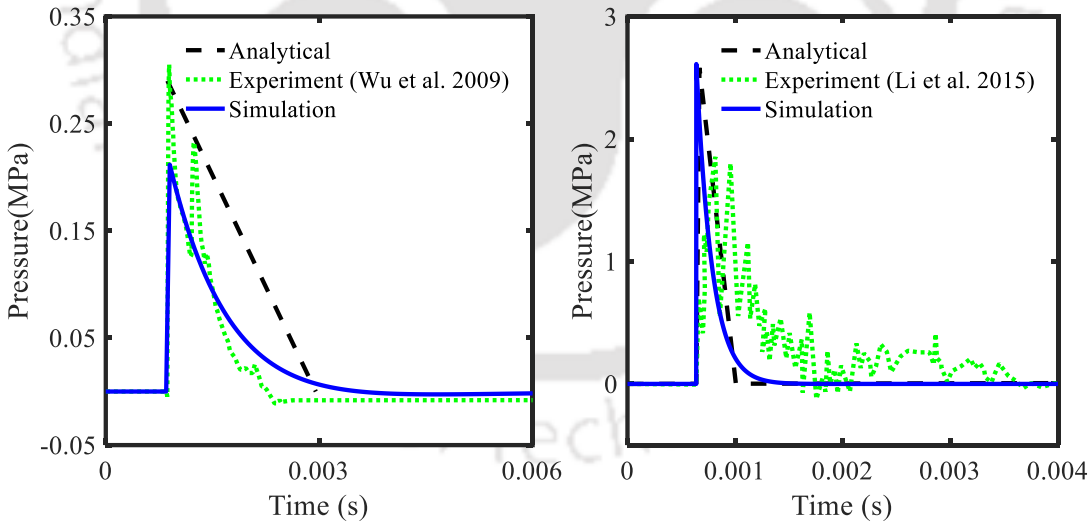

Figure 3.18 Comparison of reflected pressure histories on NRC-1 (Wu et al. 2009) (left) and free air time histories on UHPC-D3B (Li et al. 2015b) (right)

The deflection curves for UHPC slabs as seen in Figure 3.19, shows good results with an erosion criteria of 0.005 principal strain. For UHPC-D1, the maximum deflection from

simulation was obtained as 49.6 mm which is close to the obtained value of 53 mm from experiment. Though the maximum deflection of UHPC-D3B was not recorded during experiment due to some error, the failed slab and its damage was given and the comparison with the simulation is shown in Figure 3.20. From simulation, it is observed that the slab failed completely. From the results displayed in Table 3.6, it is evident that the FE simulation model with the material models is acceptable as the obtained values approximately match with the experimental results.

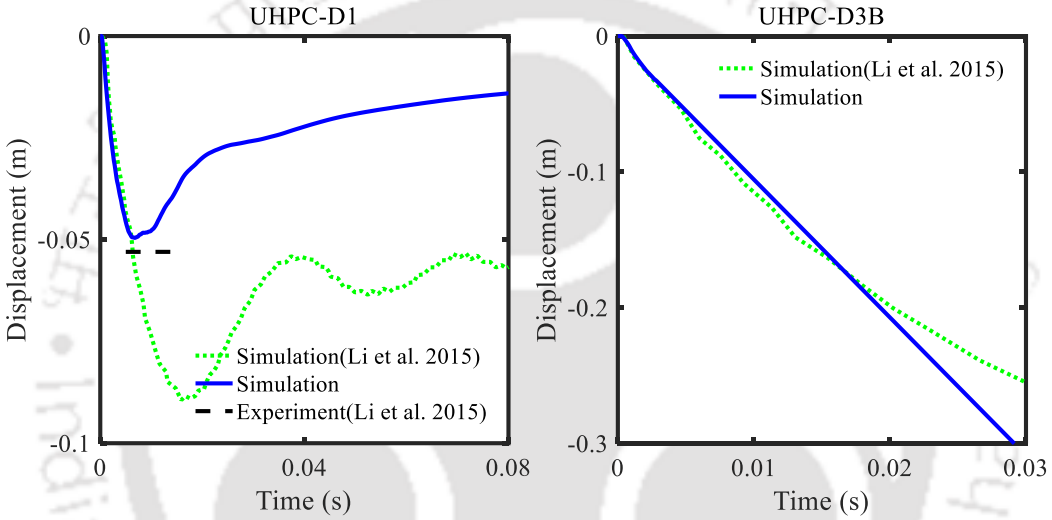

Figure 3.19 Comparison of displacement of UHPC-D1(left) and UHPC-D3B (Li et al. 2015b) (right)

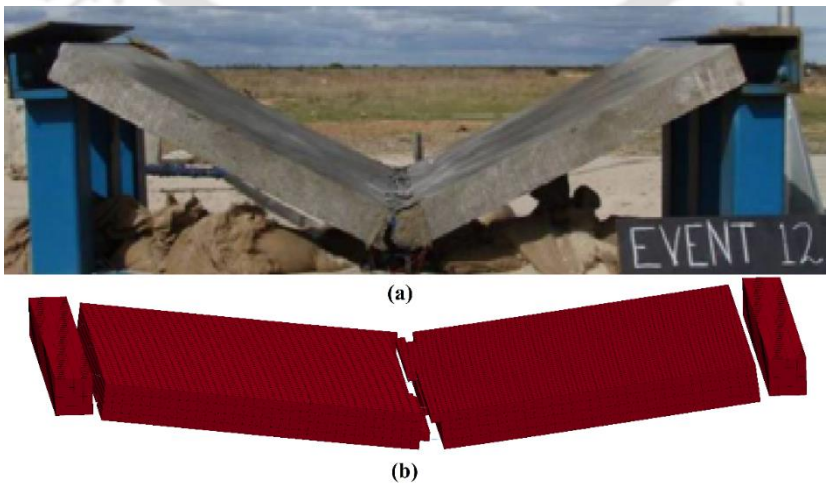

Figure 3.20 Comparison of UHPC-D3B slab damage (Li et al. 2015b)

Table 3.6 Comparison of Simulation with the Experiment (Li et al. 2015b; Wu et al. 2009)

Specimen Name		NRC-1	UHPC-D1	UHPC-D3B
Z (m/kg$^{1/3}$)		3	0.41	0.41
Reflected Overpressure (MPa)	Experimental	0.305	-	1.855
	Simulation	0.212	-	2.612
	Analytical	0.290	-	2.581
Maximum Deflection (mm)	Experimental	1.5	53.0	Failed
	Simulation	0.8	89.4 (Li et al. 2015b) 49.6	Failed

3.3.4 Validation for Contact blast

This model validation is done for panel loaded with contact charge in this study. For this, the experiment conducted by Li et al. (2015a) on an NRC slab and an ultra-high performance concrete (UHPC) slab of dimension 2 m x 1m x 0.1 m is adopted. The validation is for a 1 kg explosive charge placed on the surface of the slab. The model of the slabs is kept identical to the experiment.

Figure 3.22, the FE results from Experiment and simulation is compared and the damage diameter subject to contact blast can be seen to be almost similar to that of the experiment (Li et al. 2015a). In Figure 3.22, it can be seen that the FE approach is able to capture the damage diameter of the structure subject to contact blast with great accuracy. Table 3.7 also shows the damage diameters obtained from both experiment and simulation. All the damage diameters are in good agreement.

A proper FE method is proposed in this chapter. The rest of the FE simulations is followed with this procedure to obtain probabilistic models. Table 3.8 shows the materials, final method adopted and associated details used for the analysis.

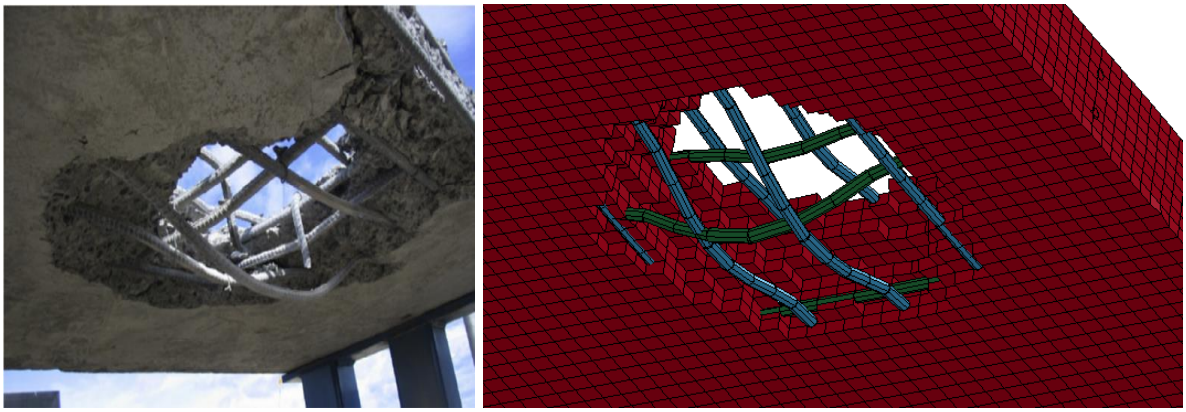

Figure 3.21 Comparison of Slab NSC bottom response of experiment (Li et al. 2015a) (left) and MM-ALE Simulation (right)

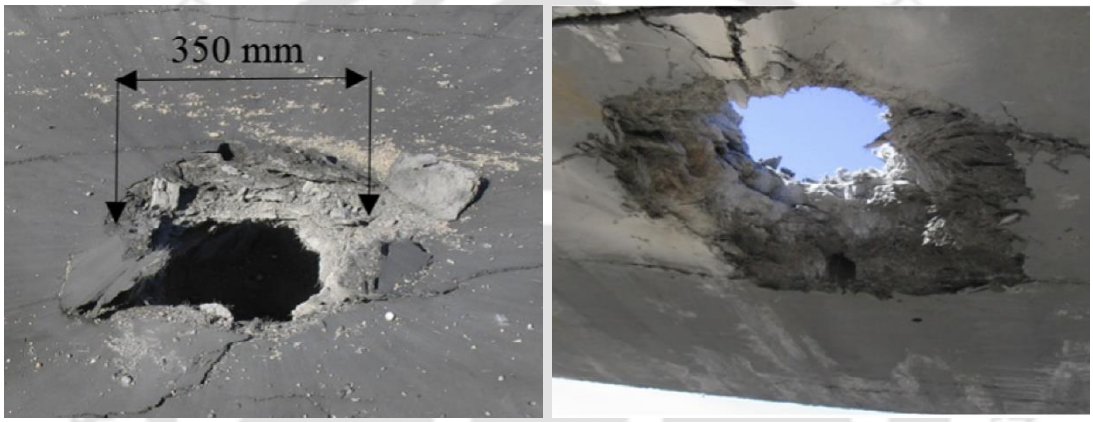

(a) Damage at top and bottom of UHPC slab from experiment (Li et al. 2015a)

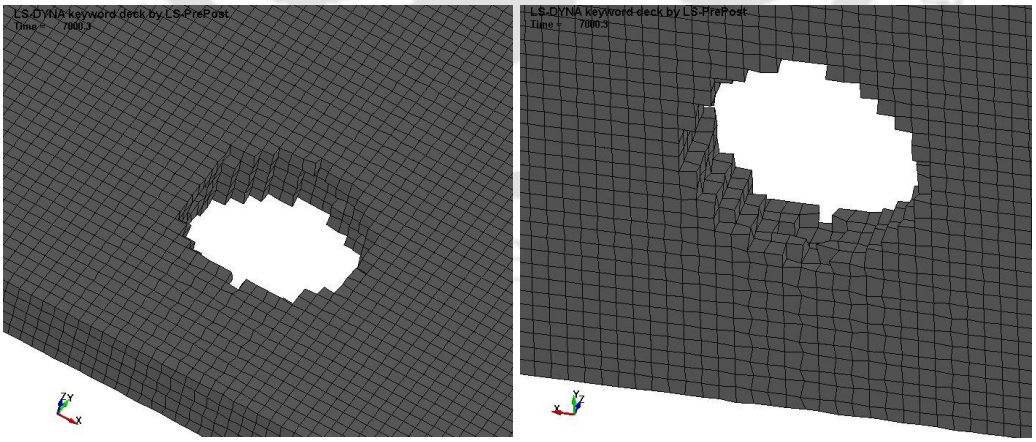

(b) Damage at top and bottom of slab from simulation

Figure 3.22 Damage comparison from (a) experiment (Li et al. 2015a) and (b) simulation.

Table 3.7 Explosive details and results from experiment (Li et al. 2015a) and simulation

Slab	Investigation	Charge description		Damage Diameters, mm	
		Weight	Shape	Top	Bottom
NRC	Experiment	1 kg	Cylindrical	390	710
	Simulation	1 kg	Cylindrical	323	702
UHPC	Experiment	1 kg	Cylindrical	350	380
	Simulation	1 kg	Cylindrical	343	371

Table 3.8 Keywords used for FE analysis of the Panels

Material	Keyword
Normal Concrete	Winfrith Concrete (MAT_084/085)
UHSC	Johnson Holmquist Concrete (MAT_111)
Reinforcement	Plastic Kinematic (MAT_003)
Explosive	High explosive (MAT_008) with EOS_JWL
Air	Null (MAT_009) with EOS_ LINEAR_POLYNOMIAL
Contact between Concrete and Steel	Lagrangian Coupling Method

This chapter thus establishes that FE technique is able to capture the complex phenomenon of blast loading on panels. The damage mechanisms, the deflection, spallation and damage diameters in case of blast can be accurately simulated by the Finite element technique. The next chapter presents the experimental design of the panels subjected to air and contact blast.

Chapter 4. EXPERIMENTAL DESIGN

4.1 GENERAL

Blast effects, panel displacement, damage diameters and capacity of panels are key parameter for performance-based design of panels in blasts. Additional effort and charges are involved in extraction of the estimated parameters from experiments.

In this study, the focus is to develop probabilistic models for estimating the effects of air blast and contact blasts on NRC panels and UHSC panels; and develop a capacity and damage models which will be used for performance-based analysis and design of such panels. The validity of a probabilistic model lies within the range of the data used for the model development. Hence, a wide range of practical data covering the input variables are necessary for the development of a precise probabilistic model. Beside the practical data range, sufficiently large amount of data ensures minimal statistical uncertainty (Gardoni et al. 2002). In order to develop the models, a set of experiments would be required. However, the availability of number of full-scale experiments on such panels subject to blast scenarios is currently limited. In absence of the significant amount of experimental results, here in this present work, simulations are conducted using refined FE analyses to generate the data.

The range of variables adopted for the experimental design is optimally selected so that they are representative of the range of actual panels and applied contact blast scenarios. Using the results of the obtained from the FE simulation, probabilistic models for estimating the deflection, damage diameter, spallation depth, capacity and demand on the panels will be calibrated in subsequent chapters.

4.2 SELECTION OF VARIABLES AND RANGE

The full-scale panels are subjected to both air and contact blast in the virtual experiments using finite element simulations. The range of entire variables should be considered for models to reflect a more genuine blast scenario. Panels are usually constructed and then transferred to the actual sites. Considering, the range of variables are selected. The geometry of panels taken in this study covers the realistic sizes and shapes of the panels that can be easily assembled to form defense structures like weapon storage and bunkers. The different blasts are adopted considering different charge weight of TNT for all the blast cases and different stand-off distances for free air blasts. The experimental design considers a total of 50 panels of each NRC and UHSC panels subject to various air blast and contact blast located at the centre of the panel.

4.3 D-OPTIMAL POINT SELECTION SCHEME

In recent years, the prominence of finite element based simulations to replace the conventional physical representations of experiments has pushed the development of simulation-based optimization (Stander and Craig 2002). Response surface methodology (RSM) has its roots in realistic experimentation statistics (Box and Hunter 1957; Myers et al. 1996). This method is utilised as a primary gradient-free simulation-based approach because of this advantage. In non-linear finite element formulation, the lack of generic analytical codes is a challenge. The use of finite differences in the absence of code provisions may result in incorrect gradient information. RSM has been a popular technique for these reasons, particularly in blast-related problems with non-linear responses. The D-Optimal design of experiments is facilitated by LS-OPT, a computer-based tool.

The methodology for this technique is to fix establish the range of the variables, i.e., the lower bound and upper bound of the design variables, based on structural configuration. A

definite number of cases is required for probabilistic analysis. In the evaluation of probabilistic models using design of experiments, ideal design requires a larger number of experimental runs to estimate the parameters with the same precision as optimal design. In general, optimal experiments can reduce the amount of time required for experimentation.

The D-optimal point selection strategy is used to find the best group of cases based on the selected range (Myers et al. 1996). In the design of experiments for estimating numerical models, optimal designs allow parameters to be estimated without bias and with minimum-variance. The D-optimal plan is used in this study, which is the suggested point selection plan for polynomial response surfaces (Gunst et al. 1996; LSTC 2007). This scheme adopts a subset of all the possible design points and is flexible for any number of designs to be arranged in the design space with an irregular boundary. Assuming to contain the optimum within a sub-region in the design space, the experiments are selected. 200 cases are simulated in total to acquire data for air and contact blast effects on these panels in order to develop probabilistic models for the required parameters. For NRC and UHSC panel, the design variables are divided into primary variables and secondary variables to avoid unrealistic random combinations. The variables capturing the basic design requirements are categorized into primary variables and rest are the derived variables from primary variables categorized as secondary variables. The ranges of primary variables selected for the design of experiments of NRC and UHSC panels is are listed out in Table 4.1. Table 4.2 gives the range of primary variables for the air and contact blast, and Table 4.3 shows the range of secondary variables for the panel.

Table 4.1 Range of Primary Variables for the Panels

Variable	Symbol	Range of NRC	Range of UHSC
Panel length (m)	L	1.50-6.00	1.50-6.00
Panel thickness (m)	t	0.20-0.50	0.20-0.50
Reinforcement Ratio (%)	ρ	0.2-0.7	0.2-0.7
Yield strength of reinforcement (MPa)	f_y	500, 550	500, 550
Compressive strength of concrete (MPa)	f_c'	25-60	60-200

Table 4.2 Range of Primary Variables for Air and Contact blast

Panel	Air blast variable range		Contact blast variable range
	Stand-off distance R (m)	Charge mass Q (kg-TNT)	Charge mass Q (kg-TNT)
NRC	3-10	50-1000	1-10
UHSC	3-10	50-1000	1-10

Table 4.3 Expression and Range of Secondary Variables of NRC & UHSC panels

Variable	Symbol	Expression/Range
Diameter of reinforcement in both direction (mm)	d_l	6, 8, 10, 12, 16, 20
Spacing of longitudinal bar	s_l	$\left(\frac{\pi}{4}d_l^2\right)\left(\frac{1000}{\rho Lt/100}\right)$

FE models of the 50 combinations each of NRC and UHSC panels are modeled to obtain the required database. Again these panels are placed under air blast and contact blast loading scenario and simulated for the development of probabilistic models. Based on literatures available and realistic condition, the panel length of 1.5-6 m range is considered. Present design of bunkers and defense structures adopts normal strength concrete of compressive strength between 25-60 MPa, which in this study is considering up to 200 MPa

for high strength concrete panels. All side fixed panels are considered in present case study with steel grades and plate thickness confirming to their availability. For air blast, the charge weight of 50-1000 kg TNT range and stand of distance from 3-30 m is adopted as shown in Table 4.2. The charge is based on the practical explosive weight and stand-off distance that can be carried by a medium size van near a protective structure. While for contact blast, the charges adopted in the accessible studies are limited to 1 kg, as the pressure and energy generated within the container boundary is tremendous. This is capable of punching through any panel. Thus, explosive weight of 1-10 kg TNT is considered for the FE simulations.

The panel geometry covers the realistic sizes and shapes of the panels that can be easily assembled to form protective structures. Present design of such structures adopts normal strength concrete, while in this study, ultra-high strength concrete range is considered as well. The boundary for all the panels are kept as fixed on all sides. The displacement at cracking strain of concrete, yielding strain of steel and crushing strain of concrete is recorded for panel under air blast. Using the results obtained from the FE simulation, probabilistic models for estimating the capacity of the panels is calibrated and presented in the next Chapter.

Chapter 5. PERFORMANCE-BASED MODELS FOR PANELS SUBJECT TO AIR BLAST

5.1 GENERAL

For the selected performance criteria, a probabilistic model will be developed for each performance level of capacity and demand imposed on it. The results from the simulations done with reference to the experiment conducted will be the basis for formulation of the predictive model for capacity of NRC panels under the defined performance levels for each blast cases as given in Section 2.3. The model will consider the pertinent uncertainties comprising the modal errors and also missing variables, measurement errors and statistical uncertainty. Through the use of a set of explanatory functions, the terms that correct the bias in the existing models can be found and these functions provide an insight into the underlying behavioural phenomena. The model will be a mathematical expression relating the damage of the panels to one or more measurable quantities like material property constants, dimensional constants, imposed boundary conditions, etc. The main purpose of model is to predict the quantities of interest for a given deterministic or random values of the variables.

5.2 GENERAL FORMULATION

The probabilistic models are generally created by accumulation of correction terms to mechanical models. Because the data used for the model assessment come from FE simulations, it can be assumed that there is no error in the data measurement. The model from where a transformation of the quantity of interest is written is shown in equation given below, as the sum of a mechanical model, a correction term to account for the bias in the mechanical model, and model error (Gardoni et al. 2002). Following the general formulation for probabilistic models, the deflection capacity/demand for ultimate limit state, is formulated as

$$\ln\left[P_{i/D}\left(x,\Theta_{P_i/D}\right)\right]=\ln\left[\hat{p}_{i/D}\left(x\right)\right]\gamma_{P_i/D}\left(x,\theta_{P_i/D}\right)+\sigma_{P_i/D}e_{P_i/D} \tag{5.1}$$

where $P_{i/D}=$ Probabilistic deflection based capacity/damage model of the panel for the defined performance level, $i=1,2,3$, $\hat{p}_{i/D}=$ Mechanical capacity/damage model for the panels at the performance level; $\gamma_{P_i/D}\left(x,\theta_{P_i/D}\right)=$ correction term for the bias inherent in the mechanical model defined as

$$\gamma_{P_i/D}\left(x,\theta_{P_i/D}\right)=\sum_{j=1}^{n}\theta_{P_{i,j}/D}h_{P_{i,j}/D}\left(x\right) \tag{5.2}$$

where $h_{P_{i,j}/D}\left(x\right)$, $j=1,...,n=$ explanatory function (or regressors) defined as functions of x, $\theta_{P_{i,j}/D}$, $j=1,...,n$ are the parameters associated with explanatory functions, $\sigma_{P_i/D}e_{P_i/D}=$ model error, $\sigma_{P_i/D}=$ standard deviation, $e_{P_i/D}=$ Gaussian error and $\Theta_{P_i/D}=\theta_{P_i/D}=$ set of unknowns model parameters. The model correction terms are used to capture the physical phenomena that are not accounted for in the mechanical model. A step-wise deletion process is used to arrive at the posterior statistics for the damage model. The standard deviation will be monitored to arrive at the adequate model.

5.3 MECHANICAL MODEL OF PANELS FOR AIR BLAST

5.3.1 Mechanical Model for Capacity

The estimates of the mechanical models for Performance levels P1, P2 and P3 for NRC and UHSC panels are based on deflection formulation. Newmark (Brooks and Newmark 1953) gave the analytical model for equivalent maximum displacement of mass, X_m subjected to initial-peak triangular pulse as:

$$\frac{X_m}{X_E}\cong 1+\left(\frac{\omega_N t_d}{\beta}\right)\left(\frac{1}{2}-\frac{1}{3}\beta\right) \tag{5.3}$$

where, X_E is the equivalent maximum elasto-plastic deflection of the slab, ω_N is the natural time period of the structure, t_d is the duration of positive blast pressure and β is the ratio of ultimate unit resistance of panel to peak applied.

The given equation was modified and used as the mechanical models for the panels at the performance levels. To analyze the panels, the failure pattern is assumed with the help of yield lines theory. The unit elastic resistance and elastic deflection is taken into account for P1, the unit elasto-plastic resistance and elasto-plastic deflection is taken for P2 and the unit elasto-plastic resistance and plastic deflection is taken into account for P3. The developed mechanical model for maximum deflection capacity at $P1_{NRC/UHSC}$, $P2_{NRC/UHSC}$ and $P3_{NRC/UHSC}$ are.

$$\hat{Y}_{P1}^{NRC/UHSC} = X_e\left[1+\left(\frac{\omega_N t_d P_{so}}{r_e}\right)\left(\frac{1}{2}-\frac{1}{3}\frac{r_e}{P_{so}}\right)\right] \tag{5.4}$$

$$\hat{Y}_{P2}^{NRC/UHSC} = X_{ep}\left[1+\left(\frac{\omega_N t_d P_{so}}{r_{ep}}\right)\left(\frac{1}{2}-\frac{1}{3}\frac{r_{ep}}{P_{so}}\right)\right] \tag{5.5}$$

$$\hat{Y}_{P3}^{NRC/UHSC} = X_p\left[1+\left(\frac{\omega_N t_d P_{so}}{r_{ep}}\right)\left(\frac{1}{2}-\frac{1}{3}\frac{r_{ep}}{P_{so}}\right)\right] \tag{5.6}$$

where, $\hat{Y}_{P1_{NRC/UHSC}}, \hat{Y}_{P2_{NRC/UHSC}}$ and $\hat{Y}_{P3_{NRC/UHSC}}$ are mechanical model for $P1_{NRC/UHSC}$, $P2_{NRC/UHSC}$ and $P3_{NRC/UHSC}$ respectively, $X_e / X_{ep} / X_p$ is the elastic/elasto-plastic/plastic deflection of the panel respectively, P_{so} is the positive peak blast overpressure, r_e is the elastic unit resistance at which first yield occurs for the panel, and r_{ep} is the unit elasto-plastic resistance where second yield subsequently occurs for the panel. The deflection for each range of behaviour of the panel can be calculated from

$$X = \frac{\gamma r L^4}{D} \tag{5.7}$$

where, γ can be obtained from Figure 3-33, 3-34 and 3-36 of (US Department of Defense 2008) according to the considered yield point, L is the span of panel, D is the flexural rigidity of the panel and r is the unit resistance corresponding to each stage and can be defined as the minimum of all the resistances calculated at a particular yield point, i.e.,

$$r = \min\left(\frac{M}{\beta L^2}\right) \tag{5.8}$$

where M is the unit negative/positive moment capacity of the panel in horizontal/vertical direction of the panel calculated at each yield point and β can be found from Figure 3-33, 3-34 and 3-36 of (US Department of Defense 2008) according to the considered yield points.

5.3.2 Mechanical Model for Demand

The estimates of the mechanical models for demand on NRC and UHSC is given based on equation (5.3) by Brooks and Newmark (1953), and accounts for the ultimate unit resistance and equivalent maximum elasto-plastic deflection of the panel,

$$\hat{Y}_D^{NRC/UHSC} = X_E\left[1+\left(\frac{\omega_N t_d P_{so}}{r_u}\right)\left(\frac{1}{2}-\frac{1}{3}\frac{r_u}{P_{so}}\right)\right] \tag{5.9}$$

where, $\hat{Y}_D^{NRC/UHSC}$ is the mechanical model for dynamic demand from blast on panels, X_E is the equivalent maximum elasto-plastic deflection of the panel calculated as

$$X_E = \frac{r_u}{K_E} = X_e\left(\frac{r_{ep}}{r_u}\right) + X_{ep}\left(1+\frac{r_e}{r_u}\right) + X_p\left(1+\frac{r_{ep}}{r_u}\right) \tag{5.10}$$

and r_u is the ultimate unit resistance of the panel and is given by

$$r_u = \frac{20\left(M_{HN} + M_{HP}\right)}{L^2} \tag{5.11}$$

where, M_{HN} and M_{HP} are ultimate unit negative and positive moment capacity in the horizontal direction respectively.

5.4 MODEL CORRECTION

Suitable model correction terms are deliberated to capture the precise phenomena which is not accounted in the mechanical models. Selected explanatory functions as given in Figure 5.1, lists the physical quantity which influences the model as well.

Table 5.1 List of Explanatory Functions for Models of Panels subject to Air Blast

Variable	Description	Expression
$h_1(x)$	Constant bias	1
$h_2(x)$	Slenderness ratio	t/L
$h_3(x)$	Reinforcement Ratio	$\rho = A_s/tL$
$h_4(x)$	Ratio of strength of concrete by strength of steel	$f_c' DIF/f_y$
$h_5(x)$	Positive blast duration to natural time period of panel	t_d/T_N
$h_6(x)$	Inertia	M_E/Q
$h_7(x)$	Ultimate unit resistance to positive peak overpressure	r_u/P_{so}
$h_8(x)$	Ratio of cracking strength of concrete by strength of steel	$f_{cr} DIF/f_y$
$h_9(x)$	Energy	$G_F Lt/EQ$
$h_{10}(x)$	Stiffness ratio	k_r

where, t is the total thickness of panel, L is the length of a panel, ρ is the reinforcement ratio, A_s is the total area of reinforcement provided along considered axis, f_c' is the concrete compressive strength, DIF is the dynamic increase factor accounting for increase in strength of concrete due to strain rate which is considered as 1.12 for far field blast and 1.16 for close

in blast, f_y is the yield strength of steel, t_d is the positive blast duration, T_N is the natural time period of the panel, M_E is the equivalent mass of the slab, Q is the applied weight of charge in kg TNT, r_u is the ultimate unit resistance of the slab, P_{so} is the applied positive peak over-pressure, f_{cr} is the cracking strength of concrete $\left(f_{cr} = 0.7\sqrt{f_c'} \right)$, G_F is the fracture energy of concrete required to propagate a tensile crack of unit area in J per square m (as calculated in Comité Euro-International du Béton (1993)), E is the energy of explosion of TNT in J/kg and k_r is the stiffness ratio, i.e., equivalent stiffness by maximum of elastic, elasto-plastic and plastic stiffness of a panel.

The first explanatory function, $h_1(x)$ accounts for the potential constant bias present in the mechanical model. The second explanatory function, $h_2(x)$ accounts for the slenderness ratio of the panels. The third explanatory function, $h_3(x)$ accounts for the contribution of the reinforcement ratio. The fourth explanatory function, $h_4(x)$ accounts for the contribution of concrete compressive strength to yield strength of steel. The fifth explanatory function, $h_5(x)$ accounts for the contribution of positive blast duration and natural time period of structure. The sixth explanatory function, $h_6(x)$ is the ratio of equivalent mass of the slab to the charge weight applied. Ultimate unit resistance to the applied peak over-pressure is accounted by the seventh explanatory function, $h_7(x)$. The eighth explanatory function $h_8(x)$, accounts for the contribution of concrete cracking strength to yield strength of steel. The ninth explanatory function, $h_9(x)$ accounts for the contribution of energy and the tenth explanatory function, $h_{10}(x)$ accounts for the contribution of stiffness ratio

5.5 MODEL ASSESSMENT

For the estimation of modal parameters (Θ), Bayesian inference with a non-informative prior is selected (Box and Tiao 1992). The parsimonious model is achieved by step-wise deletion process of the parameters adopted. Diagnostic plots are generated between the explanatory function and the residual of the dynamic capacity of the FE model and the mechanical model in this method. Explanatory functions showing the strongest correlation are chosen suitably one at a time. Also, the adequacy of the model is monitored by checking the mean of the standard deviation.

5.6 PARAMETER ESTIMATION FOR CAPACITY OF NRC PANEL

5.6.1 Parameter Estimation for Performance Level P1

The most statistically significant explanatory functions for performance level P1 are $h_1(x), h_2(x), h_4(x)$ and $h_9(x)$. Considered terms accounts for a correction of constant bias, the contribution concrete panels slenderness ratio, ratio of compressive strength of concrete to yielding strength of steel and energy contribution. The posterior statistics of the model is follows in Table 5.2.

Figure 5.1 shows the comparison between the estimation of dynamic capacity at performance level P1 in terms of deformation of NRC panel based on the proposed mechanical model and the mean of the developed probabilistic model where the mean predication for the dynamic capacity Y_{P1}^{NRC} is developed as,

$$Y_{P1}^{NRC} = \hat{y}_{P1}^{NRC} \exp\left[-2.632 + 9.08\frac{t}{L} + 15.423\frac{f_c' DIF}{f_y} + 2066\frac{G_F Lt}{EQ}\right] \qquad (5.12)$$

Where, Y_{P1}^{NRC} = Probabilistic dynamic capacity at performance level P1, $\hat{y}_{P1}^{NRC}$ = dynamic capacity at performance level P1 given by the mechanical model.

Table 5.2 Posterior Statistics of Parameters in Selected Dynamic Capacity (P1) Model

Parameter	Mean	Standard deviation	Correlation Coefficient				
			Θ_1	Θ_2	Θ_4	Θ_9	σ
Θ_1	-2.6322	0.4656	1.000				
Θ_2	9.0801	1.3756	-0.253	1.000			
Θ_4	15.4231	4.2453	-0.895	-0.106	1.000		
Θ_9	2066	838.933	-0.373	0.198	0.150	1.000	
σ	0.5471	0.2469	-0.504	0.071	0.379	0.098	1.000

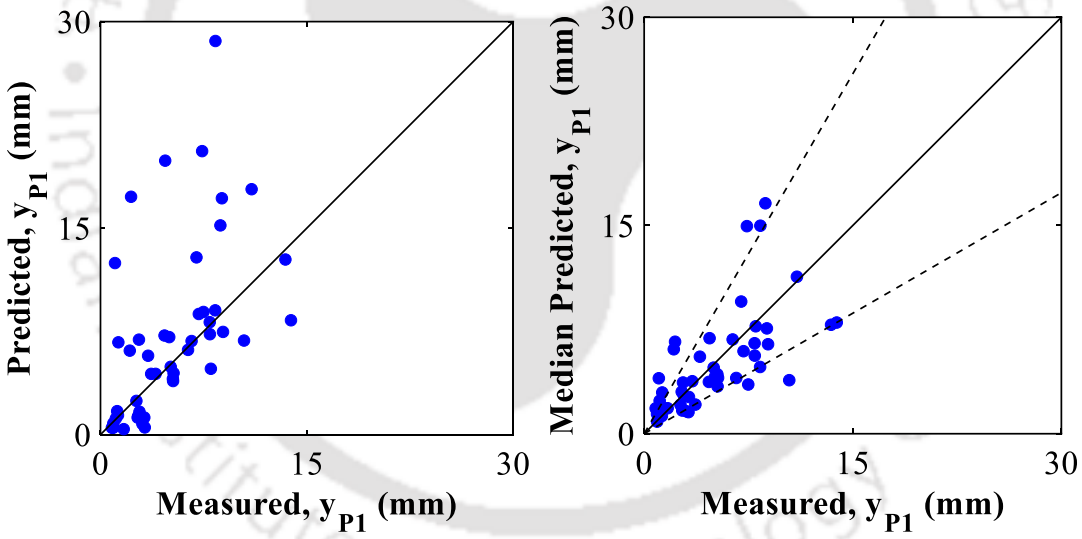

Figure 5.1 Comparison of measured and predicted Dynamic Capacity (P1) of NRC panel based on mechanical (left) and probabilistic (right) model

The mechanical and probabilistic models are both plotted against the capacity in the terms of deformation of the NRC panel values estimated from the FE simulations. Majority of data points are lying near to 1:1 line. The data contains equality data. The predictions of

probabilistic model show that the equality data lies both above and below the 1:1 line. The probabilistic model corrects this inherent bias in the model with a standard deviation of 3.0708.

5.6.2 Parameter Estimation for Performance Level P2

The most statistically significant explanatory functions for performance level P2 are $h_1(x), h_5(x), h_6(x)$ and $h_7(x)$. Considered terms accounts for a correction of constant bias, ratio of positive blast duration to natural time period, inertia and ultimate unit resistance to positive peak overpressure for the panels. The posterior statistics of the model is follows in Table 5.3.

Table 5.3 Posterior Statistics of Parameters in Selected Dynamic Capacity (P2) Model

Parameter	Mean	Standard deviation	Correlation Coefficient				
			Θ_1	Θ_5	Θ_6	Θ_7	σ
Θ_1	0.0482	0.4577	1.000				
Θ_5	-7.2304	3.0992	-0.166	1.000			
Θ_6	1.1793	0.3574	-0.862	-0.044	1.000		
Θ_7	3.8538	1.3803	-0.156	-0.801	0.123	1.000	
σ	0.5233	0.3343	-0.500	-0.126	0.373	0.251	1.000

Figure 5.2 shows the comparison between the estimation of dynamic capacity at performance level P2 in terms of deformation of NRC panel based on the proposed mechanical model and the mean of the developed probabilistic model where the mean predication for the dynamic capacity Y_{P2}^{NRC} is developed as,

$$Y_{P2}^{NRC} = \hat{y}_{P2}^{NRC} \exp\left[0.0482 - 7.2304\frac{t_d}{T_N} + 1.1793\frac{M_E}{Q} + 3.8538\frac{r_u}{P_{so}}\right] \quad (5.13)$$

Where, Y_{P2}^{NRC} = Probabilistic dynamic capacity at performance level P2, $\hat{y}_{P2}^{NRC}$ = dynamic capacity at performance level P2 given by the mechanical model.

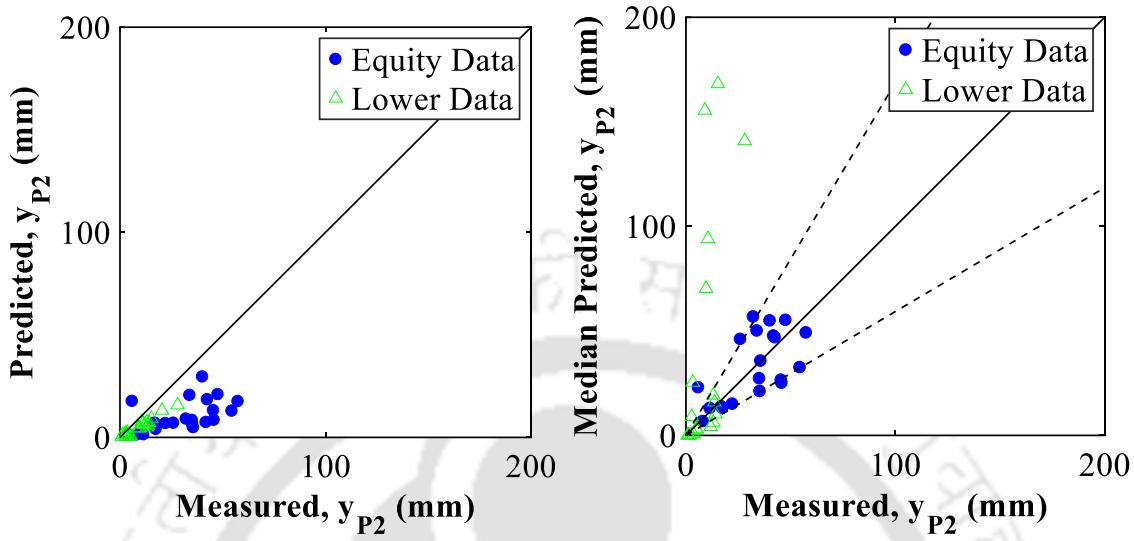

Figure 5.2 Comparison of measured and predicted Dynamic Capacity (P2) of NRC panel based on mechanical (left) and probabilistic (right) model

The mechanical and probabilistic models are both plotted against the capacity in the terms of deformation of the NRC panel values estimated from the FE simulations. Majority of data points are lying near to 1:1 line. The data contains both equality data and lower bound data. The predictions of probabilistic model show that the equality data lies both above and below the 1:1 line. The probabilistic model corrects this inherent bias in the model. The model has a standard deviation of 14.914.

5.6.3 Parameter Estimation for Performance Level P3

The most statistically significant explanatory functions for performance level P3 are $h_1(x), h_5(x), h_7(x)$ and $h_{10}(x)$. Considered terms accounts for a correction of constant bias, the slenderness ratio, time period of the system and inertia effect. The posterior statistics of the model is follows in Table 5.4.

Table 5.4 Posterior Statistics of Parameters in Selected Dynamic Capacity (P3) Model

Parameter	Mean	Standard deviation	Correlation Coefficient				
			Θ_1	Θ_5	Θ_7	Θ_{10}	σ
Θ_1	396.3784	132.2751	1.000				
Θ_5	-11.6394	2.9212	-0.026	1.000			
Θ_7	4.8222	1.1844	0.004	-0.823	1.000		
Θ_{10}	-585.2097	195.4584	-1.000	0.025	-0.005	1.000	
σ	0.4250	0.3577	0.163	-0.170	0.232	-0.163	1.000

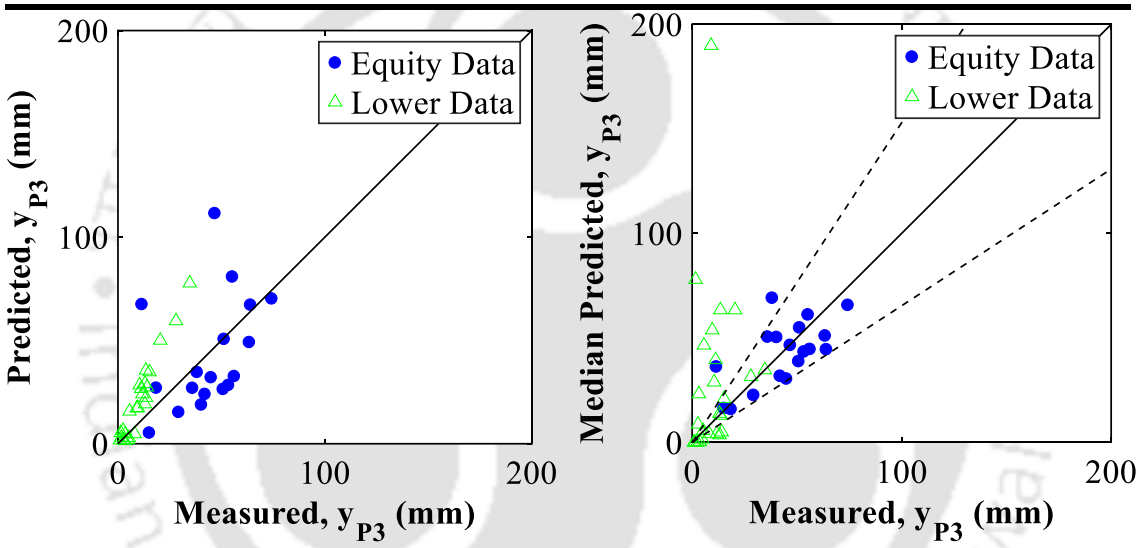

Figure 5.3 Comparison of measured and predicted Dynamic Capacity (P3) of NRC panel based on mechanical (left) and probabilistic (right) model

Figure 5.3 shows the comparison between the estimation of dynamic capacity at performance level P3 in terms of deformation of NRC panel based on the proposed mechanical model and the mean of the developed probabilistic model where the mean predication for the dynamic capacity Y_{P3}^{NRC} is developed as,

$$Y_{P3}^{NRC} = \hat{y}_{P3}^{NRC} \exp\left[396.378 - 11.639 \frac{t_d}{T_N} + 4.8222 \frac{r_u}{P_{so}} - 585.21 k_r \right] \tag{5.14}$$

Where, Y_{P3}^{NRC} = Probabilistic dynamic capacity at performance level P3, $\hat{y}_{P3}^{NRC}$ = dynamic capacity at performance level P3 given by the mechanical model.

The mechanical and probabilistic models are both plotted against the capacity in the terms of deformation of the NRC panel values estimated from the FE simulations. Majority of data points are lying near to 1:1 line. The data contains both equality data and lower bound data. The predictions of probabilistic model show that the equality data lies both above and below the 1:1 line. The probabilistic model corrects this inherent bias in the model. The model has a standard deviation of 15.3155.

5.7 PARAMETER ESTIMATION FOR CAPACITY OF UHSC PANELS

5.7.1 Parameter Estimation for Performance Level P1

The most statistically significant explanatory functions for performance level P1 are $h_1(x), h_3(x), h_7(x)$ and $h_{10}(x)$. Considered terms accounts for a correction of constant bias, reinforcement ratio, ultimate unit resistance to positive peak overpressure and stiffness ratio. The posterior statistics of the model is follows in Table 5.5.

Table 5.5 Posterior Statistics of Parameters in Selected Dynamic Capacity (P1) Model

Parameter	Mean	Standard deviation	Correlation Coefficient				
			Θ_1	Θ_3	Θ_7	Θ_{10}	σ
Θ_1	421.4116	126.7359	1.000				
Θ_3	898.5747	151.3550	0.447	1.000			
Θ_7	-0.5097	0.2169	-0.524	-0.658	1.000		
Θ_{10}	-624.3934	187.3660	-1.000	-0.447	0.534	1.000	
σ	0.5986	0.1762	-0.215	-0.094	0.101	0.215	1.000

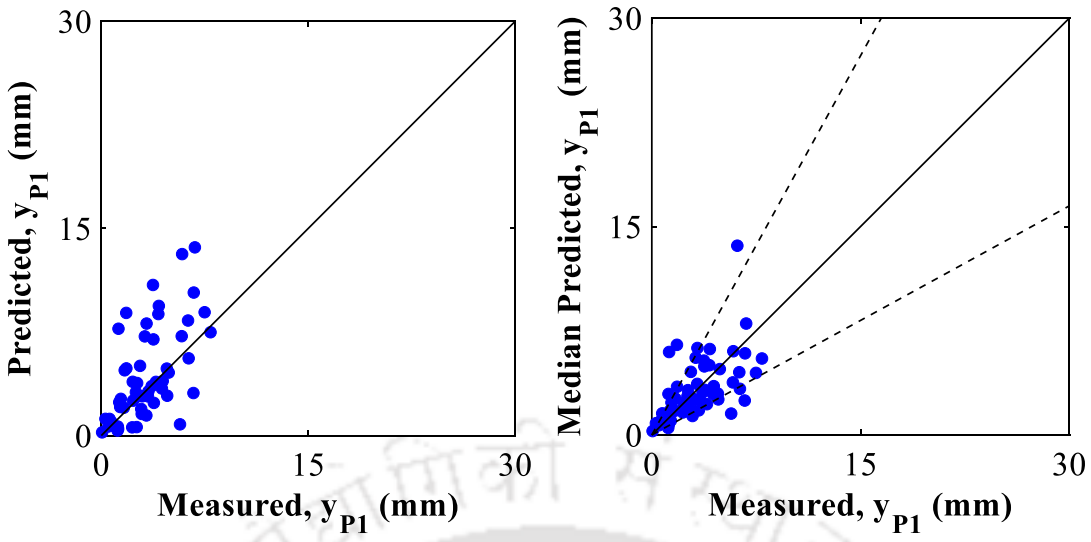

Figure 5.4 Comparison of measured and predicted Dynamic Capacity (P1) of UHSC Panel based on mechanical (left) and probabilistic (right) model

Figure 5.4 shows the comparison between the estimation of dynamic capacity at performance level P1 in terms of deformation of UHSC Panel based on the proposed mechanical model and the mean of the developed probabilistic model where the mean predication for the dynamic capacity Y_{P1}^{UHSC} is developed as,

$$Y_{P1}^{UHSC} = \hat{y}_{P1}^{UHSC} \exp\left[421.412 + 898.575\frac{A_s}{tL} - 0.5097\frac{r_u}{P_{so}} - 624.393k_r \right] \quad (5.15)$$

Where, Y_{P1}^{UHSC} = Probabilistic dynamic capacity at performance level P1, $\hat{y}_{P1}^{UHSC}$ = dynamic capacity at performance level P1 given by the mechanical model.

The mechanical and probabilistic models are both plotted against the capacity in the terms of deformation of the UHSC Panel values estimated from the FE simulations. Majority of data points are lying near to 1:1 line. The data contains equality data. The predictions of probabilistic model show that the equality data lies both above and below the 1:1 line. The model has a standard deviation of 2.113. The probabilistic model corrects this inherent bias in the model.

5.7.2 Parameter Estimation for Performance Level P2

The most statistically significant explanatory functions for performance level P2 are $h_1(x), h_2(x), h_3(x)$ and $h_7(x)$. Considered terms accounts for a correction of constant bias, the slenderness ratio, reinforcement ratio and ultimate unit resistance to positive peak overpressure for the panels. The posterior statistics of the model is follows in Table 5.6.

Table 5.6 Posterior Statistics of Parameters in Selected Dynamic Capacity (P2) Model

Parameter	Mean	Standard deviation	Correlation Coefficient				
			Θ_1	Θ_2	Θ_3	Θ_7	σ
Θ_1	0.3236	0.3498	1.000				
Θ_2	13.7151	5.6003	-0.804	1.000			
Θ_3	649.8137	279.006	-0.430	0.077	1.000		
Θ_7	-2.6364	1.1747	0.720	-0.725	-0.671	1.000	
σ	0.4512	0.5109	-0.194	-0.062	-0.117	0.168	1.000

Figure 5.5 shows the comparison between the estimation of dynamic capacity at performance level P2 in terms of deformation of UHSC panel based on the proposed mechanical model and the mean of the developed probabilistic model where the mean predication for the dynamic capacity Y_{P2}^{UHSC} is developed as,

$$Y_{P2}^{UHSC} = \hat{y}_{P2}^{UHSC} \exp\left[0.3236 + 13.715\frac{t}{L} + 649.814\frac{A_s}{tL} - 2.636\frac{r_u}{P_{so}}\right] \quad (5.16)$$

Where, Y_{P2}^{UHSC} = Probabilistic dynamic capacity at performance level P2, $\hat{y}_{P2}^{UHSC}$ = dynamic capacity at performance level P2 given by the mechanical model.

The mechanical and probabilistic models are both plotted against the capacity in the terms of deformation of the UHSC panel values estimated from the FE simulations. Majority

of data points are lying near to 1:1 line. The data contains both equality data and lower bound data. The predictions of probabilistic model show that the equality data lies both above and below the 1:1 line. The model has a standard deviation of 13.972. The probabilistic model corrects this inherent bias in the model.

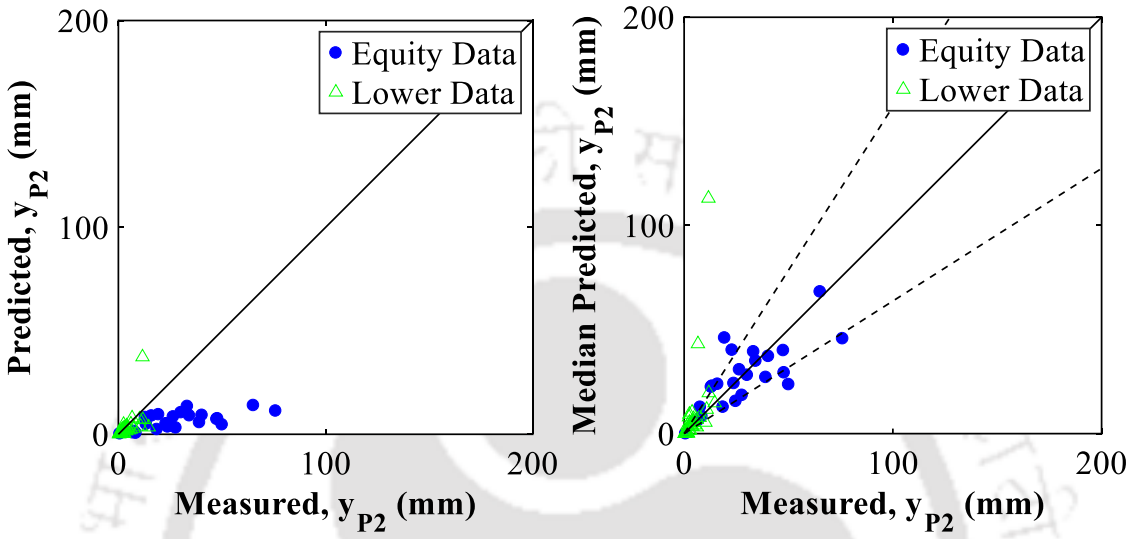

Figure 5.5 Comparison of measured and predicted Dynamic Capacity (P2) of UHSC Panel based on mechanical (left) and probabilistic (right) model

5.7.3 Parameter Estimation for Performance Level P3

The most statistically significant explanatory functions for performance level P3 are $h_1(x), h_3(x), h_4(x), h_8(x)$ and $h_{10}(x)$. Considered terms accounts for a correction of constant bias, reinforcement ratio, ratio of cracking strength of concrete by strength of steel and stiffness ratio. The posterior statistics of the model is follows in Table 5.7.

Figure 5.6 shows the comparison between the estimation of dynamic capacity at performance level P3 in terms of deformation of NRC panel based on the proposed mechanical model and the mean of the developed probabilistic model where the mean predication for the dynamic capacity Y_{P3}^{NRC} is developed as,

$$Y_{P3}^{UHSC} = \hat{y}_{P3}^{UHSC} \exp\left[269.62 + 488.26\frac{A_s}{tL} - 13.0\frac{f_c' DIF}{f_y} + 431.85\frac{f_{cr}}{f_y} - 403.52k_r \right] \quad (5.17)$$

Where, Y_{P3}^{NRC} = Probabilistic dynamic capacity at performance level P3, $\hat{y}_{P3}^{NRC}$ = dynamic capacity at performance level P3 given by the mechanical model.

Table 5.7 Posterior Statistics of Parameters in Selected Dynamic Capacity (P3) Model

Parameter	Mean	Standard deviation	Correlation Coefficient					
			Θ_1	Θ_3	Θ_4	Θ_8	Θ_{10}	σ
Θ_1	269.6149	109.0294	1.000					
Θ_3	488.2583	85.5836	0.291	1.000				
Θ_4	-12.9988	4.9669	-0.098	-0.208	1.000			
Θ_8	431.8473	159.7076	0.149	0.193	-0.982	1.000		
Θ_{10}	-403.5232	161.5574	-1.000	-0.293	0.110	-0.161	1.000	
σ	0.2697	0.9878	0.038	0.039	-0.111	0.208	-0.042	1.000

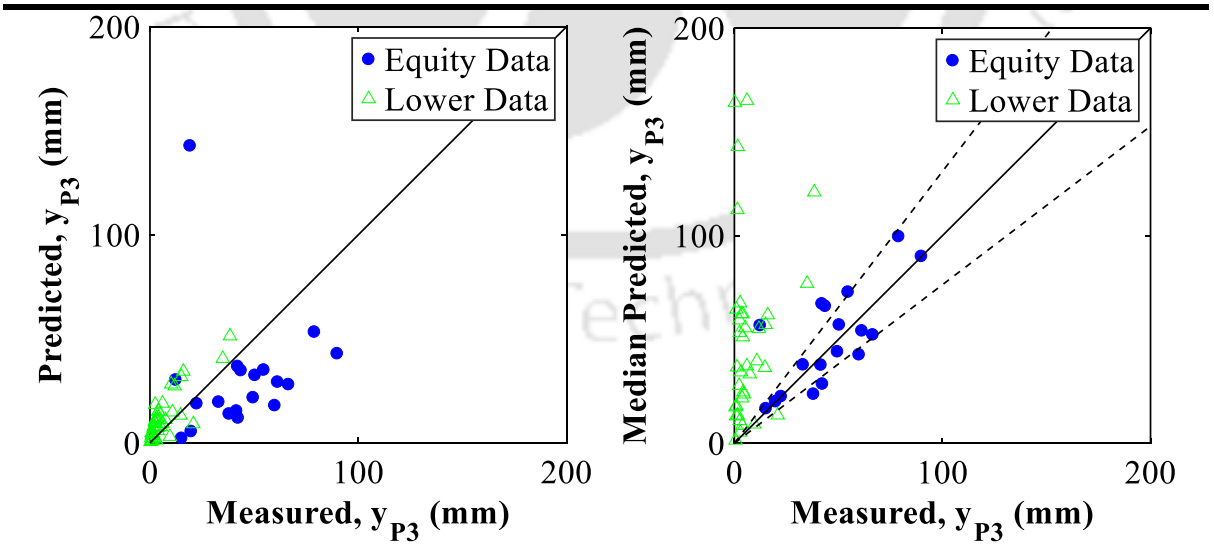

Figure 5.6 Comparison of measured and predicted Dynamic Capacity (P3) of UHSC Panel based on mechanical (left) and probabilistic (right) model

The mechanical and probabilistic models are both plotted against the capacity in the terms of deformation of the NRC panel values estimated from the FE simulations. Majority of data points are lying near to 1:1 line. The data contains both equality data and lower bound data. The predictions of probabilistic model show that the equality data lies both above and below the 1:1 line. The model has a standard deviation of 11.46. The probabilistic model corrects this inherent bias in the model.

5.8 FRAGILITY ESTIMATES

The fragility estimates provide an approximation of the structure's reliability when demand on the NRC and UHSC panels varies. It also depicts the behaviour of the different performance levels with the variation in the demand imposed on the panel. Based on the variation of the demand imposed on the panels, the fragility analysis gives an estimate of the vulnerability of the panel. The fragility of the panels subjected to different blast loadings is formulated as

$$F\left(x,\theta\right)=P\left[g\left(x,\theta\right)\le 0\middle|P_D\right] \tag{5.18}$$

where, $g_{p_i}\left(x,\theta\right)$ is the limit state function defined as,

$$g_{p_i}\left(x,\theta\right)=P_{p_i}\left(x,\theta\right)-P_D \tag{5.19}$$

and $i=1,2,3$, for all three performance levels. The fragility of blast load on NRC and UHSC panel is estimated based on varying the demand on the panel in terms of displacement for air blast. For developing the fragility curves, one NRC and UHSC panel from FE simulation were selected such that they represent the same ratio of capacity and demand as in the adopted validation. The properties and configuration of the selected panels are shown in

Table 5.8.

Table 5.8 Configuration and Dimensions of Panels for Fragility Estimate

Name of Configuration	Symbol	Dimensions of Panel	
		NRC	UHSC
Length of Panel (square)	L	5.924 m	4.974 m
Thickness of Concrete Panel	t	0.256 m	0.373 m
Weight of Charge	Q	342.78 kg	308.4 kg
Stand-off distance	R	7.16 m	3.56 m
Compressive Strength	f_c'	49.08 MPa	98.37 MPa
Yield Stress of Rebars	f_y	500 MPa	550 MPa
Diameter of Rebar	-	0.012 m	0.016 m
Area of Rebars	-	0.000667 m^2	0.001978 m^2

The fragility estimations of the NRC panel subjected to air blast for the three performance levels are shown in the Figure 5.9. Figure 5.10 depicts the fragility estimates of the UHSC panel subjected to air blast for the three performance level. The fragility estimate is directly conditioned on the normalized deflection demand. A crossed solid line represents the P1 performance level. Dashed line with plus marker denotes performance level P2, whereas dashed line with circle marker denotes performance level P3. The figure also shows the 15% and 85% confidence bounds for each performance level with colour fill (Gardoni et al. 2002). In comparison to the other performance levels, the curve for P1 is the steepest for both NRC and UHSC panel. The curve for performance level P3 is the least steep because it is the collapse limit state, and achieving a condition of collapse requires more deflection demand. The normalized dynamic deflection demand of the NRC panel is 7.97 and for UHSC is 7.15 as obtained from simulation. Performance levels P1, P2, and P3 have a failure probability of 1.0 at this value for both the panel. As illustrated in Figure 5.7 and 5.8, the NRC and UHSC panel is in damage state D4.

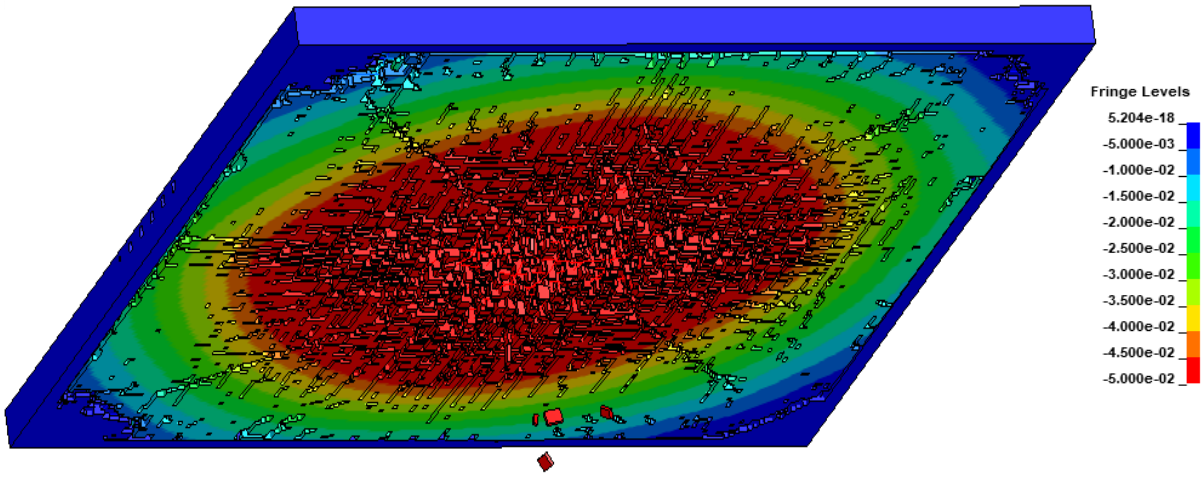

Figure 5.7 NRC Panel achieving damage state D4.

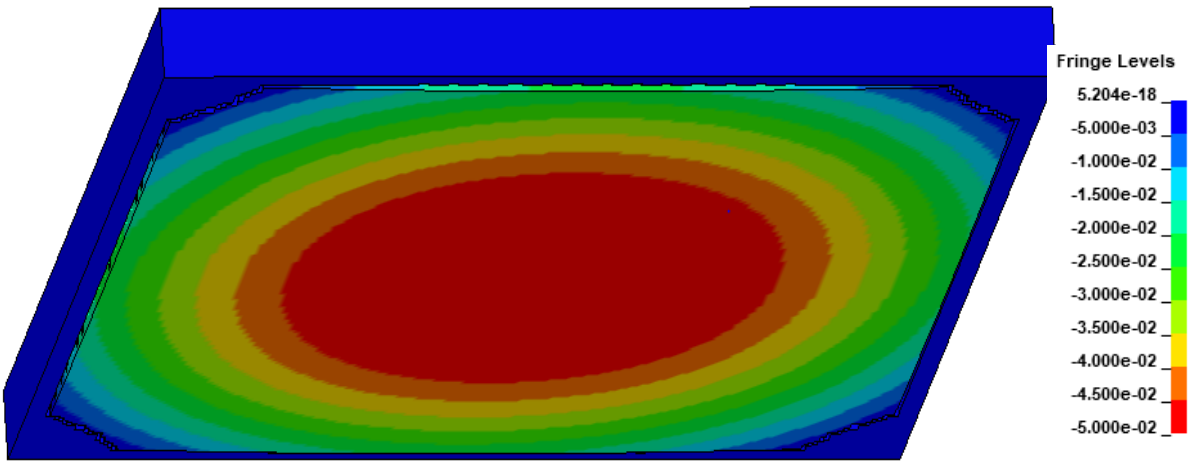

Figure 5.8 UHSC Panel achieving damage state D4.

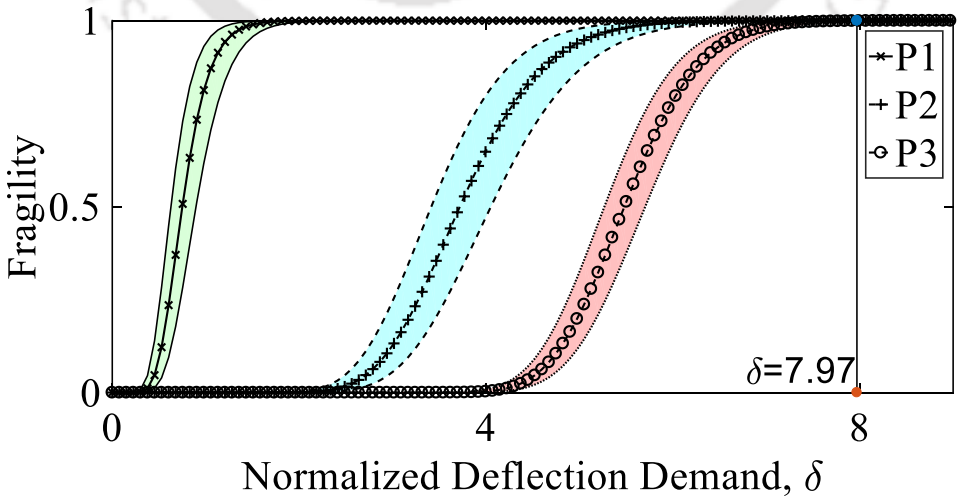

Figure 5.9 Fragility curves for NRC Panel for P1, P2 and P3.

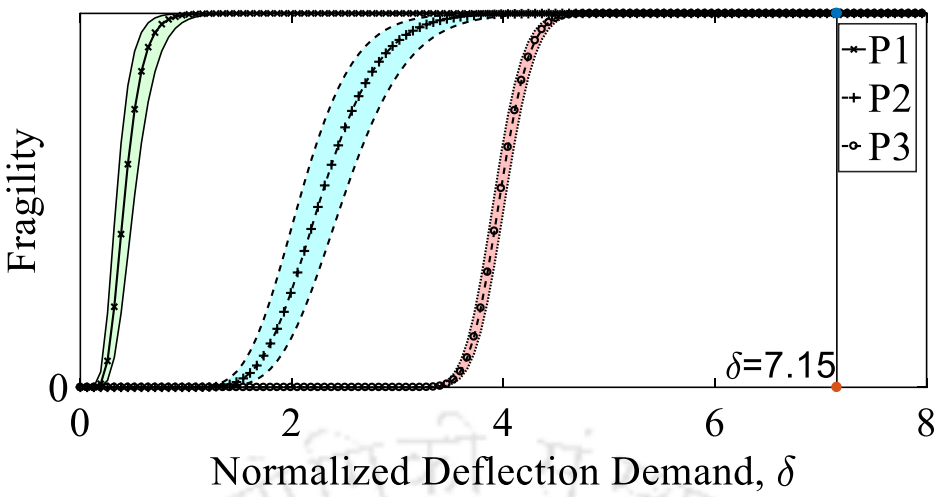

Figure 5.10 Fragility curves for UHSC Panel for P1, P2 and P3.

The panel fails due to the air blast loading which is reflected by the state of the panels being in damage state 4 and probability of failure of all performance levels being 1. This establishes the validity of the developed models for P1, P2, and P3 and the framework to estimate the reliability of both the NRC and UHSC panel.

5.9 PARAMETER ESTIMATION FOR DEMAND ON NRC PANEL

The most statistically significant explanatory functions for demand model of air blast is $h_1(x), h_2(x), h_4(x)$ and $h_8(x)$. Considered terms accounts for a correction of constant bias, slenderness ratio, ratio of strength of concrete by strength of steel and ratio of cracking strength of concrete by strength of steel. The posterior statistics of the model is follows in Table 5.9.

Figure 5.11 shows the comparison between the estimation of dynamic demand in terms of deformation of panel based on the proposed mechanical model and the mean of the developed probabilistic model where the mean predication for the dynamic demand Y_D^{AB} is developed as,

$$Y_D^{NRC} = \hat{y}_D^{NRC} \exp\left[-6.0455 + 7.039\frac{t}{L} - 62.88\frac{f_c' DIF}{f_y} + 1213.7\frac{f_{cr}}{f_y}\right] \qquad (5.20)$$

Where, Y_D^{AB} = Probabilistic maximum deflection of the panels occurred due to air blast loading,

$\hat{y}_D^{AB}$ = Maximum deflection of the panels due to air blast from mechanical model.

Table 5.9 Posterior Statistics of Parameters in Selected Dynamic Demand for NRC Panel

Parameter	Mean	Standard deviation	Correlation Coefficient				
			Θ_1	Θ_2	Θ_4	Θ_8	σ
Θ_1	-6.0455	1.4808	1.000				
Θ_2	7.0393	1.2795	-0.185	1.000			
Θ_4	-62.878	18.5805	0.907	-0.175	1.000		
Θ_8	1213.7	319.1488	-0.969	0.141	-0.980	1.000	
σ	0.5187	0.2486	0.101	0.103	0.195	-0.180	1.000

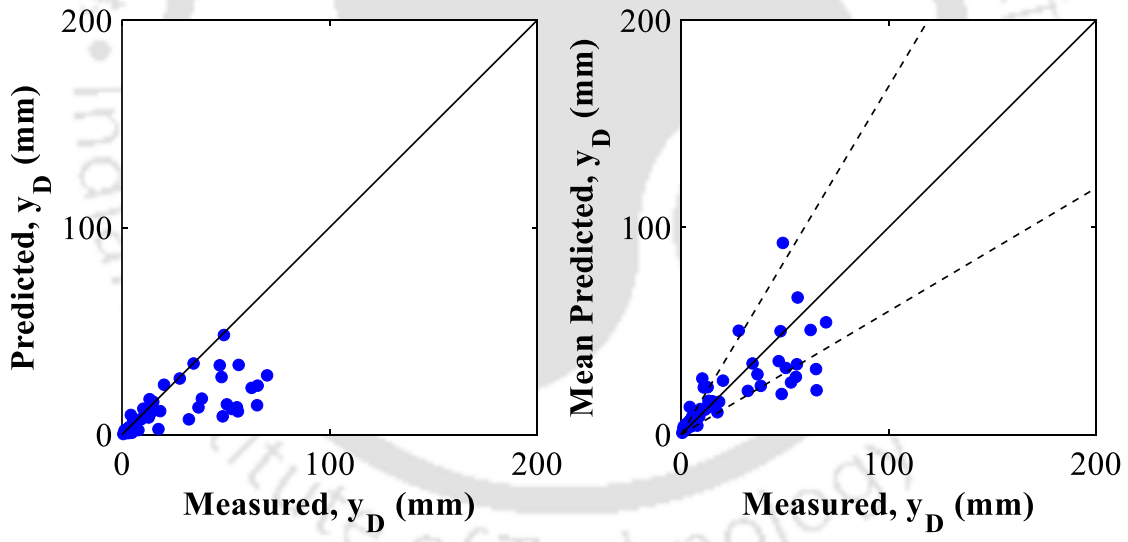

Figure 5.11 Comparison between measured and predicted Dynamic Demand based on mechanical (left) and probabilistic (right) model for NRC Panel

The mechanical and probabilistic models are both plotted against the demand in the terms of deformation of the panel values estimated from the FE simulations. Majority of data points are lying near to 1:1 line. The data contains equality data. The predictions of probabilistic model show that the equality data lies both above and below the 1:1 line. The standard deviation

of the model is found to be 15.3028. The probabilistic model corrects this inherent bias in the model.

5.10 PARAMETER ESTIMATION FOR DEMAND ON UHSC PANEL

The most statistically significant explanatory functions for demand model of air blast is $h_1(x), h_2(x), h_3(x)$ and $h_7(x)$. Considered terms accounts for a correction of constant bias, slenderness ratio, reinforcement ratio and resistance by peak positive pressure. The posterior statistics of the model is follows in Table 5.10.

Table 5.10 Posterior Statistics of Parameters in Selected Dynamic Demand Model for UHSC Panel

Parameter	Mean	Standard deviation	Correlation Coefficient				
			Θ_1	Θ_2	Θ_3	Θ_7	σ
Θ_1	0.5142	0.1452	1.000				
Θ_2	11.5977	1.9879	-0.329	1.000			
Θ_3	735.3079	121.1856	-0.211	-0.546	1.000		
Θ_7	-2.4970	0.1920	-0.083	-0.440	-0.180	1.000	
σ	0.4423	0.3008	-0.230	-0.325	0.270	0.035	1.000

Figure 5.12 shows the comparison between the estimation of dynamic demand in terms of deformation of the panel based on the proposed mechanical model and the mean of the developed probabilistic model where the mean predication for the dynamic demand Y_D^{UHSC} is developed as,

$$Y_D^{UHSC} = \hat{y}_D^{UHSC} \exp\left[0.5142 + 11.598\frac{t}{L} + 735.308\frac{A_s}{tL} - 2.497\left(\frac{r_u}{P_{so}}\right)^{0.7}\right] \qquad (5.21)$$

where, Y_D^{UHSC} = Probabilistic maximum deflection of UHSC panels occurred due to air blast loading, $\hat{y}_D^{UHSC}$ = Maximum deflection of UHSC panels due to air blast from mechanical model.

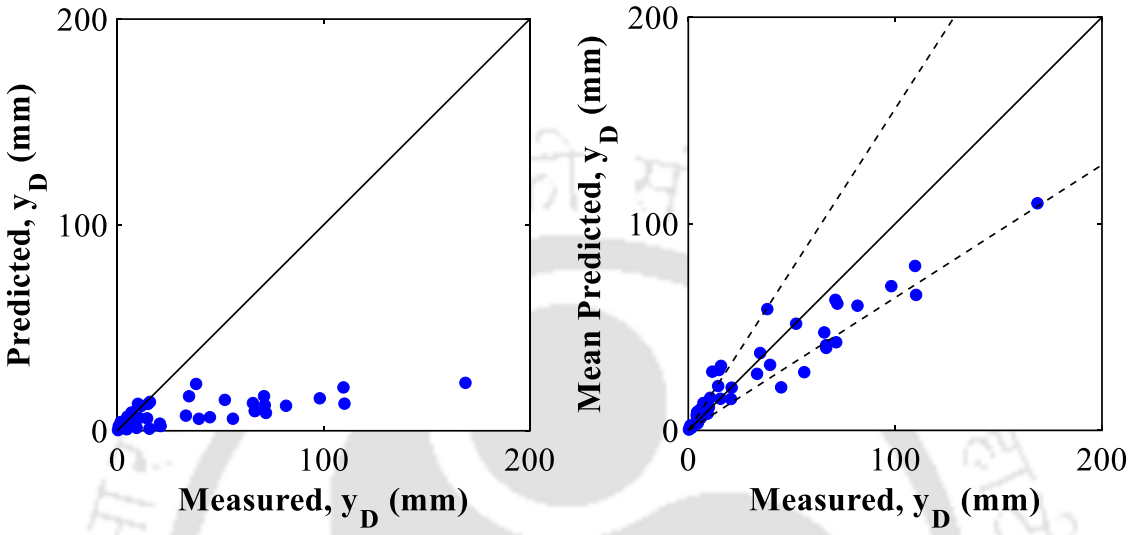

Figure 5.12 Comparison between measured and predicted Dynamic Demand based on mechanical (left) and probabilistic (right) model for UHSC Panel

The mechanical and probabilistic models are both plotted against the demand in the terms of deformation of the panel values estimated from the FE simulations. Majority of data points are lying near to 1:1 line. The data contains equality data. The predictions of probabilistic model show that the equality data lies both above and below the 1:1 line. The probabilistic model corrects this inherent bias in the model. The standard deviation of the model is 16.2286 which details the accuracy of the developed probabilistic model for estimating the Demand for panel subjected to contact blast loading.

5.11 DISCUSSION

In this Chapter, development of capacity and demand model based on deflection formulation for NRC panels subject to air blast is achieved. The probabilistic resistance model captures the dynamic behaviour of the panels and accounts for the associated uncertainties. Probabilistic

demand model accounts for the dynamic interaction between the panel during an air blast and considers associated uncertainties. The models are based on Deflection based formulation. The developed probabilistic capacity models accurately estimate the capacity of the panels at the specified performance level and probabilistic demand models accurately evaluates the demand on the panels for the air blast. A framework to assess the fragility of the panel subjected to air blast is developed in Chapter 7.

The developed models advance the knowledge of behaviour of NRC and UHSC panels subject to air blast at the different performance stages which is the novelty of this research. The model is simple and easy to use. The developed models can be used to design safer slabs with the reliability based design approach and the work can be extended to other structural members under similar loading conditions. This work can be extended to develop model for the same panel subject to contact blast.

Chapter 6. PERFORMANCE-BASED MODELS FOR PANELS SUBJECT TO CONTACT BLAST

6.1 GENERAL FORMULATION

The probabilistic models are generally created by accumulation of correction terms to mechanical models. Because the data used for the model assessment come from FE simulations, it can be assumed that there is no error in the data measurement. The model from where a transformation of the quantity of interest is written is shown in equation given below, as the sum of a mechanical model, a correction term to account for the bias in the mechanical model, and model error (Gardoni et al. 2002). Following the general formulation for probabilistic models, the capacity/demand for crater diameter formed due to a contact blast is formulated as

$$P_{i/D}\left(x,\Theta_{P_i/D}\right)=\hat{p}_{i/D}\left(x\right)\gamma_{P_i/D}\left(x,\theta_{P_i/D}\right)+\sigma_{P_i/D}e_{P_i/D} \tag{6.1}$$

where $P_{i/D}=$ Probabilistic deflection based capacity/damage model of the panel for the defined performance level due to contact blast, $i=1,2,3$, $\hat{p}_{i/D}=$ Mechanical capacity/damage model for the panels at the performance level; $\gamma_{P_i/D}\left(x,\theta_{P_i/D}\right)=$ correction term for the bias inherent in the mechanical model defined as

$$\gamma_{P_i/D}\left(x,\theta_{P_i/D}\right)=\sum_{j=1}^{n}\theta_{P_{i,j}/D}h_{P_{i,j}/D}\left(x\right) \tag{6.2}$$

where $h_{P_{i,j}/D}\left(x\right)$, $j=1,...,n=$ explanatory function (or regressors) defined as functions of x, $\theta_{P_{i,j}/D}$, $j=1,...,n$ are the parameters associated with explanatory functions, $\sigma_{P_i/D}e_{P_i/D}=$

model error, $\sigma_{P_i/D}$ = standard deviation, $e_{P_i/D}$ = Gaussian error and $\Theta_{P_i/D} = \theta_{P_i/D}$ = set of unknowns model parameters.

6.2 MODEL CORRECTION AND ASSESSMENT

To capture the physical phenomena in the probabilistic models, suitable model correction terms are selected which is not accounted in the mechanical model. Selected explanatory functions given in

Table 6.1 lists the physical quantity which influences the probabilistic models of the panels subject to contact blast. In

Table 6.1, $\lambda_0 = d_0/h_0$ is aspect ratio of TNT container, i.e., d_0 is the diameter and h_0 is the height of the TNT container; A_c is the area of contact under TNT, P_c is the perimeter of the charge, τ_u is the ultimate shear stress of concrete, τ_c is the allowable shear stress of concrete $\left(\tau_c = 0.3\sqrt{f_c'}\right)$, Q_0 is the explosive energy of TNT in J/kg, ρ_0 is the density of TNT charge and ρ_c is the density of concrete.

Table 6.1 List of Explanatory Functions for Models of Panels subject to Contact Blast

Variable	Description	Expression
$h_1(x)$	Constant bias	1
$h_2(x)$	Slenderness ratio	t/L
$h_3(x)$	Reinforcement Ratio	$\rho = A_s/tL$
$h_4(x)$	Ratio of strength of concrete by strength of steel	$f_c' DIF / f_y$
$h_5(x)$	Aspect ratio of TNT container	$\lambda_0 = d_0/h_0$
$h_6(x)$	Inertia	M_E/Q
$h_7(x)$	Area of contact by Punching area of panel covered by charge	$A_c/P_c t$
$h_8(x)$	Ratio of cracking strength of concrete by strength of steel	$f_{cr} DIF / f_y$
$h_9(x)$	Ultimate shear stress by design shear strength of concrete	τ_u/τ_c
$h_{10}(x)$	Diameter of TNT container by thickness of panel	d_0/t
$h_{11}(x)$	Contact area ratio	$A_R = \dfrac{A_c\left(1+\lambda_0^2\right)}{A_s\left(f_c' DIF/f_y\right)^2}$
$h_{12}(x)$	Energy	$\log\left(\dfrac{QQ_0\rho_0}{\rho_c t^3 f_c'}\right)$

The first explanatory function, $h_1(x)$ accounts for the potential constant bias present in the mechanical model. The second explanatory function, $h_2(x)$ accounts for the slenderness ratio of the panels. The third explanatory function, $h_3(x)$ accounts for the contribution of the reinforcement ratio. The fourth explanatory function, $h_4(x)$ accounts for the contribution of concrete compressive strength to yield strength of steel. The fifth explanatory function, $h_5(x)$ accounts for the contribution of aspect ratio of charge container. The sixth explanatory function, $h_6(x)$ is the ratio of equivalent mass of the slab to the charge weight applied. Area of contact by punching area is accounted by the seventh explanatory function, $h_7(x)$. The eighth explanatory function $h_8(x)$, accounts for the contribution of concrete cracking strength to yield strength of steel. The eleventh explanatory function, $h_9(x)$ accounts for the contribution of ultimate shear stress by allowable shear stress of concrete. The twelfth explanatory function, $h_{10}(x)$ accounts for the diameter of charge container by thickness of panel. The thirteenth and fourteenth explanatory function, $h_{11}(x)$ and $h_{12}(x)$ accounts for the contribution of charge influence on the panel in area and energy form respectively.

The Bayesian inference with a non-informative prior is selected (Box and Tiao 1992) for estimation of modal parameters (Θ). The approach adopted is explained in Section 2.7.1.

6.3 MECHANICAL MODEL FOR CONTACT BLAST

6.3.1 Mechanical Model for Capacity

Contact blast tends to fail a panel in shear and therefore, allowable shear force term is considered for mechanical capacity model of the panel. The mechanical model proposed for all the performance level is

$$\hat{c} = \frac{\tau_{ac} \pi t^2}{9.4609 \times 10^5} \tag{6.3}$$

where, t is thickness of panel (mm), τ_{Vc} is the allowable shear stress calculated as (as given in (US Department of Defense 2008))

$$\tau_{ac}\left(psi\right) = 1.9\sqrt{f_c'} + 2500\left(\frac{A_{st}}{bd_{eff}}\right) \tag{6.4}$$

where, constituent parameters are in Psi, converting the equation for SI units, we get,

$$\tau_{ac}\left(MPa\right) = 0.1578\sqrt{f_c'} + 17.237\left(\frac{A_{st}}{bd_{eff}}\right) \tag{6.5}$$

where, f_c' is the concrete compressive strength (MPa), A_{st} is the area of steel provided per meter length, b is the unit width of panel and d_{eff} is the average of effective depth of panel.

6.3.2 Mechanical Model for Demand

From the equation (1.29) given by Remennikov et al. (2015) for breaching diameter, it can be said that damage diameter for a given charge is directly proportional to the cubic root of mass of explosive. Based on this and neglecting the constant terms, the estimate of the dynamic

demand $\hat{c}_D^{NC}$ is taken as cube root of charge weight required by a panel to form a crater diameter of certain amount and is depicted by the proposed formula given below:

$$\hat{c}_D = Q^{1/3} \tag{6.6}$$

Where, $\hat{c}_D$ = dynamic demand from contact blast on the panels and Q is the weight of charge.

6.4 PROBABILISTIC MODEL FOR PANEL SUBJECT TO CONTACT BLAST

According to the damage states mentioned in Section 2.3.2, the damage parameters that are significant to define the damage states are: Crater Diameter, Crater Depth, Spall Diameter, Spall Depth and Breach Diameter. Therefore, before going to the different capacity models, we need to develop the probabilistic model for the stated damage states.

6.4.1 Probabilistic Model for Crater Diameter (C)

The newly proposed equation to estimate the probabilistic Crater diameter of NRC/UHSC Panel subject to contact blast loading after the probabilistic analysis is,

$$C^{NRC} = Q^{1/3} \exp\left[-2.41 + 118.25\frac{A_s}{tL} + 0.234\frac{d_0}{h_0} - 0.222\frac{\tau_u}{\tau_c} + 0.352\log\left(\frac{QQ_0\rho_0}{\rho_c t^3 f_c'}\right)\right] \tag{6.7}$$

$$C^{UHSC} = Q^{1/3} \exp\left[-0.4132 - 0.7487\frac{f_c' DIF}{f_y} - 0.0879\frac{d_0}{h_0}\right] \tag{6.8}$$

Where, $C^{NRC/UHSC}$ = Probabilistic dynamic Crater diameter formed for Q kg-TNT of charge in NRC/UHSC Panel respectively and other parameter are as explained in Section 6.2. Considered terms accounts for a correction of constant bias, reinforcement ratio, aspect ratio of TNT container, ultimate shear stress and allowable shear stress of concrete and energy of NRC slab. The correction terms for UHSC slab accounts for constant bias, ratio of strength of

concrete by strength of steel and aspect ratio of TNT container. The posterior statistics of the model is follows in Table 6.2 and 6.3 for NRC and UHSC respectively.

Table 6.2 Posterior Statistics of Parameters in Crater diameter of NRC Panel

Parameter	Mean	Standard deviation	Correlation Coefficient					
			Θ_1	Θ_3	Θ_5	Θ_9	Θ_{12}	σ
Θ_1	-2.4110	0.3538	1.000					
Θ_3	118.2543	43.3639	-0.487	1.000				
Θ_5	0.2335	0.0509	-0.897	0.375	1.000			
Θ_9	-0.2216	0.0493	0.449	-0.844	-0.380	1.000		
Θ_{12}	0.3520	0.0689	-0.989	0.4742	0.845	-0.485	1.000	
σ	0.1245	0.0689	0.173	-0.028	-0.154	0.097	-0.218	1.000

Table 6.3 Posterior Statistics of Parameters in Crater diameter of UHSC Panel

Parameter	Mean	Standard deviation	Correlation Coefficient			
			Θ_1	Θ_4	Θ_5	σ
Θ_1	-0.4132	0.0422	1.000			
Θ_4	-0.7487	0.1316	-0.751	1.000		
Θ_5	-0.0879	0.0153	-0.551	-0.003	1.000	
σ	0.0901	0.6215	-0.060	-0.124	0.081	1.000

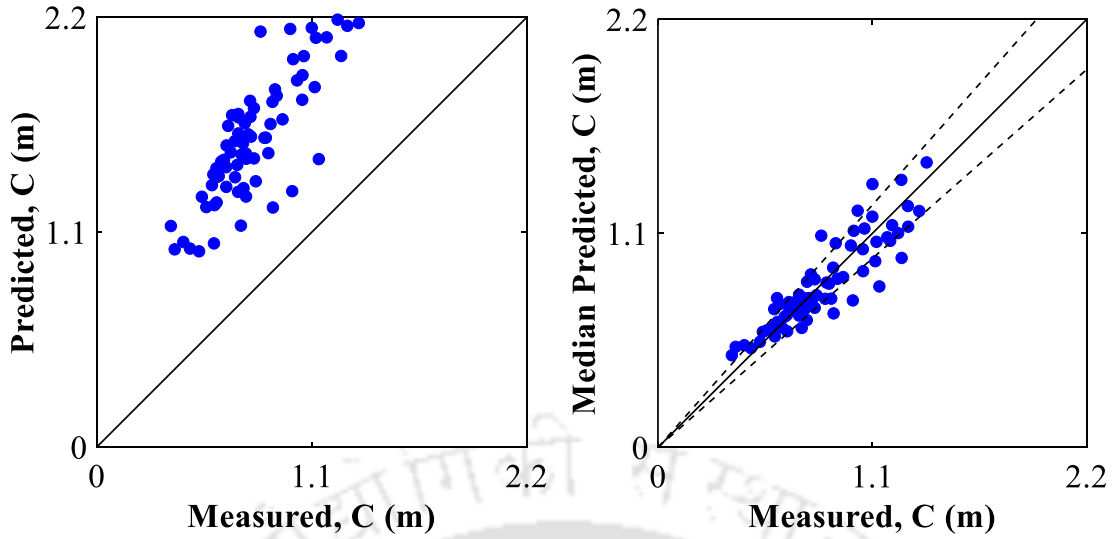

Figure 6.1 Comparison between measured and predicted Crater diameter based on mechanical (left) and probabilistic (right) model for NRC

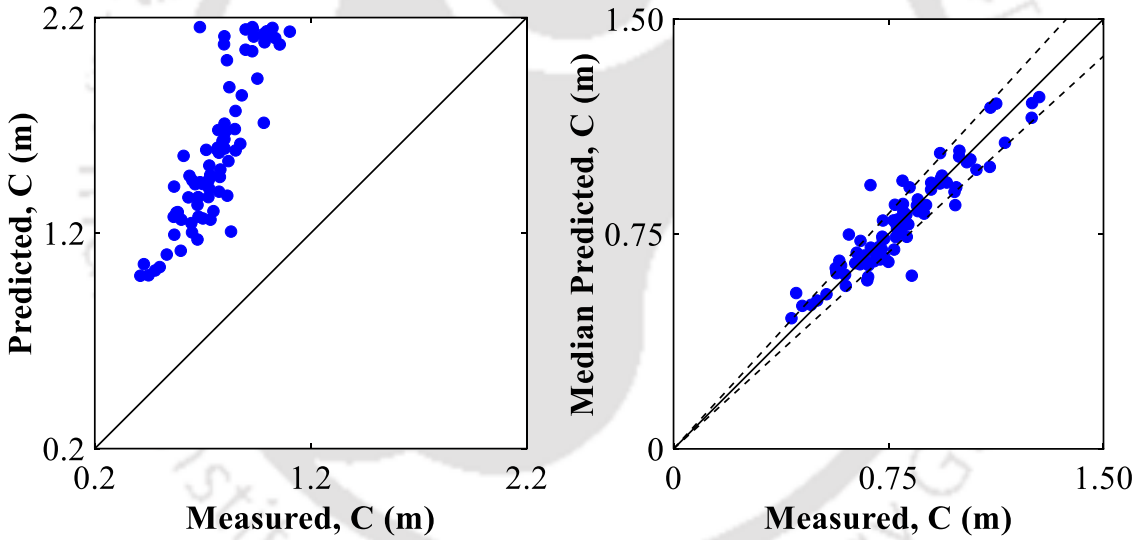

Figure 6.2 Comparison between measured and predicted Crater diameter based on mechanical (left) and probabilistic (right) model for UHSC

Figure 6.1 and 6.2 shows the comparison between the estimation of dynamic demand in terms of Crater diameter formed in the NRC and UHSC panel based on the proposed mechanical model and the mean predicated of the developed probabilistic model respectively. Majority of data points are lying near to 1:1 line in the mean predicted plot confirms the good

fit along with a standard deviation of 0.1094 for NRC and 0.0674 for UHSC Panel. The data contains only equality data. The probabilistic model corrects this inherent bias in the model.

6.4.2 Probabilistic Model for Crater Depth (C_d)

Based on the equation of Crater depth given by (Yamaguchi et al. 2011) and (Morishita et al. 2004), the adopted mechanical model is adopted as

$$\hat{C}_d^{NRC/UHSC} = t\left(-0.46\frac{t}{Q^{1/3}} + 0.42\right) \tag{6.9}$$

where, $\hat{C}_d$ is Crater depth formed for both NRC and UHSC panel and $t/Q^{1/3}$ is the scaled thickness in m/kg$^{1/3}$. The proposed probabilistic equation to estimate the Crater depth of NRC/UHSC Panel subject to contact blast loading after the probabilistic analysis is,

$$C_d^{NRC} = \hat{C}_d^{NRC}\exp\left[-1.014 - 0.1957\frac{\tau_u}{\tau_c} + 0.332\frac{d_0}{t} + 0.252\log\left(\frac{QQ_0\rho_0}{\rho_c t^3 f_c'}\right)\right] \tag{6.10}$$

$$C_d^{UHSC} = \hat{C}_d^{UHSC}\exp\left[0.8468 - 3.0119\frac{t}{L} + 150.0011\frac{A_s}{tL} - 0.3451\frac{d_0}{t}\right] \tag{6.11}$$

Where, $C^{NRC/UHSC}$ = Probabilistic dynamic Crater depth formed for Q kg-TNT of charge in NRC/UHSC Panel respectively and other parameter are as explained in Section 6.2. Considered terms accounts for a correction of constant bias, ultimate shear stress and allowable shear stress of concrete, diameter of TNT container by thickness of panel area of contact and energy term from contact blast on NRC panel. In UHSC panel, considered terms accounts for a correction of constant bias, slenderness ratio of panel, reinforcement ratio and aspect ratio of TNT

container. The posterior statistics of the model is follows in Table 6.4 and 6.5 for NRC and UHSC respectively.

Table 6.4 Posterior Statistics of Parameters in Crater depth of NRC Panel

Parameter	Mean	Standard deviation	Correlation Coefficient				
			Θ_1	Θ_9	Θ_{10}	Θ_{12}	σ
Θ_1	-1.0141	0.3702	1.000				
Θ_9	-0.1857	0.0478	-0.302	1.000			
Θ_{10}	0.3320	0.1140	-0.632	0.462	1.000		
Θ_{12}	0.2520	0.0744	-0.965	0.095	0.453	1.000	
σ	0.1867	0.4673	-0.098	-0.032	0.065	0.057	1.000

Table 6.5 Posterior Statistics of Parameters in Crater depth of UHSC Panel

Parameter	Mean	Standard deviation	Correlation Coefficient				
			Θ_1	Θ_2	Θ_3	Θ_5	σ
Θ_1	0.8468	0.1196	1.000				
Θ_2	-3.0119	0.5567	-0.314	1.000			
Θ_3	150.0011	46.7799	-0.110	-0.702	1.000		
Θ_5	-0.3451	0.0836	-0.876	0.159	-0.035	1.000	
σ	0.1386	1.1139	-0.331	0.090	0.057	0.121	1.000

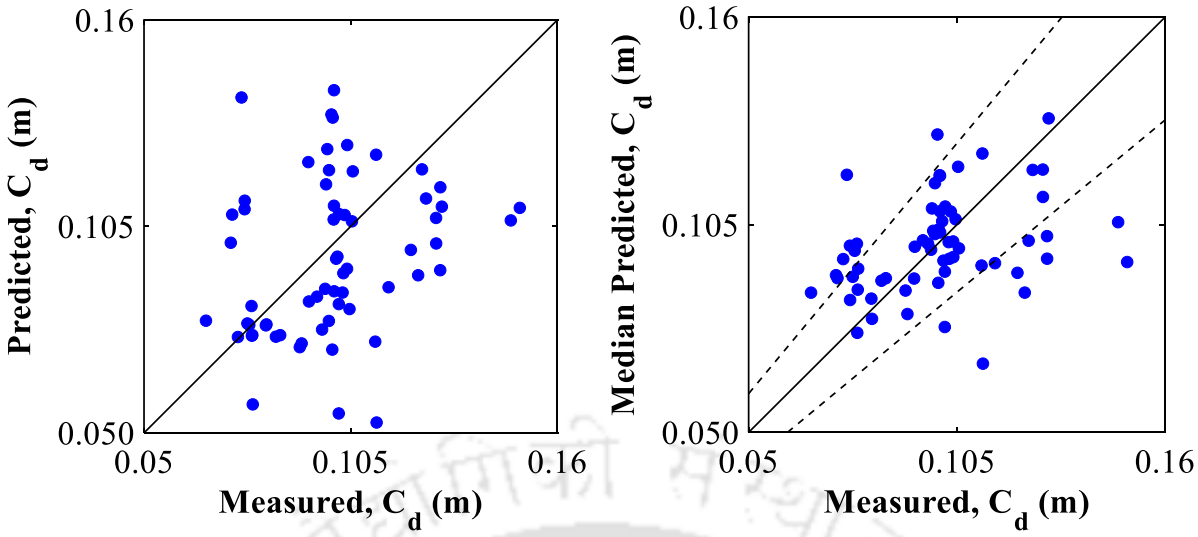

Figure 6.3 Comparison between measured and predicted Crater depth based on mechanical (left) and probabilistic (right) model for NRC

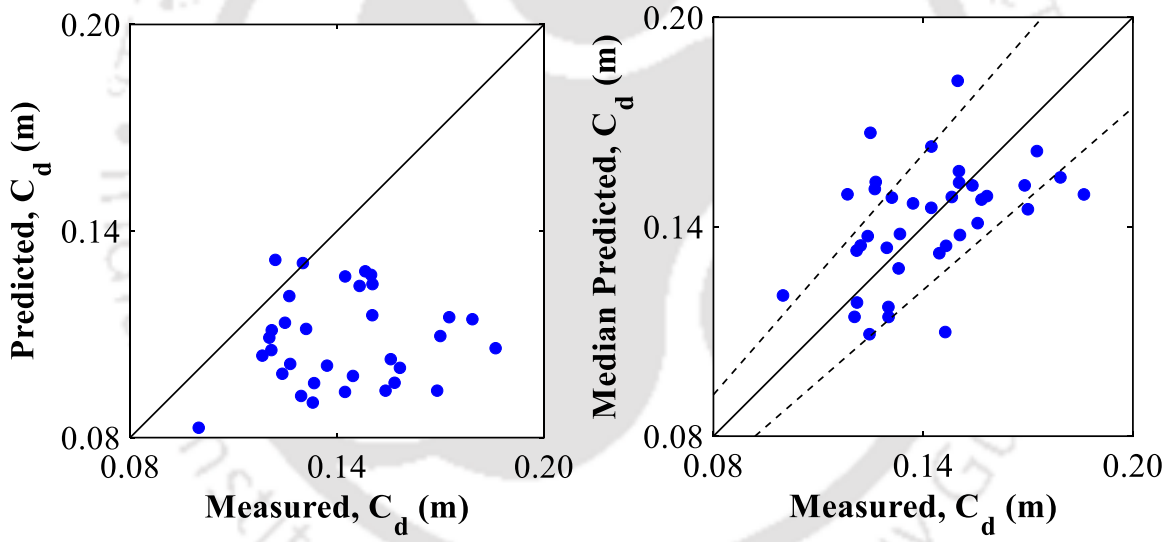

Figure 6.4 Comparison between measured and predicted Crater depth based on mechanical (left) and probabilistic (right) model for UHSC

Figure 6.3 shows the comparison between the estimation of dynamic demand in terms of Crater depth formed in the NRC panel respectively based on the proposed mechanical model and the mean predicated of the developed probabilistic model. Figure 6.4 shows the comparison between the estimation of dynamic demand in terms of Crater depth formed in the UHSC panel respectively based on the proposed mechanical model and the mean predicated of the

developed probabilistic model. Majority of data points are lying near to 1:1 line in the mean predicted plot confirms the good fit along with a standard deviation of 0.0189 for NRC and 0.0188 for UHSC. The data contains only equality data. The probabilistic model corrects this inherent bias in the model.

6.4.3 Probabilistic Model for Spall Diameter (S)

The newly proposed equation to estimate the probabilistic Spall diameter of NRC/UHSC Panel subject to contact blast loading after the probabilistic analysis is,

$$S^{NRC} = Q^{1/3} \exp\left[-0.81 - 1.10\frac{t}{L} + 0.21\frac{d_0}{t}\right] \tag{6.12}$$

$$S^{UHSC} = Q^{1/3} \exp\left[-1.0972 + 442.38\frac{A_s}{tL} - 2.9348\frac{f_c' DIF}{f_y} + 0.3961\frac{d_0}{h_0} - 1.2032\frac{\tau_u}{\tau_c}\right] \tag{6.13}$$

Where, $S^{NRC/UHSC}$ = Probabilistic dynamic Spall diameter formed for Q kg-TNT of charge in NRC/UHSC Panel respectively and other parameter are as explained in Section 6.2. Considered terms accounts for a correction of constant bias, slenderness ratio of panel and diameter of TNT container by thickness of NRC panel. Whereas for UHSC panel, considered terms accounts for a correction of constant bias, reinforcement ratio, ratio of concrete compressive strength to yield strength of steel, aspect ratio of TNT container and ultimate shear stress to allowable shear stress of concrete ratio. The posterior statistics of the model is follows in Table 6.6 and 6.7.

Table 6.6 Posterior Statistics of Parameters in Spall diameter of NRC Panel

Parameter	Mean	Standard deviation	Correlation Coefficient			
			Θ_1	Θ_2	Θ_{10}	σ
Θ_1	-0.8104	0.0951	1.000			
Θ_2	-1.1023	0.3794	-0.725	1.000		
Θ_{10}	0.2092	0.0987	-0.894	0.481	1.000	
σ	0.1411	1.1027	-0.464	0.130	0.337	1.000

Table 6.7 Posterior Statistics of Parameters in Spall diameter of UHSC Panel

Parameter	Mean	Standard deviation	Correlation Coefficient					
			Θ_1	Θ_3	Θ_4	Θ_5	Θ_9	σ
Θ_1	-1.0972	0.2773	1.000					
Θ_3	442.3784	142.0672	0.421	1.000				
Θ_4	-2.9348	0.8277	-0.781	-0.636	1.000			
Θ_5	0.3961	0.0675	-0.380	0.111	-0.097	1.000		
Θ_9	-1.2032	0.3276	-0.632	-0.853	0.623	-0.067	1.000	
σ	0.3223	0.2961	-0.079	0.229	-0.073	0.057	-0.178	1.000

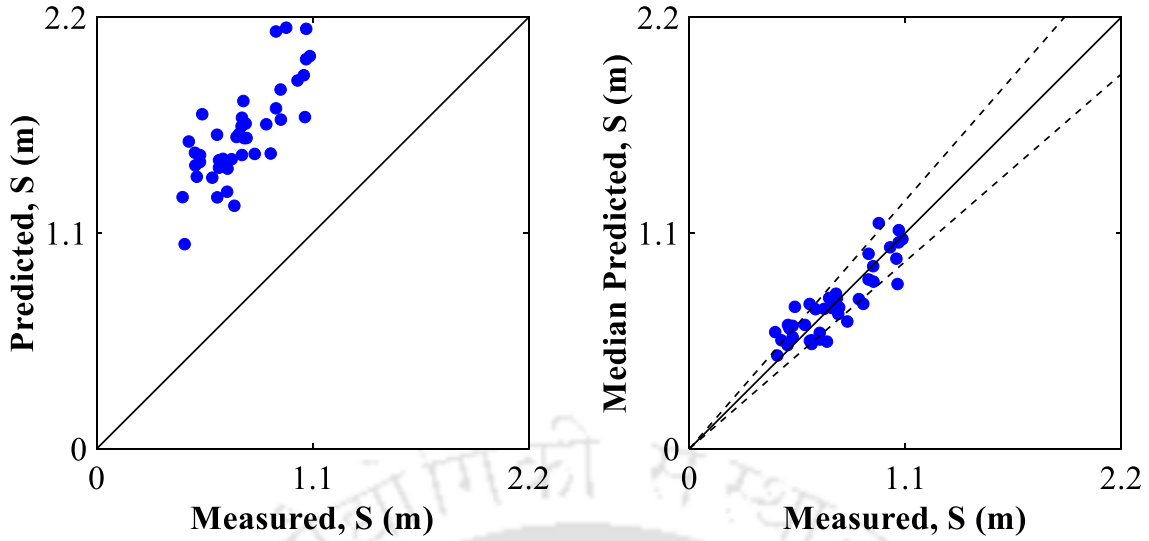

Figure 6.5 Comparison between measured and predicted Spall diameter based on mechanical (left) and probabilistic (right) model for NRC

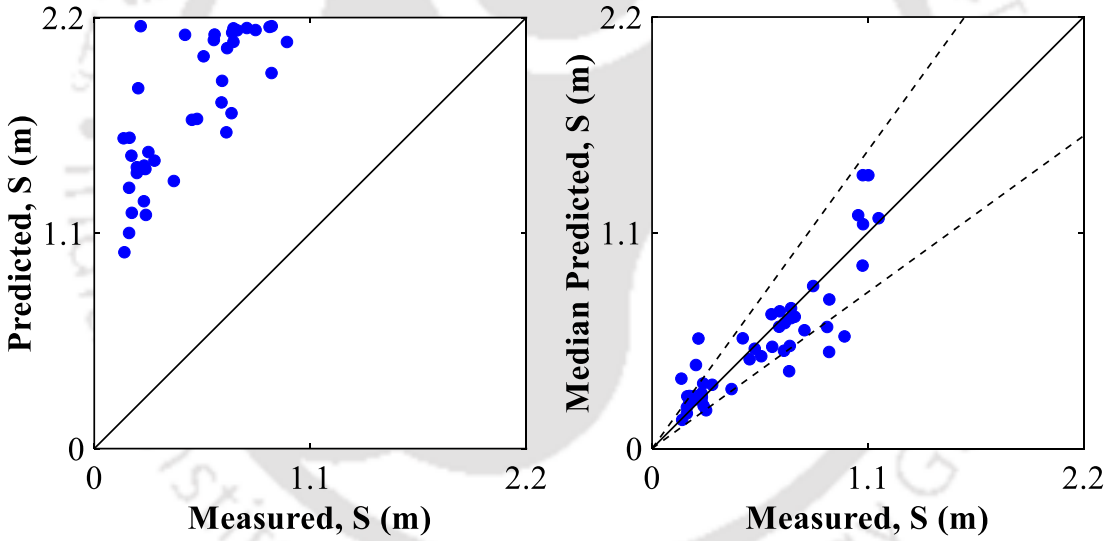

Figure 6.6 Comparison between measured and predicted Spall diameter based on mechanical (left) and probabilistic (right) model for UHSC

Figure 6.5 and 6.6 shows the comparison between the estimation of dynamic demand in terms of Spall diameter formed in the panels based on the proposed mechanical model and the mean predicated of the developed probabilistic model. Majority of data points are lying near to 1:1 line in the mean predicted plot confirms the good fit along with a standard deviation

of 0.0972 for NRC and 0.1661 for UHSC Panel. The data contains only equality data. The probabilistic model corrects this inherent bias in the model.

6.4.4 Probabilistic Model for Spall Depth (S_d)

Based on the equation of Spall depth given by (Yamaguchi et al. 2011) and (Morishita et al. 2004), the adopted mechanical model is adopted as

$$\hat{S}_d^{NRC/UHSC} = t\left(-\frac{C_d}{t} - 4.9\frac{t}{Q^{1/3}} + 2\right) \tag{6.14}$$

where, $\hat{S}_d$ is Spall depth formed for both NRC and UHSC panel, C_d is the calculated crater depth and $t/Q^{1/3}$ is the scaled thickness in m/kg$^{1/3}$. The newly proposed equation to estimate the probabilistic Spall depth of NRC/UHSC Panel subject to contact blast loading after the probabilistic analysis is,

$$S_d^{NRC} = \hat{S}_d^{NRC}\exp\left[-1.45 + 1.62\frac{t}{L} + 0.36\frac{d_0}{h_0} + 0.0034\frac{M_E}{Q}\right] \tag{6.15}$$

$$S_d^{UHSC} = \hat{S}_d^{UHSC}\exp\left[-1.309 - 317.96\frac{A_s}{tL} + 0.005\frac{M_E}{Q} + 0.9058\frac{\tau_u}{\tau_c}\right] \tag{6.16}$$

Where, $C^{NRC/UHSC}$ = Probabilistic dynamic Spall depth formed for Q kg-TNT of charge in NRC/UHSC Panel respectively and other parameter are as explained in Section 6.2. Considered terms accounts for a correction of constant bias, slenderness ratio, aspect ratio of TNT container and inertia for NRC panel. For UHSC panel, the considered terms contribute for constant bias, reinforcement ratio, ratio of equivalent mass of the slab to the charge weight applied and ultimate shear stress by allowable shear stress of concrete ratio. The posterior statistics of the model is follows in Table 6.8 and 6.9.

Table 6.8 Posterior Statistics of Parameters in Spall depth of NRC Panel

Parameter	Mean	Standard deviation	Correlation Coefficient				
			Θ_1	Θ_2	Θ_5	Θ_6	σ
Θ_1	-1.4529	0.3130	1.000				
Θ_2	1.6225	0.4792	0.116	1.000			
Θ_5	0.3552	0.1688	-0.977	-0.205	1.000		
Θ_6	0.0034	$8.2\text{x}10^{-4}$	-0.877	-0.355	0.833	1.000	
σ	0.1869	0.7741	0.069	0.040	-0.109	-0.221	1.000

Table 6.9 Posterior Statistics of Parameters in Spall depth of UHSC Panel

Parameter	Mean	Standard deviation	Correlation Coefficient				
			Θ_1	Θ_3	Θ_6	Θ_9	σ
Θ_1	-1.3092	0.0953	1.000				
Θ_3	-317.961	88.5729	-0.109	1.000			
Θ_6	0.0050	5.396e-4	-0.262	0.169	1.000		
Θ_9	0.9058	0.2234	-0.382	-0.790	-0.302	1.000	
σ	0.2683	0.1926	-0.087	0.167	-0.012	-0.160	1.000

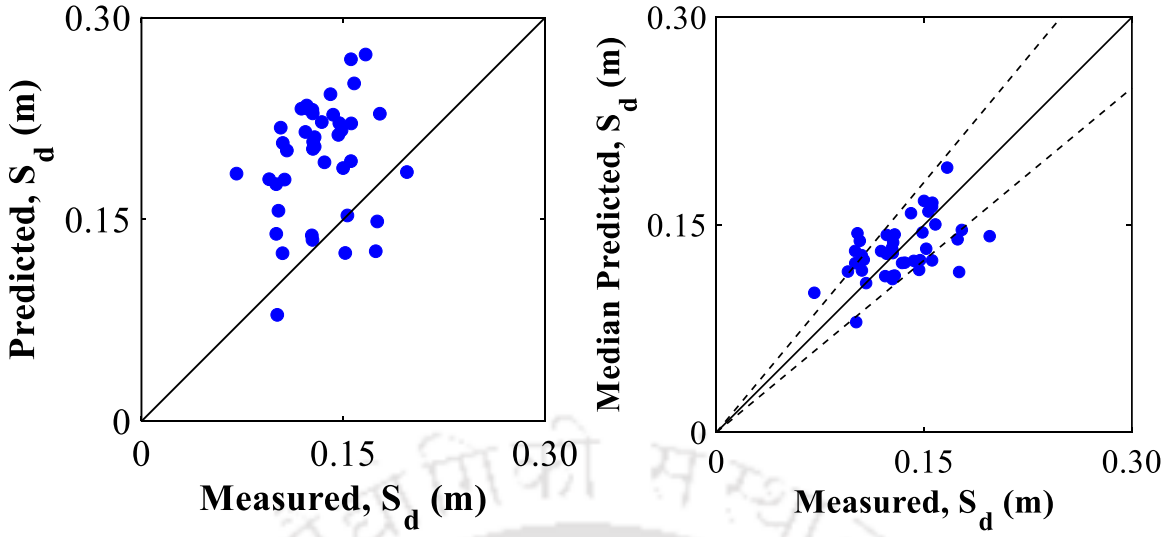

Figure 6.7 Comparison between measured and predicted Spall depth based on mechanical (left) and probabilistic (right) model for NRC

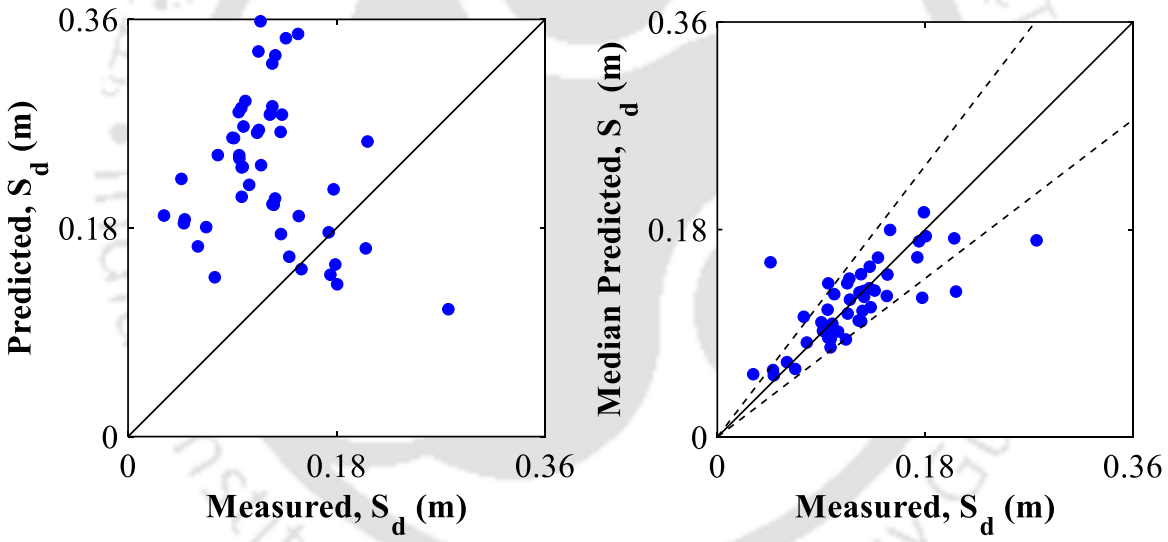

Figure 6.8 Comparison between measured and predicted Spall depth based on mechanical (left) and probabilistic (right) model for UHSC

Figure 6.7 and 6.8 shows the comparison between the estimation of dynamic demand in terms of Spall depth formed in the NRC and UHSC panels respectively, based on the proposed mechanical model and the mean predicated of the developed probabilistic model. Majority of data points are lying near to 1:1 line in the mean predicted plot confirms the good fit along with

a standard deviation of 0.0244 and 0.0305 for NRC and UHSC panel respectively. The data contains only equality data. The probabilistic model corrects this inherent bias in the model.

6.4.5 Probabilistic Model for Breach Diameter (H)

Based on the equation given by (Yamaguchi et al. 2011) and (Morishita et al. 2004), the adopted mechanical model is adopted as

$$\hat{H}^{NRC/UHSC} = t\left(-6.7\log_{10}\frac{t}{Q^{1/3}} + 2.7\right) \tag{6.17}$$

where, $\hat{H}$ is breach diameter formed for both NRC and UHSC panel and $t/Q^{1/3}$ is the scaled thickness in m/kg$^{1/3}$. The newly proposed equation to estimate the probabilistic Breach diameter of NRC/UHSC Panel subject to contact blast loading after the probabilistic analysis is given below,

$$H^{NRC} = \hat{H}^{NRC}\exp\left[-3.2206 + 2.0741\frac{d_0}{t}\right] \tag{6.18}$$

$$H^{UHSC} = \hat{H}^{UHSC}\exp\left[-1.59 + 571.91\frac{A_s}{tL} - 3.17\frac{f_c'DIF}{f_y} - 1.405\frac{\tau_u}{\tau_c} + 1.006\frac{d_0}{t}\right] \tag{6.19}$$

Where, $C^{NRC/UHSC}$ = Probabilistic dynamic Breach diameter formed for Q kg-TNT of charge in NRC/UHSC Panel respectively and other parameter are as explained in Section 6.2. Considered terms for NRC panel accounts for a correction of constant bias and diameter of TNT container by thickness of panel. For HSC panel the considered terms account for constant bias, reinforcement ratio, concrete compressive strength to yield strength of steel, contribution of ultimate shear stress by allowable shear stress of concrete and the diameter of charge container by thickness of panel. The posterior statistics of the model for NRC and UHSC panel is depicted in Table 6.10 and 6.11 respectively.

Table 6.10 Posterior Statistics of Parameters in Breach diameter of NRC Panel

Parameter	Mean	Standard deviation	Correlation Coefficient		
			Θ_1	Θ_{10}	σ
Θ_1	-3.2206	0.2324	1.000		
Θ_{10}	2.0741	0.2605	-0.961	1.000	
σ	0.2077	0.3959	-0.066	-0.102	1.000

Table 6.11 Posterior Statistics of Parameters in Breach diameter of UHSC Panel

Parameter	Mean	Standard deviation	Correlation Coefficient					
			Θ_1	Θ_3	Θ_4	Θ_9	Θ_{10}	σ
Θ_1	-1.5858	0.2775	1.000					
Θ_3	571.9073	132.3403	0.555	1.000				
Θ_4	-3.1731	0.7291	-0.767	-0.648	1.000			
Θ_9	-1.4047	0.3251	-0.748	-0.883	0.615	1.000		
Θ_{10}	1.0064	0.1308	-0.615	-0.288	0.137	0.409	1.000	
σ	0.2864	0.4880	0.037	0.347	-0.224	-0.276	-0.052	1.000

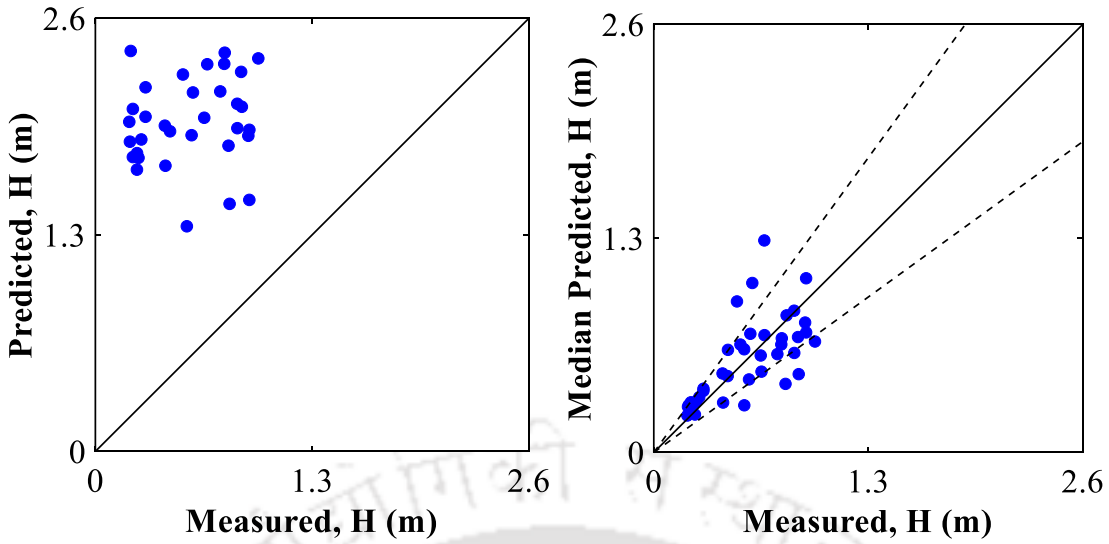

Figure 6.9 Comparison between measured and predicted Breach diameter based on mechanical (left) and probabilistic (right) model for NRC

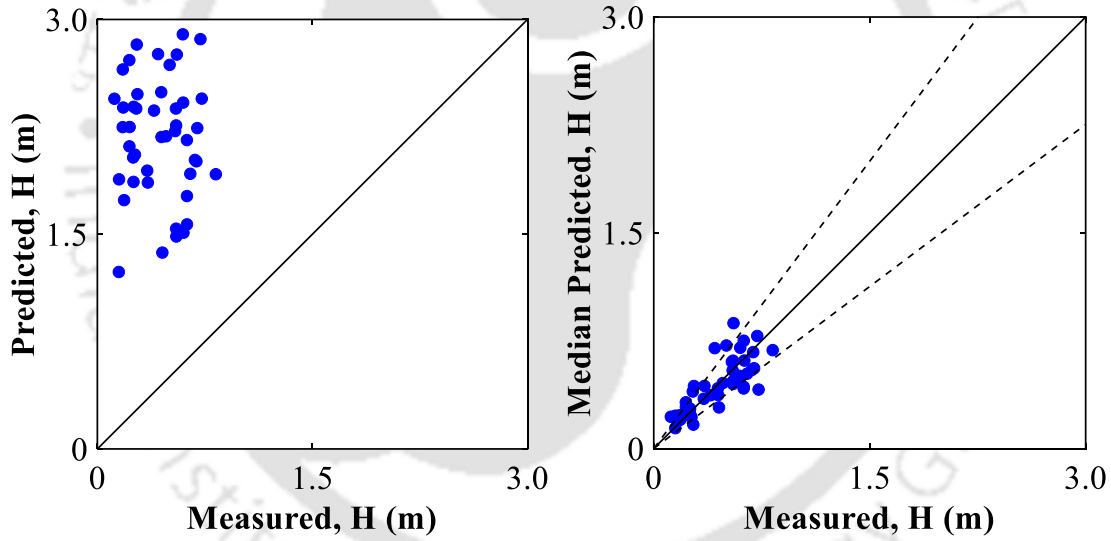

Figure 6.10 Comparison between measured and predicted Breach diameter based on mechanical (left) and probabilistic (right) model for UHSC

Figure 6.9 shows the comparison between the estimation of dynamic demand in terms of Breach diameter formed in the NRC panel based on the proposed mechanical model and the mean predicated of the developed probabilistic model. Figure 6.10 shows the comparison between the estimation of dynamic demand in terms of breach diameter formed in the UHSC panel based on the proposed mechanical model and the mean predicated of the developed

probabilistic model. Majority of data points are lying near to 1:1 line in the mean predicted plot confirms the good fit along with a standard deviation of 0.2077 for NRC and 0.1236 for UHSC panel. The data contains only equality data. The probabilistic model corrects this inherent bias in the model.

6.5 PARAMETER ESTIMATION FOR CAPACITY OF NRC PANEL

6.5.1 Parameter Estimation for Performance Level P1

The most statistically significant explanatory functions for performance level P1 are $h_1(x), h_4(x), h_6(x), h_{10}(x)$ and $h_{12}(x)$. Considered terms accounts for a correction of constant bias, ratio of strength of concrete by strength of steel, ratio of equivalent mass of the slab to the charge weight applied, ratio of charge diameter to panel thickness and energy of panel. The posterior statistics of the model is follows in Table 6.12.

Table 6.12 Posterior Statistics of Parameters in Selected Dynamic Capacity (P1) Model

Parameter	Mean	Standard deviation	Correlation Coefficient					
			Θ_1	Θ_4	Θ_6	Θ_{10}	Θ_{12}	σ
Θ_1	-8.5298	0.7587	1.000					
Θ_4	12.3577	2.0719	-0.849	1.000				
Θ_6	-0.0032	3.86e-4	0.328	-0.336	1.000			
Θ_{10}	2.4962	0.1626	-0.551	0.361	0.434	1.000		
Θ_{12}	1.6808	0.1368	-0.965	0.752	-0.495	0.385	1.000	
σ	0.2417	0.2116	0.040	0.012	0.024	-0.075	-0.066	1.000

Figure 6.11 shows the comparison between the estimation of dynamic capacity at performance level P1 in terms of deformation of NRC panel based on the proposed mechanical

model and the mean of the developed probabilistic model where the mean predication for the dynamic capacity C_{P1}^{NRC} is developed as,

$$C_{P1}^{NRC} = \hat{c}\exp\left[-8.53+12.36\frac{f_c'DIF}{f_y}-0.0032\frac{M_E}{Q}+2.5\frac{d_0}{t}+1.68\log\left(\frac{QQ_0\rho_0}{\rho_c t^3 f_c'}\right)\right] \quad (6.20)$$

Where, C_{P1}^{NRC} = Probabilistic dynamic capacity at performance level P1, $\hat{c}$ = dynamic capacity given by the mechanical model.

The mechanical and probabilistic models are both plotted against the capacity in the terms of deformation of the NRC panel values estimated from the FE simulations. Majority of data points are lying near to 1:1 line. The data contains equality data. The predictions of probabilistic model show that the equality data lies both above and below the 1:1 line. The probabilistic model corrects this inherent bias in the model with a standard deviation of 0.1541.

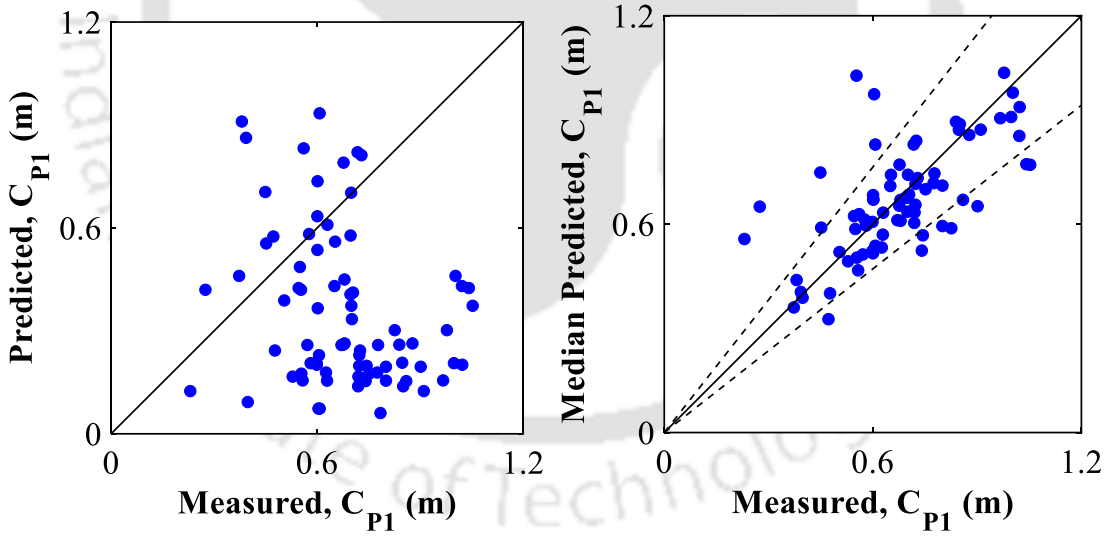

Figure 6.11 Comparison of measured and predicted Dynamic Capacity (P1) of NRC panel based on mechanical (left) and probabilistic (right) model

6.5.2 Parameter Estimation for Performance Level P2

The most statistically significant explanatory functions for performance level P2 are $h_1(x), h_3(x), h_9(x), h_{10}(x)$ and $h_{12}(x)$.Considered terms accounts for a correction of constant bias, the contribution steel reinforcement, ultimate shear stress and allowable shear stress of concrete, ratio of charge diameter to thickness of panel and energy term from contact blast. The posterior statistics of the model is follows in Table 6.13.

Table 6.13 Posterior Statistics of Parameters in Selected Dynamic Capacity (P2) Model

Parameter	Mean	Standard deviation	Correlation Coefficient					
			Θ_1	Θ_3	Θ_9	Θ_{10}	Θ_{12}	σ
Θ_1	-3.5280	0.3473	1.000					
Θ_3	369.6819	123.2198	0.041	1.000				
Θ_9	-0.4773	0.1387	-0.261	-0.874	1.000			
Θ_{10}	1.6655	0.1235	-0.596	-0.056	0.107	1.000		
Θ_{12}	0.8828	0.0681	-0.927	-0.135	0.272	0.325	1.000	
σ	0.1381	1.2166	-0.150	0.148	-0.010	0.247	-0.045	1.000

Figure 6.12 shows the comparison between the estimation of dynamic capacity at performance level P2 in terms of deformation of NRC panel based on the proposed mechanical model and the mean of the developed probabilistic model where the mean predication for the dynamic capacity C_{P2}^{NRC} is developed as,

$$C_{P2}^{NRC} = \hat{c}\exp\left[-3.53+369.68\frac{A_s}{tL}-0.477\frac{\tau_u}{\tau_c}+1.666\frac{d_0}{t}+0.882\log\left(\frac{QQ_0\rho_0}{\rho_c t^3 f_c'}\right)\right] \quad (6.21)$$

Where, C_{P2}^{NRC} = Probabilistic dynamic capacity at performance level P2, $\hat{c}$ = dynamic capacity given by the mechanical model.

The mechanical and probabilistic models are both plotted against the capacity in the terms of deformation of the NRC panel values estimated from the FE simulations. Majority of data points are lying near to 1:1 line. The data contains both equality data and lower bound data. The predictions of probabilistic model show that the equality data lies both above and below the 1:1 line. Whereas, the lower bound data lies to the left of the 1:1 line showing that the achieved damage is less than the predicted. The probabilistic model corrects this inherent bias in the model. The model has a standard deviation of 0.1118.

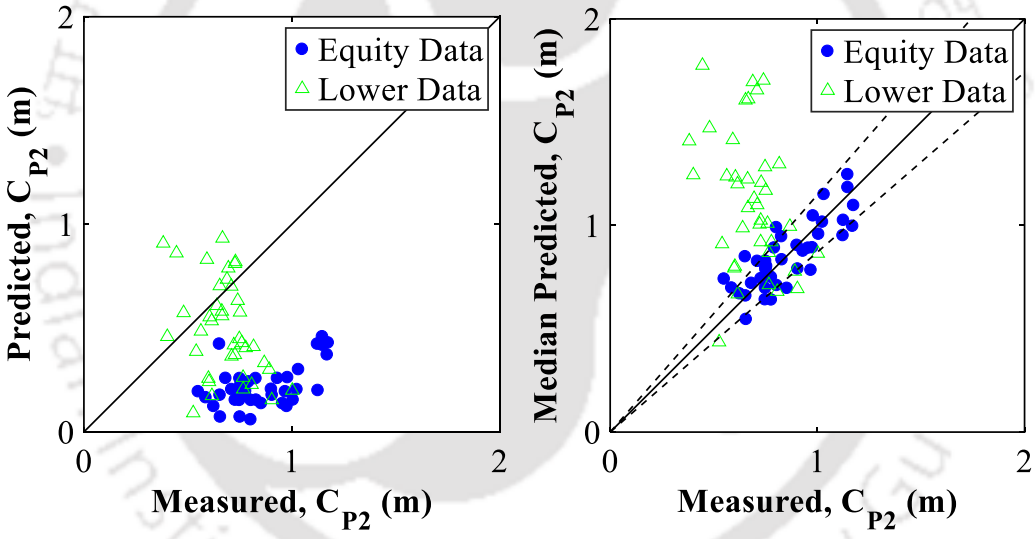

Figure 6.12 Comparison of measured and predicted Dynamic Capacity (P2) of NRC panel based on mechanical (left) and probabilistic (right) model

6.5.3 Parameter Estimation for Performance Level P3

The most statistically significant explanatory functions for performance level P3 are $h_1(x), h_2(x), h_4(x), h_{10}(x)$ and $h_{12}(x)$.Considered terms accounts for a correction of constant bias, slenderness ratio, ratio of concrete compressive strength to yield strength of steel, ratio of

charge diameter to thickness of NRC panel and energy term from contact blast. The posterior statistics of the model is follows in Table 6.14.

Table 6.14 Posterior Statistics of Parameters in Selected Dynamic Capacity (P3) Model

Parameter	Mean	Standard deviation	Correlation Coefficient					
			Θ_1	Θ_2	Θ_4	Θ_{10}	Θ_{12}	σ
Θ_1	-5.2749	0.8207	1.000					
Θ_2	-1.6262	0.8932	-0.590	1.000				
Θ_4	6.7809	2.0624	-0.827	0.378	1.000			
Θ_{10}	1.7211	0.2059	-0.704	0.352	0.476	1.000		
Θ_{12}	1.2131	0.1311	-0.957	0.540	0.735	0.522	1.000	
σ	0.1197	1.7271	-0.175	0.275	-0.031	0.236	0.129	1.000

Figure 6.13 shows the comparison between the estimation of dynamic capacity at performance level P3 in terms of deformation of NRC panel based on the proposed mechanical model and the mean of the developed probabilistic model where the mean predication for the dynamic capacity C_{P3}^{NRC} is developed as,

$$C_{P3}^{NRC} = \hat{c}\exp\left[-5.28-1.626\frac{t}{L}+6.78\frac{f_c' DIF}{f_y}+1.72\frac{d_0}{t}+1.21\log\left(\frac{QQ_0\rho_0}{\rho_c t^3 f_c'}\right)\right] \quad (6.22)$$

Where, C_{P3}^{NRC} = Probabilistic dynamic capacity at performance level P3, $\hat{c}$ = dynamic capacity given by the mechanical model.

The mechanical and probabilistic models are both plotted against the capacity in the terms of deformation of the NRC panel values estimated from the FE simulations. Majority of data points are lying near to 1:1 line. The data contains both equality data and lower bound data. The predictions of probabilistic model show that the equality data lies both above and

below the 1:1 line. The lower bound data, on the other hand, leans to the left of the 1:1 line, indicating that the actual damage is less than projected. The probabilistic model corrects this inherent bias in the model. The model has a standard deviation of 0.1242.

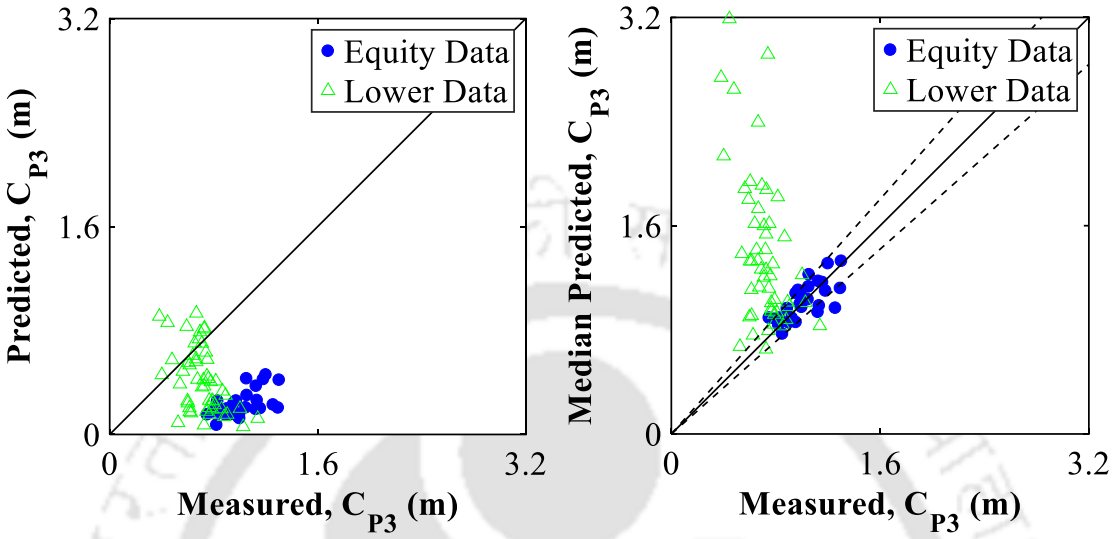

Figure 6.13 Comparison of measured and predicted Dynamic Capacity (P3) of NRC panel based on mechanical (left) and probabilistic (right) model

6.6 PARAMETER ESTIMATION FOR CAPACITY OF UHSC PANELS

6.6.1 Parameter Estimation for Performance Level P1

The most statistically significant explanatory functions for performance level P1 are $h_1(x), h_6(x), h_8(x), h_{10}(x)$ and $h_{12}(x)$. Considered terms accounts for a correction of constant bias, ratio of equivalent mass of the slab to the charge weight applied, concrete cracking strength to yield strength of steel, ratio of charge diameter to panel thickness and energy of panel. The posterior statistics of the model is follows in Table 6.15.

Table 6.15 Posterior Statistics of Parameters in Selected Dynamic Capacity (P1) Model

Parameter	Mean	Standard deviation	Correlation Coefficient					
			Θ_1	Θ_6	Θ_8	Θ_{10}	Θ_{12}	σ
Θ_1	-7.1889	0.5592	1.000					
Θ_6	-0.0033	3.361e-4	0.356	1.000				
Θ_8	109.8621	14.5023	-0.872	-0.434	1.000			
Θ_{10}	1.8183	0.1190	-0.589	0.319	0.286	1.000		
Θ_{12}	1.5404	0.1086	-0.947	-0.500	0.735	0.498	1.000	
σ	0.2159	0.4584	0.208	0.108	-0.168	-0.241	-0.241	1.000

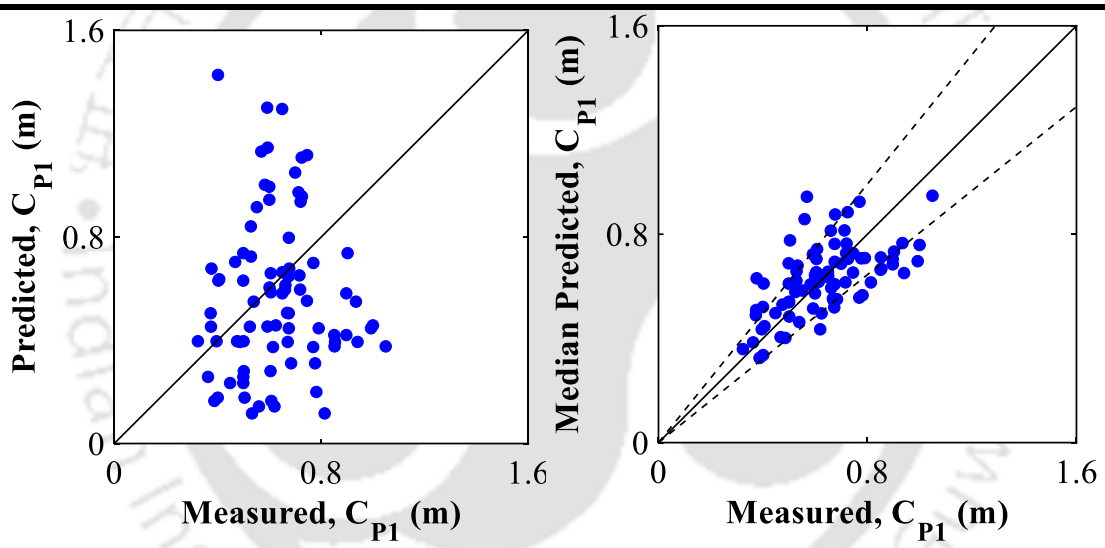

Figure 6.14 Comparison of measured and predicted Dynamic Capacity (P1) of UHSC Panel based on mechanical (left) and probabilistic (right) model

Figure 6.14 shows the comparison between the estimation of dynamic capacity at performance level P1 in terms of deformation of UHSC panel based on the proposed mechanical model and the mean of the developed probabilistic model where the mean predication for the dynamic capacity C_{P1}^{UHSC} is developed as,

$$C_{P1}^{UHSC} = \hat{c}\exp\left[\begin{array}{l} -7.19 - 0.003\dfrac{M_E}{Q} + 109.86\dfrac{f_{cr}DIF}{f_y} \\ +1.82\dfrac{d_0}{t} + 1.54\log\left(\dfrac{QQ_0\rho_0}{\rho_c t^3 f_c'}\right) \end{array}\right] \tag{6.23}$$

Where, C_{P1}^{UHSC} = Probabilistic dynamic capacity at performance level P1, $\hat{c}$ = dynamic capacity given by the mechanical model.

The mechanical and probabilistic models are both plotted against the capacity in the terms of deformation of the NRC panel values estimated from the FE simulations. Majority of data points are lying near to 1:1 line. The data contains equality data. The predictions of probabilistic model show that the equality data lies both above and below the 1:1 line. The probabilistic model corrects this inherent bias in the model with a standard deviation of 0.1377.

6.6.2 Parameter Estimation for Performance Level P2

The most statistically significant explanatory functions for performance level P2 are $h_1(x), h_3(x), h_6(x), h_9(x), h_{10}(x)$ and $h_{12}(x)$.Considered terms accounts for a correction of constant bias, the contribution steel reinforcement, inertia of system, ultimate shear stress and allowable shear stress of concrete, ratio of charge diameter to thickness of panel and energy of panel. The posterior statistics of the model is follows in Table 6.16.

Table 6.16 Posterior Statistics of Parameters in Selected Dynamic Capacity (P2) Model

Parameter	Mean	Standard deviation	Correlation Coefficient						
			Θ_1	Θ_3	Θ_6	Θ_9	Θ_{10}	Θ_{12}	σ
Θ_1	-2.9222	0.2639	1.000						
Θ_3	432.207	49.9664	0.018	1.000					
Θ_6	-0.0031	5.717e-4	-0.074	-0.124	1.000				
Θ_9	-1.1258	0.1305	-0.276	-0.821	0.065	1.000			
Θ_{10}	1.2439	0.1155	-0.682	-0.184	0.668	0.297	1.000		
Θ_{12}	1.0119	0.0673	-0.803	0.147	-0.454	0.013	0.161	1.000	
σ	0.1346	1.2486	-0.348	-0.311	-0.176	0.393	0.077	0.301	1.000

Figure 6.15 shows the comparison between the estimation of dynamic capacity at performance level P2 in terms of deformation of UHSC panel based on the proposed mechanical model and the mean of the developed probabilistic model where the mean predication for the dynamic capacity C_{P2}^{UHSC} is developed as,

$$C_{P2}^{UHSC} = \hat{c}\exp\left[\begin{array}{l} -2.92 + 432.21\dfrac{A_s}{tL} - 0.003\dfrac{M_E}{Q} - 1.13\dfrac{\tau_u}{\tau_c} \\ +1.24\dfrac{d_0}{t} + 1.01\log\left(\dfrac{QQ_0\rho_0}{\rho_c t^3 f_c'}\right) \end{array}\right] \tag{6.24}$$

Where, C_{P2}^{UHSC} = Probabilistic dynamic capacity at performance level P2, $\hat{c}$ = dynamic capacity given by the mechanical model.

The mechanical and probabilistic models are both plotted against the capacity in the terms of deformation of the UHSC panel values estimated from the FE simulations. Majority of data points are lying near to 1:1 line. The data contains both equality data and lower bound data. The predictions of probabilistic model show that the equality data lies both above and below the 1:1 line. The lower bound data, on the other hand, is to the left of the 1:1 line,

indicating that the actual damage is smaller than expected. The probabilistic model corrects this inherent bias in the model. The model has a standard deviation of 0.099.

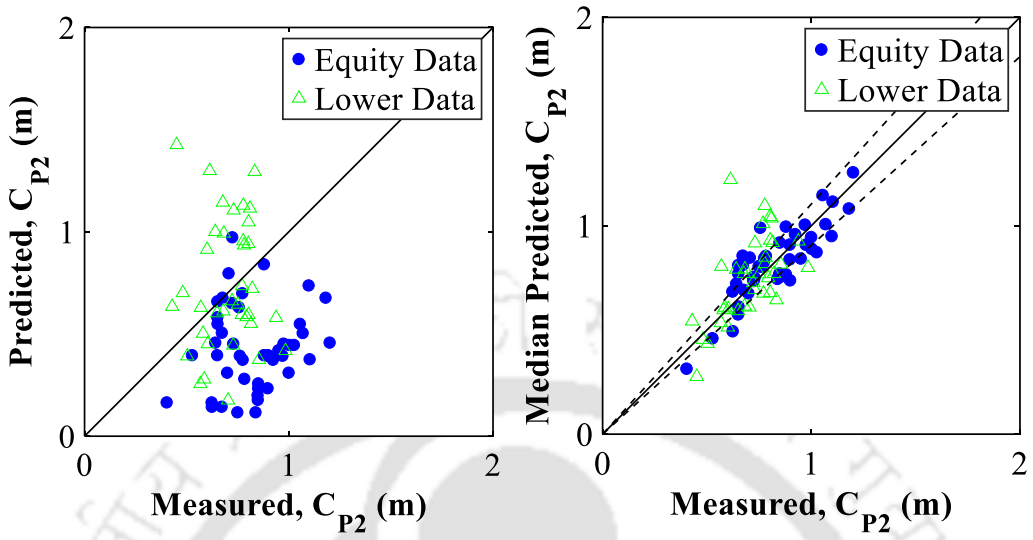

Figure 6.15 Comparison of measured and predicted Dynamic Capacity (P2) of UHSC Panel based on mechanical (left) and probabilistic (right) model

6.6.3 Parameter Estimation for Performance Level P3

The most statistically significant explanatory functions for performance level P3 are $h_1(x), h_5(x), h_{10}(x)$ and $h_{12}(x)$.Considered terms accounts for a correction of constant bias, aspect ratio of charge container, ratio of charge diameter to thickness of panel and energy term. The posterior statistics of the model is follows in Table 6.17.

Figure 6.16 shows the comparison between the estimation of dynamic capacity at performance level P3 in terms of deformation of NRC panel based on the proposed mechanical model and the mean of the developed probabilistic model where the mean predication for the dynamic capacity C_{P3}^{NRC} is developed as,

$$C_{P3}^{NRC} = \hat{c}\exp\left[-1.84 - 0.28\frac{d_0}{h_0} + 1.52\frac{d_0}{t} + 0.68\log\left(\frac{QQ_0\rho_0}{\rho_c t^3 f_c'}\right)\right] \qquad (6.25)$$

Where, C_{P3}^{NRC} = Probabilistic dynamic capacity at performance level P3, $\hat{c}$ = dynamic capacity given by the mechanical model.

Table 6.17 Posterior Statistics of Parameters in Selected Dynamic Capacity (P3) Model

Parameter	Mean	Standard deviation	Correlation Coefficient				
			Θ_1	Θ_5	Θ_{10}	Θ_{12}	σ
Θ_1	-1.8381	0.2516	1.000				
Θ_5	-0.2825	0.0382	-0.700	1.000			
Θ_{10}	1.5170	0.0830	-0.467	-0.112	1.000		
Θ_{12}	0.6770	0.0568	-0.914	0.627	0.192	1.000	
σ	0.0764	2.1415	-0.480	0.263	0.326	0.370	1.000

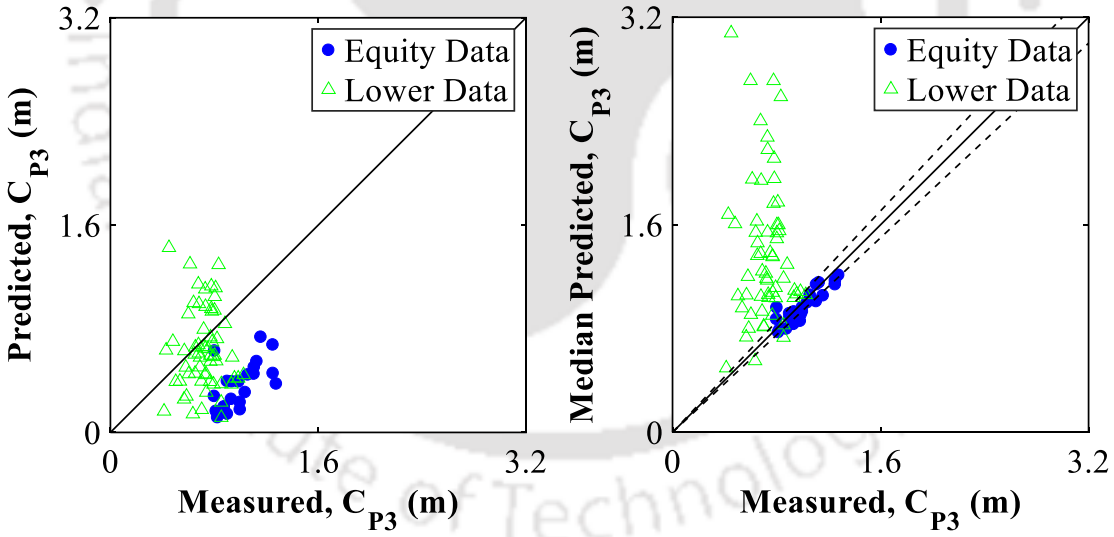

Figure 6.16 Comparison of measured and predicted Dynamic Capacity (P3) of UHSC Panel based on mechanical (left) and probabilistic (right) model

The mechanical and probabilistic models are both plotted against the capacity in the terms of deformation of the NRC panel values estimated from the FE simulations. Majority of data points are lying near to 1:1 line. The data contains both equality data and lower bound

data. The predictions of probabilistic model show that the equality data lies both above and below the 1:1 line. The probabilistic model corrects this inherent bias in the model. The model has a standard deviation of 0.0647.

6.7 FRAGILITY ESTIMATES

The fragility assessments provide an estimate of the structure's reliability when contact blast load demand on the NRC and UHSC panels varies. It also shows how the different performance levels respond to changes in the demand placed on the panel. The fragility analysis calculates the panel's susceptibility based on the fluctuation in demand exerted on the panels. The fragility of the panels subjected to different contact blast loadings is formulated similar to equation (5.18) in the previous chapter. The fragility of contact blast load on NRC and UHSC panel is estimated based on varying the demand on the panel in terms of crater diameter formed. One NRC and UHSC panel from FE simulation are selected for producing the fragility curves as they represent the same capacity and demand ratio as the adopted validation. The properties and configuration of the selected panels are shown in Table 6.18.

Table 6.18 Configuration and Dimensions of Panels for Fragility Estimate

Name of Configuration	Symbol	Dimensions of Panel	
		NRC	UHSC
Length of Panel (square)	L	4.117 m	3.860 m
Thickness of Concrete Panel	t	0.202 m	0.253 m
Weight of Charge	Q	8 kg	9.86 kg
Compressive Strength	f_c'	25 MPa	136 MPa
Yield Stress of Rebars	f_y	550 MPa	500 MPa
Diameter of Rebar	-	0.016 m	0.016 m
Area of Rebars	-	0.000840 m^2	0.001070 m^2

Figure 6.19 illustrates the fragility estimates of the NRC panel subjected to contact blast for the three performance levels, while Figure 6.20 depicts the fragility estimates of the UHSC panel subjected to contact blast for the three performance levels. The fragility estimate is directly conditioned on the normalized crater diameter demand. The P1 performance level is represented by a crossed solid line. Performance level P2 is shown by a dashed line with a plus marker, whereas performance level P3 is indicated by a dashed line with a circle marker. The graph also includes color-coded 15 percent and 85 percent confidence boundaries for each performance level fill (Gardoni et al. 2002). The curve for performance level P3 is the least steep because obtaining a condition of collapse necessitates more crater diameter as demand. The normalized dynamic crater diameter demand of the NRC panel is 0.5309 and for UHSC is 0.4376 as obtained from simulation. At this value, both the panel and performance levels P1, P2, and P3 have a failure chance of 1.0. The NRC and UHSC panels are at damage condition D4, as shown in Figure 6.17 and 6.18.

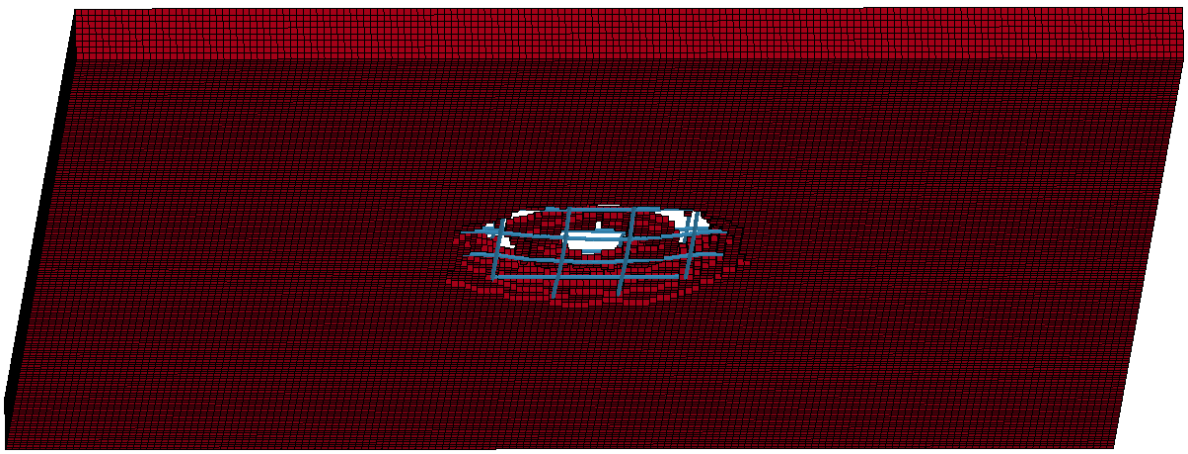

Figure 6.17 NRC Panel achieving damage state D4.

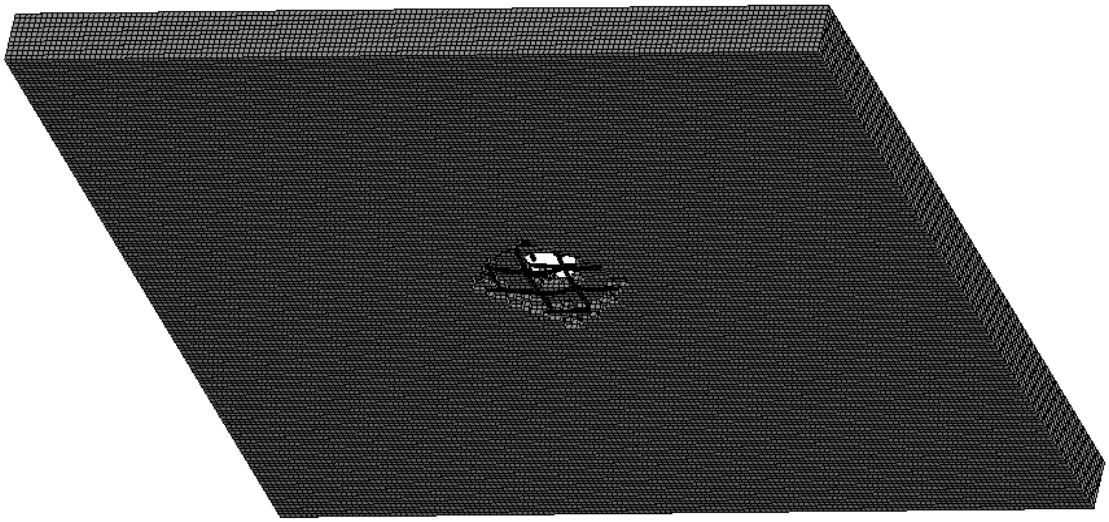

Figure 6.18 UHSC Panel achieving damage state D4.

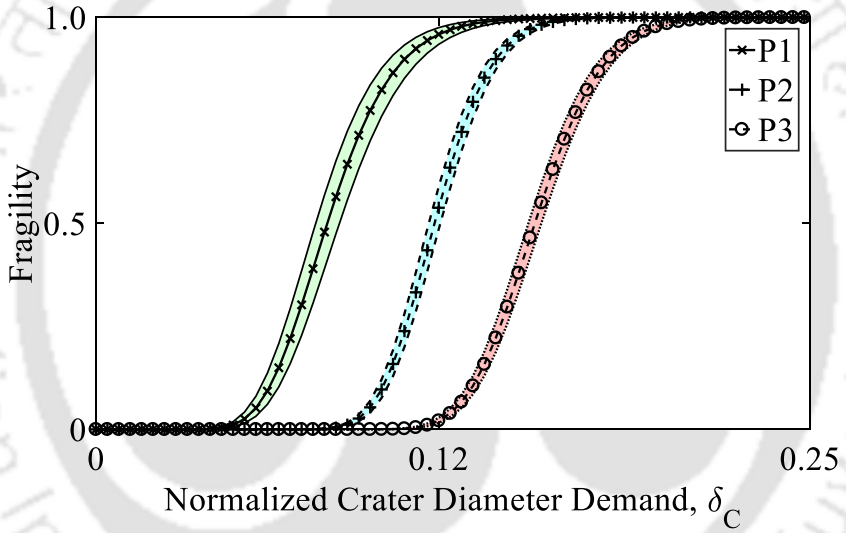

Figure 6.19 Fragility curves for NRC Panel for P1, P2 and P3.

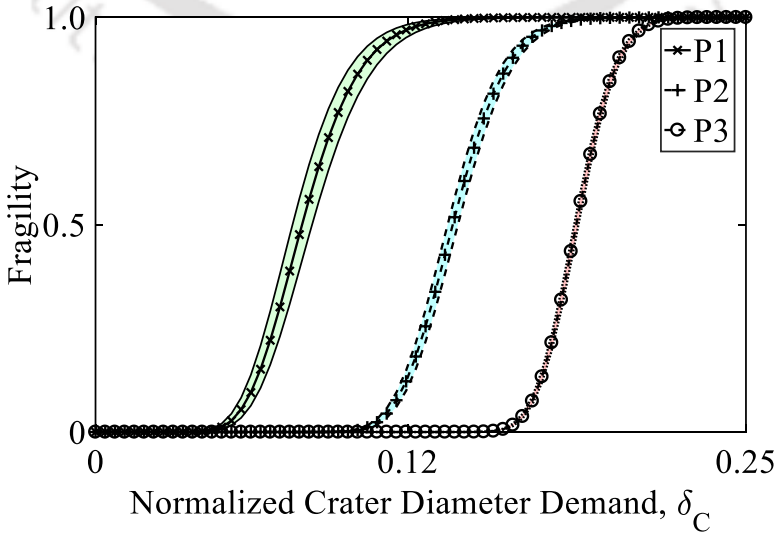

Figure 6.20 Fragility curves for UHSC Panel for P1, P2 and P3

The panel fails due to the contact blast loading which is reflected by the state of the panels being in damage state 4 and probability of failure of all performance levels being 1. This establishes the validity of the developed models for P1, P2, and P3 and the framework to estimate the reliability of both the NRC and UHSC panel.

6.8 PARAMETER ESTIMATION FOR DEMAND ON NRC PANEL

The most statistically significant explanatory functions for demand model of contact blast is $h_1(x), h_3(x), h_5(x), h_9(x)$ and $h_{12}(x)$ as given in Table 6.1. These considered terms accounts for a correction of constant bias, reinforcement ratio, aspect ratio of TNT container, ultimate shear stress and allowable shear stress of concrete and energy of NRC panel. The posterior statistics of the model is follows in Table 6.2 for NRC Panel. The equation to estimate the probabilistic Crater diameter of NRC Panel subject to contact blast loading after the probabilistic analysis can be given as,

$$C_D^{NRC} = \hat{c}_D \exp\left[-2.41 + 118.25\frac{A_s}{tL} + 0.234\frac{d_0}{h_0} - 0.222\frac{\tau_u}{\tau_c} + 0.352\log\left(\frac{QQ_0\rho_0}{\rho_c t^3 f_c'}\right)\right] \quad (6.26)$$

Where, C_D^{NRC} = Probabilistic maximum crater diameter of the panels occurred due to contact blast loading, $\hat{C}_D$ = Maximum crater diameter of the panels due to contact blast from mechanical model.

6.9 PARAMETER ESTIMATION FOR DEMAND ON UHSC PANEL

The most statistically significant explanatory functions for deman model of contact blast is $h_1(x), h_4(x)$ and $h_5(x)$ as given in Table 6.1. These considered terms accounts for a correction of constant bias, ratio of strength of concrete by strength of steel and aspect ratio of TNT container. The posterior statistics of the model is follows in Table 6.3 for UHSC Panel.

The equation to estimate the probabilistic Crater diameter of UHSC Panel subject to contact blast loading after the probabilistic analysis can be given as,

$$C_D^{UHSC} = \hat{c}_D \exp\left[-0.4132 - 0.7487\frac{f_c' DIF}{f_y} - 0.0879\frac{d_0}{h_0}\right] \tag{6.27}$$

Where, C_D^{UHSC} = Probabilistic maximum crater diameter of the panels occurred due to contact blast loading on UHSC Panel, $\hat{c}_D$ = Maximum crater diameter of the panels due to contact blast from mechanical model.

6.10 DISCUSSION

In this Chapter, development of capacity and demand model based on deformation, i.e., crater formation formulation for NRC and UHSC panels subject to contact blast is achieved. The probabilistic capacity and demand model captures the dynamic behaviour of the panels and accounts for the associated uncertainties of a contact blast. The developed probabilistic capacity models accurately estimate the capacity of the panels at the specified performance level and probabilistic demand models accurately evaluates the demand on the panels for the contact blast. These capacity and demand models are based on probabilistic-based design of NRC and UHSC panel under contact blast.

The developed models improve the design behaviour of NRC and UHSC panels subject to contact blast at the different performance stages which is the novelty of this research. The model is easy to use and can be adopted to develop reliability based design of safer slabs with the reliability based design approach. This work can be extended to other structural members under similar loading conditions. A framework for fragility assessment of the panel subjected to contact blast is developed in the next chapter.

Chapter 7. FRAGILITY ESTIMATES

7.1 GENERAL

Based on the variation of the demand imposed on the panels, the fragility analysis gives an estimate of the vulnerability of the panel. The fragility of the panels subjected to different blast loadings is formulated as

$$F(x,\theta) = P\left[g(x,\theta) \le 0 \middle| Q_0, R \right] \tag{7.1}$$

where, $g_{p_i}(x,\theta)$ is the limit state function defined as,

$$g_{p_i}(x,\theta) = P_{p_i}(x,\theta) - P_D \tag{7.2}$$

and $i = 1,2,3$, for all three performance levels. The performance-based probabilistic models for the performance levels are developed in Chapter 5 and Chapter 6.

7.2 FRAGILITY ESTIMATES FOR AIR BLAST

The fragility of blast load on NRC and UHSC panel is estimated based on varying the scaled distance Z For developing the fragility curves, one NRC and UHSC panel from FE simulation were selected such that they represent the same ratio of capacity and demand as in the adopted validation. The properties and configuration of the selected panels are shown in

Table 5.8. The NRC panel at Performance level P1, P2 and P3 are depicted through Figure 7.1, 7.2 and 7.3 respectively. Figure 7.4, 7.5 and 7.6 show the NRC panel at Performance Levels P1, P2, and P3, respectively.

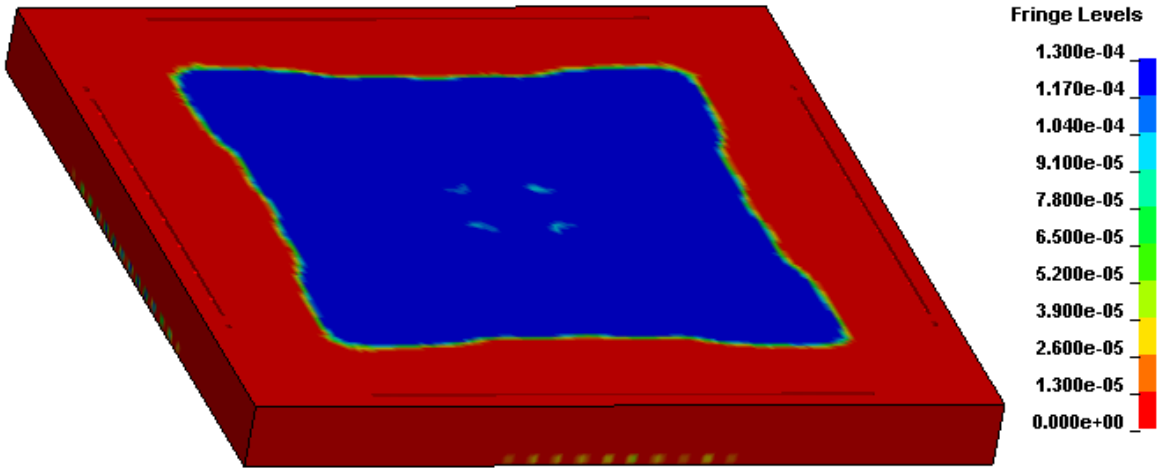

Figure 7.1 NRC Panel as the concrete reaches cracking strain (Performance level – P1)

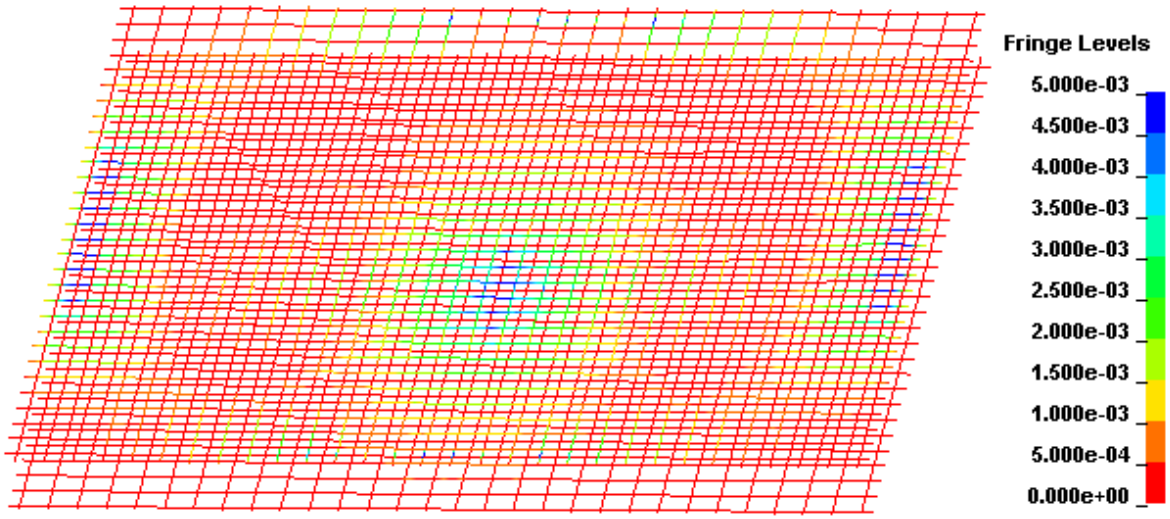

Figure 7.2 NRC Panel as the steel reaches yielding strain (Performance level – P2)

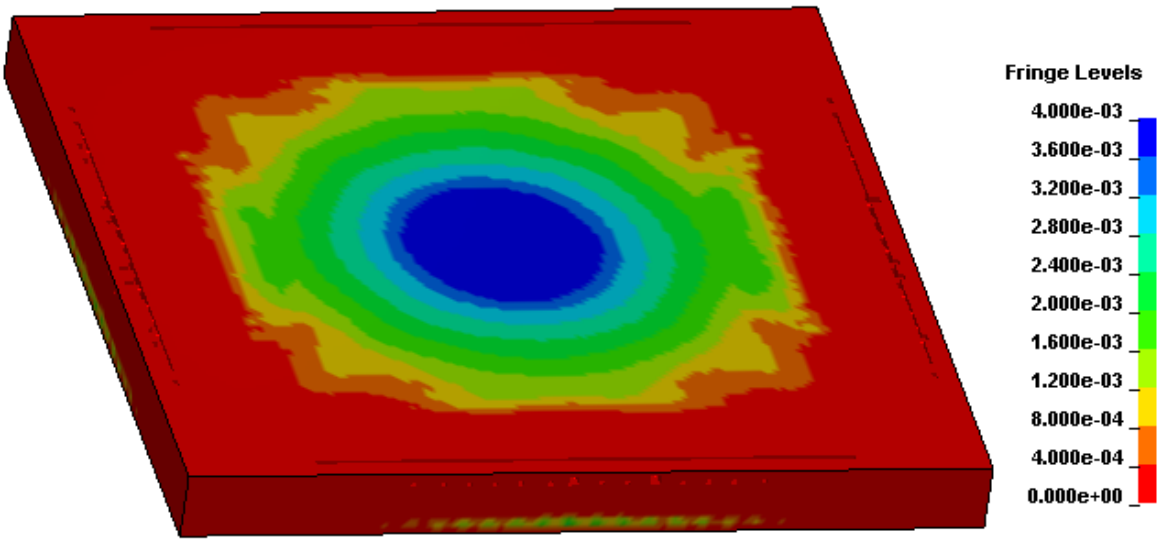

Figure 7.3 NRC Panel as the concrete reaches crushing strain (Performance level – P3)

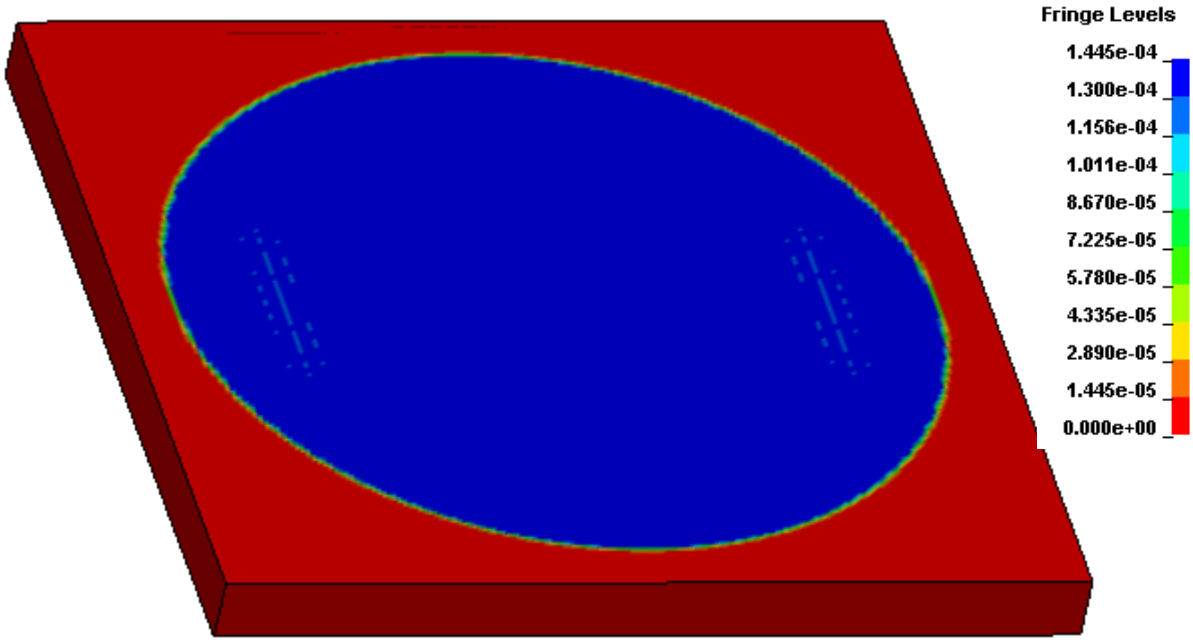

Figure 7.4 UHSC Panel as the concrete reaches cracking strain (Performance level – P1)

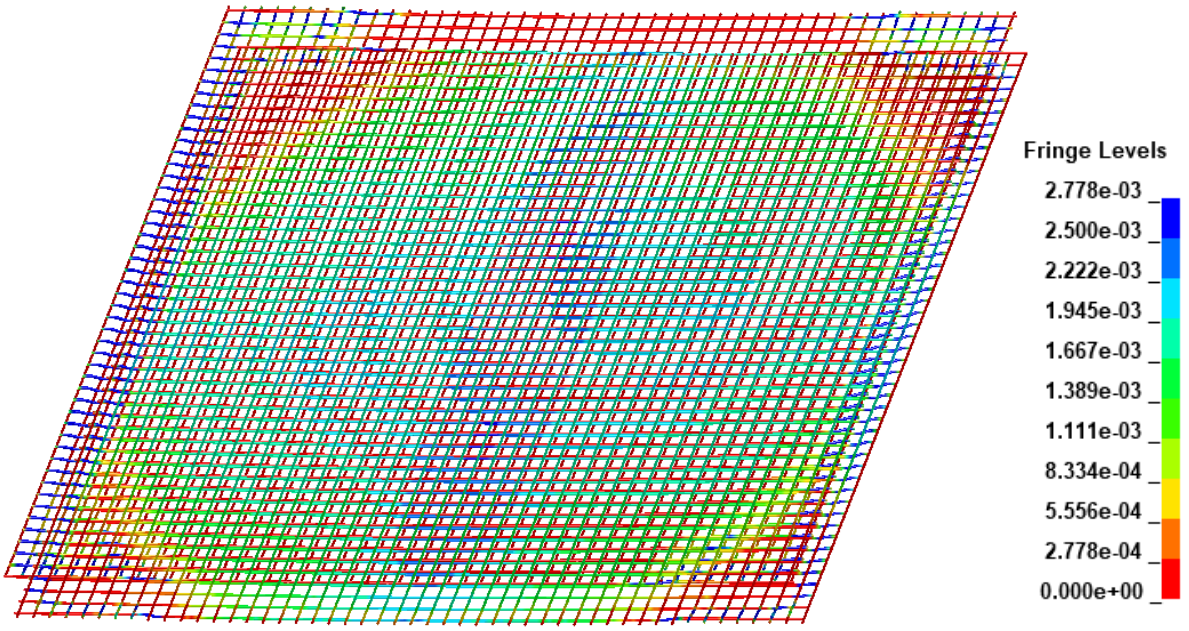

Figure 7.5 UHSC Panel as the steel reaches yielding strain (Performance level – P2)

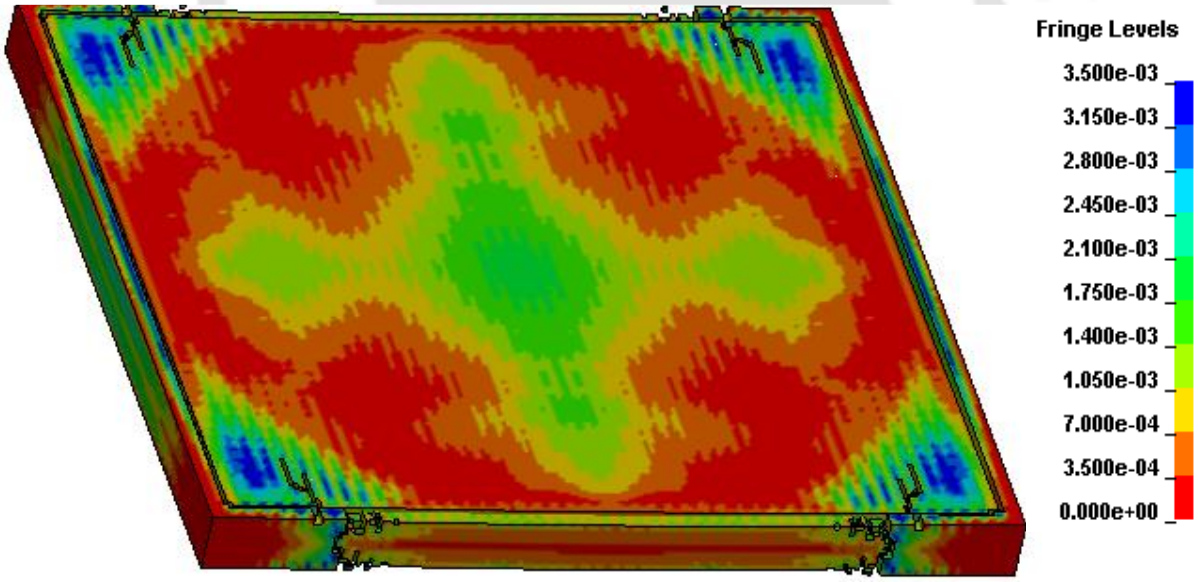

Figure 7.6 UHSC Panel as the concrete reaches crushing strain (Performance level – P3)

Figure 7.7 shows the fragility estimates of the NRC panel and UHSC panel for performance levels, (P1, P2 and P3) and the plot shows the fragility variation upon the domain of the scaled distance, Z. The plot is in normal scale which comprises of scaled distance range on x-axis and probability of failure upon y-axis. The P1 performance level is represented by a

solid line. Performance level P2 is shown by a dashed line, and performance level P3 is indicated by a dotted line. The graph also includes color-coded 15% and 85% confidence boundaries for each filled performance level (Gardoni et al. 2002).

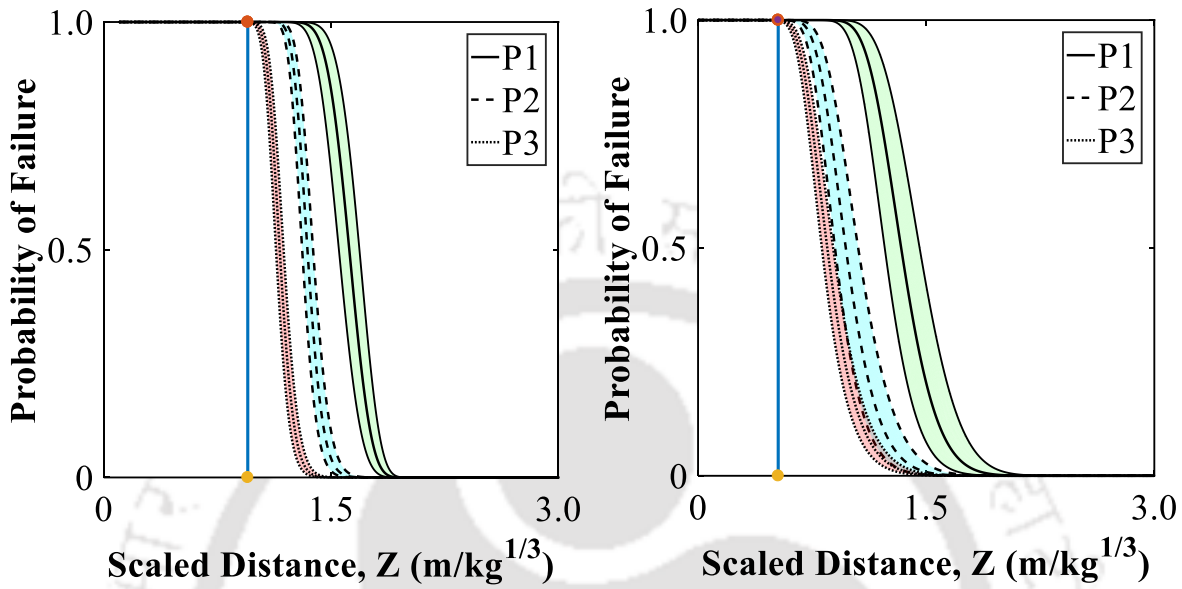

Figure 7.7 Contour plot showing the Fragility estimate for Air blast on NRC panel (left) and UHSC Panel (right) for Performance level P1, P2 and P3

From both the graphs of Figure 7.7, we can state that at any value of Z, the probability of achieving P1 level is more than that of P2 and P3. Moreover, with an increase in scaled distance the demand imposed is less and so is the probability of failure. The exceedance of performance level P1 is achieved with lower value of demand imposed, confirming to the result of the FE simulation where the exceedance of performance level P1 is achieved. The exceedance of performance level P2 is achieved with higher value of demand imposed as compared to performance level P1. Confirming to the result of Fragility as 1, with the FE simulation, the exceedance of performance level P2 is attained. The exceedance of performance level P3 is achieved with highest value of demand imposed as compared to performance level (P1) and performance level (P2) which confirms to the result of Fragility as 1, in the FE simulation as well, the exceedance of performance level P3 is achieved. This establishes the

validity of the developed FE models (Figure 7.1, 7.2 and 7.3) and probabilistic models for P1, P2, and P3 (Figure 7.7 (left)) and the framework to estimate the reliability of the NRC panel of protective structures subject to air blast. Figure 7.7 (right), also depicts that for the adopted Z of UHSC panel, all the performance are achieved levels as shown in Figure 7.4, 7.5 7.6; establishing the credibility of the proposed model.

7.3 FRAGILITY ESTIMATES FOR CONTACT BLAST

Here, the fragility of blast load on NRC and UHSC panel is estimated based on varying the charge weight Q. For developing the fragility curves, one NRC and UHSC panel from FE simulation were selected such that they represent the same ratio of capacity and demand as in the adopted validation. The properties and configuration of the selected panels are shown in Table 6.18. The NRC panels at Performance level P1, P2 and P3 due to contact blast are depicted through Figure 7.8, 7.9 and 7.10 respectively. Figure 7.11, 7.12 and 7.13 shows the UHSC panels at Performance levels P1, P2, and P3 under contact blast.

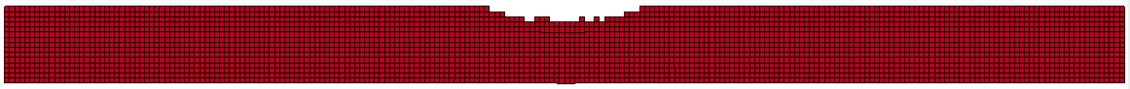

Figure 7.8 NRC Panel as the concrete spalling starts from bottom (Performance level – P1)

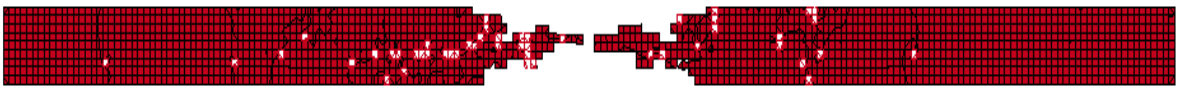

Figure 7.9 NRC Panel on the onset of Perforation (Performance level – P2)

Figure 7.10 NRC Panel reaches Punching failure (Performance level – P3)

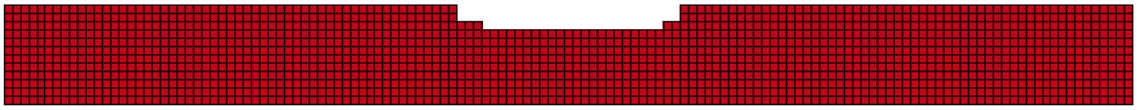

Figure 7.11 UHSC Panel as the concrete spalling starts from bottom (Performance level – P1)

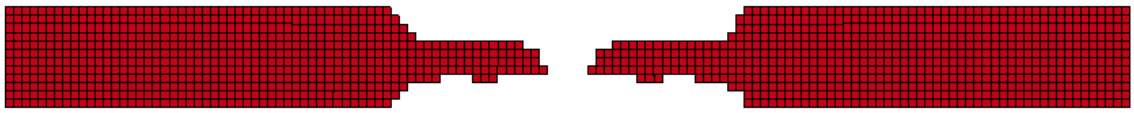

Figure 7.12 UHSC Panel on the onset of Perforation (Performance level – P2)

Figure 7.13 UHSC Panel reaches Punching failure (Performance level – P3)

Figure 7.14 shows the fragility estimates in terms of contour plot of the NRC and UHSC panel for performance level, P1, P2 and P3; for 8 kg-TNT and 9.86 kg-TNT respectively. The plot is in normal scale which comprises of charge weight (kg-TNT) range on x-axis and probability of failure upon y-axis. The plot shows the fragility variation upon the domain of the weight. A solid line represents the P1 performance level. A dashed line denotes performance level P2, whereas a dotted line denotes performance level P3. For each filled performance level, the graph additionally displays color-coded 15 percent and 85 percent confidence level (Gardoni et al. 2002). From Figure 7.14, we can state that at any value of Q, the probability of achieving P1 level is more than that of P2 and P3. Moreover, with an increase in charge weight the demand imposed is more and so is the probability of failure. The exceedance of performance level P1 is achieved with lower value of demand imposed, confirming to the result of the FE simulation where the exceedance of performance level P1 is achieved. The exceedance of performance level P2 is achieved with higher value of demand imposed as compared to performance level P1. Confirming to the result of Fragility as 1, with the FE simulation, the exceedance of performance level P2 is attained. The exceedance of performance level P3 is

achieved with highest value of demand imposed as compared to performance level (P1) and performance level (P2) which confirms to the result of Fragility as 1, in the FE simulation as well, the exceedance of performance level P3 is achieved. This establishes the validity of the proposed FE models (Figure 7.8, 7.9 and 7.10) as well as the framework for estimating the reliability of the NRC panel of protective structures due to contact blast (Figure 7.14 (left)). Figure 7.14 (right) further shows that for the adopted charge mass of UHSC panel, all performance levels are reached, as demonstrated in Figure 7.11, 7.12, and 7.13; supporting the proposed model's validity.

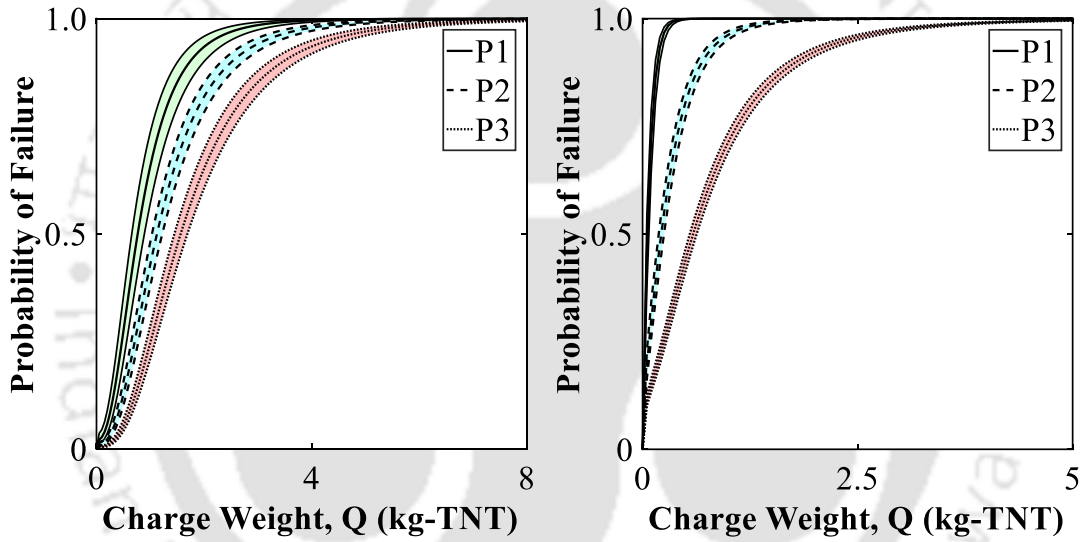

Figure 7.14 Contour plot showing the Fragility estimate for contact blast on the NRC panel (left) and UHSC Panel (right) for Performance level P1, P2 and P3

7.4 DISCUSSION

This chapter shows the framework to evaluate the fragility of NRC Panels subjected to air and contact blast based on developed performance-based capacity and demand models. Accurate estimate of fragility is provided in this framework. Performance and evaluation of the survival of structure for a given scenario can be determined using this performance-based fragility estimation. Realistic loading and structural configurations scenarios are considered in this

research for evaluation of response and development of the capacity and demand models. The developed models can be used to design protective structures using NRC and UHSC panels under air and contact blast scenarios. The next chapter, a reliability-based code calibration developed with the help of all the numerical results, obtained for all the panel types subjected to air and contact blast load are presented.

Chapter 8. RELIABILITY-BASED CODE CALIBRATION FOR PANELS

8.1 GENERAL

The performance-based capacity and demand models developed in previous sections are used to calibrate the load and resistance factors for the panels subject to the blast loading. The structural reliability is expressed as a margin of safety, or as a limit state function, Z

$$Z = R - Q \tag{8.1}$$

where, R = Resistance or capacity of the structure and, Q = maximum load imposed on the structure within its design life. The probability of structure failure, P_f limit state excess when $Z \le 0$, can be calculated by an integral convolution

$$P_f = P_r(Z \le 0) = \int_0^\infty F_R(x)\, f_q(x)\, dx = 1 - R = \Phi(-\beta), \tag{8.2}$$

where, R = Reliability of the structure, Φ = CDF of standard normal distribution, β = reliability index, F_R = CDF of the resistance and, f_q = PDF of the load effect.

This section presents a code calibration for the panels to arrive at a load and resistance factor. The hazard curve for the mass of the charge and the stand-off distance from the protective structure where these panels are used as building blocks are developed which are adopted for estimating the total probability of the failure or survival of the protective structures subject to the blast loading.

8.2 CODE CALIBRATION

The performance-based resistance and demand models developed in this study is used for the code calibration to estimate the load and resistance factors for panels of protective structure subject to blast loading. Currently, a load factor of 1.0 to 1.2 for structure under blast load is adopted. The load factor is calculated for all the limit state. So, using the performance-based models developed in this research load and resistance factors for other limit states are proposed. The equation for the load and resistance factor design corresponding to the three performance levels P1, P2, and P3 is given by

$$\phi P_{Pin} \geq \gamma P_{Dn} \qquad \text{Pi=P1,P2,P3} \tag{8.3}$$

The limit state for the three performance levels is given by

$$g_{pi} = \frac{P_{Pi}}{\phi P_{Pin}} - \frac{P_D}{\gamma P_{Dn}} \tag{8.4}$$

where, P_{Pi} = dynamic capacity for performance level P_i, P_{Pin} = nominal value of dynamic capacity for performance level P_i, ϕ = resistance factor, P_D = dynamic demand, P_{Dn} = nominal value of dynamic demand and γ = demand factor.

8.2.1 Code Calibration for Air Blast

The load and resistant factors are based on the reliability plots of NRC and UHSC panels at the different performance level when the event occurs as shown in Figure 8.1 and 8.2 respectively. These plots demonstrate for explosions with larger mass placed in a close range, the probability of failure is more than that of an explosion with smaller mass placed in far range. Moreover, the NRC panel shows more failure probability as compared to the UHSC panels for the same blast scenario. A parametric study on the variation of the reliability index β with load and

resistance factors, γ and ϕ respectively was performed for the adopted limit states. As per ISO 2394 (1998), an annual target reliability β = 4.4 is recommended for ultimate limit state corresponding to moderate magnitudes of failure and medium safety cost (Stewart and Li 2021). This research considers the three performance level which ensures that the ultimate limit states of failure is not attained. Considering the soundness of design and the cost factor for design, a lower reliability index is selected for the performance levels. The value of the target reliability index was kept at 3.0 for all the performance levels in both NRC and UHSC panel which corresponds to a probability of failure of 1.3×10^{-3} of the structure when the event occurs. The statistics for the models is given in Table 8.1, where the COV of the predicted model developed in the earlier sections were considered for the three performance levels and demand model.

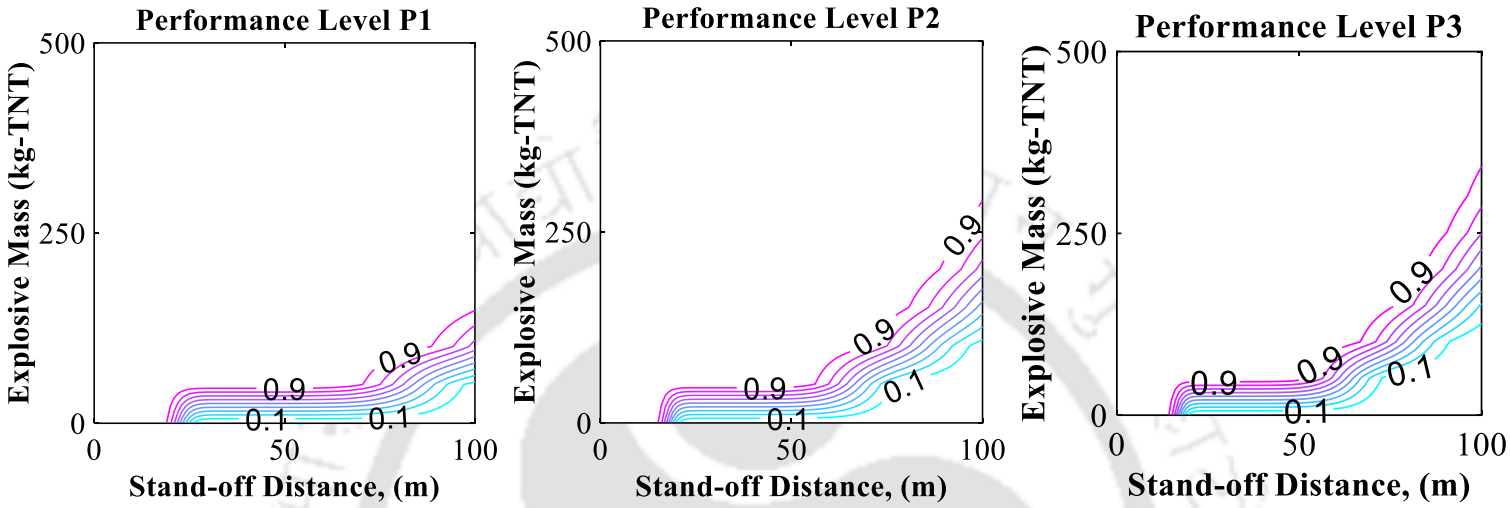

Figure 8.1 Reliability plots of NRC panel subject to air blast for all Performance Levels

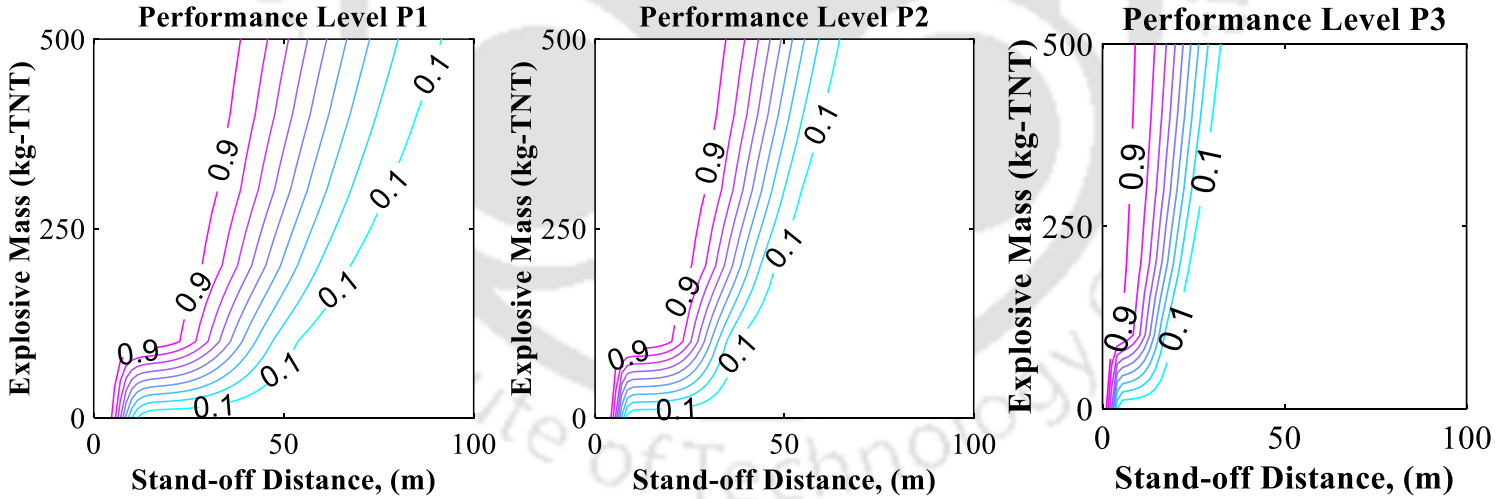

Figure 8.2 Reliability plots of UHSC panel subject to air blast for all Performance Levels

Table 8.1 Statistical Information and Proposed Load resistance factors for Air Blast

Limit state for	Statistical Information of the Models			Proposed load and resistance factors			
	Mean to Nominal	COV		β	ϕ	γ	
		NRC	UHSC			NRC	UHSC
P1	1.00	0.5928	0.6206	3.0	0.6	2.38	2.23
P2	1.00	0.4551	0.4639	3.0	0.6	1.90	1.65
P3	1.00	0.3482	0.2408	3.0	0.6	1.73	1.38
D	1.00	0.6521	0.5755	-	-	-	-

Table 8.1 lists the load and resistance factors for both NRC and UHSC panel obtained from the code calibration. Figure 8.3 and 8.4 demonstrates the variation of reliability index with load and resistance factors for all performance levels for NRC and UHSC panels respectively. From the three curves with varying values of the resistance factor, it can be said that increasing ϕ results in decrease of β value. A value of 2.38, 1.90 and 1.73 are chosen as load factor for P1, P2 and P3 respectively, corresponding to 0.6 value of resistance factor for the reliability index of 3.0 for NRC panel of protective structures. A consistent value of 0.6 is adopted for the resistance factor for all the three limit states of UHSC panel as well. For the UHSC panels of protective structures, the value of load factors is adopted as 2.23, 1.65 and 1.38 respectively for the limit states corresponding to performance levels P1, P2, and P3. It is evident that larger load factors are attributed due to the variation in the prediction of the capacity for the NRC panels.

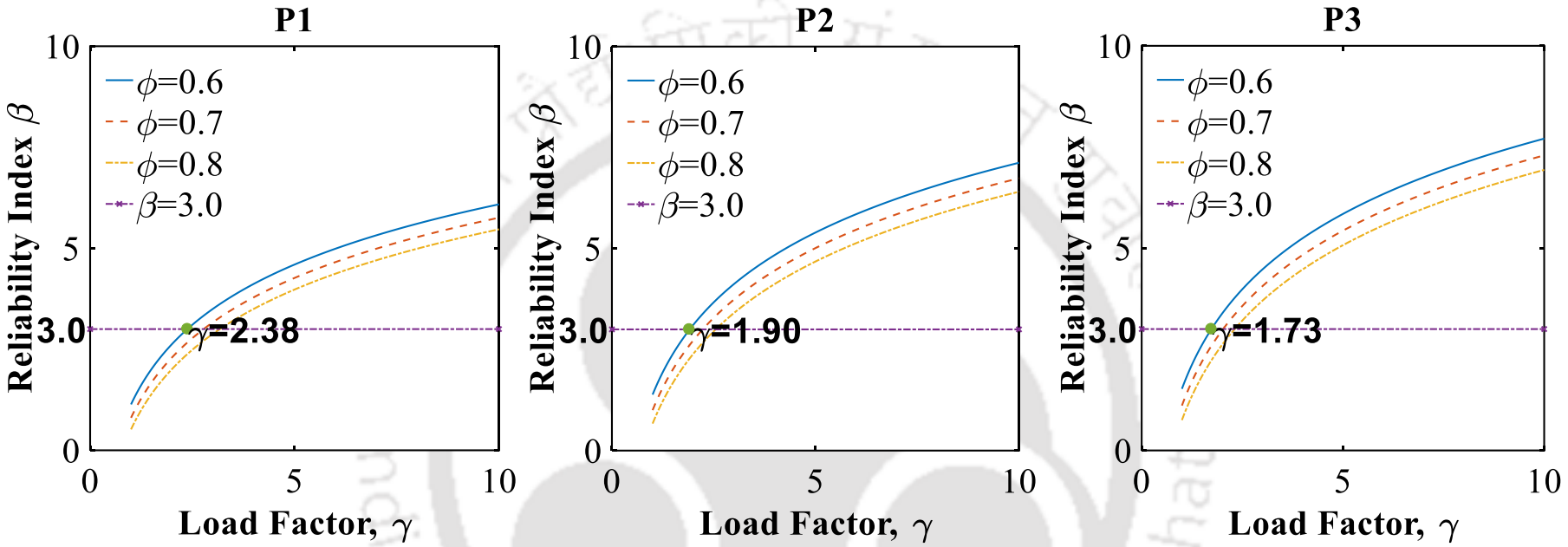

Figure 8.3 Plot of Reliability Index and Load Factor for all Performance Levels of NRC panel

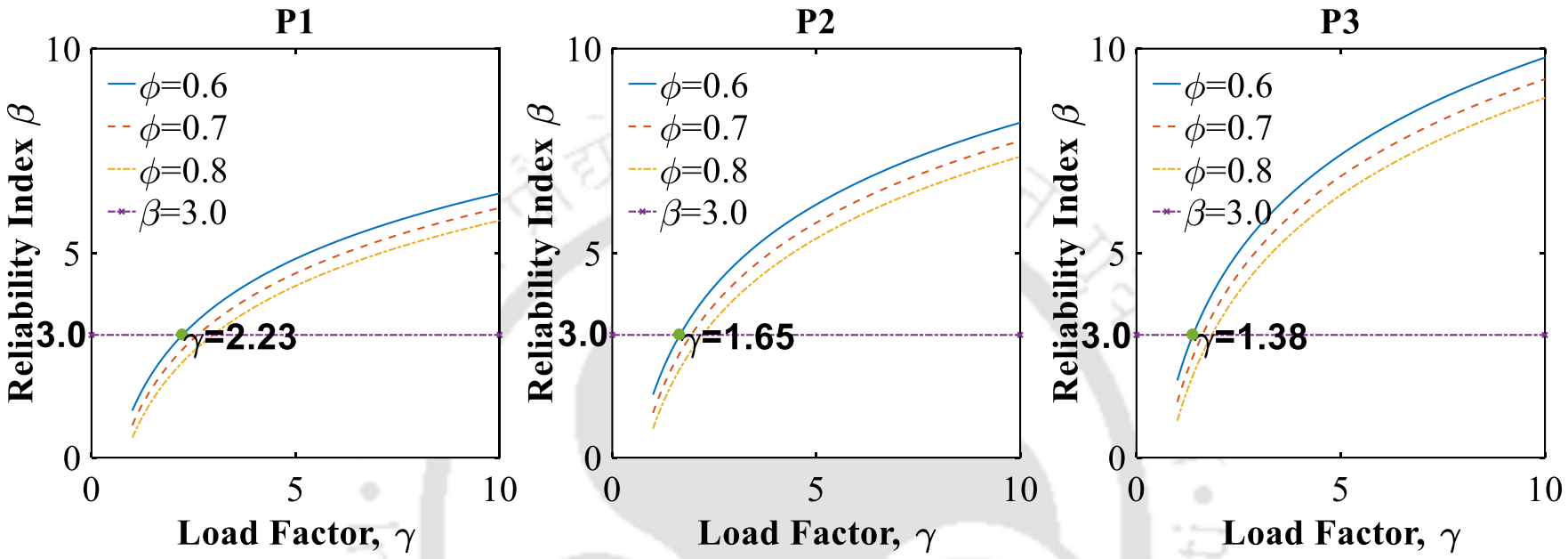

Figure 8.4 Plot of Reliability Index and Load Factor for all Performance Levels of UHSC panel

8.2.2 Code Calibration for Contact Blast

The load and resistant factors are based on the reliability plots of NRC and UHSC panels at the different performance level when the event occurs. According to ISO 2394 (1998), for ultimate limit states with moderate magnitudes of failure and medium safety costs, an annual target reliability = 4.4 is proposed (Stewart and Li 2021). The three performance levels considered in this study is not achieving the ultimate limit states of failure. A lower reliability index is chosen for the performance levels, taking into account the soundness of the design and the cost factor for design. In both the NRC and UHSC panels, the target reliability index is kept at 3.0 for all performance levels, corresponding to the failure probability of $1.3x10^{-3}$ when the event occurs. The statistics for the models is given in Table 8.1, where the COV of the predicted model developed in the earlier sections were considered for the three performance levels and demand model. A parametric study on the variation of the reliability index β with load and resistance factors, γ and ϕ respectively was performed for the adopted limit states. Considering the soundness of design and the cost factor for design, a lower reliability index is selected for the performance levels. The value of the target reliability index was kept at 3.0 for all the performance levels in both NRC and UHSC panel.

Table 8.2 Statistical Information and Proposed Load resistance factors for the Contact Blast

Limit state for	Statistical Information of the Models			Proposed load and resistance factors			
	Mean to Nominal	COV		β	ϕ	γ	
		NRC	UHSC			NRC	UHSC
P1	1.00	0.2264	0.2912	3.0	0.8	2.13	1.82
P2	1.00	0.1307	0.2098	3.0	0.8	1.43	1.23
P3	1.00	0.1215	0.1913	3.0	0.8	1.36	1.08
D	1.00	0.1307	0.0879	-	-	-	-

Table 8.2 lists the load and resistance factors for both NRC and UHSC panel obtained from the code calibration for contact blast loading. Figure 8.5 and 8.6 demonstrates the variation of reliability index with load and resistance factors for all performance levels for NRC and UHSC panels respectively. From the three curves with varying values of the resistance factor, it can be said that increasing ϕ results in decrease of β value. A value of 2.13, 1.43 and 1.36 are chosen as load factor for P1, P2 and P3 respectively, corresponding to 0.8 value of resistance factor for the reliability index of 3.0 for NRC panel of protective structures. A consistent value of 0.8 is adopted for the resistance factor for all the three limit states of UHSC panel under contact blast as well. For the UHSC panels of protective structures, the value of load factors is adopted as 1.82, 1.23 and 1.08 respectively for the limit states corresponding to performance levels P1, P2, and P3. Load factor for performance level P1 is higher due to its high probability of failure. It is evident that larger load factors are attributed due to the variation in the prediction of the capacity of the panel.

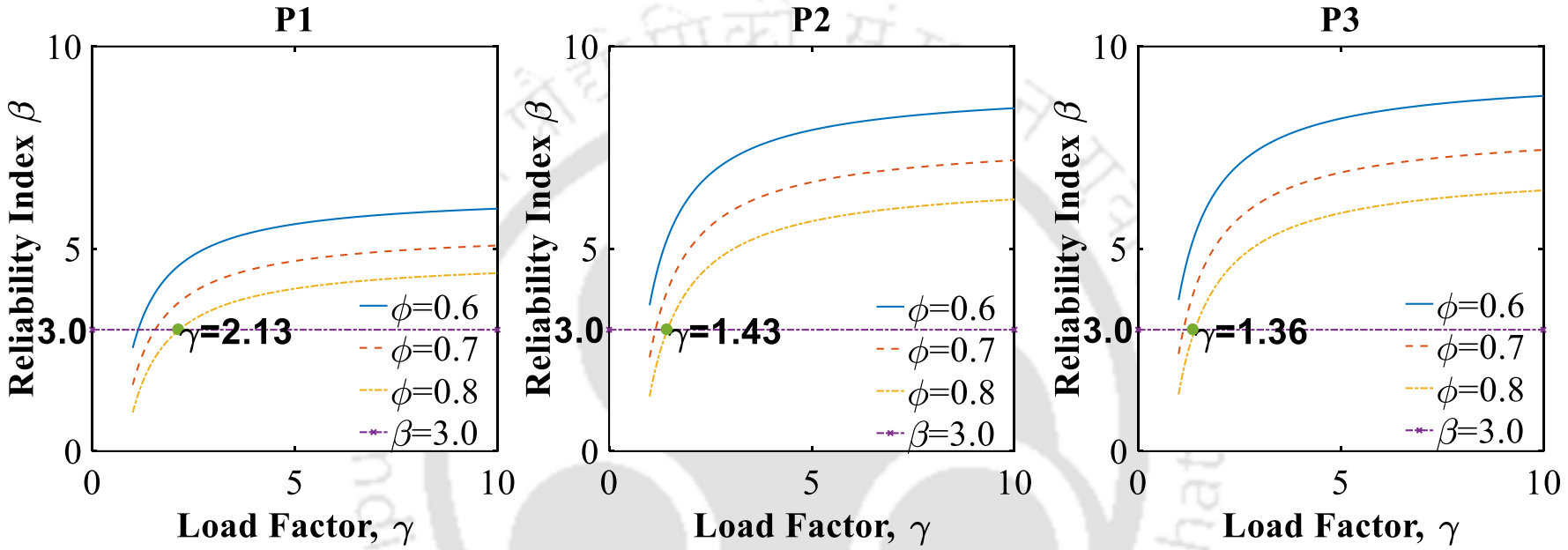

Figure 8.5 Plot of Reliability Index and Load Factor for all Performance Levels of NRC panel

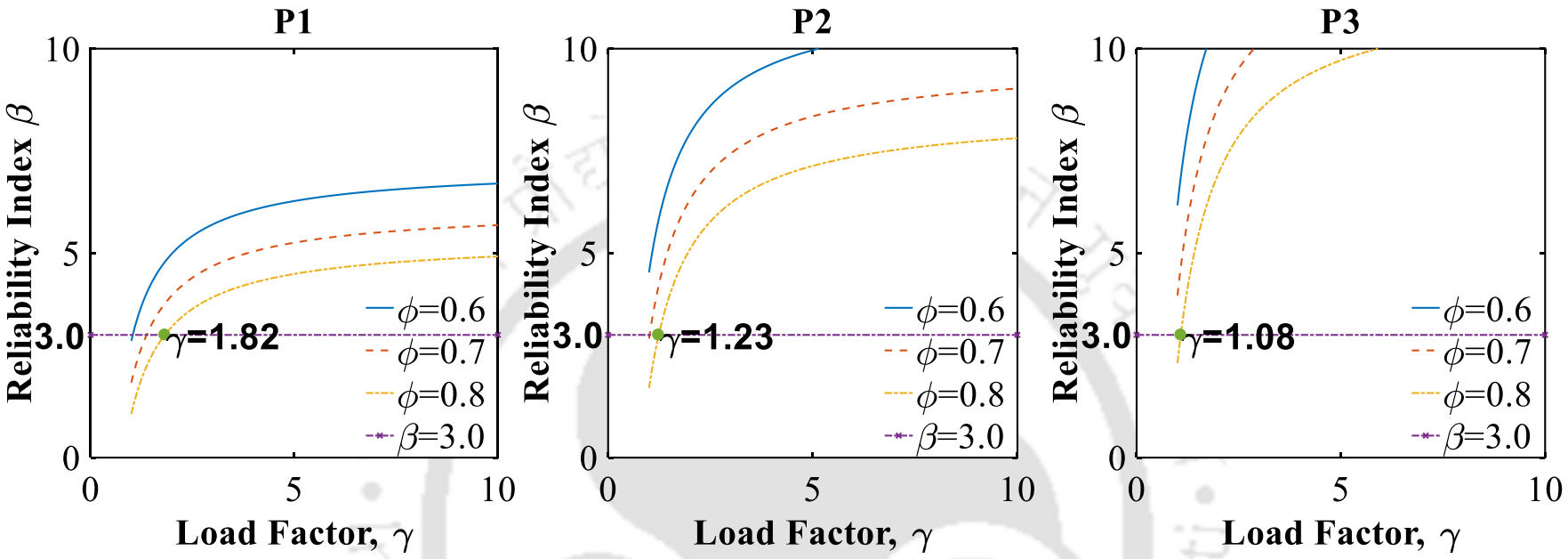

Figure 8.6 Plot of Reliability Index and Load Factor for all Performance Levels of UHSC panel

8.3 HAZARD CURVES

The hazard curve developed in the present research is inferred from the knowledge of explosive mass and its range by Stewart and Li (2021). The data is for TNT, ANFO (commercial and homemade) and high air blast variability scenarios and thus can be used for explosive loading on a protective structure. This study considers four blast scenarios with mean and COV as shown in Table 8.3. Stewart and Li (2021) found the data for both mass of charge and stand-off distance to be in Log-normal distribution which is also confirmed in the present study. The inverse CDF approach is used to find the goodness-of-fit of the candidate distribution where a random value from 0 to 1 is selected by MATLAB function that is used as CDF (cumulative distribution function) and to calculate PDF (probability distribution function) taking reference mean value and selected COV (coefficient of variance).

Table 8.3 Variability of mass and range of charge with blast scenarios (Stewart and Li 2021)

Scenarios	Mean of Stand-off distance (R)	Variability of Stand-off distance	Mean of mass of charge (Q)	Variability of mass of charge
EO-TNT	30 m	0.00	3500 kg	0.01
ANFO (commercial)	22 m	0.07	1300 kg	0.11
ANFO (homemade)	22 m	0.07	960 kg	0.31
High Air blast variability	30 m	0.30	3500 kg	0.30

8.3.1 Hazard curve for Mass of Charge

Figure 8.7 and 8.8 shows the comparison of the goodness-of-fit for the candidate distributions for air and contact blast respectively. The data collected is plotted on the x-axis as mass of charge in kg. The mass of charge predicted by the distributions is plotted on the y-axis in kg. The distributions compared are ‘Normal’, ‘Log-Normal’ and ‘Extreme Type - I’. The prediction of Log-Normal and Extreme Type I distribution is closer than that of the ‘Normal’ distribution. Log-Normal distribution is chosen as the best fit as it is closer than the Normal distribution and is best fit for lower range of data as adopted in this research. Hazard

curve based on the Log-Normal distribution for the mass of charge has parameters mean of 2309 kg-TNT and COV of 0.576 for air blast and mean of 2.9 kg-TNT and COV of 1.867 for contact blast. Figure 8.9 (a) and 8.10 (a) shows the Probability density function (PDF) for the Log-Normal distribution. The $f(m_m)$ PDF is plotted in the y-axis against mass of charge plotted on the x-axis. PDF of log-normal distribution for mass of charge can be expressed as

$$f_m(m) = \frac{1}{\sqrt{2\pi\zeta_m m}} \exp\left[-\frac{1}{2}\left(\frac{\ln m - \lambda_m}{\zeta_m}\right)^2\right] \tag{8.5}$$

where $\lambda_m = \ln \mu_m - 0.5\zeta_m^2$ and $\zeta_m = \ln\left[1+\left(\sigma_m/\mu_m\right)^2\right] = \ln\left(1+\delta_m^2\right)$.

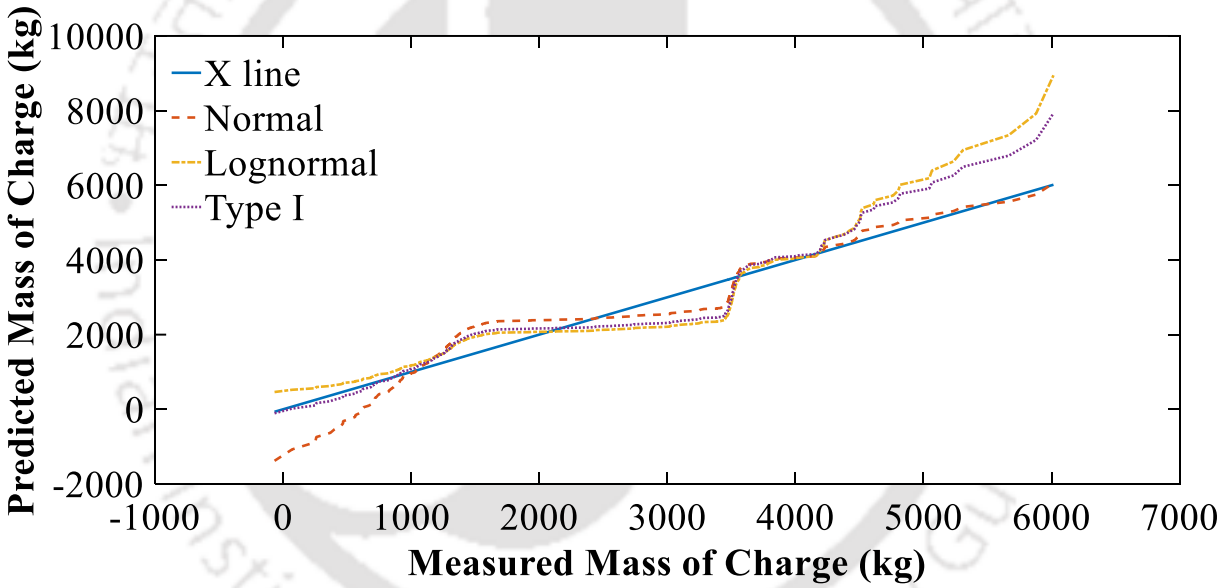

Figure 8.7 Predicted Mass of charge for Air Blast

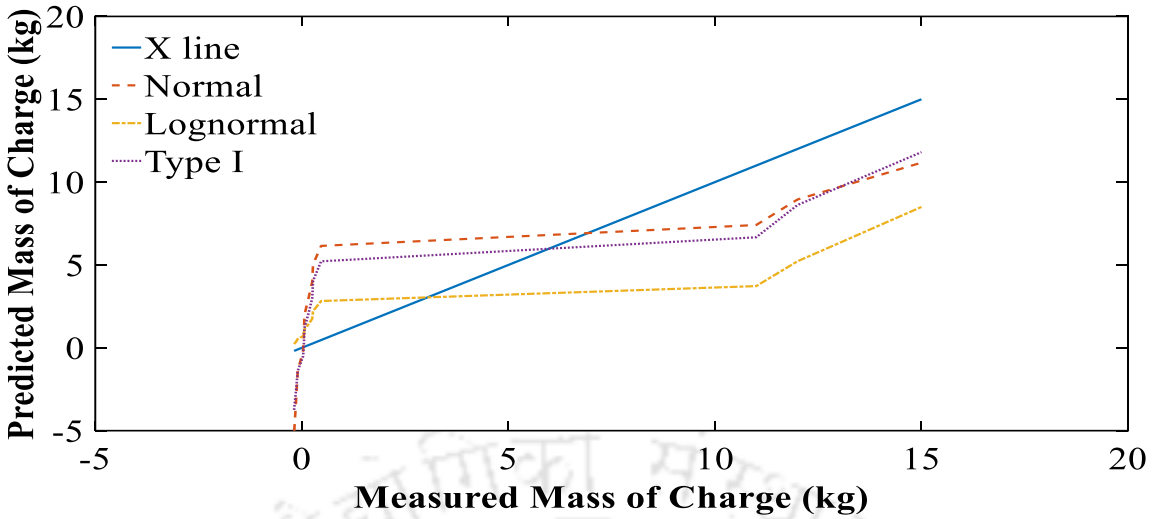

Figure 8.8 Predicted Mass of charge for Contact Blast

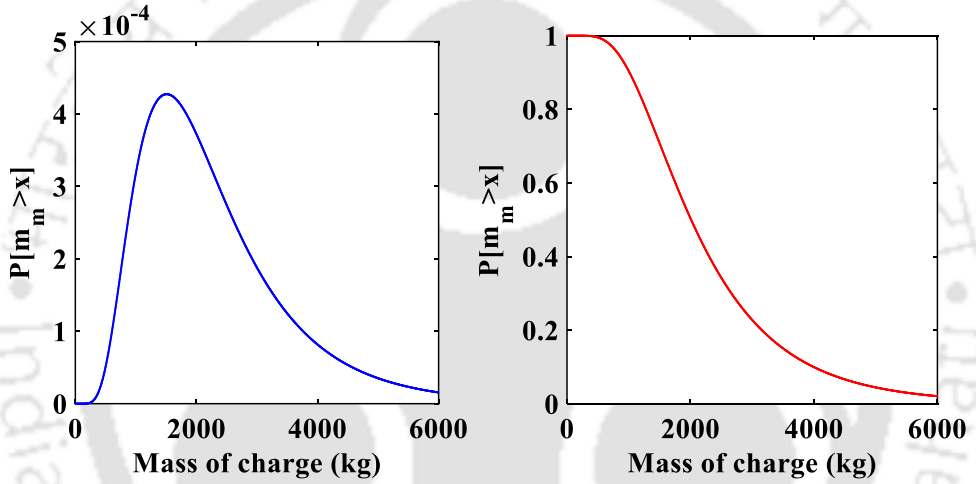

Figure 8.9 (a) PDF and (b) Probability of Exceedance of mass of air blast charge Log-Normal Distribution

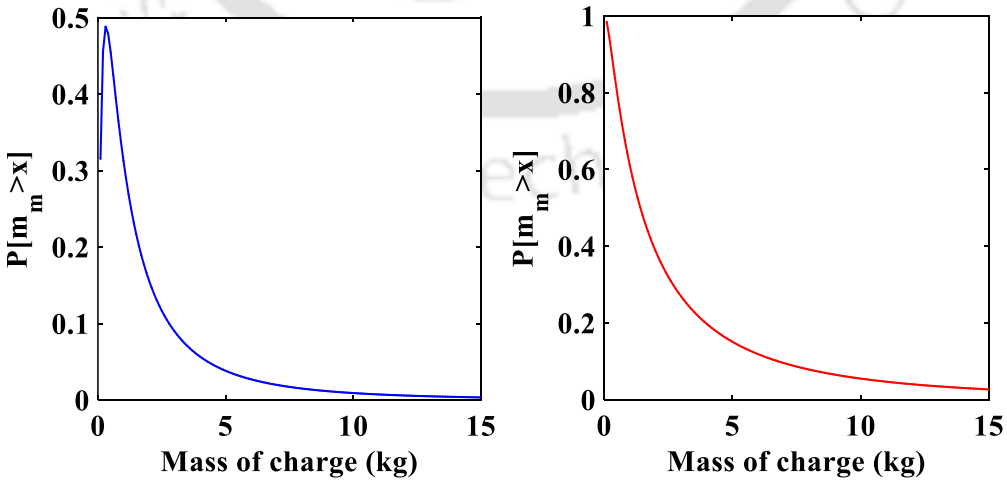

Figure 8.10 (a) PDF and (b) Probability of Exceedance of mass of contact blast charge Log-Normal Distribution

Figure 8.9 (b) and 8.10 (b) shows the hazard curve developed for the exceeding probability (1-CDF) of the mass of charge for the log-normal distribution. The exceeding probability $P\left[m_m > x\right]$ is plotted in the y-axis against mass of charge is plotted on the x-axis. CDF of log-normal distribution of mass of charge can be given by

$$F_m(m) = \Phi\left[-\frac{1}{2}\left(\frac{\ln m - \lambda_m}{\zeta_m}\right)\right] \tag{8.6}$$

$$P\left[m_m > x\right] = 1 - F_m(m) \tag{8.7}$$

8.3.2 Hazard curve for Stand-off Distance

The goodness-of-fit for the candidate distributions is compared in Figure 8.11. The data collected is plotted on the x-axis as stand-off distance in m. The stand-off distance predicted by the distributions is plotted on the y-axis in m. The distributions compared are 'Normal', 'Log-Normal' and 'Extreme Type - I'. The prediction of Log-Normal and Extreme Type I distribution is closer than that of the 'Normal' distribution. Log-Normal distribution is chosen as the best fit as it is closer than the Normal distribution and is best fit for lower range of data as adopted in this research. Hazard curve based on the Log-Normal distribution for the stand-off distance has parameters mean = 26.02 m and COV = 0.245.

Figure 8.12 (a) shows the Probability density function (PDF) for the Log-Normal distribution. The $f\left(m_m\right)$ PDF is plotted in the y-axis against mass of charge plotted on the x-axis. PDF of log-normal distribution for mass of charge can be expressed as

$$f_m(d) = \frac{1}{\sqrt{2\pi\zeta_d m}} \exp\left[-\frac{1}{2}\left(\frac{\ln d - \lambda_d}{\zeta_d}\right)^2\right] \tag{8.8}$$

where $\lambda_d = \ln \mu_d - 0.5\zeta_d^2$ and $\zeta_d = \ln\left[1+\left(\sigma_d/\mu_d\right)^2\right] = \ln\left(1+\delta_m^2\right)$

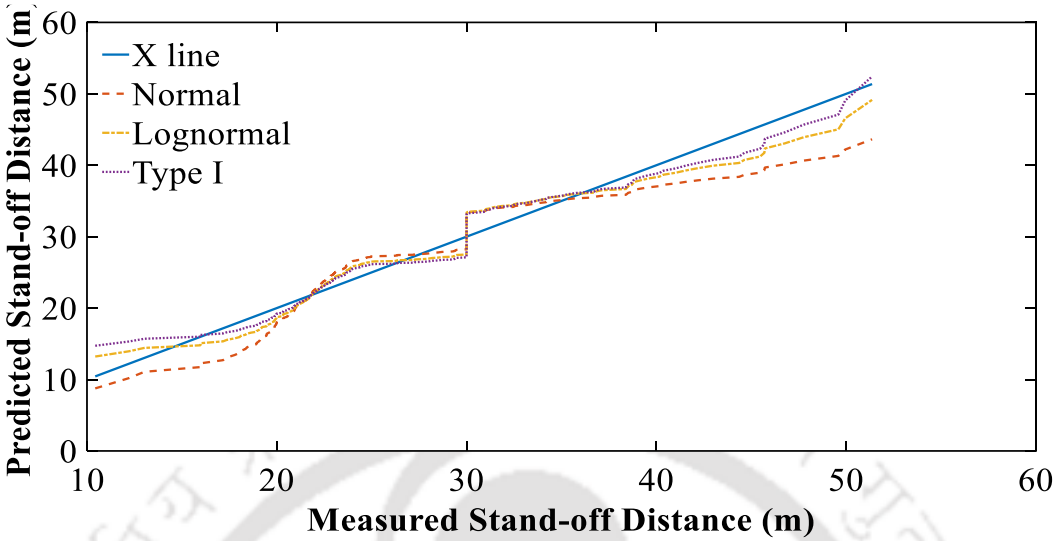

Figure 8.11 Predicted Stand-off Distance

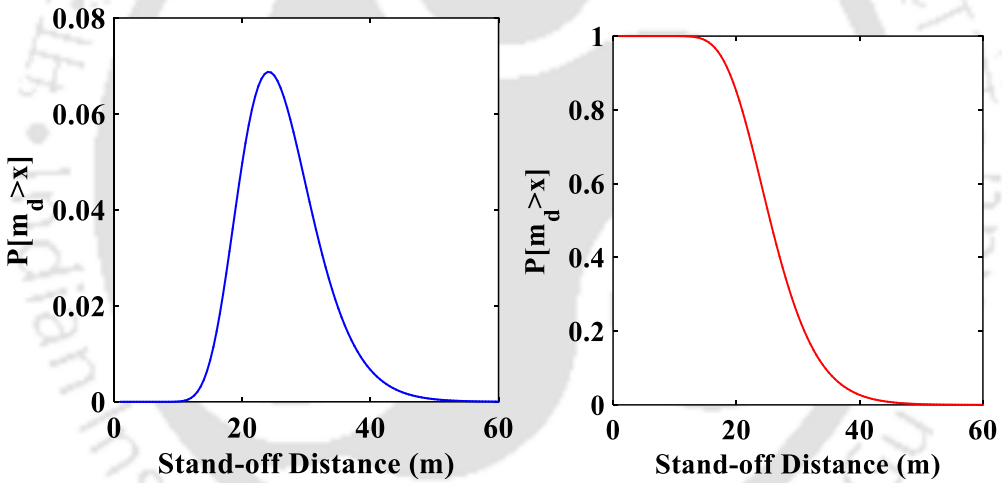

Figure 8.12 (a) PDF and (b) Probability of Exceedance of Stand-off Distance Log-Normal Distribution

Figure 8.12 (b) shows the hazard curve developed for the exceeding probability (1-CDF) of the mass of charge for the log-normal distribution. The exceeding probability $P\left[m_m > x\right]$ is plotted in the y-axis against mass of charge is plotted on the x-axis. CDF of log-normal distribution of mass of charge can be given by

$$F_m(d) = \Phi\left[-\frac{1}{2}\left(\frac{\ln d - \lambda_d}{\zeta_d}\right)\right] \tag{8.9}$$

$$P\left[m_d > x\right] = 1 - F_d\left(d\right) \tag{8.10}$$

8.4 TOTAL PROBABILITY AND COUPLED RELIABILITY INDEX

The performance-based dynamic resistance and demand model are used to develop framework to estimate total probability of the failure and coupled reliability index β of panels subject to explosion. The generalized form to evaluate total probability of failure of panel subject to blast loading is given by

$$P_{fPi} = \iint P\left[g_{Pi}\left(x,\Theta\right) \le 0 \middle| \left(m_c, s_d\right)\right] f\left(m_c\right) f\left(s_d\right) dmds \qquad \text{Pi=P1,P2,P3} \tag{8.11}$$

$$F_{Pi}\left(x,\Theta\right) = g_{Pi}\left(x,\Theta\right) \le 0 \middle| \left(m_c, s_d\right) \qquad \text{Pi=P1,P2,P3} \tag{8.12}$$

$$g_{Pi}\left(x,\Theta\right) = s_{Pi} - s_D \qquad \text{Pi=P1,P2,P3} \tag{8.13}$$

where, P_{fPi} = Probability of failure for the performance levels P1, P2 and P3, $g_{Pi}\left(x,\Theta\right)$ = limit state for the performance levels P1, P2 and P3, $f\left(m_c\right)$ = PDF of the distribution of the mass of charge and, $f\left(s_d\right)$ = PDF of the distribution of the stand-off distance.

The generalized equation can be used to estimate the probability of failure or reliability of the panels subject to blast loading based on desired design performance objectives given in Table 2.1 and 2.2 for air and contact blast respectively. The integration operation adds up the conditional probabilities of exceedance associated with all possible mass of the charge and the stand-off distance. The limit state and fragility for the performance levels P1, P2 and P3 are developed in the previous sections. The PDF of the distribution of the mass of the charge and the stand-off distance has been developed earlier in this section.

8.4.1 Total Probability for Air Blast on Panel

The probability of the failure of NRC and UHSC Panel for performance level P1 is estimated by

$$P_{fP1} = \int_0^{l_s}\int_0^{l_m} P\left[g_{P1}(x,\Theta) \le 0 \middle| (m_c, s_d)\right] f(m_c)\, f(s_d)\, dm ds \tag{8.14}$$

where, P_{fP1} = Probability of failure for the performance levels P1, $g_{P1}(x,\Theta)$ = limit state for the performance levels P1, $f(m_c)$ = PDF of the distribution of the mass of charge, $f(s_d)$ = PDF of the distribution of the stand-off distance, l_m = upper limit of the mass of charge and l_s = upper limit of the stand-off distance.

The probability of the failure of NRC and UHSC Panel for performance level P2 is estimated by

$$P_{fP2} = \int_0^{l_s}\int_0^{l_m} P\left[g_{P2}(x,\Theta) \le 0 \middle| (m_c, s_d)\right] f(m_c)\, f(s_d)\, dm ds \tag{8.15}$$

where, P_{fP2} = Probability of failure for the performance levels P2, $g_{P2}(x,\Theta)$ = limit state for the performance levels P2, $f(m_c)$ = PDF of the distribution of the mass of charge, $f(s_d)$ = PDF of the distribution of the stand-off distance, l_m = upper limit of the mass of charge and l_s = upper limit of the stand-off distance.

The probability of the failure of NRC and UHSC Panel for performance level P3 is estimated by

$$P_{fP3} = \int_0^{l_s}\int_0^{l_m} P\left[g_{P3}(x,\Theta) \le 0 \middle| (m_c, s_d)\right] f(m_c)\, f(s_d)\, dm ds \tag{8.16}$$

where, P_{fP3} = Probability of failure for the performance levels P3, $g_{P3}(x,\Theta)$ = limit state for the performance levels P3, $f(m_c)$ = PDF of the distribution of the mass of charge, $f(s_d)$ = PDF of the distribution of the stand-off distance, l_m = upper limit of the mass of charge and l_s = upper limit of the stand-off distance.

The total probability plots for each performance level of NRC panel is depicted in Figure 8.13 and that of UHSC panel is presented in Figure 8.14. The plots represent the total probability of failure with variation of mass of charge and stand-off distance. Since the mean of mass of charge and stand-off distance is 2300 kg-TNT and 30 m respectively, the plots show a peak at these values. The probability peaks for P1, P2, and P3 decrease as a higher performance level is reached, showing the probability of failure for P3 is less than P2 and the probability of failure for P3 is less than P2. Approximately, the total probability for the NRC panel at the performance level P1 ranges from 5e-06 to 2.5e-5, P2 ranges from 2.5e-06 to 1.5e-5 and P3 ranges from 2.5e-06 to 1e-5. For UHSC panel the total probability approximately ranges from 5e-06 to 2.5e-5 for P1, 2.5e-06 to 1.5e-5 for P2 and 2.5e-06 to 7.5e-6 for P3.

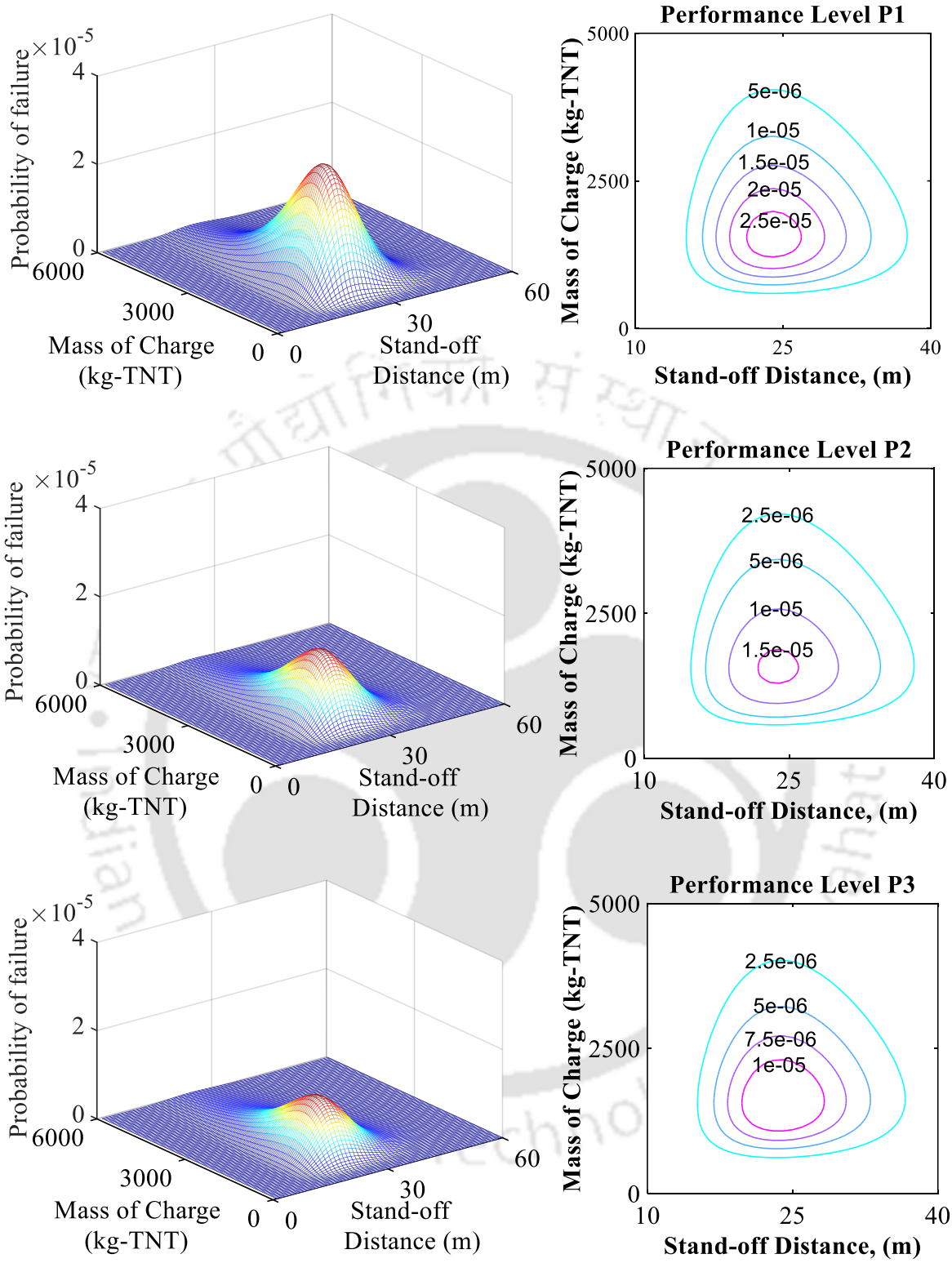

Figure 8.13 Plot of joint lognormal probability density function for NRC Panel

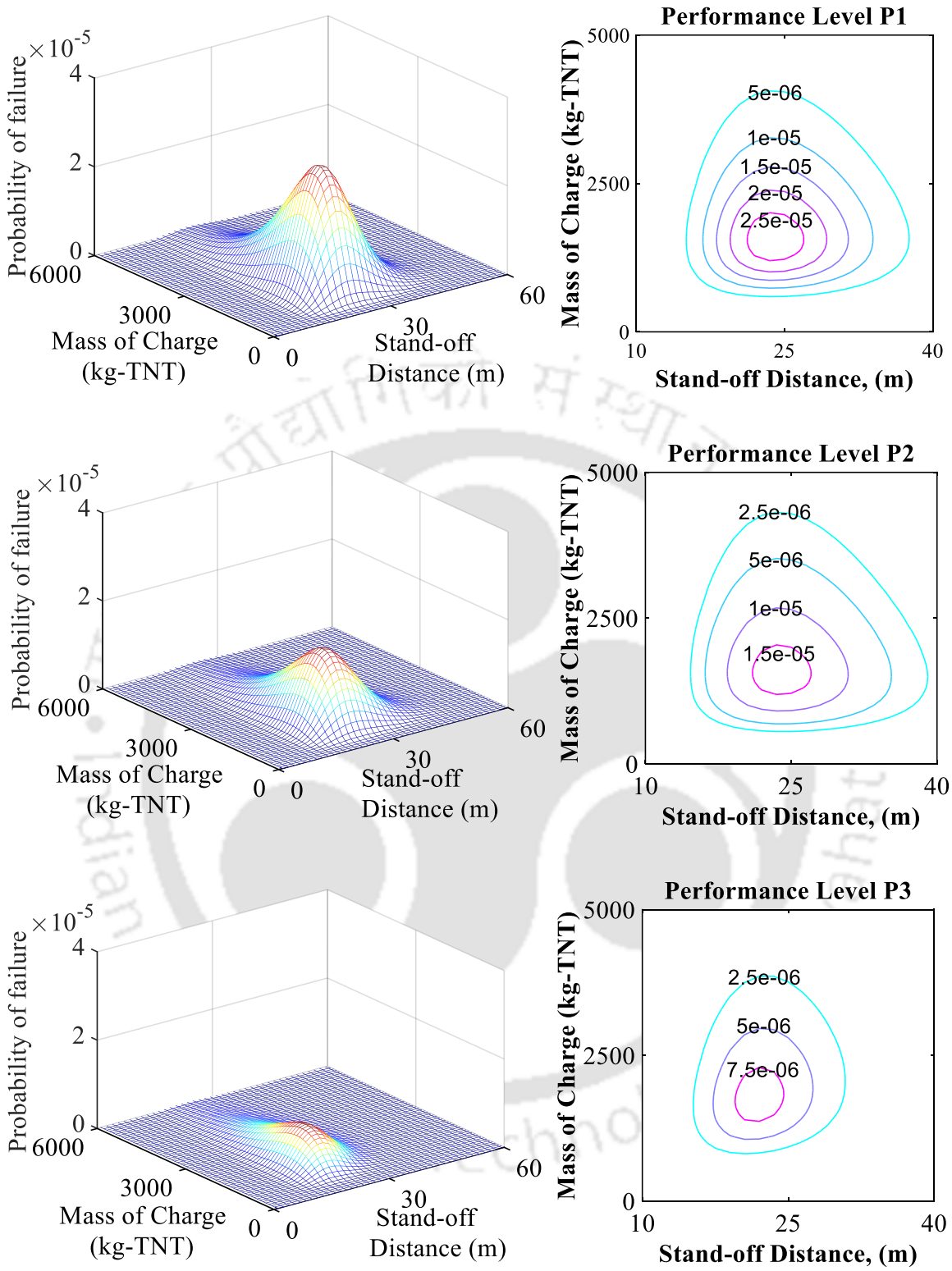

Figure 8.14 Plot of joint lognormal probability density function for UHSC Panel

8.4.2 Total Probability for Contact Blast on Panel

The probability of the failure of Panel for performance level P1 is estimated by

$$P_{fP1} = \int_0^{l_m} P\left[g_{P1}(x,\Theta) \le 0 \middle| m_c \right] f(m_c)\, dm \tag{8.17}$$

where, P_{fP1} = Probability of failure for the performance levels P1, $g_{P1}(x,\Theta)$ = limit state for the performance levels P1, $f(m_c)$ = PDF of the distribution of the mass of charge and l_m = upper limit of the mass of charge.

The probability of the failure of NRC and UHSC Panel for performance level P2 is estimated by

$$P_{fP2} = \int_0^{l_m} P\left[g_{P2}(x,\Theta) \le 0 \middle| m_c \right] f(m_c)\, dm \tag{8.18}$$

where, P_{fP2} = Probability of failure for the performance levels P2, $g_{P2}(x,\Theta)$ = limit state for the performance levels P2, $f(m_c)$ = PDF of the distribution of the mass of charge and l_m = upper limit of the mass of charge.

The probability of the failure of NRC and UHSC Panel for performance level P3 is estimated by

$$P_{fP3} = \int_0^{l_m} P\left[g_{P3}(x,\Theta) \le 0 \middle| m_c \right] f(m_c)\, dm \tag{8.19}$$

where, P_{fP3} = Probability of failure for the performance levels P3, $g_{P3}(x,\Theta)$ = limit state for the performance levels P3, $f(m_c)$ = PDF of the distribution of the mass of charge and l_m = upper limit of the mass of charge.

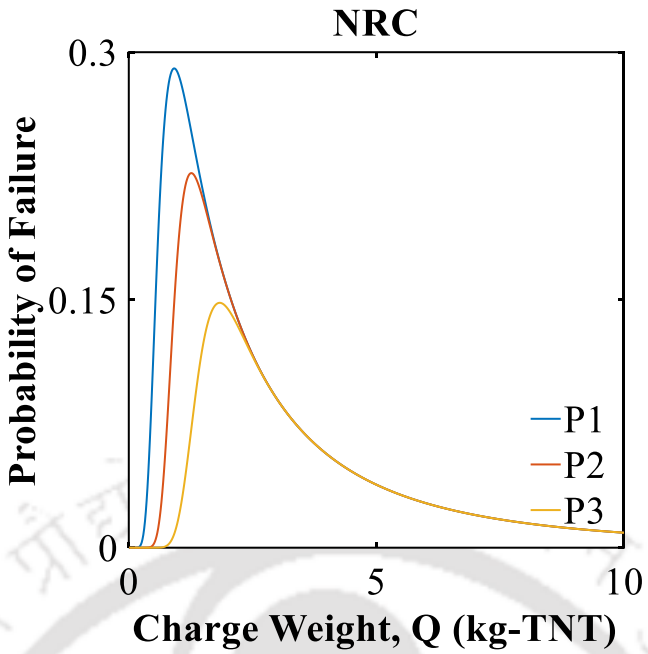

Figure 8.15 Plot of joint lognormal probability density function for NRC panel

The total probability plots for each performance level of NRC panel and UHSC panel is depicted in Figure 8.15 and 8.16 respectively. The plots depict the total probability of failure as a function of charge mass variation only, as stand-off distance plays no role in contact blasts. Since the mean of mass of charge is 2.9 kg-TNT, the plots shows a peak at these values. As a higher performance level is reached, the probability peaks for P1, P2, and P3 fall, indicating that the chance of failure for P3 is less than P2 and the probability of failure for P3 is less than P2. The demand model is separately developed for the two panel, due to which the NRC panel shows less probability of failure than UHSC panel. If the demand model is same, the values obtained for total probability of failure of UHSC panel will be less than that of NRC panel. Again, the total probability is more in contact blast for the panels than the air blast.

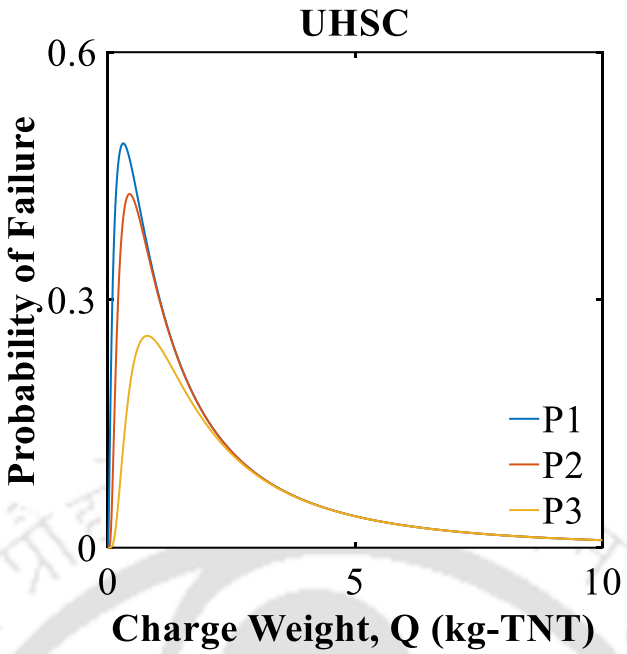

Figure 8.16 Plot of joint lognormal probability density function for UHSC panel

8.5 DISCUSSION

In the section, hazard curves are developed for the mass of the charge for both air and contact charge and standoff distance for air blast. Code calibration to estimate the load and resistance factor for the three performance level is performed and load and resistance factors are proposed for the desired reliability index for the two panels separately for air and contact blast. The developed hazard curve in this section with the performance-based dynamic resistance and demand models are used to develop framework to evaluate the total probability or the reliability of the Panels subject to air and contact blast. The performance level is tied to the damage levels to estimate the reliability of the slab/wall for the desired performance objectives. The equations to estimate the reliability for critical cases like the Panel subject to air and contact explosion being fully operational and sustaining minor damage during low damage events, the panel subject to similar loading being operational with sustaining structural damage during medium damage events, and NRC and UHSC panel being in state of total collapse during severe damage events is established for air and contact blast. The section thus presents the code calibration to

estimate the load and resistance factors as well as equations to achieve desired performance objectives of Slab/walls of Protective structure with NRC and UHSC panel as building blocks subject to air and contact blast.

The following Chapter describes the in-house development of a high strength materials to be adopted in the panel configuration described above.

Chapter 9. DEVELOPMENT OF MATERIAL

9.1 OVERVIEW

This chapter presents the detailed review to high strength concrete development to be adopted for the panels. Development of high strength concrete (HSC) can be marked as an amazing progress in concrete technology. These developments help to optimize the use of materials in a broader way. Many materials are taken in research and development of what is also known as high performance concrete (HPC). Material selection process for the concrete requires proper understanding of the materials, their functions and influence on fresh and hardened concrete properties. Proper study of such materials has thus become necessary to utilize the materials to their full potential. High strength concrete has been used in bridges since many years and now is also finding its ways to defense and nuclear establishments. Dry mixed ultra-high performance concrete products are commercially available, and had been successfully applied for bridges and other spectacular structures in several countries. Iran recently developed an ultra-high performance concrete also known as “Smart concrete” to protect N-sites from US bunker busters. Sectors with high durability and strength demand are adopting HSC but due to it high cost, its use is limited.

The constituents usually used for the high strength concrete matrix are cement, fine aggregate, coarse aggregate, superplasticizer, low water-cement ratio and mineral admixtures like fly ash, ground granulated blast-furnace slag, silica fume, silica sand etc. As proper mix designs are not available for high strength concrete till date, trial mixes are very important in achieving the desired concrete performance. Knowing the effect of each material on the fresh as well as hardened concrete helps a lot in adopting the proportion in the trial mixes. Thus, the current work summarises the outcome of the microstructural study of material and application

of the materials in developing a high strength concrete mix by adopting compressive strength test.

9.2 PRESENT STATE OF ART

Many research works have been conducted over the years to achieve high mechanical performance with cementitious matrix materials. Eugene Freyssinet during the 1930s demonstrated that in order to improve the strength of concrete applying pressure to the fresh concrete is advantageous. During the 1960s, compressed samples were prepared and heat cured under elevated pressures which attained compressive strength of 650 MPa. Naaman and Wille gave an overview on five decades of progress on UHSC as shown in Table 9.1 (Naaman and Wille 2012). Most of the research conducted on ultra-high performance concrete used cement, silica fume, quartz and superplasticizer along with fibers (Habel et al. 2006; Kim et al. 2015; Matte and Moranville 1999; Wille and Naaman 2010) and with various percentage of volume fraction (Courtial et al. 2013; Prem et al. 2012; Reda et al. 1999; Richard and Cheyrezy 1995; Wille et al. 2011, 2012).

High amount of superplasticizer in the mix causes the hydration reaction to start at 26 hours after water addition and gets retarded. Yang et al. (2009) investigated ultra-high performance concrete by replacing expensive silica sand by recycled glass cullet and two types of local natural sand; and some part of cement with ground granulated blast-furnace slag and silica fume. Addition of deformed fibers by volume lead to an increase direct tensile strength which was about three times more than that for UHP-FRC with smooth fibers. Higher fibre volume produced drastic changes in the cube strength, cylinder strength, post peak response, load-crack mouth opening displacement, fracture energy flexural strength, split tensile strength, residual strength and durability.

Table 9.1 Chronological Advances in the matrix and fibers since the 1960's (Naaman and Wille 2012)

Decade	Cementitious Matrix and Concrete	Fiber
1970's	• Better understanding of hydration reactions; gel structure; • Better understanding shrinkage, creep, porosity • High strength concrete to 50 MPa in practice • Development of water reducers • Advances in concrete treatments and curing conditions	• Smooth steel fibers; normal strength • Glass fibers • Some synthetic fibers
1980's	• Increased development of chemical additives: HWRA, etc. • Increased utilization of fly ash and silica fume, and other mineral additives, etc. • Increased flowability (flowable concrete) • Reduction in W/C ratio; • High-Strength-Concrete terminology: up to 60 MPa; special high strength: up to 80 MPa; exotic high strength (special aggregate and curing): up to 120 MPa • High-Performance-Concrete terminology: high strength concrete with improved durability properties.	• Deformed steel fibers: normal and high strength • Low-modulus synthetic fibers (PP, nylon, etc.) • Increased use of glass fibers • Micro fibers • High performance polymer fibers (carbon, Spectra, Kevlar, etc..)
1990's	• Increased development of chemical additives: HWRA, etc. • Increased development in chemical additives: superplasticizers; viscosity agents; etc. • Increased use of supplementary cementitious materials as cement replacement • UHPC: application of concept of high packing density; addition of fine particles; low porosity; lower water to cementitious ratio; • Self-consolidating concrete; self-compacting concrete;	• New steel fibers with a twist (untwist during pullout) • PVA fibers with chemical bond to concrete • Improved availability of synthetic fibers
2000's	• Increased developments of proprietary and non-proprietary UHPC/UHP-FRC • UHPC: improved understanding of high packing density; application of nanotechnology concepts	• Ultra high strength steel fibers: smooth or deformed with strengths up to 3400 MPa • Carbon nano-tubes; carbon nano-fibers
2010's	• Increased understanding of the cementitious matrix at the nano-scale	• Carbon nano-fibers, graphene

Applying pressure squeezes out water, decreasing the water/cement ratio and increasing the packing density of the cement matrix; thus reducing porosity of concrete. So, many used pressurization technique for developing UHPC and RPC (Ahlborn et al. 2008; Reda et al. 1999; Richard and Cheyrezy 1995) which was governed by the compaction to be attained and workability needed. Heat-treating methods adoption is also there in the previous research including hot water bath and oven-drying (Ahlborn et al. 2008; Reda et al. 1999; Yang et al. 2009). Curing at low temperature minimizes the expected shrinkage and thermal cracking from the hydration of high cement content mixtures. Optimization of packing density of the cementitious matrix, use of very high strength steel fibers, and optimization of the matrix-fiber interface properties are some of the performance enhancement techniques. No proper mix designs are available for UHSC till date.

9.3 MATERIALS REQUIRED FOR HIGH STRENGTH CONCRETE

All materials used in a concrete mix has its significance. Optimizing the particle size distribution of the cementitious materials increases the potential packing density and can also reduce the capillary porosity as it also favours the formation of fine-textured hydration products that have a higher strength than the coarser equivalents. It is assumed that small aggregate particles will contain less internal flaws and hence produce a higher concrete strength. Ingredients of high strength concrete matrix should possess these properties to ensure maximum particle density and minimum flaws.

Cement

Compared to conventional concrete, cement content is relatively higher in high strength concrete matrix. Cements with low C_3A content lowers the water demand and give better results from the chemical composition view point. Cement which are coarsely grounded is unsuitable, but for fine particle size, the water demand rises. In the present work, Ordinary

Portland cement (OPC) of 53-grade conforming to IS: 8112-2013 (Specific gravity = 3.15) was used in the preparation of concrete mixes. Cement was selected based C_3A content; lower the content means less water demand. The physical properties of cement given in Table 9.2.

Table 9.2 Test results of OPC 53 grade cement

S.No.	Test	Results	Conforming to
1	Specific Gravity	3.09	IS 4031(PART-11): 1988
2	Consistency	30%	IS 4031(PART-4): 1988
3	Initial setting time	93 minutes	IS 4031(PART-5): 1988
4	Final setting time	6 hours	IS 4031(PART-5): 1988
5	Fineness	96%	IS 4031(PART-1): 1996
6	Specific surface area	2.152 m^2/g	
7	28 day compressive strength	53.4 MPa	

If the specific gravity of cement is larger than 3.19 then, the cement is either not minced finely as per the industry standard or it has more moisture content which will affect the mix and bonding. This is why you find lots of chunks while mixing old stock cement for concrete. Consistency is to know the amount of water required to make a plastic mix. Setting time of cement is seen as moderate. Sieve analysis and surface area tests proved that fineness of cement is good but the water demand will be more.

Mineral Admixture

Here in this study, silica fume is used as the mineral admixture. Silica fume is a by-product from manufacturing of Silicon metal and alloys in electric arc furnace. Papadakis et al. (Papadakis et al. 1999) investigated that silica fume has particle diameters of about 0.1 micron. Two particle shapes are present, one spheroid and one cylindrical. And further added that, this particular shape can help in SF identification in cement paste during the hydration process. The silica fume agglomerations are almost spherical. The agglomeration consists of much ultra-fine

silica. Some agglomerations have sizes larger than 100 mm. Due to the spherical particles, lubrication effect is developed which improves the rheological characteristics; and it also reacts (pozzolanic reaction) with the lime resulting from primary hydration producing secondary hydrates. The silica fume used in high strength concretes has three main functions. That are – filling the voids between the next larger class particles (cement), enhancement of rheological characteristics by the lubrication effect resulting from the perfect sphericity of the basic particles; and production of secondary hydrates by pozzolanic reaction with the lime resulting from primary hydration.

For the present trial mixes, silica is collected from two sources, Source A- Elkem Microsilica® Grade 920 D and Source B- Silica fume from a local source. Specific gravity of silica is determined with Le Chatelier flask. The value of specific gravity is found to be 2.22 for Source A and 2.12 for Source B. Specific surface area of silica from source A is found to be 16.085 m^2/g and of source B is 9.452 m^2/g. Some other test performed on both the silica are FESEM test, XRD test and EDX test to verify the sample and know its texture and morphology.

Quartz

Quartz is a very hard material and possesses excellent paste/aggregate interfaces. For heat-treated concretes crushed crystalline quartz powder is an essential ingredient as maximum reactivity is obtained for a mean particle size of between 5 and 25 µm during heat-treating. Quartz powder is used as a filler material in the concrete mixes.

For the present trial mixes, quartz is also collected from two sources, Source A is already in powder form and Source B is in stone form collected from a local source. Quartz stones obtained from Source B was grinded and sieved with 75 µm sieve. The specific gravity was determined using pycnometer and the obtained value of specific gravity of quartz from Source A is 2.65 and from Source B is 2.66. The particle size of quartz powder used is less

than 75 µm. Some other test performed on both the silica are FESEM test, XRD test and EDX test to verify the sample and know its texture and morphology.

Fine Aggregate

The improvement of transition zone between the paste and the aggregate causes the transfer of stresses more effective from the paste to the aggregate particles. Limitation of achievable concrete strength is consequently because the mechanical properties of the aggregate particles themselves must be the 'weakest link'. Therefore, crushed rock aggregates are generally preferred to smooth gravels as there is some evidence that the strength of the transition zone is weakened by smooth aggregates (Aitcin and Mehta 1990). So appropriate sources should be considered for making higher grade of concrete.

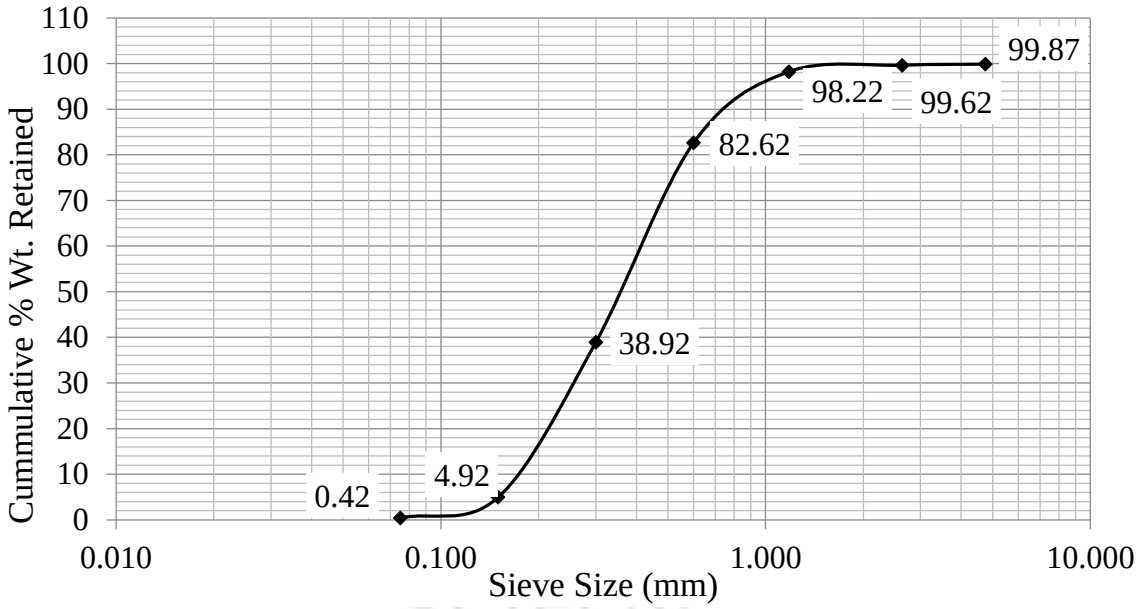

Figure 9.1 Particle Size distribution of Fine aggregate

Local river sand was adopted in this experiment conforming to Zone-II as per IS: 383-1970 with specific gravity of 2.65 and Fineness modulus (F.M.) as 2.75. Prior to mixing, the available sand was sieved by 600 µm sieve to maintain the particle size in the concrete matrix.

The sieve analysis test results are shown in Table 9.3 and the distribution is shown in Figure 9.1.

Coarse Aggregate

Mechanical properties of aggregate particles are a major cause of limitation of concrete strength achievable as they themselves are the weakest link. The improvement of transition zone between the paste and the aggregate causes the transfer of stresses more effective from the paste to the aggregate particles. In the current work, coarse aggregate (specific gravity = 2.67) of maximum size 10 mm was adopted in some mixes. The particle size distribution is presented in Table 9.3.

Table 9.3 Sieve Analysis of fine and coarse aggregate.

SIEVE SIZES (mm)	CUMULATIVE % WEIGHT PASSING
Fine Aggregate	
4.750	99.87
2.360	99.62
1.180	98.22
0.600	82.62
0.300	38.92
0.150	4.92
0.075	0.42
Coarse Aggregate	
12.50	99.97
10.00	97.39
4.75	18.33
2.36	3.10

Chemical Admixture

Superplasticizers plays an important role in high strength concrete production as it produces workable concrete at very low levels of water/cement ratios without needing high cement content. They also increase early and ultimate compressive strengths, offer better resistance to carbonation, reduce shrinkage and creep; and make concrete durable. Poly-

carboxylate ether-based dispersing agents are the most efficient superplasticizers, but also exhibit a retarding characteristic which is sometimes a problem. In the present work, a poly-carboxylate ether based superplasticizers are used namely, FOSROC - Structuro 201 and Structuro 203 with specific gravity of 1.09 for both, SIKA - Viscoconcrete 2004 with specific gravity of 1.12 and BASF - MasterGlenium ACE 30UG with specific gravity of 1.09 (as per the data supplied by the manufacture). The solids content of superplasticizer was 30.18%, 37%, 34% and 44.34% by mass respectively (as per the data supplied by the manufacture).

9.4 MICRO-STRUCTURAL STUDIES OF MATERIALS

To understand the materials used in concrete mix, it is necessary to study the morphology and chemical composition of silica fume, cement, and concrete. In this section some of the study conducted on cement, silica fume and quartz are described.

9.4.1 X-Ray Diffraction (XRD) Test

The X-Ray diffraction (XRD) are used to study the quantitative and qualitative characteristics of poly phase materials. A unique diffraction pattern is produced for each material independently and intensity of pattern is directly proportional to the concentration of material. This test is used for the analysis of materials, that are silica fume and quartz. XRD is a technique used to study the crystalline structure and physical properties of materials and thin films. Kocak (2010) conducted XRD to determine the mineralogical structure of silica fume and suggested that the silica fume have amorphous mineralogical structures. Concrete specimens containing 10% silica fume are stable for thermal treatment up to 300°C and increase of silica fume ratios (20 and 30%) leads to appearance of micro cracks after thermal treatment (Saad et al. 1996). Arroudj et al. (2011) studied the reactivity of fine quartz in presence of silica fume and slag and concluded that the mineralogy of additions has a great influence on the pozzolanic reactivity at early ages.

The structural and compositional variations of material in mixture influence the peak and intensity of the reflected rays. The horizontal axis represents the diffraction angle while, the intensity of refracted rays is represented by vertical axis. The XRD pattern of silica fume is like a hump as the silica fume mainly consist of vitreous silica. Flatter the hump, more is the amorphous fume. The hump is located near 2θ=22°, which indicates the distribution of silicon tetrahedron in vitreous particles over a range of short distance. The XRD pattern of silica fume from Source A and Source B are shown in Figure 9.2 and 9.3 respectively. Quartz powder from Source A and Source B shows an XRD pattern as presented in Figure 9.4 and 9.5 respectively.

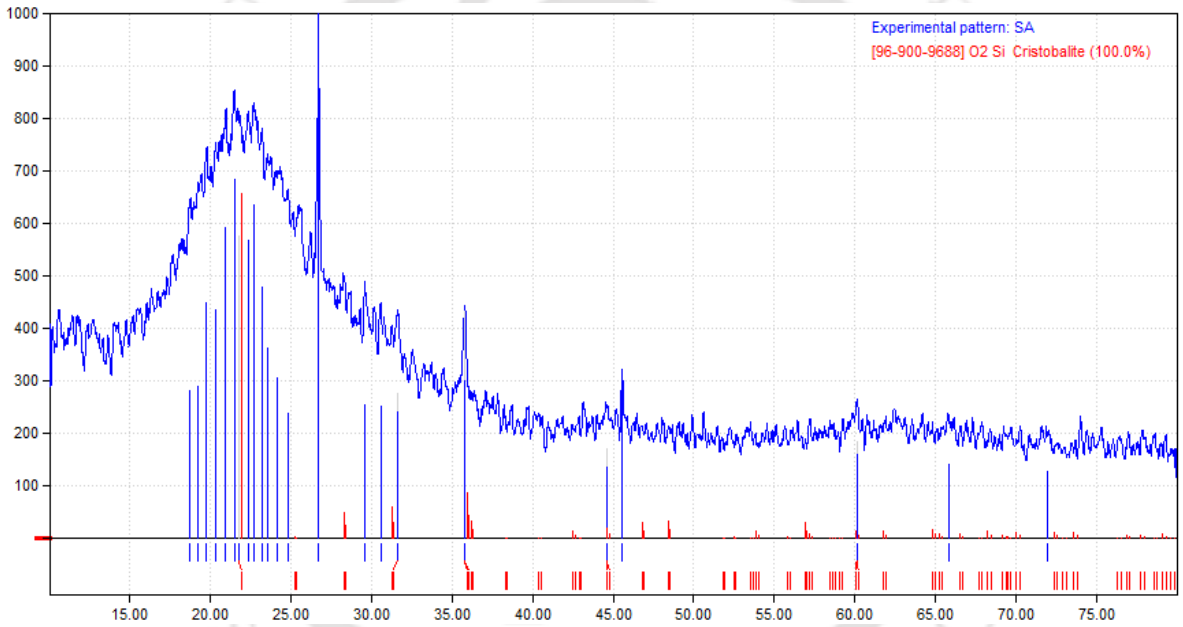

Figure 9.2 XRD pattern of silica fume (Source A)

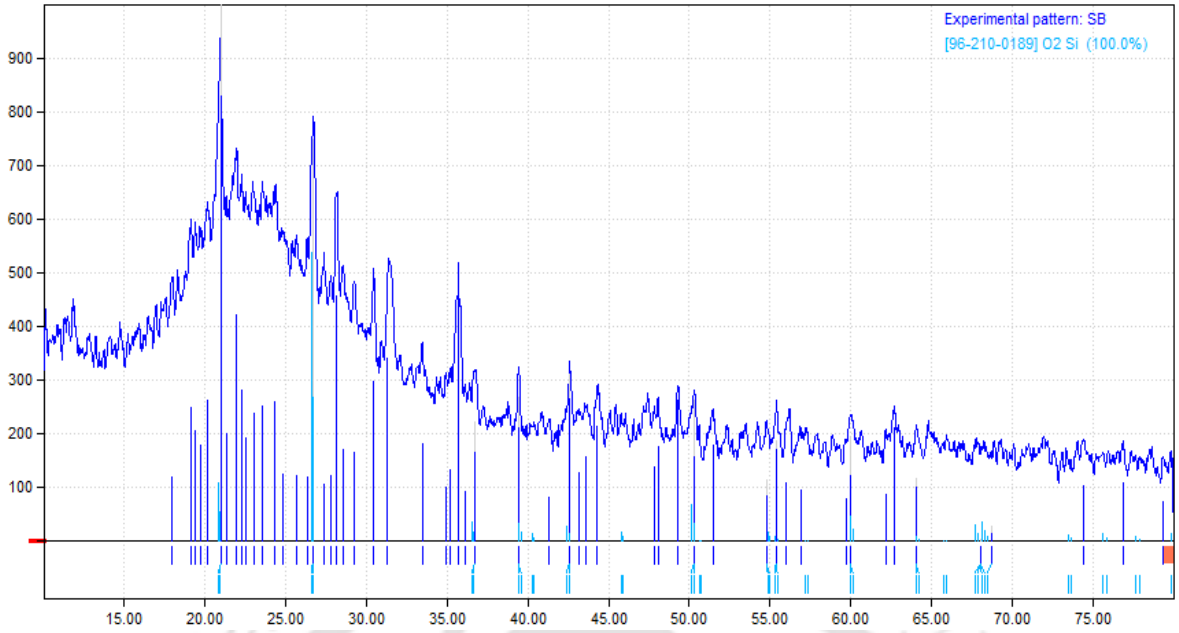

Figure 9.3 XRD pattern of silica fume (Source B)

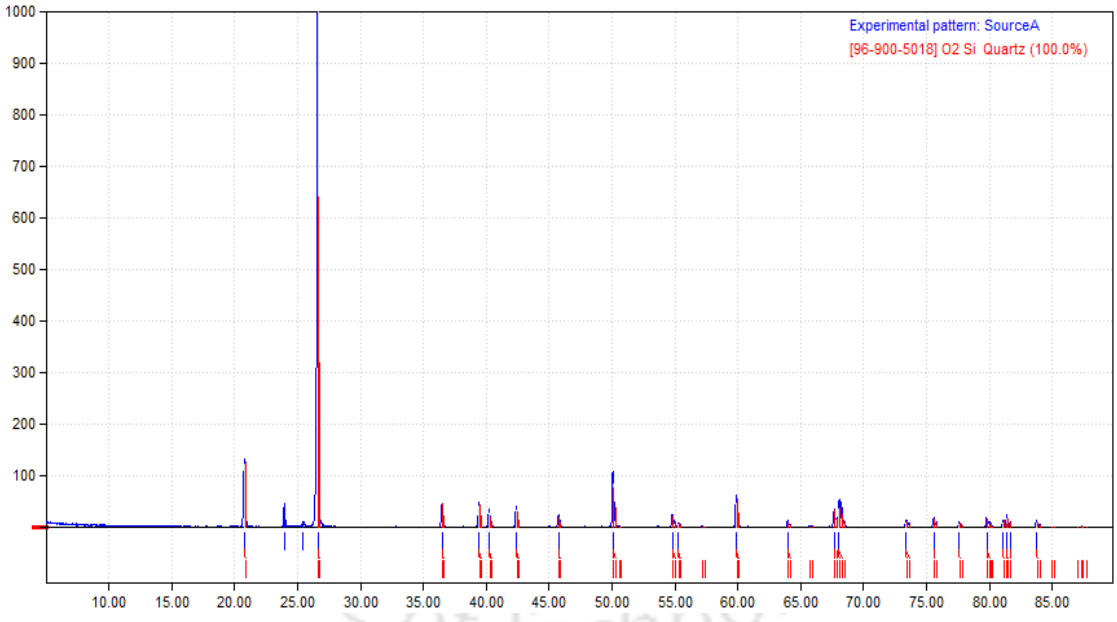

Figure 9.4 XRD pattern of quartz (Source A)

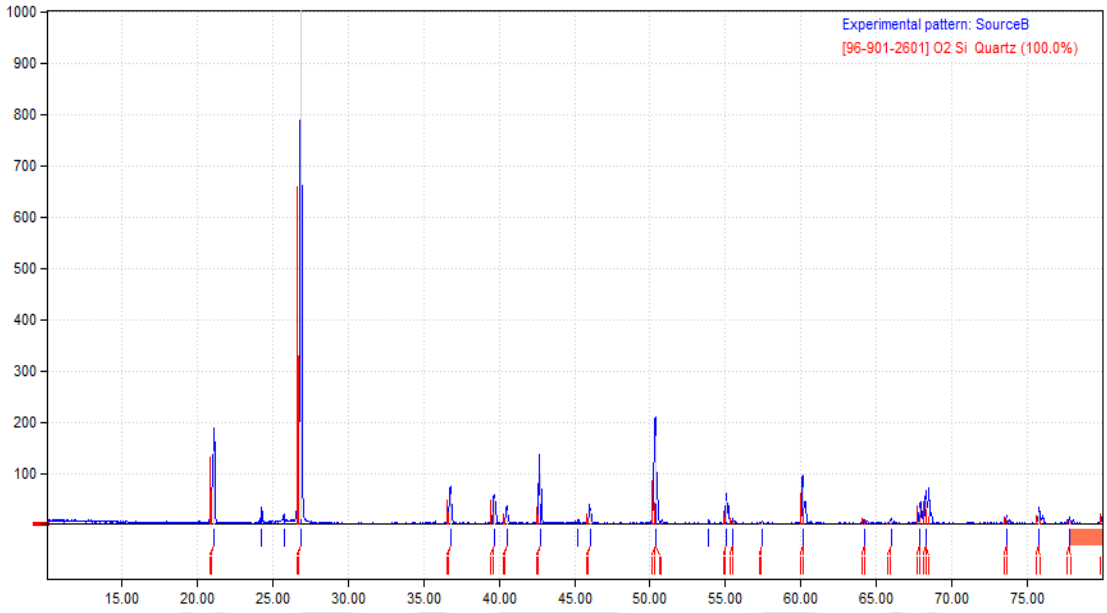

Figure 9.5 XRD pattern of quartz (Source B)

9.4.2 Field Emission Scanning Electron Microsoft (FESEM) Test

Field Emission Scanning Electron Microscopy (FESEM) is a technique to investigate the microstructure, morphology and composition of cementitious materials. Energy dispersive X-Ray Analysis (EDX) is an x-ray technique used to identify the elemental composition of materials. Silica fumes collected from Pioneer Carbide Pvt. Ltd. Guwahati (India) has been used in this present study. FESEM represents a high performance method used to investigate the structure of the materials. It is defined by easiness to prepare samples to be tested, large diversity of information reached, good resolution associated with high field depth, large and continuous range of magnifying. Papadakis et al. (1999) investigated that silica fume has particle diameters of about 0.1 micron. Two particle shapes are present, one spheroid and one cylindrical. and further added that, this particular shape can help in SF identification in cement paste during the hydration process. The silica fume agglomerations are almost spherical. The agglomeration consists of much ultra-fine silica. Some agglomerations have sizes larger than 100 mm.

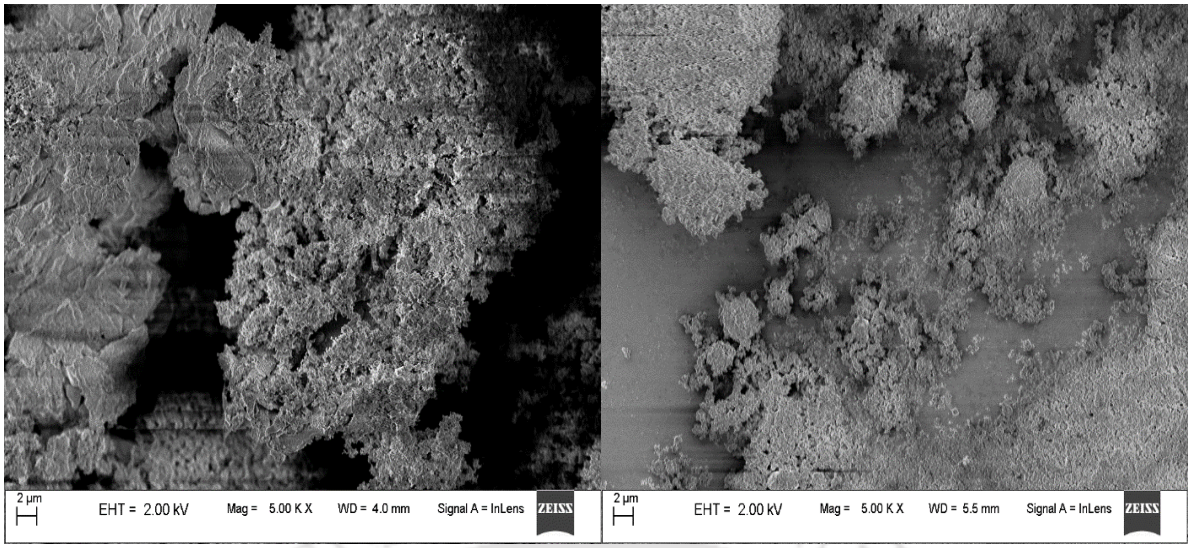

Figure 9.6 FESEM image of Silica fume (a) Source A (b) Source B

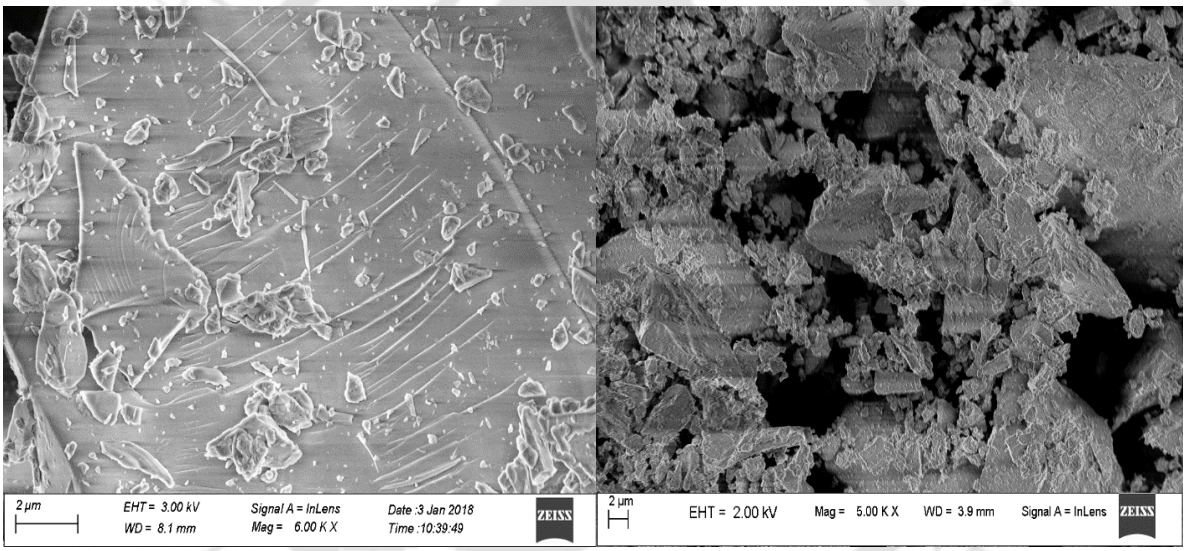

Figure 9.7 FESEM image of Quartz (a) Source A (b) Source B

FESEM images of Silica fume and Quartz powder are obtained at 4 KX and 5 KX and presented in Figure 9.6 and 9.7 respectively. Silica fume particles are appearing to be very fine, round and agglomerated.

9.4.3 Energy Dispersive X-Ray (EDX) Analysis

Energy Dispersive X-Ray (EDX), analysis is an x-ray technique used to identify the elemental composition of materials. These are attachments to SEM instruments which generates different spectra showing peaks corresponding to various elements. Moreover, image analysis and

elemental mapping of the elements is also possible. With the help of EDX rapid identification of contaminant and source can be done. EDX tests are performed on cement, silica fume and quartz from both the sources. EDX study has been conducted in a small area (area under study is limited) and at a point individually. Hence, these results do not show the same elemental composition of the materials.

EDX test on cement was done to know the proper elemental composition of it. The elemental map of cement (OPC 53) is show in Figure 9.8. EDX analysis on silica fume has been done and it is observed that silicon, oxygen shows higher peaks. Source A (Figure 9.10) of silica shows presence of silica, oxygen and calcium only but Source B (Figure 9.12) has many other elements like Al, Fe, K, etc. EDX images of quartz is represented in Figure 9.14 and 9.16. Quartz obtained from both the sources showed some impurities.

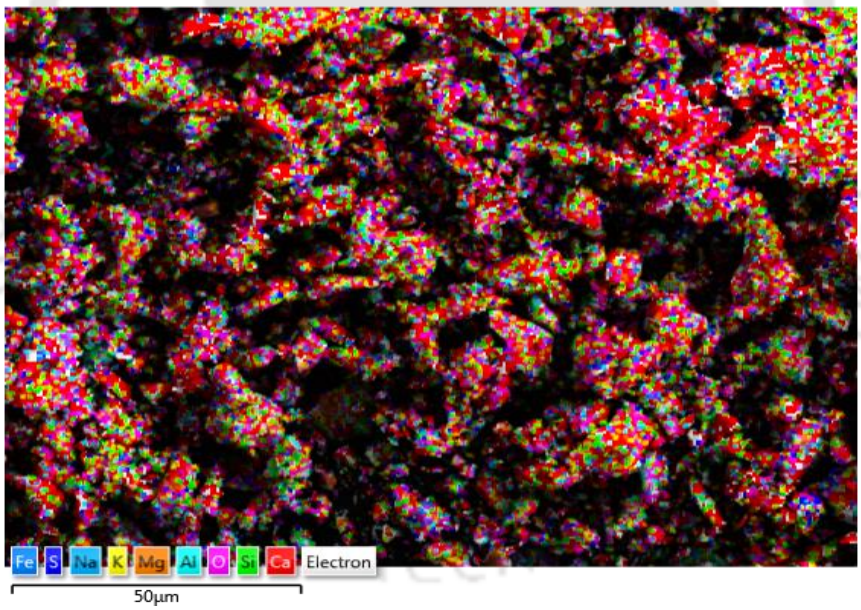

Figure 9.8 Elemental map of OPC 53 grade cement

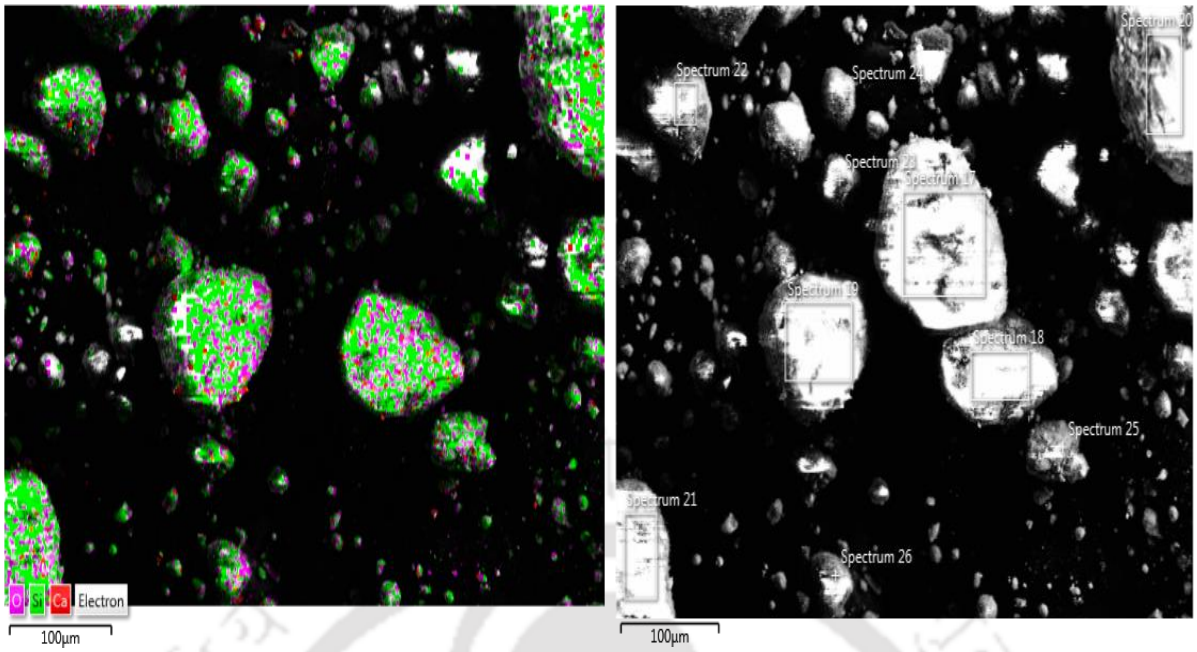

Figure 9.9 (a) Elemental map and (b) SEM image of Silica fume (Source A)

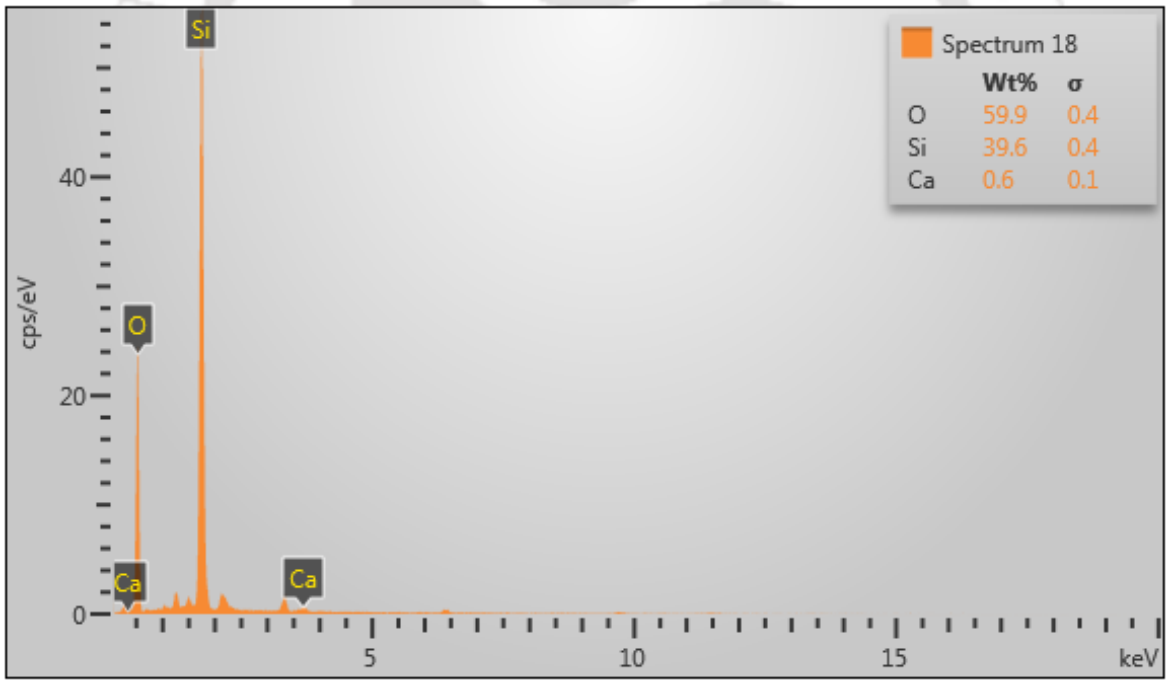

Figure 9.10 EDX pattern of Silica fumes (Source A)

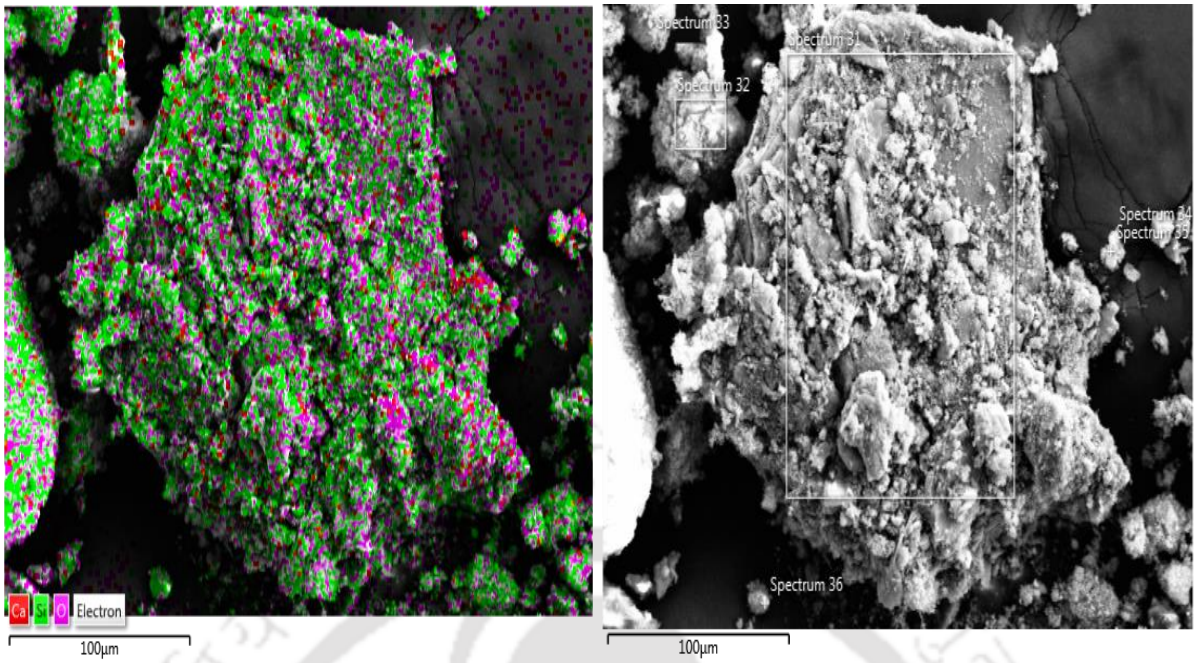

Figure 9.11 (a) Elemental map and (b) SEM image of Silica fume (Source B)

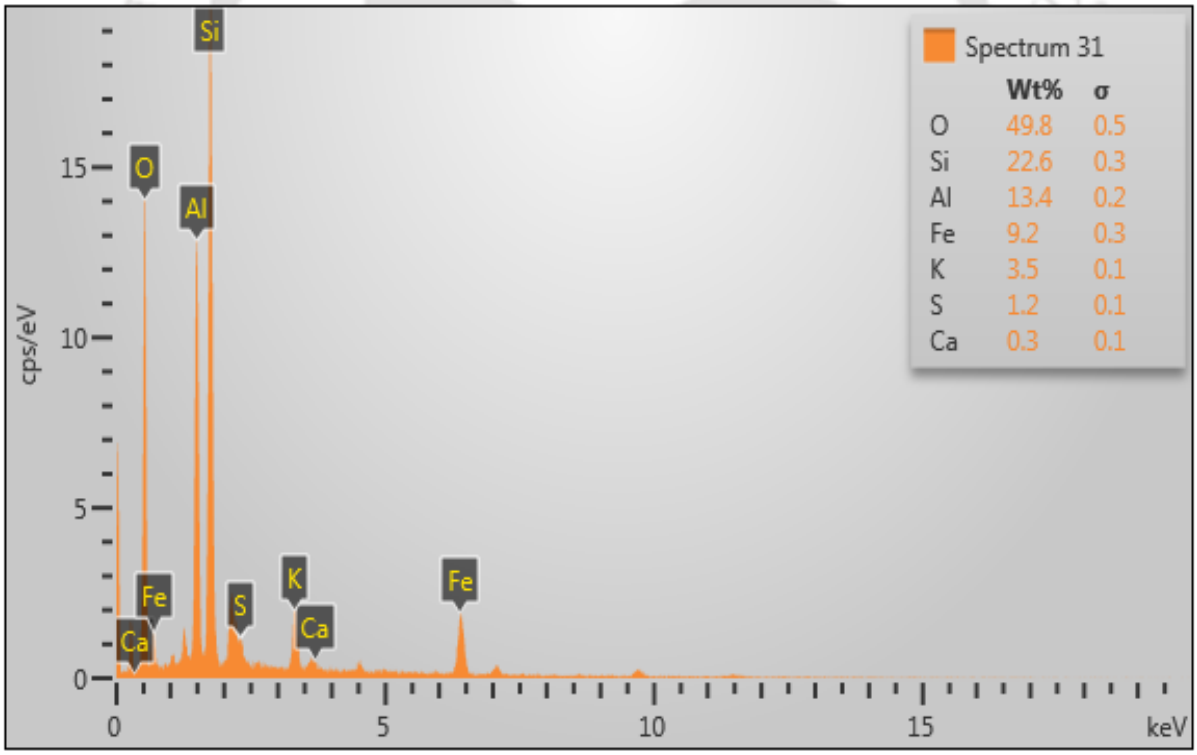

Figure 9.12 EDX pattern of Silica fumes (Source B)

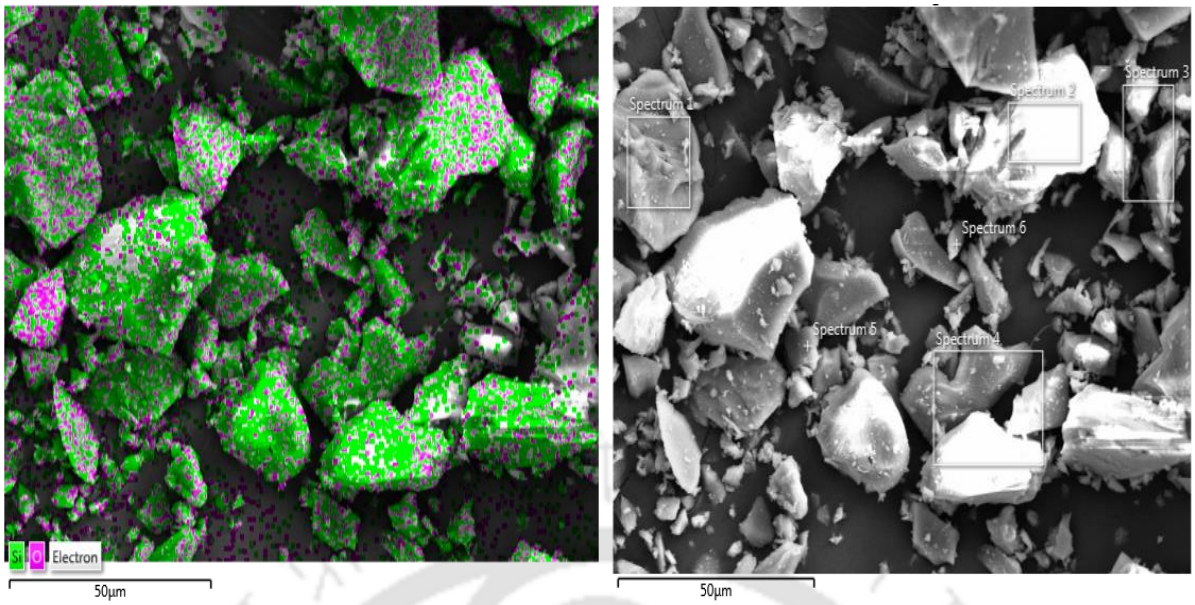

Figure 9.13 (a) Elemental map and (b) SEM image of Quartz (Source A)

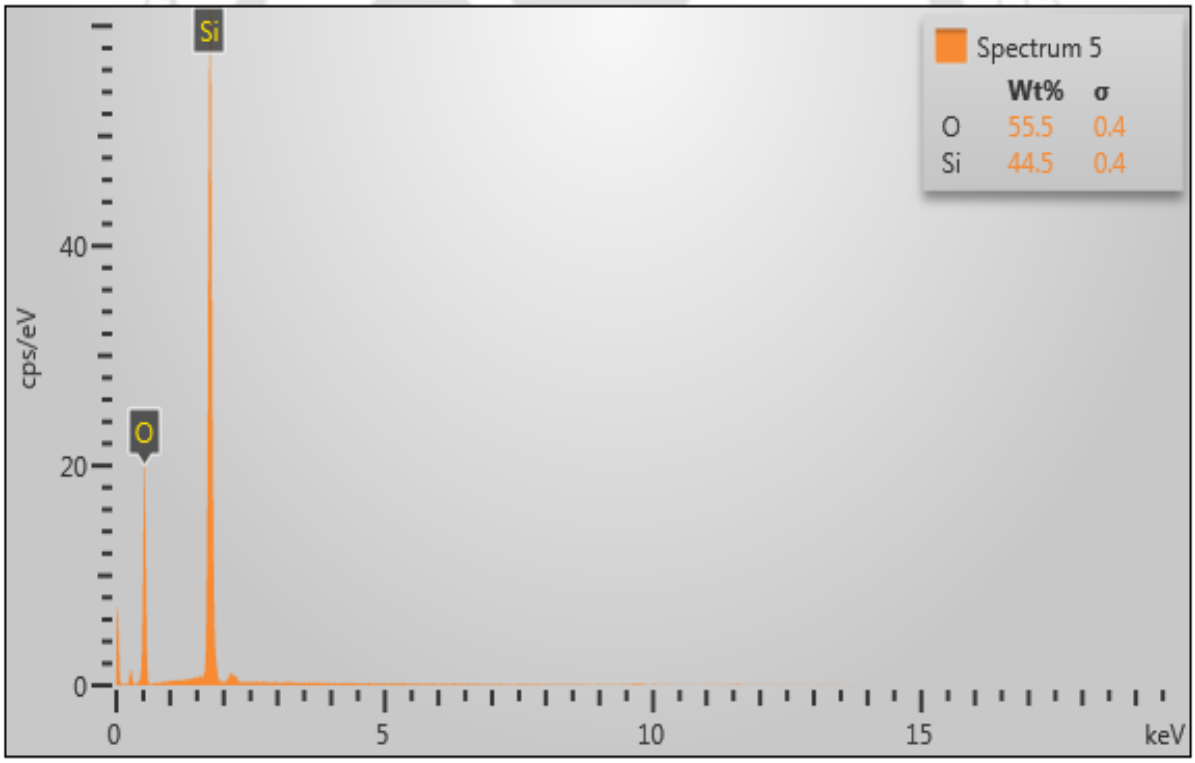

Figure 9.14 EDX pattern of Quartz (Source A)

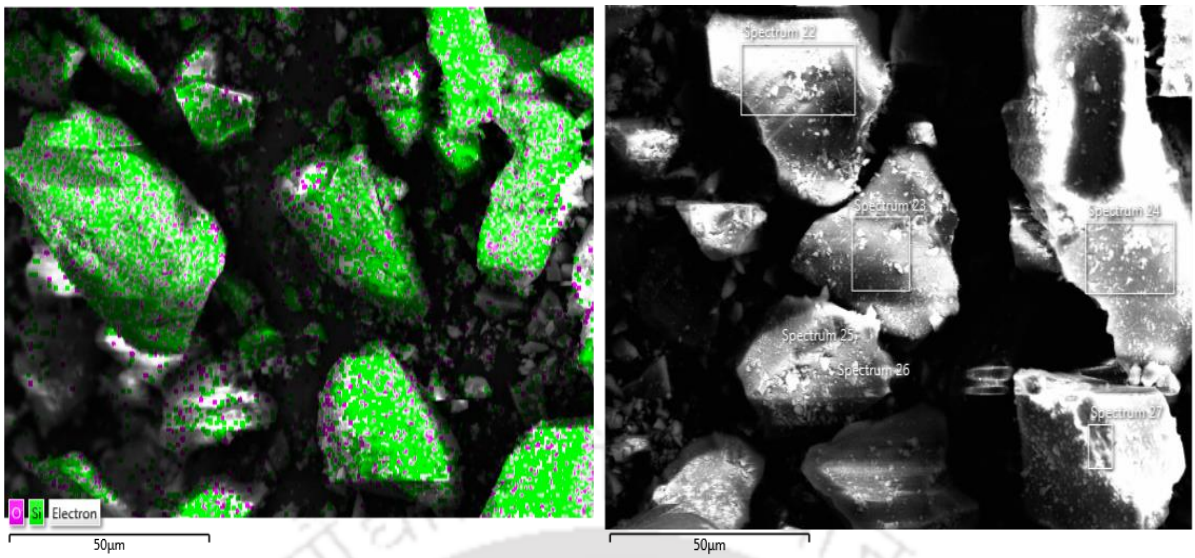

Figure 9.15 (a) Elemental map and (b) SEM image of Quartz (Source B)

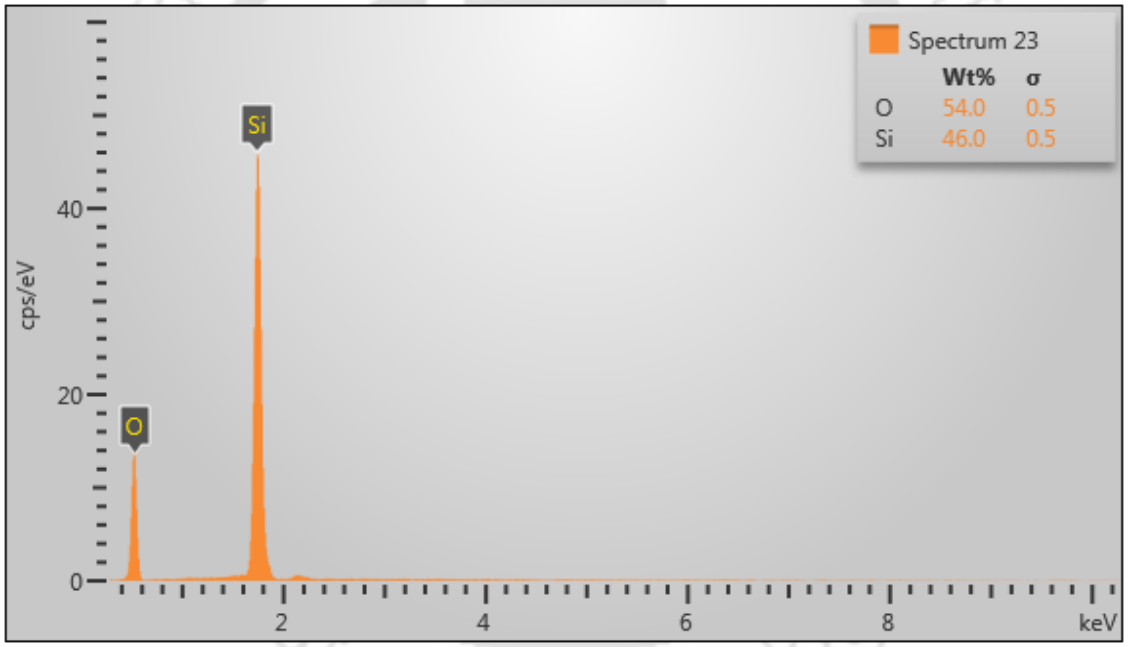

Figure 9.16 EDX pattern of Quartz (Source B)

9.5 MATERIAL PROPORTIONING

In this experimental work, the mix proportioning of concrete matrix is carried out on the basis of literature review and thus carrying out several trial mixes. As reported in the literature for high strength concrete, the range of silica fume varies from 15% to 30% of mass of cement and quartz powder about 20-40% of mass of cement. Whereas, water/binder ratio fluctuates from

0.24 to 0.28. The range of the proportions of materials used in this study in terms of cement content is given in Table 9.4. It is seen that water content or superplasticizer dosage needed increases with increase in silica or quartz content. The standard guidelines for mix design of high strength concrete is not available. Mix design calculations are done as per conventional mix design techniques. Nine cubes of size 100 x 100 x 100 mm for each mix were casted for testing under compressive testing machine.

Table 9.4 Range of different variable used in the mixes.

PARAMETERS	**RANGE**
Silica fume	0.15-0.30
Quartz	0.20-0.40
Fine Aggregate	0.8-1.4
Coarse Aggregate	0.9
Superplasticizer	0.006-0.018
Water-binder ratio	0.24-0.32

Figure 9.17 Concrete mix with aggregates (left) and without aggregates (right)

9.6 MIXING OF CONCRETE

In this experimental work, the mix proportioning of concrete matrix is carried out on the basis of literature review and thus carrying out several trial mixes. As reported in the literature for high strength concrete, the range of silica fume varies from 10% to 30% of mass of cement and quartz powder about 15-40%. Most of the mixes were mixed manually without any mixing unit. Dry materials were mixed for about 5 minute until a homogenous mix was seen. Then water mixed with the superplasticizer dosage was added and again mixed for 10 minutes. 100 x 100 x 100 mm concrete moulds were then filled with the mix with proper vibration technique. Figure 9.17 shows a concrete mix with and without aggregates, it can be seen that the powdered concrete mix is not workable. Mix C17 was machined mixed using a tilting mixer in the laboratory with same composition as mix C16. The casted cubes were demoulded after 72 hours and the curing procedure was kept as mentioned in the next section.

Table 9.5 Curing regime of concrete cubes

Curing method	**Description**
Air curing	After casting, cubes are left for 72 hours at room temperature and then demolded.
Standard curing	After demolding, cubes are kept in water until the days of testing.
Thermal curing	Cubes are kept in oven for 72 hours at 200ºC after air curing and then transferred to the water curing tank until the days of testing.

9.7 CURING CONDITIONS

All the specimens were demoulded after 3 days of casting and kept in a curing tank for standard curing for the required curing ages. Almost all mixes standard curing method is adopted. But 6 cubes of the mix C1, C2 and C3 were also kept for thermal curing following the curing details as presented in the Table 9.5. Thermal curing was done in oven (without moisture control) at a temperature of 200º C. Steam curing helps in maintaining the moisture content in the cubes while oven curing results in extracting the moisture in the cube which results in micro-cracks.

9.8 COMPRESSIVE STRENGTH TEST

After completion of curing, the cube specimens were removed from the curing tank. The compressive strength test was performed on the cube specimens in a compressive testing machine of capacity 2000 kN at the curing ages of 7, 28 and 56 days from the day of casting. Three cubes of each mix was tested from each curing age and the value of cube strength was recorded as the average value of three replicate cubes. Table 9.6 shows the cube compressive strength test results for all the ages of the concrete mix. It is observed in this study that thermal curing does not adequately improves the compressive strength of cube as presented in Table 9.7. Figure 9.18 shows the testing of concrete cubes.

Figure 9.18 Compressive Strength Testing of Cubes

Figure 9.19 (a) demonstrates that concrete mix with 20% silica fume shows better results of cube test. Although increase in its percent displays increase in strength, but with higher content, water requirement is more and the mix becomes unworkable. Excess of silica also delays the setting time of the concrete. Quartz effects the cube strength as depicted in Figure 9.19 (b). Mixes without quartz and with 30% of its content exhibits almost similar cube strength at 56 days. 20% of quartz also proves to be the optimum quantity whereas increment to 40% did not improve the strength of concrete. Increase of quartz beyond a certain percentage content is not much of use.

Table 9.6 Cube compressive strength results.

Mix	Materials				SP Dosage (%)	W/B Ratio	Average Compressive Strength (MPa)		
	Silica Fume	Quartz	F.A.	C.A.			7 D	28 D	56 D
C1	0.15	0.25	1.10	-	1.60	0.24	46.67	52.33	58.67
C2	0.20	0.25	1.10	-	1.60	0.24	42.00	56.00	74.67
C3	0.25	0.25	1.10	-	1.60	0.24	43.83	54.67	64.50
C4	0.30	0.25	1.10	-	1.60	0.24	45.83	56.33	65.50
C5	0.25	-	1.10	-	1.60	0.24	40.00	47.33	65.00
C6	0.25	0.20	1.10	-	1.60	0.24	42.33	68.33	74.33
C7	0.25	0.30	1.10	-	1.60	0.24	46.00	65.33	70.33
C8	0.25	0.40	1.10	-	1.60	0.24	41.00	48.00	52.67
C9	0.20	0.25	1.20	-	1.60	0.24	36.67	46.33	60.33
C10	0.20	0.25	1.40	-	1.60	0.24	43.33	59.83	70.00
C11	0.25	0.25	1.10	-	-	0.32	36.67	48.33	54.67
C12	0.25	0.25	1.10	-	1.00	0.28	52.00	63.67	80.33
C13	0.25	0.25	1.10	-	1.20	0.26	44.00	55.33	71.00
C14	0.25	0.25	1.10	-	1.80	0.24	37.00	47.33	60.67
C15	0.20	-	1.35	-	0.06	0.24	43.33	51.67	65.00
C16	0.20	-	0.80	0.9	0.06	0.24	41.50	58.33	67.50
C17	0.20	-	0.80	0.9	0.06	0.24	62.67	71.33	83.33

Table 9.7 Compressive strength results for cubes in standard and thermal curing.

Mix	Standard Curing		Thermal Curing	
	7 Days	28 Days	7 Days	28 Days
C1	46.67	52.33	49.33	53.17
C2	42.00	56.00	45.33	58.00
C3	43.83	54.67	45.67	57.00

Sand or fine aggregate using 1.1 times of cement content performed better than the other two mixes as seen in Figure 9.19 (c). Sand content did not show any defined pattern of effect on cube strength.

Thermal curing increased the compressive strength of concrete as shown in Figure 9.19 (d) for mix C1 but with increased silica fume content in mix C2 showed reduction in compressive strength under thermal curing. Superplasticizer dosage influences the water/binder ratio which in turn effects the concrete. Dosage of 1% of binder prove to be the optimum dosage with water/binder ratio of 0.28 than the other high dosage mix. As observed in Figure 9.19 (e), with increase in superplasticizer content, the cube strength reduces. Cube strength of mix C15 without coarse aggregate (CA) and C16 with CA 0.9 times of cement are quite close to each other as shown in Figure 9.19 (f). But mix C17 with similar material composition when machine mixed and tested, exhibits much higher strength. This may be due to homogeneity of the machine mixed concrete is way better than that of the hand mixed.

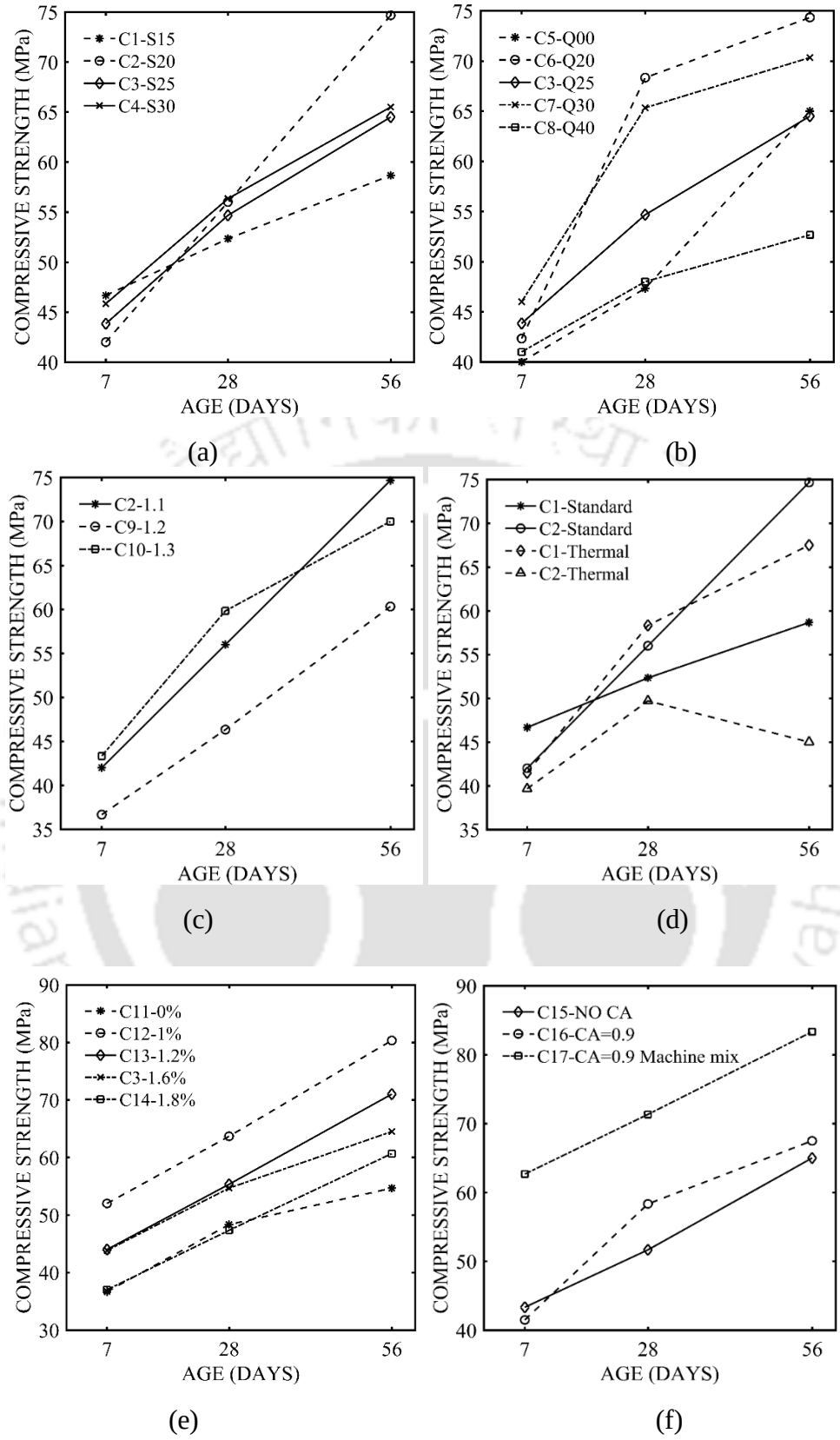

Figure 9.19 Effect of (a) silica fume, (b) quartz, (c) fine aggregate, (d) curing, (e) superplasticizer dosage and (f) coarse aggregate content on cube strength.

9.9 MICROSTRUCTURE OF CONCRETE

The morphology of one mix (C1) with no coarse aggregates was examined under Field Emission Scanning Electron Microscopy (FESEM) and Energy Dispersive X-Ray (XRD). The FESEM images of concrete powder is presented in the Figure 9.20. From the FESEM images, presence of calcium-silicate hydrate (C-S-H) gel at the 7 days of concrete is clearly observed, whereas there was lesser C-S-H gel present at 28 days that means it converted into solid form. The C-S-H is the most important component as it contributes to the strength of concrete by providing the necessary binding properties at the final stage. The morphology of C-S-H is confirmed by the reticular network formed by the irregular grains. The morphologies of the concrete clearly show ettringite phase (AFt) as needle like crystals. Ettringite is calcium sulfoaluminate formed due to the reaction of gypsum with hydrated Tricalcium aluminate (C_3A). Agglomerates of these crystals formed later absorbs water and expands in a confine space, due to which they are known to cause disruption. Calcium hydroxide (CH) having a morphology of large thin elongated crystals are not clearly visible in the FESEM images, conforming the presence of silica fume. Agglomerations of spherical particles can be identified as silica fume (SF) in hydrated cement. Along with these morphology, some micro cracks are visible. Sulphates of sodium, calcium and magnesium ions in water reacts with all phases of hydrated cement starting from CH to calcium aluminate hydrate and eventually attacks C-S-H gel at more advanced stage. The reaction results in formation of gypsum, secondary ettringite and sodium or magnesium hydroxide, which causes significant increase in volume causing cracking in concrete (Ramachandran and Beaudoin 2001). EDX plots provide the information about the comparative difference in weight (%) of various elements present in the mix and the plot is shown in Figure 9.21. EDX analysis conducted for the concrete powder and graphs are observed which shows that silicon peak with maximum intensity that is most desirable in concrete and contribute to the strength. From EDX, Ca/Si ratio of C-S-H is found to be 1.76

which is high due to a w/b ratio of 0.24 in the concrete mix. Along with Ca and Si, other elements present are O, Al, Fe, C, K, S, Mg and Na.

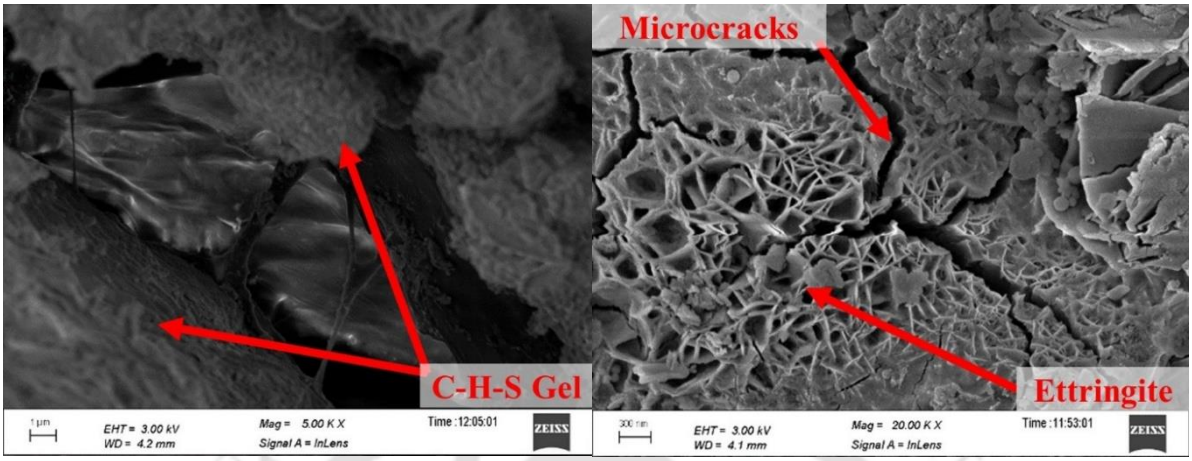

(a) (b)

Figure 9.20 FESEM images of HSC at (a) 7 days and (b) 28 days

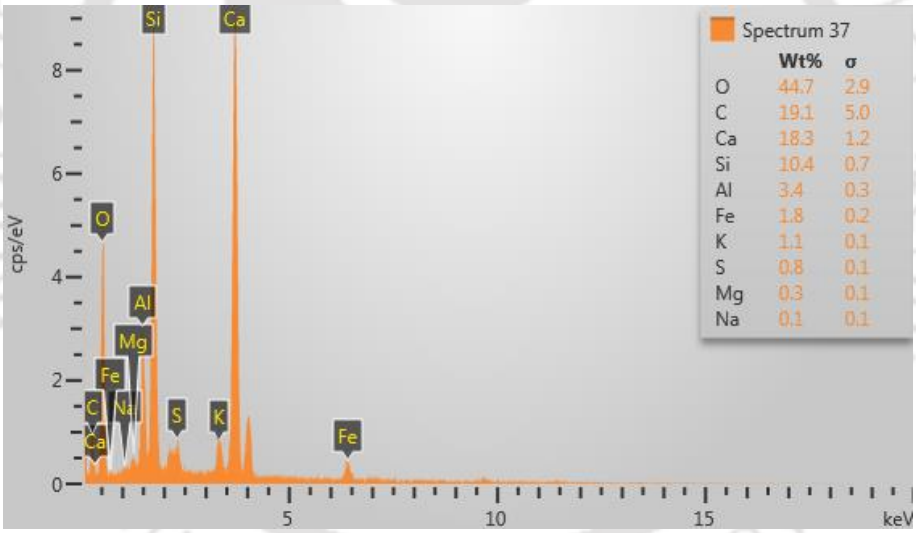

Figure 9.21 EDX pattern of concrete powder at 28 days

9.10 DISCUSSION

Though both silica fume and quartz shows more good properties in microstructural studies due to its fineness water demand is high. This extra water added in turn reduces the cube strength. No significant improvement is seen on adding quartz. So, we casted some special mixes with coarse aggregates and without quartz. The concrete mixes with coarse aggregate aggregates

(10 mm down) in an uncontrolled way gave us 63 MPa on an average at just 7 days from casting.

Reduction in water/binder ratio causes closer packing of the cementitious particles in fresh concrete and produces a paste which has less capillary porosity in the hardened paste and so a greater strength can be achieved. Mineral admixtures attributes to improvement in packing density and reduction of capillary porosity. For the concrete matrix to attain high strength, water/binder ratio is kept well below the theoretical minimum for full cement hydration but hydration of cementitious particles within the paste is enough to pack the unhydrated cores of the particles together and to reduce the interstitial porosity between these hydrated particles. Here comes the critical role of superplasticizers of making concrete workable. The flocculation of Portland cement particles and distributing material such as silica fume homogeneously through the freshly mixed concrete is also taken care of by the superplasticizers making the paste homogeneous. Hand mixing of concrete in our case is leading to, inhomogeneity and capillary pores which are considered the weakest links and thus limiting the strength of the paste. The last special concrete mix with course aggregate is mixed in machine and has more homogeneity.

The present material developed can be used in the practical development of the panels and other structure with better blast resistance in uncontrolled situations. The next chapter discusses the design and development of a blast resistant framed structure with the developed high strength concrete.

Chapter 10. DEVELOPMENT OF BLAST RESISTANT FRAMED STRUCTURE

In the present chapter, with the results obtained from all the mix, a building frame and a floor slab was casted. Concrete with the same composition as C17 was adopted for this application. The casting was conducted in an uncontrolled manner. The local fine and coarse aggregates were used directly without sieving and mixing was done by labourer in a tilting mixing machine. The maximum compressive strength obtained from the concrete casted in the slab at present from Non-destructive test is 134.5 MPa on an average. The details are discussed in this Chapter.

10.1 THREAT LEVEL

As per TM 5-1300 (1990), the blast resistant frame design is characterized by (i) simultaneous application of horizontal and vertical pressure-time loadings with peak pressures significantly in addition to conventional loads, (ii) design conditions allowing inelastic local and overall dynamic structural deformations (deflections and rotations), and (iii) design essentials given by the operational requirements of the structure. For the protective structures designed for resisting blast (both internal and external), are designed for a peak pressure of 10 bar. So, for the current structure, an 891 kg-TNT is considered at a distance of 9.6 m, which produces a blast positive peak pressure of 1 MPa (10 bar). The calculation is given below:

For a charge of TNT, $Q = 891\ \text{kg}$ and stand-off distance, $R = 9.6\ \text{m}$,

Scaled distance, $Z = \frac{R}{Q^{1/3}} = \frac{9.6}{891^{1/3}} = 0.9977\ \text{m/kg}^{1/3}$

Positive peak over pressure as given by (Kinney and Graham 1985) –

$$P_{so} = \frac{808\left[1+\left(\frac{Z}{4.5}\right)^2\right]}{\sqrt{\left[1+\left(\frac{Z}{0.048}\right)^2\right]\left[1+\left(\frac{Z}{0.32}\right)^2\right]\left[1+\left(\frac{Z}{1.35}\right)^2\right]}} \tag{10.1}$$

$$P_{so} = 10.0068 \text{ bar } (1.0 \text{ MPa})$$

The positive over pressure duration as given by (Kinney and Graham 1985) –

$$t_d = Q^{1/3} \frac{980\left[1+\left(\frac{Z}{0.54}\right)^{10}\right]}{\left[1+\left(\frac{Z}{0.02}\right)^3\right]\left[1+\left(\frac{Z}{0.74}\right)^6\right]\sqrt{\left[1+\left(\frac{Z}{6.9}\right)^2\right]}} \tag{10.2}$$

$$t_d = 4.984 \text{ m-sec} (0.00498 \text{ sec})$$

10.2 Design and Model of Blast Resistant Framed Structure

The inherent ability of rigid frames to absorb energy by formation of consecutive plastic hinges until the ultimate capacity is reached, makes a rigid framed structure suitable for blast resistant system. Moreover, this type of structure provides considerable resistance to lateral forces.

10.2.1 Model details

In the current work, the design is a preliminary design of blast resistant frames based on the design principles and the techniques recognized for the design of individual members, as given in TM 5-1300 (1990). The standard gives preliminary dynamic load factors for both the local and overall frame mechanism that helps in arriving at an equivalent static loads. Approximate estimates for required plastic bending capacities, axial loads and shears in the frame members are done based on the mechanism assumed in static plastic design. Single degree-of-freedom analyses is adopted for determining the dynamic deflection and rotations in the lateral sway

and local beam mechanism modes. A rigorous frame analysis should be executed to validate the member size adequacy designed on the basis of expected dynamic forces and moments and to also check that a trial design has meets the required deformation criteria.

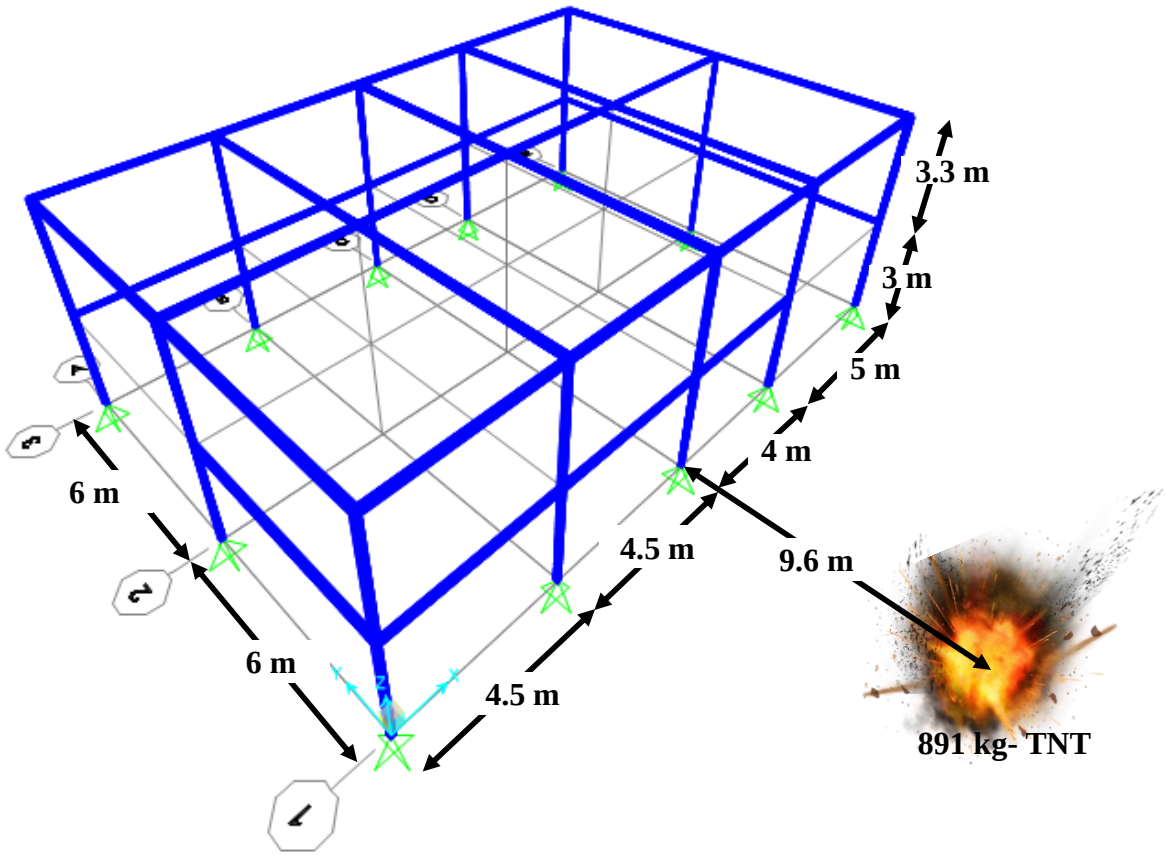

Figure 10.1 3D Frame modeled in SAP 2000

The 3D frame elements were modeled in SAP 2000 as shown in Figure 10.1 represented by a series of straight line segments. The beam and column frame is placed along the grids as shown.

10.2.2 Section and Material Model

The frame section of steel infilled with high strength concrete was developed with the help of section designer in SAP 2000 with steel tube and high strength concrete, which was manually detailed as shown in Figure 10.2. The steel tube adopted is SHS 150x150x6 of Fe 250 grade. The mass per unit volume is considered as 7850 kg/m^3 and Poisson's ratio 0.3. The remaining

parameter are set to default for Fe 250 grade steel in SAP 2000. For high strength concrete, the material properties are set for M70. The density is adopted as 2400 kg/m^3 and Poisson's ratio 0.2. the specified concrete compressive strength is given as 70 N/mm^2. The defined section is then assigned to the beams and column of the frame.

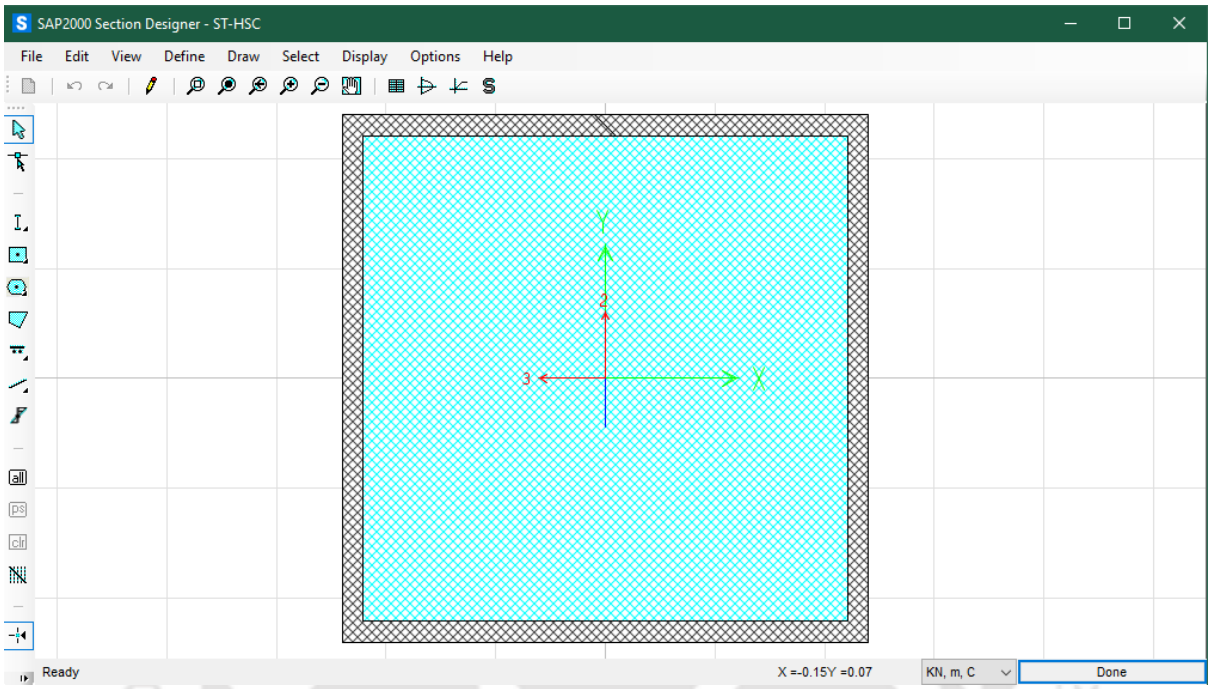

Figure 10.2 Steel tube infilled with HSC in Section designer of SAP 2000

10.2.3 Blast Load Model

Consider the buildings subjected to a blast equivalent in yield to 891 kg of TNT at a 9.6 m standoff distance. The blast effects were represented by a loading-time history that is applied to the structural members as transient loading for the dynamic analysis of the structure. It was assumed that, time varying triangular forces are acting on each beam-column joint on the front face of the buildings. These pulses have zero rise time and decay linearly as shown in Figure 10.4. The blast is applied in Y direction, where 5 columns and 7 beams are on the front face of building. For each member in the front face of the building, triangular loading functions were separately calculated taking into account their individual stand-off distance. The magnitude and the pressure-time history of the blast load is calculated using the equations given by Kinney

and Graham (1985) and is shown in the Table 10.1. The reflected pressure was multiplied with tributary area to get the peak load acting on the joints numbered in Figure 10.3.

Table 10.1 Peak magnitude and the pressure-time history of the blast load on joints

Floor	Point	R (m)	Q (kg-TNT)	Z ($m/kg^{1/3}$)	t_d (ms)	P_{so} (kN/m^2)	Load (kN)
	1	13.50	891	1.40	7.91	467.69	378.83
	2	11.02	891	1.15	6.19	739.56	848.65
I	3	10.06	891	1.05	5.40	904.28	1003.75
	4	10.82	891	1.12	6.04	769.39	594.35
	5	13.50	891	1.40	7.91	467.69	220.98
	1	14.59	891	1.52	8.59	390.98	228.72
	2	12.33	891	1.28	7.14	574.34	529.83
II	3	11.48	891	1.19	6.54	674.56	596.98
	4	12.16	891	1.26	7.02	593.04	547.08
	5	14.59	891	1.52	8.59	390.98	360.68

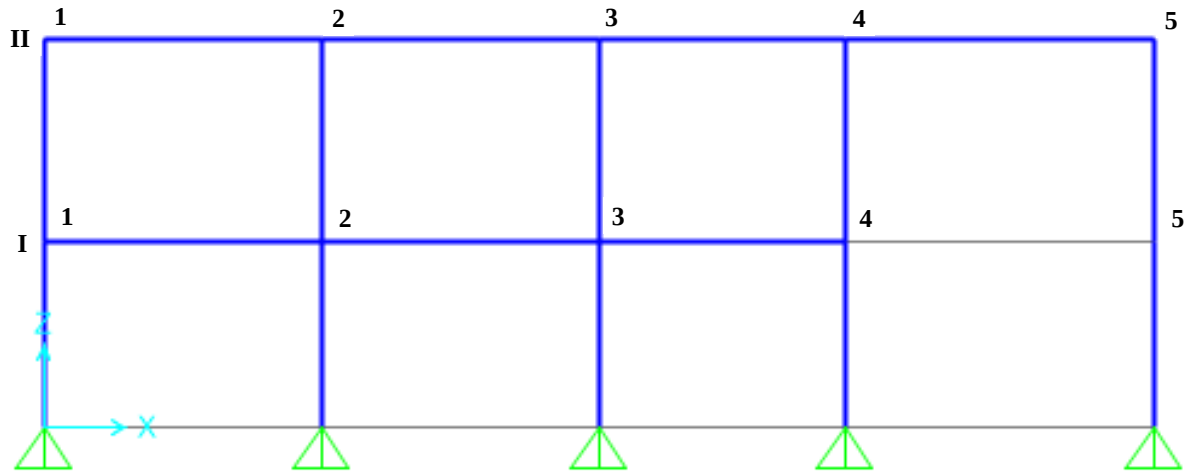

Figure 10.3 Joints of frame for blast calculation

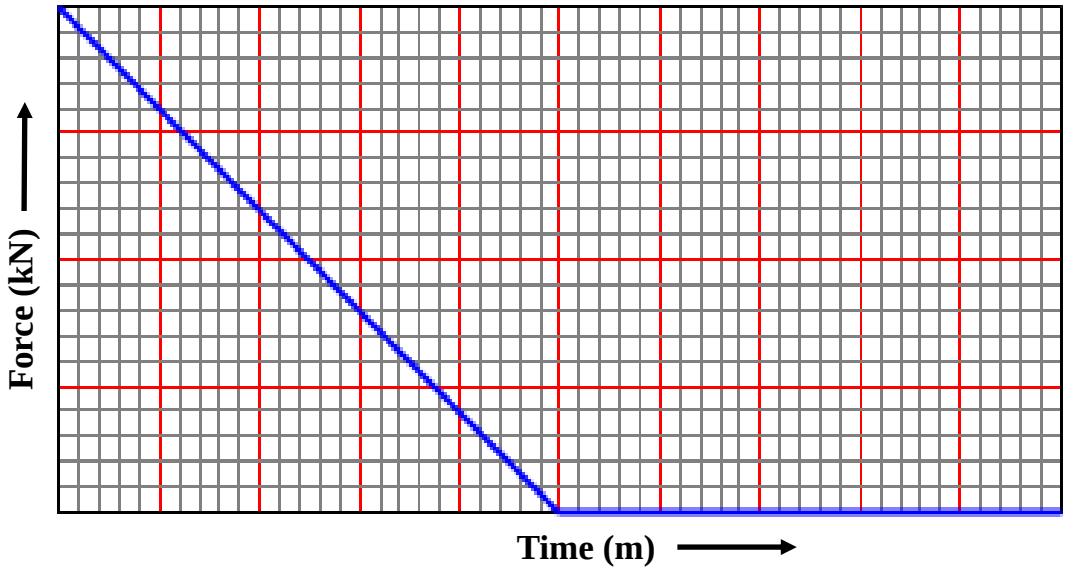

Figure 10.4 Loading-time history applied in SAP 2000

10.2.4 Analysis

The analysis was performed in SAP 2000 and the obtained modal frequencies are given in Table 10.2 and shown in Figure 10.5. The moments obtained due the blast loading is depicted in Figure 10.6.

Table 10.2 Modal Periods and Frequencies of the 3D Frame

OutputCase	StepType	StepNum	Period	Frequency	CircFreq	Eigenvalue
Text	Text	Unitless	Sec	Cyc/sec	rad/sec	rad2/sec2
MODAL	Mode	1	0.843	1.187	7.455	55.580
MODAL	Mode	2	0.602	1.661	10.436	108.910
MODAL	Mode	3	0.544	1.837	11.543	133.242
MODAL	Mode	4	0.331	3.024	19.001	361.036
MODAL	Mode	5	0.317	3.157	19.836	393.451
MODAL	Mode	6	0.295	3.385	21.266	452.243
MODAL	Mode	7	0.238	4.199	26.382	696.011
MODAL	Mode	8	0.211	4.741	29.790	887.448
MODAL	Mode	9	0.189	5.286	33.215	1103.224
MODAL	Mode	10	0.146	6.844	43.005	1849.402
MODAL	Mode	11	0.136	7.328	46.044	2120.011
MODAL	Mode	12	0.132	7.598	47.741	2279.172

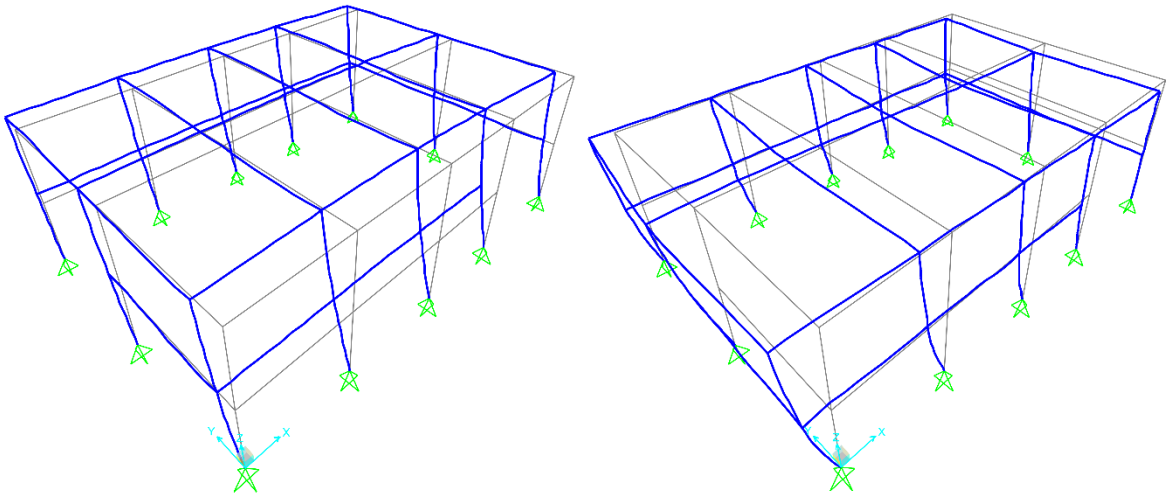

Figure 10.5 Modal Deformed shape of Frame for 1st mode (left) and 2nd mode (right)

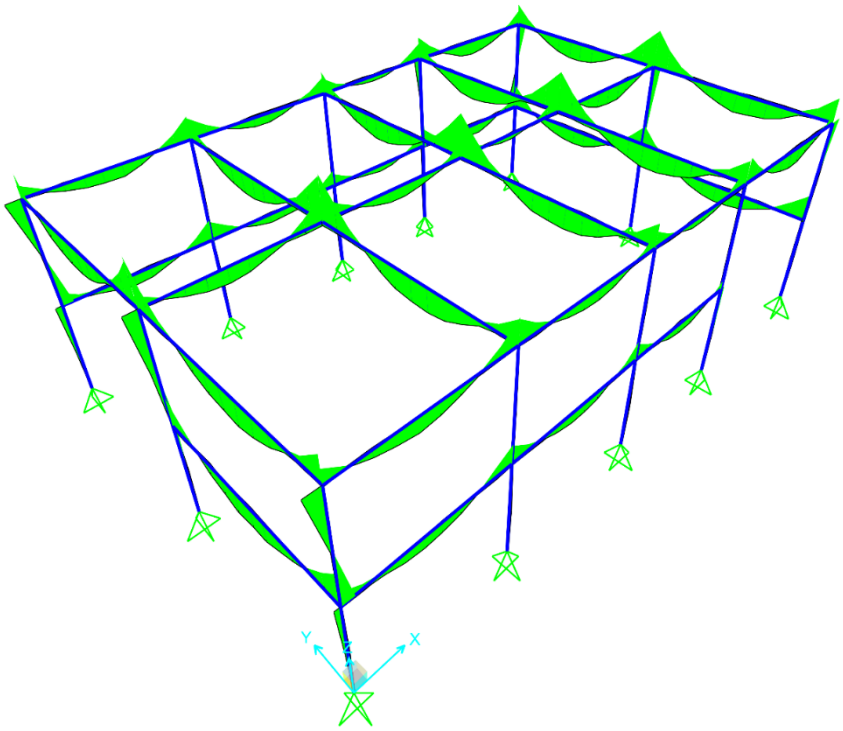

Figure 10.6 Moments obtained from analysis in SAP 2000

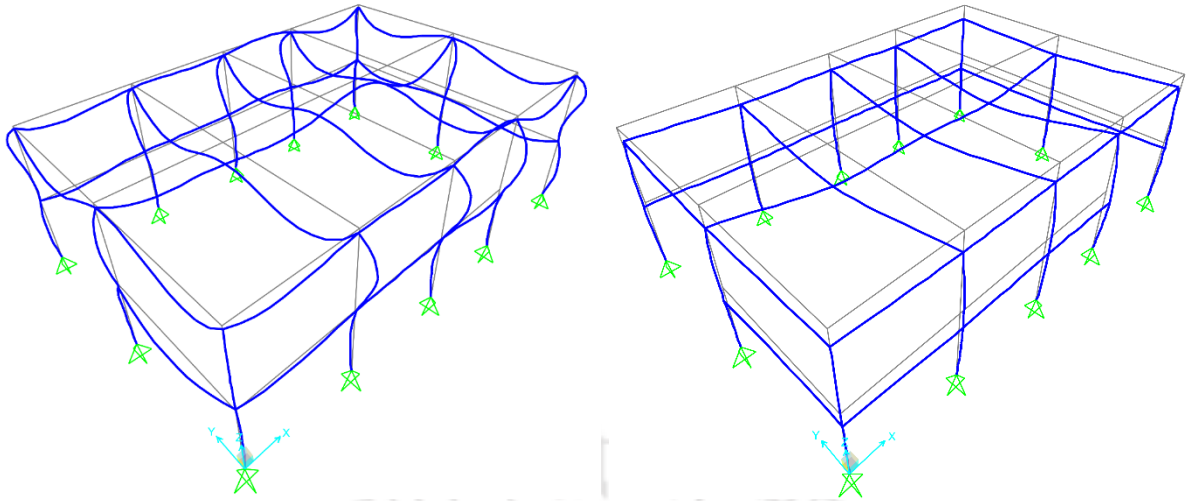

Figure 10.7 Maximum and minimum deformation (left) and deformation at 0.00498 sec (right) of Frame members for Blast loading

Time history analysis was carried out by considering non-linearity and response up to 0.01 second. Figure 10.7 shows the maximum and minimum deformations of individual members of the 3D frame and also the deformations of members at a time period of 0.00498 sec, i.e. at the end of triangular blast loading. After non-linear dynamic analysis of building subjected to blast load, we have seen that the designed section was adequate for all load types applied.

10.3 CONSTRUCTION OF BLAST RESISTANT FRAMED STRUCTURE

10.3.1 Building layout

The building site was located in a plain area cut out from a hill and was surrounded by hills on two sides. One of the building corners was first fixed at the junction of the lines parallel to two hills, keeping a safe distance from the edge of the hill. We marked one straight line with the help of thread and pegs along the longer direction of the building such that the thread suspended with the pegs is longer than 18 m. Next, along the previously suspended thread, the second corner is marked at a distance of 18 m by tying small threads, such that the pegs are almost 2.5 m away from the marked distance on both sides. Then a line perpendicular to the previous edge is established with a thread so long as it crosses one marked corner of the building and is long

enough to exceed the shorter span. With the help of the Pythagorean theorem (3m in the shorter span, 4m in the longer span, and 5m along the hypotenuse), the perpendicular angle is confirmed. Again, a small thread is tied at a distance of 12 m along the perpendicular side, and the third corner is fixed. The fourth corner is then found by measuring the edge distance of the building, i.e., 12 m and 18 m along the corresponding sides from the second and third corner, respectively, and a corner angle of ninety degrees is also ensured at the same time by the Pythagorean theorem method, which completes the building layout.

10.3.2 Column layout

Firstly, column lines along the shorter span are established with suspended threads and pegs at distances of 4.5 m, 4.5 m, 4 m, and 5 m, respectively, as shown in Figure 10.8, and columns are simultaneously marked along the grid with small thread knots. Later, the two columns in the centre line in the longer direction are recognised with a thread such that it intersects all the shorter column lines at a distance of 6 m from the longer edge of the building. After all the column points are marked with thread, the points are transferred to the ground with the help of a plumb bob and pegs.

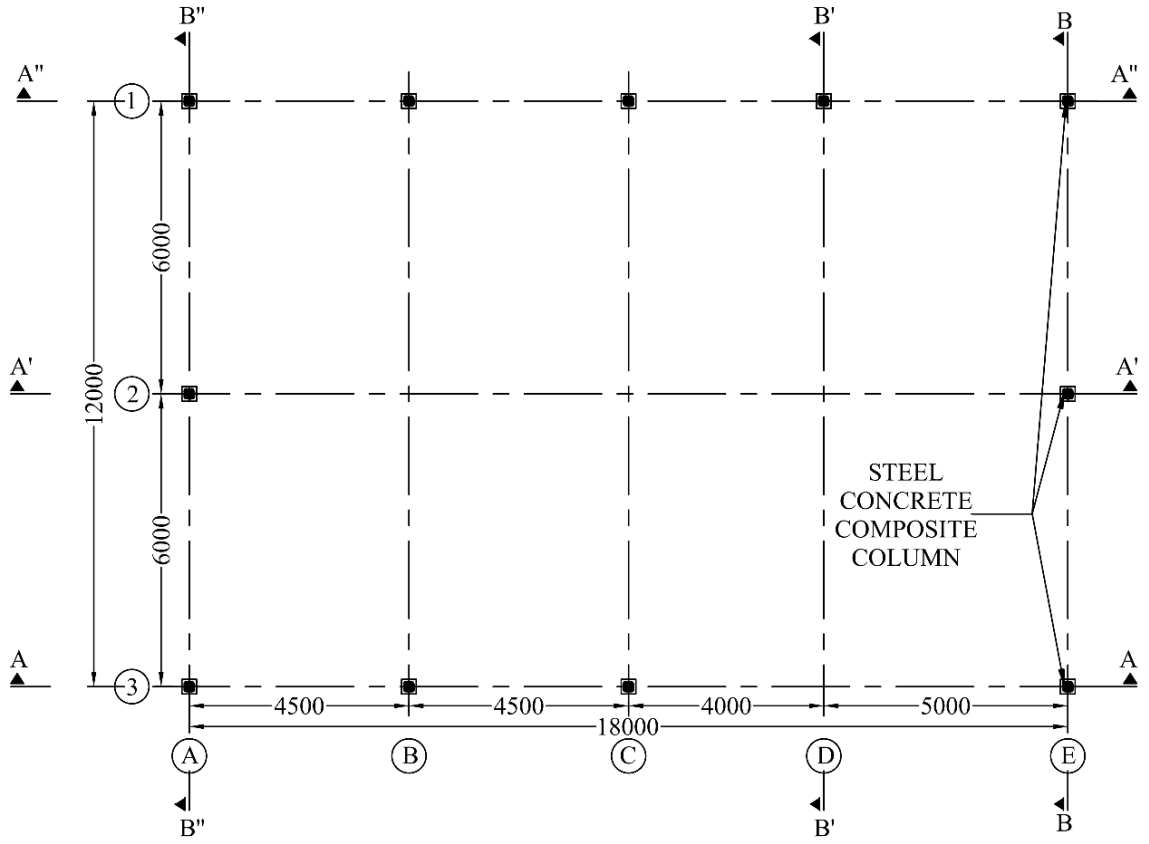

Figure 10.8 Column Layout

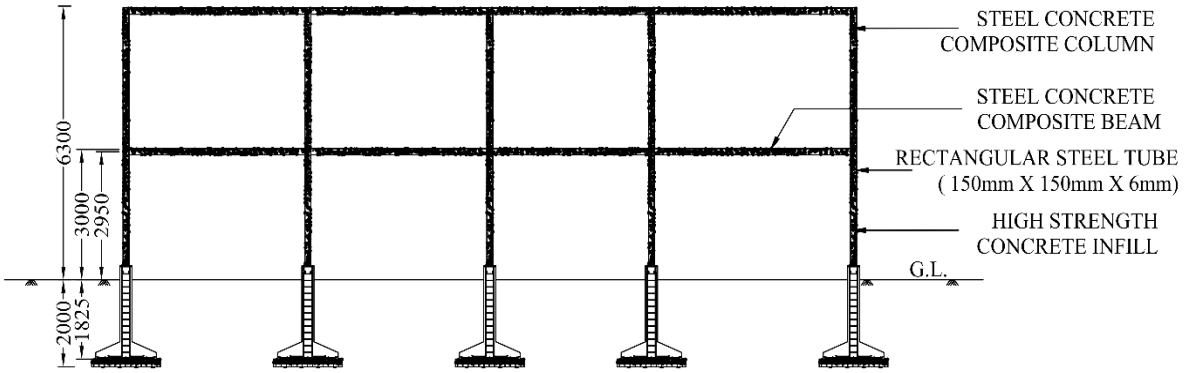

Figure 10.9 Section A"-A"

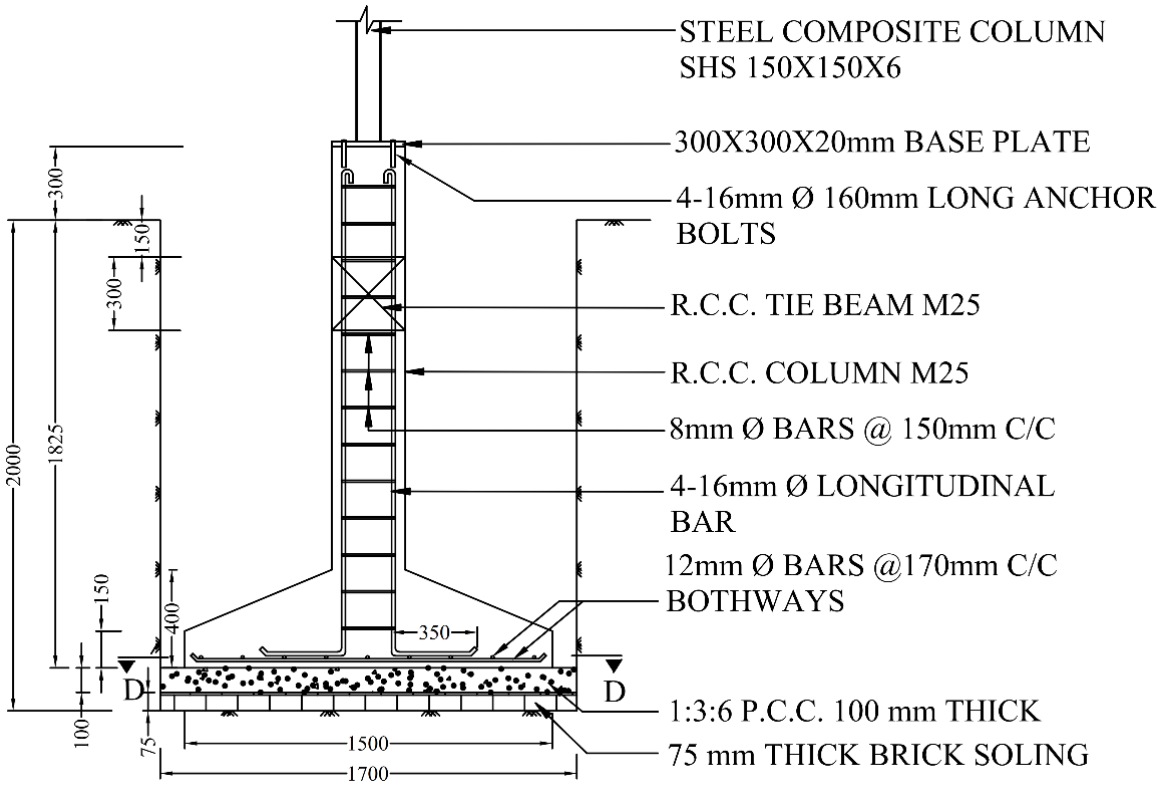

SECTION C-C

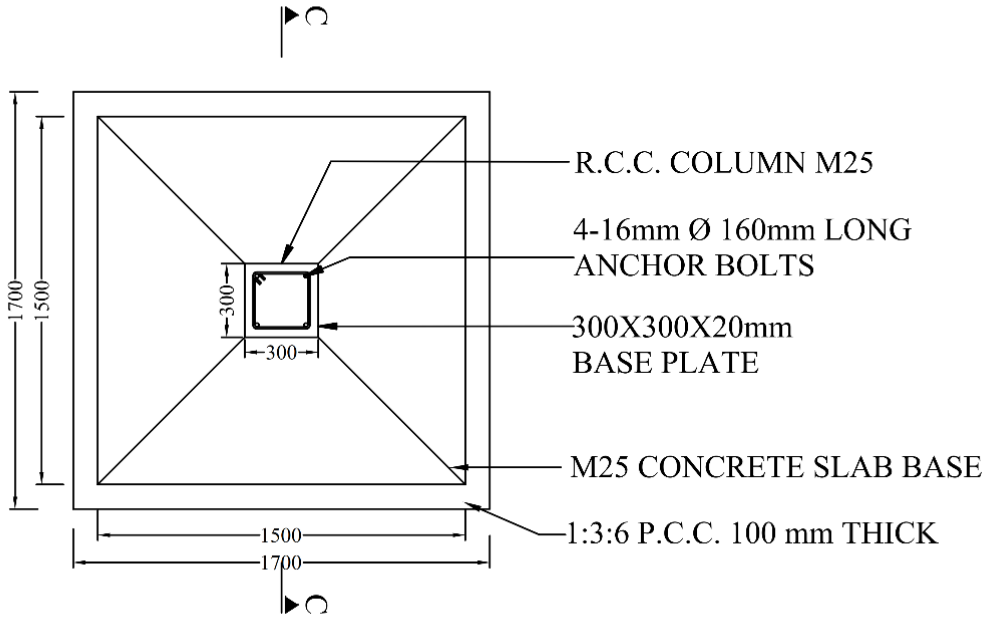

TOP VIEW

Figure 10.10 Footing Details

Figure 10.11 Photographs of laying of footing (left) and tie beam (right)

10.3.3 Excavation and Construction of Foundation and Tie Beam

The column and foundation dimensions were marked on the ground, and the earth was excavated more than the sides and depth of the foundation. The floor of the foundations was compacted first, and then a 75 mm thick brick soling was laid at the bottom. Above it, a PCC layer of 150 mm was placed so as to lay the reinforcement mesh and the column reinforcement as depicted in Figure 10.10. The formwork was placed and a clear cover was maintained for the bottom and side reinforcements (Figure 10.11). A normal strength concrete mix of M25 was adopted for the casting of footing and the columns. The columns were cast to the bottom level of the tie beam and the foundation pits were refilled with earthwork after a period of 7 days of casting. After that, the level of the tie beam was checked along the required length of the beam and the adjustments were made wherever required. The soil below the tie beams was compacted and brick soling and PCC were laid similar to that of a foundation (Figure 10.11). The reinforcements were laid for the tie beam, after which formwork was set up and then casting was completed.

10.3.4 Slab Construction

The soil is filled and levelled to the bottom of the slab with compaction. Similar to the foundation and the tie beam, a brick soling of 75 mm was first done, after which a PCC of 150

mm was laid. The dimensions of the slab were 12 m x 18 m x 0.175 m and the reinforcement was provided as per the detailing given in Figure 10.12. High strength concrete with the same composition as C17 was adopted for the casting in an uncontrolled manner with locally available fine and coarse aggregate without sieving. A tilting concrete mixing machine was used for the mixing. The maximum compressive strength achieved for the floor slab was 70 MPa in 28 days on average and 134.5 MPa on average from non-destructive tests conducted a year after. Figure 10.13 shows the concreting phases of the floor slab.

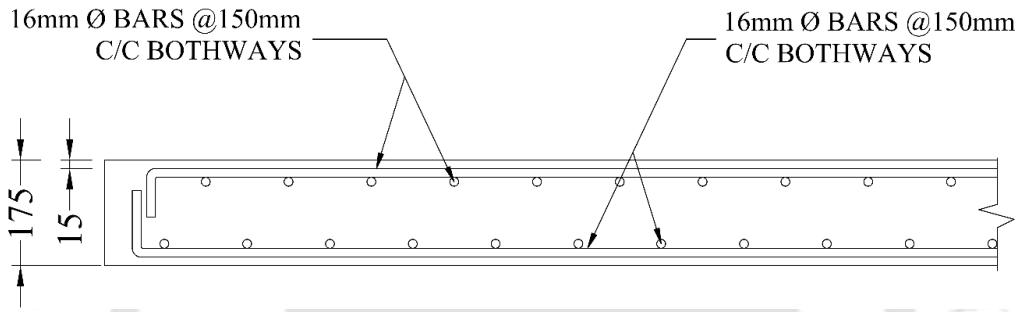

Figure 10.12 Detailing of a Floor Slab Section

Figure 10.13 Photographs of high strength concrete slab during casting.

10.3.5 Columns and Beams Construction

The elevation plan of a section of the frame is shown in Figure 10.9. Simultaneously with the slab casting, a column head of 0.3 m was also cast with high strength concrete. Before concreting, pre-fabricated columns of the specified size were marked with the help of steel plates larger than the column. The plates had bolt holes in them, and they were in the pre-fabricated structure. According to those hole placements, bolts were fixed in place by welding with the column reinforcements. During casting, the steel plate was kept to ensure the position of the column as shown in Figure 10.14. After a period of 7 days of casting and curing, the pre-fabricated steel columns were erected in place of the plates, as can be seen in Figure 10.15. Once all the columns were in place and fixed with the help of nuts and bolts, high strength concrete was poured with a funnel inside the column section, and the beam sections were also placed in an inclined position for high strength concrete infill. To ensure that the concrete compaction was good, vibrators were used during concreting. Lastly, the high strength concrete infilled steel tube beams were lifted and placed in positions with steel supports from the bottom, and then the joints were welded to secure their position.

Figure 10.14 Photographs of laying (left) and casting (right) of column base with Base plate

Figure 10.15 Photographs of steel sections for columns & beams (left); erected column sections (middle); and casting of columns & beams (right)

Figure 10.16 Photographs of the framed structure before (left) and after providing walls with CGI sheets (right)

Now the framed structure is used as Blast and Heavy Impact Simulating Mechanism (BHISM) Laboratory in located in Indian Institute of Technology Guwahati. The walls for the laboratory are of corrugated galvanized sheets (CGI) placed with the help of screws with extra steel strips provided along the height of the building (Figure 10.16 and 10.18). Roof trusses are placed along shorter span and roofing is done with corrugated galvanized sheets (CGI).

Figure 10.17 Strong floor with High compressive strength of concrete in Blast and Impact Resistant Prototype Building at IIT Guwahati having present day Compressive Strength of 134.5 MPa

Figure 10.18 Blast Resistant Framed structure used as Blast and Heavy Impact Simulating Mechanism (BHISM) Laboratory, IIT Guwahati

The cost of high strength concrete is more due to which it is not considered in construction as much as normal strength concrete. The cost per unit volume of the current HSC is approximately 45% more than normal strength concrete, but the depth of slab required also reduces. The reduction in the depth of the slab leads to deduction in the demand of material which in turn reduces the cost of construction. Moreover, the cost of labour, formwork and all other ancillaries also minimizes as the dimension and time required for constructing a slender slab is less than that of a thicker one. Finally, the cost of construction of the slab with high strength concrete is approximately 50% less than normal strength concrete. Practical application of high strength concrete mix showed that with proper consideration and planning done in mix design, high grade of concrete can also be obtained in construction field within the same overall construction cost.

Thus, for civilian as well as defense establishments, where structures are huge and limited area is available for it, application of UHSC will bring considerable changes in the present scenario of construction. This implementation will not only strengthen the structures but also will minimize the sections of the members required. The design of such structure with the panels as building blocks can be easily designed with the proposed probabilistic models and reliability factors.

CONCLUSION AND FUTURE SCOPE

The research proposed a novel probabilistic model for normal strength concrete (NRC) and Ultra-high strength concrete (UHSC) panels under air and contact blast loading individually, that is computationally efficient. The key findings of this research is jotted below:

- ✓ Three performance levels of the NRC and UHSC panel of protective structure was quantified, based on the damage occurring when subject to air and contact blast loading and with the help of D-optimal point selection scheme, the best set of cases for FE models was generated.
- ✓ Validated FE simulations were adopted to identify and record the response of the panels at the performance level when subject to air and contact explosion.
- ✓ A shape study of TNT container was also performed to determine the pressure generated by equivalent mass of charge with spherical, cubical and cylindrical shapes.
- ✓ A pressure model with correction terms for cylindrical shaped charge was developed for free air blast based on an analytical formulation.
- ✓ The data from FE simulation was used to develop deflection-based capacity and demand model for air blast, that accounts for the multi-modal response of the structure, transition of failure modes and their interaction and inherent uncertainty associated with the modeling, configuration and material properties.
- ✓ As, the damage phenomena in contact explosion is local, the capacity and demand model is based on crater diameter formed during a contact explosion.
- ✓ The developed Fragility curves verifies the proposed models of panels subjected to air and contact blast loading and accurately predicts the probability of failure of the panels at the three performance levels.

- ✓ Hazard curves were also developed for the mass of the charge for any explosion and the stand-off distance for air blast on the protective structure to identify the probabilistic distribution of the data.
- ✓ Reliability-based code calibration with a particular reliability index was performed to arrive at the load and resistance factor for the three performance level of the NRC and UHSC panel when subject to air blast.
- ✓ Similarly, the load and resistance factors were determined for the NRC and UHSC panel for contact blast.
- ✓ High strength concrete mix was developed under uncontrolled condition based on the previous literature available.
- ✓ The developed mix a used in the construction of a Blast resistant framed structure, which was modeled and designed in SAP 2000.

The developed hazard curve together with the deflection-based capacity and demand models are used to develop framework to evaluate the reliability of the panels subject to air explosion and crater diameter based for contact blast. The model takes into account the inherent uncertainties of loading and the structure. The developed probabilistic models are simple, efficient and convenient to use. The model considers the effect strain rate and of inertia due to dynamic loading.

This study circumvents the existing limitations of the current Code provisions. This study presents load and resistance factors for Code provisions are tied in turn to the Operational with Minimum Damage, Medium damage and Collapse Prevention as Performance levels unlike the load factors for the Ultimate limit state as mentioned in the present guidelines. The factors in the proposed models are based on probabilistic studies and hazard curves and not on any assumptions as currently practiced in Blast-resistant design of structures. The developed

Load and Resistance Factors for Code provisions can be used for the design of NRC and UHSC panel when subject to air blast without performing exhaustive analysis and/or experiments.

LIMITATION OF THE PRESENT RESEARCH

- Contact blast models take into account a cylindrical explosive container, which may not always be the case.
- No pressure or heat curing is utilised in the development of high-strength concrete mixtures, which can push the concrete compressive strength to new heights.

SCOPE FOR FUTURE RESEARCH

- Probabilistic analysis of one way panels and two-way rectangular panels can be performed in the same manner as this research focuses only two-way square panels.
- This research gives formulation for air blast and contact blast as a whole but separate formulations can be developed for far-field, near-field, close-in and contact blast.
- Design formulation for a complete structure made from such panels can be developed.
- Due to the constraints in processing unit, 50 FE models are considered for analysis in present study which can be refined in future by adding more simulations.

REFERENCE

Abbas, A., Adil, M., Ahmad, N., and Ahmad, I. (2019). "Behavior of reinforced concrete sandwiched panels (RCSPs) under blast load." *Engineering Structures*, 181, 476–490.

ACI. (2006). "Code Requirements for Nuclear Safety-Related Concrete Structures (ACI 349-06) and Commentary." MI, USA.

Ahlborn, T. M., Misson, D. L., Peuse, E. J., and Gilbertson, C. G. (2008). "Durability and strength characterization of ultra-high performance concrete under variable curing regimes." *Second International Symposium on Ultra High Performance Concrete*, Kassel, Germany.

Aitcin, P. C., and Mehta, P. K. (1990). "Effect of coarse aggregate characteristics on mechanical properties of high strength concrete." *ACI Materials Journal*, 87(2).

Aktan, A. E., Ellingwood, B. R., and Kehoe, B. (2007). "Performance-Based Engineering of Constructed Systems." *Journal of Structural Engineering*, 133(3), 311–323.

Alañón, A., Cerro-Prada, E., Vázquez-Gallo, M. J., and Santos, A. P. (2018). "Mesh size effect on finite-element modeling of blast-loaded reinforced concrete slab." *Engineering with Computers*, 34(4), 649–658.

Altar, L. (2010). "Ea O Ka Aina: Albania's Concrete Mushrooms." <http://islandbreath.blogspot.com/2010/05/albanias-concrete-mushrooms.html> (Aug. 10, 2021).

Arroudj, K., Zenati, A., Oudjit, M. N., Bali, A., and Tagnit-Hamou, A. (2011). "Reactivity of Fine Quartz in Presence of Silica Fume and Slag." *Engineering*, 03(06), 569.

ASCE59-11. (2011). "Blast protection of buildings." *ASCE Standard*, (59–11), 1–125.

Baker, W. E., Cox, P. A., Westine, P. S., Kulesz, J. J., and Strehlow, R. A. (1983). *Explosion Hazards and Evaluation*. Elsevier, Amsterdam.

BBC Bitesize. (2020). "What was life like in a World War One trench? - BBC Bitesize." <https://www.bbc.co.uk/bitesize/topics/zqhyb9q/articles/z8sssbk> (Aug. 10, 2021).

Beck, A. T., and De Souza, A. C. (2010). "A first attempt towards reliabilitybased calibration of brazilian structural design codes." *Journal of the Brazilian Society of Mechanical Sciences and Engineering*, 32(2), 119–127.

Becker, R. (2008). "Fundamentals of performance-based building design." *Building Simulation*, 1(4), 356–371.

Bendix, A. (2019). "A Navy weapons station full of WWII-era ammunition bunkers could be transformed into 13,000 new homes in the Bay Area | Business Insider India." <https://www.businessinsider.in/science/news/a-navy-weapons-station-full-of-wwii-era-ammunition-bunkers-could-be-transformed-into-13000-new-homes-in-the-bay-area/articleshow/71928464.cms> (Aug. 10, 2021).

Benjamin. (2014). "Bunker Allemand Saint-Malo.jpg - Wikimedia Commons." <https://commons.wikimedia.org/wiki/File:Bunker_Allemand_Saint-Malo.jpg> (Aug. 10, 2021).

Bennett, L. (2011). "The Bunker: Metaphor, materiality and management." *Culture and Organization*, 17(2), 155–173.

Beshara, F. B. A. (1994). "Modelling of Blast Loading on Above Ground Structures- I. general Phenomenology and External Blast." *Computers & Structures*, 51(5), 585–596.

Bischoff, P., and Perry, S. (1991). "Compressive Behaviour of Concrete at High Strain Rates."

Materials and Structures, 24(6), 425–450.
Box, G. E. P., and Hunter, J. S. (1957). "Multi-Factor Experimental Designs for Exploring Response Surfaces." *The Annals of Mathematical Statistics*, 28(1), 195–241.
Box, G. E. P., and Tiao, G. C. (1992). *Bayesian Inference in Statistical Analysis*. *Bayesian Inference in Statistical Analysis*, John Wiley & Sons, New York.
Brode, H. L. (1955). "Numerical Solutions of Spherical Blast Waves." *Journal of Applied Physics*, 26(6), 766–775.
Brooks, N. B., and Newmark, N. M. (1953). *The Response of Simple Structures to Dynamic Loads*. Illinois.
Castedo, R., Santos, A. P., Alañón, A., Reifarth, C., Chiquito, M., López, L. M., Martínez-Almajano, S., and Pérez-Caldentey, A. (2021). "Numerical study and experimental tests on full-scale RC slabs under close-in explosions." *Engineering Structures*, 231, 111774.
Castedo, R., Segarra, P., Alañon, A., Lopez, L. M., Santos, A. P., and Sanchidrian, J. A. (2015). "Air blast resistance of full-scale slabs with different compositions: Numerical modeling and field validation." *International Journal of Impact Engineering*, 86, 145–156.
Chauhan, R., Copeland, C. C., and Murray, M. (2018). "Improvised Explosive Devices: Anesthetic Implications." *Current Anesthesiology Reports*, 8(1).
Chen, L., Hu, Y., Ren, H., Xiang, H., Zhai, C., and Fang, Q. (2019). "Performances of the RC column under close-in explosion induced by the double-end-initiation explosive cylinder." *International Journal of Impact Engineering*, Elsevier Ltd, 132, 103326.
Chen, R., Liu, Y., Guo, X., Xia, K., and Lu, F. (2011). "Dynamic tensile properties of steel fiber reinforced concrete." *Dynamic Behavior of Materials, Springer New York*, 1, 37–42.
Chhina, R. (2014). "Last Post: Indian War Memorials Around the World." *Centre for Armed Forces Historical Research, United Service Institution of India*, <https://www.mea.gov.in/Uploads/PublicationDocs/23460_IWM_Book__11-06-2014_.pdf> (Aug. 10, 2021).
Choudhury, S., and Singh, S. M. (2013). "A Unified Approach to Performance-Based Design of RC Frame Buildings." *Journal of The Institution of Engineers (India): Series A*, 94(2), 73–82.
Ciampoli, M., and Petrini, F. (2010). "Performance-based design of offshore wind turbines." *Proceedings of the 12th International Conference on Engineering, Science, Construction, and Operations in Challenging Environments - Earth and Space 2010*, 2063–2078.
Comité Euro-International du Béton. (1993). *CEB-FIP model code 1990: Design code*. Thomas Telford Publishing.
Cooper, P. W. (1994). "Comments on TNT equivalence." *20th International Pyrotechnics Seminar*, 215–226.
Courtial, M., Noirfontaine, M. De, Dunstetter, F., Signes-frehel, M., Mounanga, P., Cherkaoui, K., and Khelidj, A. (2013). "Effect of polycarboxylate and crushed quartz in UHPC : Microstructural investigation." *Construction and Building Materials*, Elsevier Ltd, 44, 699–705.
Curione, C. (1958). "Influence of dynamic loading on structural design." *Ziviler Luftschutz*, 22(2/3), 58–66.
Daventry, B. J. (1944). "Bombs being stacked in one of the tunnels at RAF Fauld." *RAF Fauld explosion - Wikipedia*, <https://en.wikipedia.org/wiki/RAF_Fauld_explosion#/media/File:RAF_Fauld_tunnel_bombs.jpg> (Aug. 10, 2021).
Ditlevsen, O., and Madsen, H. O. (1996). *Structural reliability methods*. Wiley, New York.
Du, H., and Li, Z. (2009). "Numerical analysis of dynamic behavior of RC slabs under blast

loading." *Transactions of Tianjin University*, 15(1), 61–64.
Dusenberry, D. O. (2010). *Handbook for Blast Resistant Design of Buildings*. *Handbook for Blast Resistant Design of Buildings*, John Wiley & Sons, New Jersey, U.S.
Easa, S. M., and Yan, W. Y. (2019). "Performance-based analysis in civil engineering: Overview of applications." *Infrastructures*.
EN 1991-1-7. (2006). "Eurocode 1 - Action on structures - Part 1-7: General actions - Accidental actions." *European Committee for standardization*, 54(2).
Faber, M. H., and Sørensen, J. D. (2002). "Reliability Based Code Calibration Joint Committee on Structural Safety." *Paper for the Joint Committee on Structural Safety Draft*.
Fabrizio, L. (2004). "Fake Chalets: Unmasking the Bunkers disguised as Quaint Swiss Villas." <https://www.messynessychic.com/2015/06/26/fake-chalets-unmasking-the-bunkers-disguised-as-quaint-swiss-villas/> (Aug. 10, 2021).
FEMA-428 /BIPS-07. (2012). *Primer to Design Safe School Projects in Case of Terrorist Attacks and School Shootings*. *FEMA-428/BIPS-07 Edition 2*.
Feng, W., Chen, B., Yang, F., Liu, F., Li, L., Jing, L., and Li, H. (2021). "Numerical study on blast responses of rubberized concrete slabs using the Karagozian and Case concrete model." *Journal of Building Engineering*, 33, 101610.
Frangopol, D. M. (2008). "Probability concepts in engineering: emphasis on applications to civil and environmental engineering." *Structure and Infrastructure Engineering*, 4(5).
Gangolu, J., Kumar, A., Bhuyan, K., and Sharma, H. (2022). "Performance-based probabilistic capacity models for reinforced concrete and prestressed concrete protective structures subjected to missile impact." *International Journal of Impact Engineering*, Elsevier, 164, 104207.
Gardoni, P., Der Kiureghian, A., and Mosalam, K. M. (2002). "Probabilistic Capacity Models and Fragility Estimates for Reinforced Concrete Columns based on Experimental Observations." *Journal of Engineering Mechanics*, 128(10), 1024–1038.
Gingold, R. A., and Monaghan, J. J. (1977). "Smoothed particle hydrodynamics: theory and application to non-spherical stars." *Monthly Notices of the Royal Astronomical Society*, 181(3), 375–389.
Ginsburg, S., and Kirsch, U. (1983). "Design of Protective Structures Against Blast." *Journal of Structural Engineering*, 109(6), 1490–1506.
Godement, F. (2020). "What does India Think." <https://ecfr.eu/special/what_does_india_think/?utm_content=buffer36b65&utm_medium=social&utm_source=twitter.com&utm_campaign=buffer> (Apr. 12, 2022).
Goldenberg, R. (2020). "75 years ago, US soldiers spent their first days in Europe fighting 'the other Battle of the Bulge' | Business Insider India." <https://www.businessinsider.in/defense/news/75-years-ago-us-soldiers-spent-their-first-days-in-europe-fighting-the-other-battle-of-the-bulge/articleshow/73146814.cms> (Aug. 10, 2021).
Gong, S., Lu, Y., Tu, Z., and Jin, W. (2009). "Validation study on numerical simulation of RC response to close-in blast with a fully coupled model." *Structural Engineering and Mechanics*, Techno-Press, 32(2), 283–300.
Gunst, R. F., Myers, R. H., and Montgomery, D. C. (1996). "Response Surface Methodology: Process and Product Optimization Using Designed Experiments." *Technometrics*, 38(3).
Gurung, S. K. (2018). "Indian Army: Army makes bulletproof plan for border with modular bunkers - The Economic Times." *The Economic Times*, <https://economictimes.indiatimes.com/news/defence/army-makes-bulletproof-plan-for-border-with-modular-bunkers/articleshow/61094310.cms?from=mdr> (Aug. 10, 2021).

Ha, J. H., Yi, N. H., Choi, J. K., and Kim, J. H. J. (2011). "Experimental study on hybrid CFRP-PU strengthening effect on RC panels under blast loading." *Composite Structures*, 93(8), 2070–2082.
Habel, K., Denarie, E., and Bruhwiler, E. (2006). "Time Dependent Behavior of Elements Combining Ultra-High Performance Fiber Reinforced Concrete (UHPFRC) and Reinforced Concrete." *Materials and Structures*, 39(5), 557–569.
Hallquist, J. (2006). *LS-DYNA® theory manual*. *Livermore Software Technology Corporation*, Livermore Software Technology Corporation, Livermore, California (USA).
Harlow, E. (2018). "1941: A blast-proof brick building." *30 Rare Photos of Bomb Shelters From World War II and Beyond*, <https://www.cheatsheet.com/culture/rare-photos-of-bomb-shelters-through-history.html/> (Aug. 10, 2021).
Hassan, I. (2018). "Intense artillery shelling along LoC in Uri." *Daily News and Analysis*, <https://www.dnaindia.com/india/report-intense-artillery-shelling-along-loc-in-uri-2588212> (Aug. 10, 2021).
Held, M. (1983). "Blast Waves in Free Air." *Propellants Explosives Pyrotechnics*, 8(1), 1–8.
Henrych, J. (1979). *The Dynamics of Explosion and Its Use*. *Nuclear Technology*.
Hentz, S., Daudeville, L., and Donzé, F. V. (2004). "Identification and Validation of a Discrete Element Model for Concrete." *Journal of Engineering Mechanics*, 130(6), 709–719.
Holmquist, T. J., Johnson, G. R., and Cook, W. H. (1993). "A computational constitutive model for concrete subjected to large strains, high strain rates, and high pressures." *Proc. 14th International Symposium on Ballistics*, Quebec, 591–600.
Hu, R. W. (1999). "India's nuclear bomb and future Sino-Indian relations." *East Asia*, Transaction Periodicals Consortium, 1(17), 40–68.
Hughes, T. J. R., and Liu, W. K. (1981a). "Nonlinear finite element analysis of shells: Part I. three-dimensional shells." *Computer Methods in Applied Mechanics and Engineering*, 26(3), 331–362.
Hughes, T. J. R., and Liu, W. K. (1981b). "Nonlinear finite element analysis of shells-part II. two-dimensional shells." *Computer Methods in Applied Mechanics and Engineering*, 27(2), 167–181.
Hunter, M. T. (2014). "File:2012 Poverty distribution map in India by its states and union territories.svg - Wikipedia." *Wikipedia*, <https://en.wikipedia.org/wiki/File:2012_Poverty_distribution_map_in_India_by_its_states_and_union_territories.svg> (Aug. 10, 2021).
Hyde, D. W. (1988). *Microcomputer Programs CONWEP and FUNPRO, Applications of TM 5-855-1,'Fundamentals of Protective Design for Conventional Weapons'(User's Guide)*. Vicksburg, MS.
India Times. (2014). "The RSS Help During Indo China War." <https://www.indiatimes.com/lifestyle/self/the-rss-help-during-indo-china-war-277811.html> (Aug. 10, 2021).
ISO 2394, I. (1998). "General principles on reliability for structures." *Zurich: ISO*.
Izadifard, R. A., and Foroutan, M. (2010). "Blastwave Parameters Assessment at Different Altitude using Numerical Simulation." *Turkish J. Eng. Env. Sci.*, 34, 25–41.
Jeong, U. Y., and Tarrant, K. (2018). "Wind Loading on Tall Building Structures in Consideration of Performance-Based Design." *In Wind Engineering for Natural Hazards: Modeling, Simulation, and Mitigation of Windstorm Impact on Critical Infrastructure*, 79–95.
Johann, M. A., Albano, L. D., Fitzgerald, R. W., and Meacham, B. J. (2006). "Performance-based structural fire safety." *Journal of performance of constructed facilities*, American

Society of Civil Engineers, 20(1), 45–53.
Jones, J., Wu, C., Oehlers, D. J., Whittaker, A. S., Sun, W., Marks, S., and Coppola, R. (2009). "Finite difference analysis of simply supported RC slabs for blast loadings." *Engineering Structures*, 31(12), 2825–2832.
Joshi, M. (2018). "This book gives a detailed historical account of the 1962 Sino-Indian war - Lifestyle News." *India Today*, <https://www.indiatoday.in/lifestyle/people/story/this-book-gives-a-detailed-historical-account-of-the-1962-sino-indian-war-1207339-2018-04-08> (Aug. 10, 2021).
Jr, R. P. (2009). "Risk Assessment of Highway Bridges: A Reliability-based Approach." *The Technology Interface Journal*, 10(2), 165–172.
Jumeau, J., Wolf, D., Guthmann, L., Gorlero, N., Burel, F., and Handrich, Y. (2018). "The use of military bunkers by the European badger and red fox in Western Europe." *Urban Ecosystems*, 21(2), 395–403.
Kakogiannis, D., Van Hemelrijck, D., Wastiels, J., Palanivelu, S., Van Paepegem, W., Vantomme, J., Kotzakolios, A., and Kostopoulos, V. (2010). "Assessment of pressure waves generated by explosive loading." *Computer Modeling in Engineering and Sciences (CMES)*, 65(1), 75.
Kapoor, R. (2019). "Heavy Pak shelling in Poonch, Rajouri, Uri." *Daily Excelsior*, <https://www.dailyexcelsior.com/heavy-pak-shelling-in-poonch-rajouri-uri/> (Aug. 10, 2021).
Kecko. (2015). "Bunker - Main Entrance (18909211023).jpg - Wikimedia Commons." <https://commons.wikimedia.org/wiki/File:Bunker_-_Main_Entrance_(18909211023).jpg> (Aug. 10, 2021).
Kim, H. S., Chin, W. J., Cho, J. R., Kim, Y. J., and Yoon, H. (2015). "An Experimental Study on the Behavior of Shear Keys According to the Curing Time of UHPC." *Engineering*, 7(4), 212–218.
Kinney, G. F., and Graham, K. J. (1985). *Explosive Shocks in Air*. Springer-Verlag, New York Inc.
Klinke, I. (2018). "The Bunker and the Camp." *Camps Revisited: Multifaceted Spatialities of a Modern Political Technology*, Rowman \& Littlefield International, 281.
Kocak, Y. (2010). "A study on the effect of fly ash and silica fume substituted cement paste and mortars." *Scientific Research and Essays*, 5(9), 990–998.
Kot, C. A. (1977). "SPALLING OF CONCRETE WALLS UNDER BLAST LOAD." *Loading Cond and Struct Anal of React Containment*, J(b).
Kristoffersen, M., Pettersen, J. E., Aune, V., and Børvik, T. (2018). "Experimental and numerical studies on the structural response of normal strength concrete slabs subjected to blast loading." *Engineering Structures*, 174, 242–255.
Krošlák, J. (2017). "Partizánska základňa Matúšová - fotogaléria - mybystrica.sme.sk - SME | MY Banská Bystrica." <https://mybystrica.sme.sk/g/62553/partizanska-zakladna-matusova?gref=https%253A%252F%252Fmybystrica.sme.sk%252Fc%252F20537661%252Fpartizanska-zakladna-matusova-je-unikat-obec-k-nej-chce-skratit-cestu.html&photo=p2537620> (Aug. 10, 2021).
Lan, S., Lok, T. S., and Heng, L. (2005). "Composite structural panels subjected to explosive loading." *Construction and Building Materials*, 19(5), 387–395.
Leppänen, J. (2005). "Experiments and numerical analyses of blast and fragment impacts on concrete." *International Journal of Impact Engineering*, 31(7), 843–60.
Li, J., and Hao, H. (2013). "Influence of brittle shear damage on accuracy of the two-step method in prediction of structural response to blast loads." *International Journal of Impact*

Engineering, 54, 217–231.
Li, J., and Hao, H. (2014). "Numerical study of concrete spall damage to blast loads." *International Journal of Impact Engineering*, 68, 41–55.
Li, J., Wu, C., and Hao, H. (2015a). "Investigation of ultra-high performance concrete slab and normal strength concrete slab under contact explosion." *Engineering Structures*, 102, 395–408.
Li, J., Wu, C., and Hao, H. (2015b). "An experimental and numerical study of reinforced ultra-high performance concrete slabs under blast loads." *Materials and Design*, 82, 64–76.
Li, J., Wu, C., Hao, H., Wang, Z., and Su, Y. (2016). "Experimental investigation of ultra-high performance concrete slabs under contact explosions." *International Journal of Impact Engineering*, 93, 62–75.
Lin, X., Zhang, Y. X., and Hazell, P. J. (2014). "Modelling the response of reinforced concrete panels under blast loading." *Materials and Design*, 56, 620–628.
Lonnquist, L. (1993). "The effects of high explosives in contact with reinforced concrete slabs." *6th International Symposium on Interaction of nonnuclear Munitions with Structures*, 262–266.
Low, H. Y., and Hao, H. (2001). "Reliability analysis of reinforced concrete slabs under explosive loading." *Structural Safety*, 23(2), 157–178.
Low, H. Y., and Hao, H. (2002). "Reliability analysis of direct shear and flexural failure modes of RC slabs under explosive loading." *Engineering Structures*, 24(2), 189–198.
LSTC. (2007). *LS-DYNA Keyword User's Manual Volume I R7.1*. *Materials & Design*.
Luccioni, B. M., Ambrosini, R. D., and Danesi, R. F. (2004). "Analysis of building collapse under blast loads." *Engineering Structures*, 26(1), 63–71.
Lucy, L. B. (1977). "A numerical approach to the testing of the fission hypothesis." *The Astronomical Journal*, 82, 1013–1024.
Magnusson, J., and Hallgren, M. (2004). "Reinforced high strength concrete beams subjected to air blast loading." *Structures under shock and impact VIII*, 53–62.
Malik, Y., and Chaliha, R. R. (2012). "Serial bomb blasts in north-east india: A postmortem study." *Journal of Indian Academy of Forensic Medicine*, 34(1), 52–54.
Malindine, E. G. (Lt). (1941). "Raid on Vaagso, British commandos watch as an ammunition dump burns." *Raid (military) - Wikipedia*, <https://en.wikipedia.org/wiki/Raid_(military)#/media/File:Ammunition_dump_burns_norway.jpg> (Aug. 10, 2021).
Malvar, L. . (1998). "Review of static and dynamic properties of steel reinforcing bars." *ACI Materials Journal*, 95(5), 609–616.
Malvar, L. J., Crawford, J. E., and Morrill, K. B. (2000). "K&C concrete material model release III-automated generation of material model input." *Karagozian and Case Structural Engineers, Technical Report*, TR-99-24.3.
Mander, J. B., Priestley, M. J. N., and Park, R. (1988). "Theoretical Stress-Strain Model for Confined Concrete." *Journal of Structural Engineering*, 114(8), 1804–1826.
Mao, L., Barnett, S., Begg, D., Schleyer, G., and Wight, G. (2014). "Numerical simulation of ultra high performance fibre reinforced concrete panel subjected to blast loading." *International Journal of Impact Engineering*, 64, 91–100.
Mao, L., Barnett, S. J., Tyas, A., Warren, J., Schleyer, G. K., and Zaini, S. S. (2015). "Response of small scale ultra high performance fibre reinforced concrete slabs to blast loading." *Construction and Building Materials*, Elsevier Ltd, 93, 822–830.
Matsagar, V. A. (2016). "Comparative performance of composite sandwich panels and non-composite panels under blast loading." *Materials and Structures/Materiaux et*

Constructions, 49(1–2), 611–629.
Matte, V., and Moranville, M. (1999). "Cement & Concrete Composites Durability of Reactive Powder Composites: influence of silica fume on the leaching properties of very low water/binder pastes." *Cement and Concrete Composites*, 21, 1–9.
McVay, M. K. (1988). *Spall damage of concrete structures*.
Melchers, R. E., and Beck, A. T. (2018). *Structural reliability analysis and prediction*. John wiley & sons, Chichester, U.K.
Millard, S., Molyneaux, T., Barnett, S., and Gao, X. (2010). "Dynamic enhancement of blast-resistant ultra high performance fibre-reinforced concrete under flexural and shear loading." *International Journal of Impact Engineering*, 37(4), 405–413.
Mizokami, K. (2018). "The World's Biggest Non-Nuclear Bomb Just Got Better." *Popular Mechanics*, <https://www.popularmechanics.com/military/weapons/a15885658/massive-ordnance-penetrator-worlds-biggest-non-nuclear-bomb/>.
Moan, T. (2006). "Reliability-based structural design and code development." *16th international ship and offshore structures congress, 2006*.
Montgomery, D. C., and Runger, G. C. (2007). *Applied statistics and probability for engineers, (With CD)*. John Wiley & Sons.
Morishita, M., Tanaka, H., Ando, T., and Hagiya, H. (2004). "Effects of Concrete Strength and Reinforcing Clear Distance on the Damage of Reinforced Concrete Slabs Subjected to Contact Detonations." *Concrete Research and Technology*, Japan Concrete Institute, 15(2), 89–98.
Myers, R. H., Montgomery, D. C., and Anderson-Cook, C. M. (1996). *Response surface methodology: process and product optimization using designed experiments*. John Wiley \& Sons.
Naaman, A. E., and Wille, K. (2012). "The Path to Ultra-High Performance Fiber Reinforced Concrete (UHP-FRC): Five Decades of Progress." *3rd International Symposium on UHPC and Nanotechnology for High Performance*, 3–15.
Naito, C., Olmati, P., Trasborg, P., Davidson, J., and Newberry, C. (2015). "Assessment of Insulated Concrete Walls to Close-In Blast Demands." *Journal of Performance of Constructed Facilities*, 29(6), 04014149.
Newmark, N. M., and Hansen, R. J. (1961). *Design of blast resistant Structures*. *Shock and vibration handbook*.
Ngo, T., Mendis, P., Gupta, A., and Ramsay, J. (2007a). "Blast loading and blast effects on structures - An overview." *Electronic Journal of Structural Engineering*, 7(S1), 76–91.
Ngo, T., Mendis, P., and Krauthammer, T. (2007b). "Behavior of Ultrahigh-Strength Prestressed Concrete Panels subjected to blast loading." 133(May 2004), 1582–1590.
Nichols, G. (2016). "Munitions." <https://www.airforcemedicine.af.mil/News/Photos/igphoto/2001687588/> (Aug. 10, 2021).
Nowak, A. S., and Collins, K. R. (2012). *Reliability of structures*. CRC press.
Olmati, P., Petrini, F., and Gkoumas, K. (2014). "Fragility analysis for the Performance-Based Design of cladding wall panels subjected to blast load." *Engineering Structures*, 78, 112–120.
Olovsson, L., and Souli, M. (2000). "ALE and fluid-structure interaction capabilities in LS-DYNA." *ASME-PUBLICATIONS-PVP*, ASME; 1998, 414(1), 71–78.
Papadakis, V. G., Pedersen, E. J., and Lindgreen, H. (1999). "AFM-SEM investigation of the effect of silica fume and fly ash on cement paste microstructure." *Journal of Materials Science*, 34(4), 683–690.

Prabir, B., Pierre, L., and Naus, D. J. (2013). “NUCLEAR POWER PLANT CONCRETE STRUCTURES.” *22nd Conference on Structural Mechanics in Reactor Technology*, San Francisco, California, USA.

Prem, P., Bharatkumar, B., and Iyer, N. (2012). “Mechanical properties of ultra high performance concrete.” *Proceedings of World Academy of …*, 6(8), 1680–1689.

Priestley, M. J. N. (2000). “Performance based seismic design.” *Bulletin of the New Zealand society for earthquake engineering*, 33(3), 325–346.

Puryear, J. M. H., Stevens, D. J., Marchand, K. A., Williamson, E. B., and Crane, C. K. (2012). “ALE modeling of explosive detonation on or near reinforced-concrete columns.” *12th International LS-DYNA Users Conference, Detroit, Michigan*.

Ramachandran, V. S., and Beaudoin, J. J. (2001). *HANDBOOK OF ANALYTICAL TECHNIQUES IN CONCRETE SCIENCE AND TECHNOLOGY Principles, Techniques, and Applications*. *Handbook of Analytical Techniques in Concrete Science and Technology*.

Rao, B., Chen, L., Fang, Q., Hong, J., Liu, Z. xian, and Xiang, H. bo. (2018). “Dynamic responses of reinforced concrete beams under double-end-initiated close-in explosion.” *Defence Technology*, 14(5), 527–539.

Razaqpur, A. G., Campidelli, M., and Foo, S. (2012). “Experimental versus analytical response of structures to blast loads.” *Advances in Protective Structures Research: IAPS Special Publication 1 - Proceedings of the IAPS Forum on Recent Research Advances on Protective Structures*, CRC Press, London, 163–194.

Razaqpur, A. G., Tolba, A., and Contestabile, E. (2007). “Blast loading response of reinforced concrete panels reinforced with externally bonded GFRP laminates.” *Composites Part B: Engineering*, 38(5–6), 535–546.

Rebentrost, M., and Wight, G. (2008). “Behaviour and Resistance of Ultra High Performance Concrete to Blast Effects.” *2nd Int. Symp. On Ultra High Performance Concrete (UHPC)*, Kassel, Germany, 735–742.

Reda, M. M., Shrive, N. G., and Gillott, J. E. (1999). “Microstructural investigation of innovative UHPC.” *Cement and Concrete Research*, 29(3), 323–329.

Reddit. (2015). “Neighbors assemble Anderson air raid shelters in their backyard gardens, 1940 : TheWayWeWere.” <https://www.reddit.com/r/TheWayWeWere/comments/3kspll/neighbors_assemble_anderson_air_raid_shelters_in/> (Aug. 10, 2021).

Reifarth, C., Castedo, R., Santos, A. P., Chiquito, M., López, L. M., Pérez-Caldentey, A., Martínez-Almajano, S., and Alañon, A. (2021). “Numerical and experimental study of externally reinforced RC slabs using FRPs subjected to close-in blast loads.” *International Journal of Impact Engineering*, Elsevier Ltd, 156, 103939.

Remennikov, A., Mentus, I., and Uy, B. (2015). “Explosive breaching of walls with contact charges: Theory and applications.” *International Journal of Protective Structures*, 629–647.

Ren, G. M., Wu, H., Fang, Q., and Kong, X. Z. (2017). “Parameters of Holmquist–Johnson–Cook model for high-strength concrete-like materials under projectile impact.” *International Journal of Protective Structures*, SAGE Publications Inc., 8(3), 352–367.

Richard, P., and Cheyrezy, M. (1995). “Composition of reactive powder concretes.” *Cement and Concrete Research*, 25(7), 1501–1511.

Saad, M., Abo-El-Eneinf, S. A., Hanna, G. B., and Kotkata, M. F. (1996). “Effect of temperature on physical and mechanical properties of concrete containing silica fume.” *Cement and Concrete Research*, 26(5), 669–675.

Sadovskiy. (2004). *Mechanical Effects of Air Shock Waves from Explosions according to Experiments (1952)*. Geophysics and Physics of Explosion, Nauka Press, Moscow.
Schwer, L. (2016). "Jones-Wilkens-Lee (JWL) Equation of State with Afterburning." *14th International LSDYNA Users Conference Session: Constitutive Modelling*.
Sharma, H., Hurlebaus, S., and Gardoni, P. (2012). "Performance-based response evaluation of reinforced concrete columns subject to vehicle impact." *International Journal of Impact Engineering*, 43, 52–62.
Smilowitz, R., Blewett, W., Williams, P., and Chipley, M. (2006). "Design guidance for shelters and safe rooms." *US Department of Homeland Security, Federal Emergency Management Agency, Washington DC, FEMA*, 453.
Speier, O. (2013). "Historic bunker Stock Photo by ©OlafSpeier 23596787." <https://depositphotos.com/23596787/stock-photo-historic-bunker.html> (Aug. 10, 2021).
Stander, N., and Craig, K. J. (2002). "Response Surface and Sensitivity-Based Optimization in LS-OPT: A Benchmark Study." *7th International LS-DYNA Users Conference*, 9–18.
Stewart, M. G. (2019). "Reliability-based load factors for airblast and structural reliability of reinforced concrete columns for protective structures." *Structure and Infrastructure Engineering*, 15(5), 634–646.
Stewart, M. G., and Li, J. (2021). "Risk-based assessment of blast-resistant design of ultra-high performance concrete columns." *Structural Safety*, 88, 102030.
Stochino, F., Tabandeh, A., Gardoni, P., and Sassu, M. (2021). "Physics-based probabilistic demand model and reliability analysis for reinforced concrete beams under blast loads." *Engineering Structures*, 248, 112932.
Szydlowski, R., and Bednarz, K. (2018). "Material and construction solutions of war shelters with the example of Hitler's main headquarters in the Wolf's Lair." *Czasopismo Techniczne*, 11(1), 87–101.
Tabatabaei, Z. S., Volz, J. S., Baird, J., Gliha, B. P., and Keener, D. I. (2013a). "International Journal of Impact Engineering Experimental and numerical analyses of long carbon fi ber reinforced concrete panels exposed to blast loading." *International Journal of Impact Engineering*, Elsevier Ltd, 57, 70–80.
Tabatabaei, Z. S., Volz, J. S., Baird, J., Gliha, B. P., and Keener, D. I. (2013b). "Experimental and numerical analyses of long carbon fiber reinforced concrete panels exposed to blast loading." *International Journal of Impact Engineering*, 57, 70–80.
Tai, Y. S. (2009). "Flat ended projectile penetrating ultra-high strength concrete plate target." *Theoretical and Applied Fracture Mechanics*, 51(2), 117–128.
Tan, S. H., Poon, J. K., Chan, R., and Chng, D. (2012). "Retrofitting of reinforced concrete beam-column via steel jackets against close-in detonation." *12th international LS-DYNA users conference*, 1–12.
Task Committee on Blast-Resistant Design of the Petrochemical Committee of the Energy Division of ASCE. (2010). *Design of Blast-Resistant Buildings in Petrochemical Facilities*. American Society of Civil Engineers.
Tellgmann, O. (1961). "German soldiers of the 11th Reserve Hussar Regiment fighting from a trench, on the Western Front, 1916." *Bundesarchiv Bild 136-B0560, Frankreich, Kavalleristen im Schützengraben - Trench warfare - Wikipedia*, <https://en.wikipedia.org/wiki/Trench_warfare#/media/File:Bundesarchiv_Bild_136-B0560,_Frankreich,_Kavalleristen_im_Schützengraben.jpg> (Aug. 10, 2021).
The Economic Times. (2018). "Bunkers: Government approves 14,460 bunkers for civilians hit by Pak firing - The Economic Times."

<https://economictimes.indiatimes.com/news/defence/government-approves-14460-bunkers-for-civilians-hit-by-pak-firing/articleshow/62804901.cms> (Aug. 10, 2021).

The Statesman. (2020). "Construction of bunkers sped up in border areas of Jammu." <https://www.thestatesman.com/india/construction-of-bunkers-sped-up-in-border-areas-of-jammu-1502763305.html> (Aug. 10, 2021).

Thiagarajan, G., Kadambi, A. V., Robert, S., and Johnson, C. F. (2015). "Experimental and finite element analysis of doubly reinforced concrete slabs subjected to blast loads." *International Journal of Impact Engineering*, 75, 162–173.

Thoft-Christensen, P., and Baker, M. J. (1982). *Structural Reliability Theory and Its Applications*. *Structural Reliability Theory and Its Applications*.

TM 5-1300. (1990). "Structures to Resist the Effects of Accidental Explosions." *Departments of the Army, The Navy and The Air Force*, 1796.

Trajkovski, J., Kunc, R., Perenda, J., and Prebil, I. (2014). "Minimum mesh design criteria for blast wave development and structural response – MMALE method." *Latin American Journal of Solids and Structures*, 11(11), 1999–2017.

TranSystems Corporation. (2017). "Ammunition & Explosive Magazines | WBDG - Whole Building Design Guide." <https://www.wbdg.org/building-types/ammunition-explosive-magazines> (Aug. 11, 2021).

U.S. War Department. (1944). "German Stone Bunkers, WWII Tactical and Technical Trends, No. 47, June 1, 1944 (Lone Sentry)." *Tactical and Technical Trends, No. 47*, <https://www.lonesentry.com/articles/ttt09/stone-bunkers.html> (Aug. 10, 2021).

Uche, O. A. U., and Afolayan, J. O. (2008). "Reliability-based Rating for Reinforced Concrete Columns." *Journal of Engineering Technology*, 3(1), 1–20.

US Department of Defense. (2008). "UFC 3-340-02. Structures to resist the effects of the accidental explosions." *Unified Facilities Criteria*, (May 2005).

Wang, W., Zhang, D., Lu, F., Wang, S. C., and Tang, F. (2012). "Experimental study on scaling the explosion resistance of a one-way square reinforced concrete slab under a close-in blast loading." *International Journal of Impact Engineering*, 49, 158–164.

Weidner, A. M. (2013). *Dynamic properties of concrete and fiber reinforced concrete at room and elevated temperatures*.

Whittaker, A., Hamburger, R., and Mahoney, M. (2003). "Performance-Based Engineering of Buildings for Extreme Events." *In AISC-SINY Symposium on Resisting blast and Progressive Collapse*, 55–66.

Wikipedia. (2017). "Terrorist incidents map of India1970-2016.svg - Wikimedia Commons." <https://commons.wikimedia.org/wiki/File:Terrorist_incidents_map_of_India1970-2016.svg> (Aug. 10, 2021).

Wille, K., Kim, D. J., and Naaman, A. E. (2011). "Strain-hardening UHP-FRC with low fiber contents." *Materials and Structures*, 44(3), 583–598.

Wille, K., and Naaman, A. E. (2010). "Fracture energy of UHP-FRC under direct tensile loading." *Fracture Mechanics of Concrete and Concrete Structures*, (May 23-28), 65–72.

Wille, K., Naaman, A. E., El-Tawil, S., and Parra-Montesinos, G. J. (2012). "Ultra-high performance concrete and fiber reinforced concrete: achieving strength and ductility without heat curing." *Materials and Structures*.

Wu, C., Oehlers, D. J., Rebentrost, M., Leach, J., and Whittaker, A. S. (2009). "Blast testing of ultra-high performance fibre and FRP-retrofitted concrete slabs." *Engineering Structures*, 31(9), 2060–2069.

Xu, J., Wu, C., and Li, Z. X. (2014). "Analysis of direct shear failure mode for RC slabs under external explosive loading." *International Journal of Impact Engineering*, 69, 136–148.

Yamaguchi, M., Murakami, K., Takeda, K., and Mitsui, Y. (2011). "Scientific paper: Blast resistance of polyethylene fiber reinforced concrete to contact detonation." *Journal of Advanced Concrete Technology*, 9(1), 63–71.

Yamawaki, K., Kitamura, H., Tsuneki, Y., Mori, N., and Fukai, S. (2000). "Introduction of a Performance-Based Design." *Wcee, Paper 1511*.

Yang, S. L., Millard, S. G., Soutsos, M. N., Barnett, S. J., and Le, T. T. (2009). "Influence of aggregate and curing regime on the mechanical properties of ultra-high performance fibre reinforced concrete (UHPFRC)." *Construction and Building Materials*, Elsevier Ltd, 23(6), 2291–2298.

Yao, S., Zhang, D., Chen, X., Lu, F., and Wang, W. (2016). "Experimental and numerical study on the dynamic response of RC slabs under blast loading." *Engineering Failure Analysis*, 66, 120–129.

Yi, N. H., Kim, J. H. J., Han, T. S., Cho, Y. G., and Lee, J. H. (2012). "Blast-resistant characteristics of ultra-high strength concrete and reactive powder concrete." *Construction and Building Materials*, 28(1), 694–707.

Yue, S., Qiu, Y., Zhang, N., and Wang, M. (2017). "Analytical study of local damage on concrete slab subjected to a contact explosion." *Journal of Vibroengineering*, 19(2), 908–929.

Zhang, X., Yang, X., Chen, Z., and Deng, G. (2006). "Explosion spalling of reinforced concrete slabs with contact detonations." *Qinghua Daxue Xuebao/Journal of Tsinghua University*, 46(6), 765–768.

Zhao, C., Lu, X., Wang, Q., Gautam, A., Wang, J., and Mo, Y. L. (2019a). "Experimental and numerical investigation of steel-concrete (SC) slabs under contact blast loading." *Engineering Structures*, 196, 109–337.

Zhao, C., Wang, Q., Lu, X., and Wang, J. (2019b). "Numerical study on dynamic behaviors of NRC slabs in containment dome subjected to close-in blast loading." *Thin-Walled Structures*, 135, 269–284.

Zhou, X. Q., and Hao, H. (2009). "Mesoscale modelling and analysis of damage and fragmentation of concrete slab under contact detonation." *International Journal of Impact Engineering*, 36(12), 1315–1326.

Zhou, X. Q., Kuznetsov, V. A., Hao, H., and Waschl, J. (2008). "Numerical prediction of concrete slab response to blast loading." *International Journal of Impact Engineering*, 35(10), 1186–1200.

LIST OF PUBLICATIONS

Book Chapter:

- Bhuyan, Kasturi, Kiran Kumar Jujjavarapu, and Hrishikesh Sharma. "Performance Evaluation of Two-Way RC Slab Subjected to Blast Loading Using Finite Element Analysis." In *Advances in Structural Technologies*, pp. 57-70. Springer, Singapore, 2021.

Conference:

- Rahman, T. and Bhuyan, K. "Ground Response Analysis at the Rukni Irrigation Project Site located in Assam, India", in Proceedings of International Conference on Sustainable Energy and Built Environment, VIT University, Vellore, 2015, pp. 594-600.
- Bhuyan. K., Kumar, S. and Sharma, H. "Rapidly Constructed Pre-fabricated Ultra High Performance Composite (RCPUC) Solution For Seismic Resistant Construction", Seminar on Pre Fab Structures, MES Chandigarh, 2018
- Bhuyan, Kasturi, Sah, A. K., and Sharma, H. "Practical Application of High Strength Concrete Matrix for Use in Defense Establishments." In Proceedings of the International UKIERI Concrete Congress, Jalandhar, India, March 2019, pp. 90.

Journal:

- Gangolu, J., Kumar, A., Bhuyan, K. and Sharma, H., 2022. Performance-based probabilistic capacity models for reinforced concrete and prestressed concrete protective structures subjected to missile impact. *International Journal of Impact*

Engineering, 164, p.104207. https://doi.org/10.1016/j.ijimpeng.2022.104207 [Impact Factor: 4.208]

- Gangolu, J., Kumar, A., Bhuyan, K. and Sharma, H., 2022. Probabilistic demand models and performance-based fragility estimates for concrete protective structures subjected to missile impact. *Reliability Engineering & System Safety*, 223, p.108497. https://doi.org/10.1016/j.ress.2022.108497 [Impact Factor: 6.188]
- Kasturi Bhuyan and Hrishikesh Sharma, Reliability-based Code Calibration for Slabs/Walls of Protective Structures Subject to Air Blast Loading, Submitted: Reliability Engineering & System Safety (JRESS-D-22-00784)
- Kasturi Bhuyan, Jaswanth Gangolu and Hrishikesh Sharma, Sustainable High Strength Concrete (HSC) Framed Structure Subjected to Blast Loading, Submitted: Sustainable Futures (SFTR-D-22-00060)
- Kasturi Bhuyan and Hrishikesh Sharma, Probabilistic Capacity Model and Fragility estimate for NRC and UHSC panel subject to Contact Blast, Submitted: International Journal of Impact Engineering (IE-D-22-00588)
- Kasturi Bhuyan and Hrishikesh Sharma, Probabilistic Demand Model and Code Calibration for NRC and UHSC panel subject to Blast Loading, to be submitted: Computer-Aided Civil and Infrastructure Engineering, Impact Factor: 11.775.
- Kasturi Bhuyan and Hrishikesh Sharma, Development of a Blast Resistant Framed Structure using High Strength Concrete under uncontrolled condition, to be submitted: Construction and Building Materials, Impact Factor: 6.141.
- Kasturi Bhuyan and Hrishikesh Sharma, Shape and size effect of TNT container on Free Air Blast Pressure, to be submitted: Journal of Engineering Structures, Impact Factor: 4.471.

CURRICULUM VITAE

Name: Kasturi Bhuyan

Address: Indian Institute of Technology Guwahati

Guwahati 781039

Assam, India

b.kasturi@iitg.ac.in

Education: Diploma (Civil Engineering) 2010 Assam Engineering Institute, Chandmari, Guwahati, Assam, India

B.E. (Civil Engineering) 2013 Gauhati University, Guwahati, Assam, India

M. Tech (Structural Dynamics and Earthquake Engineering) 2015 National Institute of Technology (NIT) Silchar, Assam, India